Synthesis and characterization of carbonated hydroxyapatite and bioinspired polymer-calcium phosphate nanocomposites

by

Yusuf Yusufoglu

A dissertation submitted to the graduate faculty

in partial fulfillment of the requirements for the degree of

DOCTOR OF PHILOSOPHY

Major: Materials Science and Engineering

Program of Study Committee:
Mufit Akinc, Major Professor
Surya K. Mallapragada
Klaus Schmidt-Rohr
Matthew J. Kramer
Zhiqun Lin

Iowa State University

Ames, Iowa

2009

TABLE OF CONTENTS

CHAPTER 1. GENERAL INTRODUCTION

1.1 Thesis Introduction

Nature offers many exciting ideas and inspiration for the development of new materials and processes. The toughness of spider silk, the strength and lightweight of bone, and the adhesion abilities of the gecko's feet are some of the many examples of high-performance natural materials, which have attracted the interest of scientist to duplicate their properties in man-made materials [1]. Materials found in nature combine many inspiring properties such as miniaturization, sophistication, hierarchical organization, hybridization, and adaptability. In all biological systems, whether very basic or highly complex, nature provides a multiplicity of materials, architectures, systems and functions [2, 3]. Generally, the architectural configurations and material characteristics are the important features that have been duplicated from nature for building synthetic structural composites.

Many biological materials have mechanical properties that are far beyond those that can be achieved using the same synthetic materials with the present technologies [4]. Biomaterials, such as bone, teeth, nacre, diatoms, antlers, arthropod cuticle, and sea shell are some examples of organic-inorganic nanocomposites from nature, which have been studied extensively as models for synthetic structural composites because of their unusual combinations of mechanical properties [5]. These biological materials incorporate both biomacromolecules such as proteins, lipids and polysaccharides, and inorganic materials, such as hydroxyapatite, silica, and calcite. The organic component of the biomaterials provides toughness to the otherwise brittle inorganic phase and they are arranged in intricate ways to achieve specific combinations of stiffness, strength and toughness [6, 7]. For instance, human femur can withstand loads up to 1650 kg [8]. In addition, sea shells, another example, are twice as hard and several thousands times as tough as the pure minerals of which they are composed [9, 10].

Biological systems use very few components to construct increasingly complex materials from a relatively small set of building blocks. The same component is used in many different ways to meet several different needs as exemplified by type I collagen, which serves as the building block for a variety of tissues in the human body: bone; cartilage; skin; or eye cornea [2]. Moreover, natural materials are self-generating, self-repairing, and biodegradable. They also show complex hierarchical organization from nanometer to the macroscopic scale and every structural level contributes to the mechanical stability and toughness of the resulting design [11, 12]. Additionally, most biological materials are multifunctional. For instance, bone provides structural support for the body, protects organs, and produces blood cells and exoskeleton in arthropods provides an attachment for muscles, environmental protection, and a water barrier [13].

Living organisms are known to develop different ways to produce high-performance materials. Approximately 60 different biological minerals have been already reported [14]. Among these, calcium phosphates have received considerable attention over many years, and in particular hydroxyapatite (HAp), as it is the most important inorganic component of vertebrate bones and mammalian teeth. In the form of carbonated hydroxyapatite (CO_3HAp), it is present in the bone, teeth and tendons to give these organs the stability, hardness, and function [7, 15]. It is believed that in the bone both the size and the orientation of the apatite crystals are dictated specifically by the collagen template, and the precise structural relationship between the collagen and apatite minerals is critical to bone's resilience and strength [16].

The field of biomimetics (the science of imitating nature) and bioinspired approach to materials design has grown quickly in recent years and become one of the most promising scientific and technological challenges of the coming years [2, 17]. Having extraordinary chemical and mechanical properties, being synthesized in aqueous environments under ambient conditions, bone and other rigid biological structures have inspired a large class of biomimetic advanced materials and organic-inorganic composites [18, 19].

Taking the inspiration from natural bone, where type I collagen (a hydrogel that acts as a template) provides sites for the nucleation and growth of an inorganic dahllite (CO_3HAp), different polymeric substrates namely, triblock Pluronic® F127, self-assembling thermo-reversibly gelling pentablock copolymers with different ionic functional groups, block copolymers conjugated to hydroxyapatite-nucleating peptides, polylysine-polyleucine diblock copoly-peptides, and poly(methylmethacrylate) (PMMA) films were employed as a template for the precipitation of nano-sized calcium phosphates from aqueous solutions. In this regard, the overall theme of this work is to develop and characterize hierarchical multiscale self-assembly of polymer-calcium phosphate nanocomposites using a bottom up approach. In addition, synthesis and characterization of carbonated hydroxyapatite, a mineral found in biological systems, is also investigated in this study.

1.2 Thesis Organization

This thesis adopts a journal paper format described in the Graduate College Thesis Manual, as such each manuscript, some of which are already published, appears as a separate chapter. In addition, a general introduction and an overall conclusion are included as the first and last chapter respectively of the dissertation.

The second chapter is general background of calcium phosphate compounds, which are the main mineral phase of bone and other hard tissues in human body. An extensive review on the structure and formation of bone and other biological hard composite materials is included in this chapter. In addition, a detailed literature review on the synthesis of hydroxyapatite and bioinspired hydroxyapatite-polymer composites is also given in this chapter. The background and literature review provide a context for the inspiration and the objectives of this study as described in the research objectives in the third chapter.

The fourth chapter is a manuscript, entitled "Effect of pH on the carbonate incorporation into the hydroxyapatite prepared by an oxidative decomposition of calcium-EDTA chelate", which has been already published in the *Journal of American Ceramic Society* [20]. It discusses the possible roles pH plays on the incorporation of carbonate into the HAp lattice and its effects on lattice parameters.

The fifth chapter is a manuscript, entitled "Deposition of carbonated hydroxyapatite (CO_3HAp) on poly(methylmethacrylate) surfaces by decomposition of calcium-EDTA chelate", which has also been published in the *Journal of American Ceramic Society* [21]. In this study, the development of organic-inorganic composites between synthetic polymers and carbonated HAp has been investigated.

The sixth chapter is a manuscript, entitled "Synthesis and characterization of ionic block copolymer templated calcium phosphate nanocomposites", which has been published in *Chemistry of Materials* [22]. It addresses on the use of anionic and zwitterionic pentablock copolymers as templates for precipitation of calcium phosphate nanostructures, controlling their size and ordered arrangement.

The seventh chapter is a manuscript, entitled "Bioinspired synthesis of self-assembled calcium phosphate nanocomposites using block copolymer-peptide conjugates", which has been published in the *Journal of Materials Research* [23]. This work offers routes for bioinspired bottom-up approach for the development of novel, self-assembling polymer calcium phosphate nanocomposites.

The eighth chapter is a manuscript, entitled "Self-assembled calcium phosphate nanocomposites using block copolypeptide templates", which has been accepted by *Soft Matter* [24]. In this work, compared to our previous studies, a novel nanocomposite with significantly increased calcium phosphate content has been developed. The studies presented in sixth, seventh, and eighth chapters were collaborative work and the author of this dissertation was one of the primary contributors to each of these manuscripts.

The ninth chapter covers the general conclusions of the study and future directions for the development of novel polymer-inorganic composite materials.

1.3 References

1. F. Barthelat. *Philos. Trans. R. Soc., A: Mathematical, Physical & Engineering Sciences*, (2007); 365, p: 2907-2919.
2. C. Sanchez, H. Arribart, M. Madeleine, and G. Guille. *Nat. Mater.*, (2005); 4, p: 277-288.
3. Y. Bar-Cohen. *Biomimetics: Biologically Inspired Technologies,* (2006)*;* p: 2-511; Boca Raton, CRC Press, Taylor&Francis Group.
4. J. Vincent. *Structural Biomaterials,* (1990)*;* p: 1-244; New Jersey, Princeton University Press.
5. G. Mayer. *Science*, (2005); 310, p: 1144-1147.
6. Z. Tang, N.A. Kotov, S. Magonov, and B. Ozturk. *Nat. Mater.*, (2003); 2, p: 413-418.
7. L.A. Heinz and S. Weiner. *On Biomineralization,* (1989)*;* p: 3-324; New York, Oxford University Press.

8. M. Vallet-Regi and J.M. Gonzalez-Calbet. *Prog. Solid State Chem.*, (2004); 32, p: 1-31.
9. S. Mann. *Biomimetic Materials Chemistry,* (1996)*;* p: 1-383; New York, John Wiley & Sons, Inc.
10. B.L. Smith, T.E. Schaffer, M. Viani, J.B. Thompson, N.A. Frederick, J. Kind, A. Belcher, G.D. Stucky, D.E. Mors, and P.K. Hansma. *Nature*, (1999); 399, p: 761-763.
11. J.D. Currey. *Science*, (2005); 309, p: 253-254.
12. J. Aizenberg, J.C. Weaver, M.S. Thanawala, V.C. Sundar, D.E. Morse, and P. Fratzl. *Science*, (2005); 309, p: 275-278.
13. M.A. Meyers, A.Y.M. Lin, Y. Seki, P.-Y. Chen, B.K. Kad, and S. Bodde. *Congr. Anu. ABM*, (2006); 61st, p: 4310-4338.
14. S. Mann. *Biomineralization Principles and Concepts in Bioinorganic Materials Chemistry,* (2001)*;* p: 1-198; New York, Oxford University Press.
15. S.V. Dorozhkin and M. Epple. *Angew. Chem., Int. Ed.*, (2002); 41, p: 3130-3146.
16. T.A. Taton. *Nature*, (2001); 412, p: 491-492.
17. E. Dujardin and S. Mann. *Adv. Mater.*, (2002); 14, p: 775-788.
18. S. Mann. *Nature* (1988); 332, p: 119-124.
19. M.L. Oyen. *MRS Bull.*, (2008); 33, p: 49-55.
20. Y. Yusufoglu and M. Akinc. *J. Am. Ceram. Soc.*, (2008); 91, p: 77-82.
21. Y. Yusufoglu and M. Akinc. *J. Am. Ceram. Soc.*, (2008); 91, p: 3147-3153.
22. M. Kanapathipillai, Y. Yusufoglu, A. Rawal, Y.Y. Hu, C.T. Lo, P. Thiyagarajan, Y.E. Kalay, M. Akinc, S. Mallapragada, and K. Schmidt-Rohr. *Chem. Mater.*, (2008); 20, p: 5922-5932.
23. Y. Yusufoglu, Y. Hu, M. Kanapathipillai, M. Kramer, Y.E. Kalay, P. Thiyagarajan, M. Akinc, K. Schmidt-Rohr, and S. Mallapragada. *J. Mater. Res.*, (2008); 23, p: 3196-3212.
24. Y. Hu, Y. Yusufoglu, M. Kanapathipillai, C.-Y. Yang, Y. Wu, P. Thiyagarajan, T. Deming, M. Akinc, K. Schmidt-Rohr, and S. Mallapragada. *Soft Matter*, (2009); accepted.

CHAPTER 2. BACKGROUND AND LITERATURE REVIEW

2.1 Calcium Phosphate Bioceramics

The structure of the calcium phosphate (CaP) solid phase in bone was first determined in 1926 as a crystalline calcium phosphate by chemical analysis and X-ray diffraction [1]. Calcium phosphate ceramics are the most important inorganic component of biological hard tissues and have been used in medicine and dentistry for more than 20 years [2-4]. Some of the applications are dental implants, skin treatments, gum treatment, jawbone reconstruction, orthopedics, facial surgery, ear, nose, and throat repair, and spinal surgery. Depending on whether a resorbable or bioactive material is desired, different phases of calcium phosphate ceramics are used [5]. The common calcium phosphate compounds and their chemical formulas are given in Table 2.1. The crucial parameters of calcium orthophosphates are the atomic Ca/P ratio, acidity-alkalinity, and solubility in water. All these parameters are strongly related with the pH of solution.

The temperature and the presence of water (either during processing or during use in the environment) affect the stability of the calcium phosphate phases. At body temperature only two calcium phosphates are stable in contact with aqueous media. At $pH < 4.2$ the stable phase is dicalcium phosphate dihydrate ($CaHPO_4 \cdot 2H_2O$, brushite), whereas at $pH \geq 4.2$ the stable phase is hydroxyapatite [$Ca_{10}(PO_4)_6(OH)_2$)]. Moreover, at higher temperatures other phases, such as β-tricalcium phosphate and tetracalcium phosphate are present [5]. As shown in Figure 2.1, the pH solubility diagrams of various calcium phosphate isotherms have a negative slope in the acidic and neutral regions ($pH \leq 8$), which suggests that they become less soluble as pH increases up to a certain pH value. Furthermore, the plots indicate that the order of solubility changes as the pH increases and they also show the regions of undersaturation (below the curve) and supersaturation (above the curve) for respective mineral phase. The isotherm lying below those of others is less soluble and more stable at a given pH. For instance, at pH=7, the solubility decreases in the order of TTCP > α-TCP > DCPD > DCPA ~ OCP > β-TCP > HAp (see Figure 2.1). The pH dependency is due to the fact that orthophosphoric acid is both a weak acid and a polybasic acid; the concentrations of HPO_4^-, $H_2PO_4^{2-}$, and PO_4^{3-} change significantly with the pH of the solution. In addition, it is also worth noting that while the solubility of most salts increases as temperature increases, the trend is opposite for the calcium phosphates and temperature change may be invoked as a strategy for HAp precipitation. Moreover, in a recent study, Pan and Darvell [6] have provided a good review on the solubility of calcium phosphates.

2.1.1 Hydroxyapatite

Hydroxyapatite (HAp) is one of the naturally occurring calcium phosphate bioceramics with the chemical formula of $Ca_5(PO_4)_3(OH)$, but is usually written as $Ca_{10}(PO_4)_6(OH)_2$ to denote that the crystal unit cell consists of two formula units. It has a hexagonal structure with space group $P6_3/m$ and lattice parameters $a = b = 9.4225$ Å and $c = 6.8850$ Å (see Figure 2.2) [7]. HAp is one of the most used calcium phosphate in implant fabrication since it is the most similar compound to the mineral phase of the bones [8, 9]. Even though HAp exhibits good properties as a biomaterial, such as biocompatibility, bioactivity, osteoconductivity, and direct bonding to bone, the brittleness, low strength and poor fatigue resistance severely restricts its application for load-bearing purposes in orthopedics [10-12]. One solution is to develop composites such as HAp-polymer, HAp-metals, HAp-ceramics, which are widely used in medicine for repair of bone tissue [5, 13-16].

When HAp is combined with organic polymers in biological process (biomineralization), the resulting biocomposite material overcome the intrinsic brittleness observed in pure HAp [17]. Bones, teeth, shell of marine mollusks, and the arthropod cuticle are some examples of highly complex organic-inorganic composite materials produced in nature. In addition, HAp can be used for coating metallic prostheses which result in combination of the good mechanical properties of metals and alloys with the excellent biocompatibility and bioactivity of hydroxyapatite [10].

The bioactive and mechanical behavior of HAp can be improved by introducing some substitutions in the structure [18, 19]. The apatite structure can incorporate CO_3^{2-} and substitute for PO_4^{3-} and OH^- sites and electrical neutrality is usually achieved by the incorporation of Na^+, K^+, Mg^{2+}, Fe^{2+}, Sr^{2+}, Cl^-, F^-, HPO_4^{2-}, and possibly other elements [4, 20]. The presence of CO_3^{2-} in the structure has paramount importance [4, 7, 21, 22] and it influences the crystal structure, stability, surface charge and biological activity of the apatite. Most biological apatites contain carbonate in the lattice and carbonates in biological apatites usually occupy lattice positions in the PO_4^{3-} sublattice (B-type apatites) [21]. Moreover, incorporation of other ions as well as carbonate allows designing, developing and characterizing new and better apatites for certain applications. These ionic substitutions can alter the surface structure and electrical charge of hydroxyapatite, with potential influence on the material properties in biological environments [4]. For instance, small amounts of strontium, zinc, or silicates have been found to play a role in facilitating the bone regeneration [23].

2.1.2 Brushite

Brushite also has biological importance because it is often found in pathological calcifications [24]. It has been proposed as an intermediate in both bone mineralization and dissolution of enamel in acids. Due to its large resorption rate, brushite is desirable over hydroxyapatite when resorption of synthetic material and reforming of natural bone is preferred like bone cements. Brushite also has good biocompatibility and can be applied as coating for orthopedic implants [25]. The significance and different applications of all calcium phosphates have been reported recently with an extensive literature review by Dorozhkin [3].

2.2 Nucleation of Calcium Phosphates on a Template

Biologically mineralized crystals are typically formed in an organic matrix with precise regulation of synthesis mechanisms through proteins [26]. Deposition of calcium phosphate (CaP) on the functionalized surfaces takes place in three stages: (i) Calcium ions are attracted to the functionalized surface, followed by the attraction of phosphate ions, (ii) CaP precipitates from the physiological fluid, and (iii) growth of CaP with time. Schematic representation of this process is shown in Figure 2.3. The organic surface has important functions in promoting mineral deposition. These include physisorption of ions and colloidal precipitates, orientation of crystal lattices, preferential deposition of particular crystal phases, and heterogeneous nucleation [27].

Even though the organic matrix in bone and other biological systems certainly have important functional roles in the mechanical strength and toughness of the mineralized composite, the well-defined crystallographic relationship indicates there is an underlying molecular function of the macromolecules in the organic matrix. As will be explained in more detail in the following sections, the formation of crystals with preferred orientations at specific sites on the organic matrix shows evidence that interactions at the mineral-matrix interface are the key to the regulation of nucleation [28].

Nucleation theory has been studied elsewhere numerous times [27, 29]. In general, nucleation represents an activation energy barrier to the spontaneous formation of a solid phase from a supersaturated solution. The starting point for both heterogeneous and homogenous nucleation is that the free energy for formation of a cluster size *r,* in a solution of a supersaturation *S,* is given by the balance between the energy gained by formation of bulk phase, (*kTInS* per molecule, where *k* is the Boltzmann constant and *T* is the temperature) and the energy required to form new surface area. The equation can be written as;

$$\Delta G = -r\,k\,T\,In\,S + \sigma A \qquad (1)$$

where σ is the interfacial free energy for nucleation, and A is the surface area of nucleus. For the HAp, the degree of supersaturation may be expressed in terms of the lattice ion activities:

$$S = \left(IP / K_{sp}\right)^{1/9} \qquad (2)$$

where $IP = \left(Ca^{2+}\right)^5 \left(PO_4^{3-}\right)^3 (OH)$ and K_{sp} is the solubility product which has value of $4.7\text{x}10^{-59}$ at 25 °C [30].

The kinetic constraints of nucleation may be sufficient to offset the thermodynamic driving force for inorganic precipitation, supersaturation. While homogeneous nucleation occurs in the bulk of the supersaturated solution, heterogeneous nucleation involves the formation of nuclei on the surfaces of a substrate present in the aqueous medium. Although the homogenous nucleation does not generally take place in biomineralization, the basic knowledge of this process helps the understanding of nucleation at the surface of a template [31].

The free energy of formation of a nucleus, ΔG_N, is given by the difference between the surface (interfacial), ΔG_I, and bulk energies, ΔG_B;

$$\Delta G_N = \Delta G_I - \Delta G_B \tag{3}$$

For the classical case of a spherical nucleus;

$$\Delta G_I = 4\pi r^2 \sigma \tag{4}$$

where σ is the interfacial free energy per unit surface area, and

$$\Delta G_B = \frac{4\pi r^3 \Delta G_V}{3V_m} \tag{5}$$

where ΔG_V represents the free energy per mole associated with the solid-liquid phase change, and V_m is the molar volume.

$$\Delta G_N = 4\pi r^2 \sigma - \frac{4\pi r^3 \Delta G_V}{3V_m} \tag{6}$$

$at\ r = r^*\ dG_N = 0$

$$r^* = \frac{2\sigma V_m}{\Delta G_V} \tag{7}$$

As shown in Figure 2.4, the combination of plots of ΔG_I and ΔG_B goes through a free energy maximum, (ΔG_N^*), (which is the activation energy for homogenous nucleation) at the critical radius of a particle (r^*). Substituting r^* into the r in $Equation\ 6$ yields;

$$\Delta G_N^* = \frac{16\pi\sigma^3 \upsilon^2}{3\left(kT\, In\, S\right)^2} \tag{8}$$

where υ is the molecular volume. The rate of homogenous nucleation, J_r, is given by an Arrhenius equation with a pre-exponential factor, A.

$$J_r = A\exp\left(-\Delta G_N^* / RT\right) \tag{9}$$

Equation 8 is also applicable for heterogeneous nucleation and the Gibbs free energy for the heterogeneous nucleation, ΔG_{het}, is lower than that for the homogenous nucleation, ΔG_{hom}, by a factor of $f(\theta) \langle 1$, as follows;

$$\Delta G_{het} = f(\theta)\Delta G_{\mathrm{hom}} \tag{10}$$

where $f(\theta)$ is the function of the contact angle, θ, between the crystalline deposit and the surface, corresponding to the wettability, and can be expressed as:

$$f(\theta) = \frac{(2+\cos\theta)(1-\cos\theta)^2}{4} \tag{11}$$

The above equations illustrate which factors are critical in biological systems for regulation of biomineralization. The activation energy for nucleation can be reduced by decreasing the interfacial energy and/or increasing the supersaturation. Supersaturation levels are regulated by confining the mineralization reactions to diffusion-limited sites, such as intracellular vesicles and membrane-bound extracellular compartments, where selective ion-transport to and from the mineralization zone can effectively be controlled [28]. Furthermore, interfacial energies can be decreased by the presence of surfaces at the nucleation site. Therefore in biological systems and synthetic HAp-polymer composites, the primary function of the organic matrix in controlling the inorganic nucleation is to lower the activation energy by reducing the interfacial energy [32]. This is illustrated in Figure 2.5. The specific level of lowering of the activation energy for nucleation is related to the matching of charge, polarity, structure and stereochemistry at the interface between an inorganic nucleus and an organic macromolecular surface [31].

2.3 Natural Organic-Inorganic Composites

2.3.1 Bone

Bone is a dynamic and highly vascularized tissue serving physiological, protective and mechanical functions. Bone also provides a protective site for the blood-forming system (bone marrow) and a reservoir for minerals, particularly calcium and phosphate [33]. In addition, bone appears to be one of the strongest materials developed by nature. One cubic inch of bone can withstand loads up to 20,000 pounds, which is over four times the strength of concrete [33].

When considering the structure and formation of the bone, there are two main stages of bone formation, which is called as primary and secondary ossification (osteogenesis), and the mechanism of bone formation is different to some degree in these two stages [34-38]. Primary bone formation (endochondral ossification) takes place in epiphysial cartilage, which is composed of very loose and small fibril bundles of collagen [37, 39]. In this stage of bone formation, the collagen fibrils are arranged more or less randomly and the mineralization is unorganized, forming a woven bone microstructure. The inorganic crystals do not form in close association with the collagen and therefore the collagen does not appear to play an important role in directing the mineralization process [34, 40]. In the secondary bone formation, the primary woven bone is remodeled into a more organized structure (parallel-fibered or lamellar bone), which in the case of humans is organized into concentric lamellae that make up the osteons of the haversian systems. Human bone is similar to that of many primates and carnivores in that primary fibrolamellar bone is laid down first, but this bone type is soon replaced by haversian bone [36]. Most mammalian bone is lamellar and when discussing the unique structure of the bone, people usually refer to secondary bone, which is often described in terms of its hierarchical levels of structure [34, 40].

Bones contain five types of cells including osteogenic, osteoblasts, osteocytes, osteoclasts, and bone-lining cells, and they are involved in regulating bone growth [33, 37, 41]. Osteogenic cells are found mostly in the periosteum and bone marrow. These cells can be transformed into bone-forming cells (osteoblasts) or bone-destroying cells (osteoclasts) during healing [42]. Osteoblasts are bone-forming cells and are involved in the production of type I collagen and noncollagenous proteins in the bone matrix. They also regulate the flow of calcium and phosphate ions in and out of bone tissue and are usually found in the growing portions of bones [41, 42]. Osteocytes are the main cells in mature bone. They have an active role in homeostasis by helping to release calcium from bone tissue into the blood, which regulates the concentration of calcium in the body fluids. Osteocytes are also involved in keeping the matrix in a stable and healthy state by secreting enzymes and maintaining its mineral content [37]. Osteoclasts are giant cells mostly responsible for resorption of bone minerals. Bone-lining cells act as ion barrier around bone tissue. This barrier helps to regulate the flux of calcium and phosphate in and out of bone matrix that in turn helps to control the deposition of hydroxyapatite in the bone tissue [37].

In order to truly understand the structure and extraordinary properties of the bone, it is necessary to examine the bone at different level of organization. In a pioneering study, Currey [36] investigated the structure of the bone by clearly differentiating between several levels of organization. According to Currey, bone has a very complex structure and there is no level of organization at which one can truly be said to be looking at “bone” as such. Later, to better understand the structure and exceptional mechanical properties of the bone, Weiner and Wagner [43] described the structure of the bone in terms of up to seven hierarchical discrete levels of organization (see Figure 2.6). In their model, bone is considered as a family of materials in which mineralized collagen fiber is the basic building block. Moreover, Rho and his colleagues have [44] also presented a similar structural hierarchy of bone as schematically demonstrated in Figure 2.7. Drawing upon these outstanding studies, the structure of the bone will be described at different levels of organization in the next few sections.

2.3.1.1 Bone at the macrostructure level

The highest level of organization differentiates between a relatively dense, very hard compact (or cortical) bone and a less dense, porous cancellous (or spongy) bone (see Figures 2.7 and 2.8). These two bone types can extend for centimeters or more. Even though porosity and density plays an important factor in distinguishing compact and cancellous bone, true differentiation arise from histological evaluation of the tissue’s microstructure [35, 44]. Compact bones consist of organized and densely packed collagen fibers and minerals. Approximately 80% of the skeletal mass in the adult human skeleton is compact bone, which forms the outer wall of all bones [42]. They are made of a number of cylindrical structures known as osteons or haversian systems (see Figure 2.7) and the bulk of the compact bone is found mostly in the shafts of long bones where a strong, tubular structure is required [45]. Furthermore, the mechanical properties of compact bone are affected significantly by the porosity, the mineralization level and the organization of the solid matrix [44]. Cancellous bones, on the other hand, are composed of a loosely packed and disordered porous matrix. They are filled with a gel-like tissue called as bone marrow and are found in the parts of the most bones where low density and strength are required. Cancellous bones are in the form an open, lacy pattern which withstands maximum stress and supports shifts in weight distribution. In the interior structure of the cancellous bone, there are trabeculae which form the internal support structure of the bone [37, 45]. In general, the microstructural difference between compact and cancellous bone is related to their functions in the body because compact bone provides structural support and protection, whereas cancellous bone mainly has metabolic functions [41]. In addition, cancellous bone is metabolically more active and remodeled more often than compact bone. Therefore, although cancellous and compact bones are composed of the same kind of material, the maturation of the compact bone material may change the mechanical properties at the microstructural level, which results in a mechanically extremely important distinction between compact and cancellous bone [40, 44].

2.3.1.2 Bone at the microstructure level

At the microstructure level, Currey [36] recognizes four main types of bone in mammals, two of which are simply woven and lamellar bone that extend over longer distances and these two types of bone will be discussed in more detail in the next section (at the sub-microstructural level). The third type is the haversian system or secondary osteon, which is observed in many bones, particularly those of advanced mammal-like reptiles and mammals. The formation of haversian systems or secondary osteons is as follows; mineralized collagen fibers form concentric layers called lamellae (3-7 μm wide) as illustrated in the Figures 2.6 and 2.7. In some cases, these lamellae are arranged in a wider and wider cylindrical motif, each one nestled inside the next one and finally form what is known as an osteon or haversian systems (200-250 μm in diameter). In the center of the osteons, there are other even smaller capillary-like channels and these numerous longitudinal channels contain blood vessels and other cells (osteocytes) that remain within the bone material itself [43]. As was shown by Weiner *et al*. [43] these central channels tend to radiate out from the central blood vessel and thus, the structure of an osteon appears basically onion-like in cross section with layers of lamellae surrounding a central hole (see Figure 2.6, Level 5). The structure of osteons provides the great strength needed to resist typical, everyday compressive forces on long bones [37]. The fourth characteristic type of mammalian bone is laminar or fibrolamellar bone. It is found mainly in large mammals, whose bones have to grow in diameter rather quickly [36].

2.3.1.3 Bone at the sub-microstructure level

Above the level of the collagen fibril and its associated mineral, mammalian bone usually exists in three distinct forms, namely woven bone, lamellar bone, and parallel-fibered bone [36]. In woven bone, the collagen is finely fibered (around 0.1 μm in diameter) and is oriented almost randomly and calcium phosphate crystals are not as uniformly oriented along the line of the collagen fibers as is the case in lamellar bone [40]. Woven bone is put down rapidly during growth or repair but as growth is in progress, it is usually replaced by lamellar bone [3]. Lamellar bone, on the other hand, is much more ordered, and laid down much more slowly than woven bone. The collagen and its associated mineral are arranged in sheets called lamellae and these sheets have average thicknesses around 5 μm [35, 36]. In general, lamellar bone is much stronger than woven bone. Finally, parallel-fibered bone is structurally intermediate between woven and lamellar bone and found in particular bones and situations [36]. Recent observations showed a variety of toughening mechanism at the microscale such as viscoplastic flow, crack deflection, microcracking and crack bridging [46].

2.3.1.4 Bone at the nanostructure level

The most prominent structures observed at this scale are the collagen fibers with mineral embedded in its structure. In the bone family of materials, the mineralized collagen fibrils are usually arranged in bundles or arrays aligned along their lengths (see Figure 2.6, Level 3) [43, 47]. Furthermore, the four different arrangements of these fibrils (parallel, woven, plywood, and radial) are shown in Figure 2.6, Level 4. Even though the detailed internal structural organization of the fibril arrays is poorly documented, it is known that these bundles are not discrete and fibers from one bundle may fuse with a neighboring bundle [43].

2.3.1.5 Composition of the bone

At the molecular level, the bone family of materials can be considered as a composite material composed of approximately 65 wt % mineral phase, 25 wt % organic, and 10 wt % water. By volume, the mineral phase accounts for 40 %, whereas the organic matrix comprises 45 % and 15 % is water [34, 35, 48]. The mineral phase is mainly carbonated HAp including traces of other ionic substitutions in its structure. The organic phase, on the other hand, is mostly type I collagen with non-collagenous proteins that comprise around 10 % of the total organic content [35]. Furthermore, it is reported that the relative amounts of mineral, collagen, and water vary in a systematic manner between different bone types [49]. The volume relationship show that collagen content remains mainly the same, whereas the increase in mineral content occurs at the expense of the water content [43].

2.3.1.6 Mineral phase of the bone

The mineral phase in bone has two major functions [50]. First of all, it acts as an ion reservoir and regulates the appropriate concentrations of calcium, sodium, magnesium, phosphate, and other ions in the extracellular fluid, which are crucial for many physiological functions and biochemical reactions. The other important function is that the combination of mineral phase with the organic matrix components in an extraordinary manner gives the bone both lightweight and extremely tough properties.

Even though the bone mineral is commonly referred to as hydroxyapatite (HAp) [$(Ca_{10}(PO_4)_6(OH)_2$], it is carbonated hydroxyapatite (dahllite) including trace ions such as, Cl^-, F^-, HPO_4^{2-}, Na^+, Mg^{2+}, Fe^{2+}, and several other elements as shown in Table 2.2. [51-53]. Consequently, a more appropriate structural formula for the composition of bone mineral can be written as $(Ca, X)_{10}(PO_4, CO_3, Y)_6(OH, Z)_2$ with X substituting cations and Y and Z substituting anions (with the indices 10, 6, and 2 changing according to stoichiometry) [54]. The carbonate content in the bone mineral ranges between 5–8 wt % [23] and about half of the carbonate present in the bone is incorporated in the PO_4 sites while the remaining carbonate is on the bone mineral crystal surface where it is easily available for surface exchange [55]. An important contribution carbonate makes to the properties of bone is the increased reactivity imparted to bone mineral by the structural disorder resulting from its substitution within the crystal [56]. Moreover, the trace ions incorporated into the structure of carbonated hydroxyapatite accounts for approximately 2 wt % of total bone mineral but they play a crucial role in the biochemical reactions associated with bone metabolism. The quantitative composition of the bone mineral is complex and can vary within one bone, between bones, between individuals, between species, with diet/age, and with pathological conditions and [24, 42, 57]. Therefore, it is difficult to assign a unique chemical formula for the bone mineral. Legeros *et al.* [58] offered the following formula for the bone mineral: $Ca_{8.3}(PO_4)_{4.3}(CO_3)_x(HPO_4)_y(OH)_{0.3}$, where y decreases and x increases with increasing age but ($x+y$) remains constant and equal to 1.7. Recently, Schmidt-Rohr [59] has suggested the chemical formula of $(Ca^{2+})_8(Mg^{2+})_{0.32}(Na^{+})_{0.4}(PO_4)^{3-}_{4.74}(HPO_4)^{2-}_{0.53}(CO_3)^{2-}_{0.73}\ (OH)^{-}_{0.3}$, which includes other ionic substitutions. In addition, it is also worth noting the near-absence of the hydroxyl ions in the bone mineral. Several studies have proven repeatedly that bone apatite leaves little place for hydroxyl ions and it was suggested to refer to bone mineral as carbonated apatite rather than hydroxyapatite [53, 60, 61].

Although there is no universal agreement on the exact chemical mechanism of mineral formation in the bone, it is clear that the mineral phase is carbonated hydroxyapatite with ionic substitutions but reduced amounts of hydroxide and with Ca/P molar ratio of less than 1.67 (stoichiometric value of pure HAp). However, various studies on the precipitation of CO_3HAp and pure HAp have shown that none of these compounds directly precipitates from supersaturated aqueous solutions containing calcium and phosphate ions. Some intermediate phases (precursors) are always involved. Amorphous calcium phosphate, brushite, and octacalcium phosphate (OCP) have all been implicated as being precursor phase in the formation of CO_3HAp and HAp in vitro. Therefore, these compounds are also suggested as the precursors to in vivo bone formation [24, 54, 62, 63].

The majority of studies in the literature describe the mineral crystals of the bone as irregular plate-like in shape. In a very early transmission electron microscopy (TEM) study, Robinson [64] in a landmark paper reported plate-shaped crystal with 10 nm in thickness, 25 nm in width, and 50 nm in length for the mineral phase of normal human bone. Recently, in another TEM study, Rubin *et al.* [65] also observed plate-like crystals with almost the same dimensions for the mineral phase in a normal human bone. By using TEM and 3D-TEM techniques, the plate-like morphology of the crystals in human bone and other bones has been repeatedly confirmed with the thickness of the platelets ranging from 2-8 nm, the width from 10-30 nm, and the length from 35-80 nm [24, 66-71]. Recent measurements by atomic force microscopy also confirmed plate-like shape of the crystals in normal bone but with a rather wide range of geometrical dimensions [72, 73]. However, researchers still debate about the nature of the mineral crystal shape in the bone, rod-like versus plate-like. Fratzl *et al*. used small angle X-ray scattering (SAXS) to determine the size and shape of mineral particles and the authors reported rod-like morphology with 3.5 x 3.5 x 50 nm dimensions [74, 75]. Moreover, at least during the early stages of crystal development, these nano-sized mineral crystals grow preferentially in the *c*-axial direction (lengthwise) with other growth present in the crystal width but not thickness. In other words, the *c* axes of the crystals are roughly parallel to the long axes of the collagen fibrils [76]. These features are important especially when considering the structural organization of collagen and the interaction between collagen and the apatite crystals, which will be discussed in the following sections [66, 77].

Small dimensions, low crystallinity, high surface-area-to-volume ratio, and non-stoichiometric composition with a defect structure incorporating ion substitutions, as well as lattice vacancies are distinct features of the bone mineral, which make it especially difficult to describe and at the same time allows to explain their special characteristics and function. These factors significantly influence both physiological and mechanical functions of bone [50]. For instance, the small size and/or non-stoichiometry of the crystals are very important factors related to the solubility needed for resorption of the bone by osteoclasts [34, 78]. Furthermore, the small size of mineral crystals also contributes to the superior mechanical properties of bone. As explained before, at the lowest level of hierarchical organization, bone is composed of tiny crystals that are smaller than the ‘Griffith length’ necessary for cracks to spread [79]. For more detail on bone mineral, the reader is referred to extensive reviews available in the literature [80-82].

2.3.1.7 The organic matrix of the bone

The organic phase of bone comprise an insoluble framework of cross-linked type I collagen in association with non-collagenous proteins that are soluble in water. Type I collagen accounts for about 90 wt% of the total organic matrix, whereas 200 different non-collagenous proteins are found in the remaining 10 wt% [31, 35]. Many of these originate from the circulating blood and become trapped in the bone matrix and therefore, they are not directly involved in biomineralization.

Among the 11 types of collagen known in biology, bone collagen is type I and it is produced by bone-forming cells (osteoblasts). Collagen consists of 3 polypeptide chains, each about 1000 amino acids in length and containing glycine, proline, and hydroxyproline as compositional hallmarks [31]. The polypeptide chains are arranged helically and three chains fold together to form a triple helical structure (see Figure 2.9). This triple helical molecule is rod-shaped, approximately 300 nm in length and 1.2 nm in diameter and is the basic building block of the large collagen fibril [83]. The arrangement of the helical polypeptides to form a fibril is a distinct feature of the collagen molecule and Miller provided an excellent review and discussion about the collagen fibril structure and its relation to bone mineralization [84].

The most important discovery in collagen fibril structure was reported in 1963 by Hodge and Petruska [85] who proposed a two-dimensional model with the triple helical molecules are organized in a highly specific manner through unique chemical crosslinks that dictate a lateral staggering of adjacent molecules approximately 0.25 to 0.20 of their 300 nm length. As illustrated in Figures 2.9 and 2.10, this unusual orderly arrangement of collagen molecule creates a hole zone or gap (~ 40 nm in length) and overlap (~ 27 nm in length) regions in the packed arrays, together giving rise to a ~ 67 nm periodicity characteristic of this pattern. The hole and overlap regions provide sites for the nucleation of the bone crystals and their directional growth [67, 70, 78, 85, 86]. Robinson and Watson's [87] pioneering study showed that the 67-nm banding pattern of stained unmineralized collagen fibrils (see Figure 2.6, right side of Level 1) can also be observed in unstained but mineralized collagen fibrils (see Figure 2.6, Level 2). This suggest that the stain and mineral are at the same location within the fibril, mainly within the hole zones [43]. Similarly, the characteristic banding pattern of type I collagen in natural bone can be also seen in Figure 2.11, which is reported by Olszta *et al.* [34] in a recent TEM study.

Furthermore, the 3-dimensional organization of the collagen has been studied extensively. In 3D, the assembly of collagen also appears to be highly ordered by particular chemical bonding [88, 89] and triple helical molecules are organized in a such way that the hole and overlap zones of adjacent collagen molecules and their 2D arrays are in very close register, which create channels through 3D assemblage (see Figure 2.12) [78, 85, 86]. These channels may accommodate the crystal growth in width. A schematic representation of the collagen molecular assembly in this manner is illustrated in Figure 2.12 [66, 67, 90, 91].

In addition to the type I collagen, it is also believed that other proteins in the extracellular, organic matrix facilitate the nucleation of the crystals within the collagen fibrils, and/or are part of the nucleation itself. While collagen fibrils alone may be capable of initiating mineralization, some studies showed they may require the presence of specific macromolecules (noncollagenous components) in order to be able to biologically function efficiently as nucleation catalysts [92, 93]. The most abundant noncollagenous components in bone organic matrix are osteocalcin, osteonectin, bone phosphoproteins including osteopontin, matrix gamma-carboxyglutamic acid protein, sialoproteins, and proteoglycans. Although some of these proteins may contribute to the mechanical functions, more importantly, they play a crucial role in the formation of bone structure through the generation of nucleation sites for mineral deposition [48, 94, 95].

Glimcher [82] investigated the potential role of phosphoproteins of the bone matrix in biomineralization. He found that carboxylic acid side chain groups and organic phosphate groups of Ser(P) and Thr(P) together account for approximately one half of all the amino acid residues of the bone phosphoproteins, therefore providing many sites for the binding of calcium ions. The ability to bind calcium ions is one of the requirements for a component to involve in the nucleation of CaP crystals from a solution. Many other studies have also showed that phosphoproteins play a crucial role in the initiation of mineralization of vertebrate mineralized tissues [31, 92, 95]. It was shown that collagen complexed with phosphoproteins was a better substrate for the nucleation of hydroxyapatite crystals in vitro than bone collagen fibrils alone. In addition, osteonectin consists of relatively large amounts of deprotonated aspartic acid and glutamic acid residues, each of which have strong calcium-binding properties and is involved in the nucleation of hydroxyapatite in the bone matrix [31, 96].

2.3.1.8 The role of water in the bone structure

Although water is a minor component of the bone, its significance should not be underestimated, because it contributes to the overall toughness of the nanocomposite. The mechanical measurements of dry bone have been shown to be significantly different than that of wet bone [40, 97]. The water is accommodated within the collagen fibril, in the gaps, and between triple-helical molecules. It is also located between fibrils and between fibers [43, 86].

2.3.1.9 Collagen-mineral interaction

Even though the details of the precise structural events of the collagen-mineral interaction are still incomplete particularly regarding the size and shape of the mineral crystals and their location and orientation within the organic matrix, it is now generally accepted that the deposition of mineral crystals in bone and other tissues occurs in association with the type I collagen [71, 95, 98-100]. The underlying physicochemical basis and mechanism for the CaP formation in the bone is a heterogeneous nucleation by the type I collagen and possibly by other non-collagenous proteins in the organic matrix [101]. Similar to heterogeneous nucleation, this theory assumes that organic components, which serve as the nucleators or substrates, contain regions in which certain chemical groups (e.g., the amino acid side chains of proteins) have a particular three-dimensional stereochemical geometry and electrical charge distribution with respect to each other. The controlled nucleation and growth of bone mineral are initiated within specific locations within each individual collagen fibril by specific physical and chemical interactions between certain of the organic components and the mineral phase [70, 78, 82]. A schematic illustrating the nucleation sites in a collagen fibril is given in Figure 2.13.

Electron micrographs, low-angle neutron and x-ray diffraction studies have shown that mineralization of collagen fibrils occurs in an extremely intimate and highly organized fashion [102]. The studies clearly showed that the initiation of mineralization in bone begins with the formation of individual, small CaP crystals within the collagen fibrils in the hole zone regions [70, 82]. A schematic demonstration of this phenomenon is shown in Figure 2.9. The hole zone region of the fibrils not only provides the actual loci where nucleation occurs, but also provides the volume of space within which the solid mineral crystals are deposited without physically destroying and disrupting the structure of the fibrils [70, 98]. Moreover, the mineral particles are not randomly distributed in the bone but are organized in a highly ordered fashion and long axes (*c*-axis) of the crystals are aligned roughly parallel to the long axis of the collagen fibril within which they are associated [92]. As reported by Glimcher [82], the ultrastructural and crystallographic data of bone clearly show a very intimate relationship between certain specific regions within the collagen fibrils and the initial crystals deposited and make it probable that nucleation sites are in the collagen fibrils within the hole zone regions. Mineralization is initiated in these spatially distinct nucleation sites of individual collagen fibrils and such regions within a single, undirectional fibril represent independent nucleation sites for heterogeneous nucleation [92]. The side chain groups in the organic matrix, such as the collagen α-chains and possibly non-collagenous proteins, serve to nucleate the mineral phase heterogeneously, as shown schematically in Figure 2.13 [70]. The increase in the mass of CaP occurs mostly by secondary nucleation from the crystals initially deposited in the hole zone or by primary heterogeneous nucleation by sites within the hole zones and/or the pores (overlap zone of the collagen fibrils). Furthermore, the progression of mineralization (increase in the amount of CaP formation) within an individual fibril or from one fibril to another does not occur by the direct extension of the crystallization process, that is from one collagen fibril to another via the extracellular space but is initiated simultaneously and independently within spatially separate and distinct collagen fibrils [98]. Further increase in the mass of mineral phase being principally the result of increase in the number of crystals (multiplication) rather than size of the crystals (crystal growth) already formed [102]. As a result, the CaP crystals within the collagen fibers grow in number and possibly in size to extend into the overlap zone of the collagen fibrils (pores) so that all of the available space within the fibrils, which has possibly expanded in volume compared to its unmineralized level, is eventually occupied by the mineral phase of the bone [70, 102]. In addition, many other studies in the literature also support the observations explained above on the location of the crystals in the bone [66, 101, 103, 104]. Glimcher provided an outstanding review on the nucleation and interaction of CaP crystals with the collagen fibrils [70, 82].

Weiner and Traub [90, 91] discussed whether or not the bone crystals can fit the individual holes that are formed by collagen fibrils as explained previously. According to the authors, the crystals are larger than the individual holes and have quite different shapes, which states that the crystals may not fit in the individual holes. For that reason, they studied the organization of the crystals in single collagen fibrils isolated from the mineralized portions of the leg tendons of turkeys. The authors suggested that the primary location for the crystals is within grooves (collagen channels) formed by contiguous adjacent gaps (see Figure 2.12). In this theory, the plate-shaped crystals are stacked more or less like a deck of cards across the collagen fibril diameter. The Figure 2.12 illustrates how the crystals may be arranged in this manner inside a collagen fibril.

As reported by Landis [78] from several outstanding studies [66, 67, 87-90, 100, 105-107] conducted on the investigation of collagen-mineral interaction, different aspects of the organic matrix-mineral interaction can be summarized as follows; 1) crystal nucleation takes place at multiple spatially and temporally independent sites both on collagen surface and within collagen in its hole and overlap regions; 2) crystals are mainly nucleated in the hole zone regions at the earliest stages of mineralization; 3) crystals grow preferentially in length, corresponding to their crystallographic *c*-axis; 4) crystals would appear to grow in their width along the channels which are created by adjacent collagen hole regions in register; 5) the crystal size may exceed the dimension of single collagen hole zones; 6) the *c*-axes of respective particles are almost parallel to one another and to the long axis of the collagen fibrils with which they associate; 7) crystals located in different collagen fibrils may be coherent in their orientation and alignment so that their organization is highly uniform over large matrix volumes. Many of these features are illustrated schematically in Figures 2.9, 2.10, and 2.12.

In 2007, using different TEM techniques, Olszta and his colleagues [34] suggested that mineral platelets in the bone are not quite as ordered as previously described. In a recent study, Burger *et al.* [50] has also found similar results from the SAXS and TEM data. According to the authors, the lateral packing of nanoscale crystals in collagen fibrils can be represented by irregular stacks of platelet-shaped crystals, intercalated with organic layers of collagen molecules.

2.3.2 Structural biological composites

In addition to the bone, there are many other examples of biological structures and materials, such as sea shells, nacre, crab carapace, teeth, horns, the inner structure of birds' wings, and insect cuticles that are mainly composed of two components; inorganic phase (brittle) and organic molecules (ductile). These structures are developed through template-assisted self-assembly, where self-assembled organic materials such as proteins, or lipids, or both form the structural scaffolding for the deposition of inorganic material [108]. Table 2.3

shows the main components of several biological systems found in nature. Moreover, Lowenstam [109] provided more examples of minerals formed by organisms in nature. Their mechanical properties are usually remarkable, considering the weak constituents from which they are assembled [110].

Another common feature of all biological systems is that they are hierarchically structured, that is, the structure is different at many different length scales from the nanometer to the microscale and macroscale [111]. It is worth to mention that this hierarchical organization is inherent to design. The hierarchy is a direct outcome of the self-assembly system in biology, itself driven by the information at molecular level [112]. The hierarchical arrangements have crucial roles in the mechanical function of these materials. They produce interfaces that will open up in the presence of the cracks, deflecting the cracks and making their travel energetically expensive [79]. This makes biomineralized materials surprisingly tough, given that they are made almost entirely of mineral. The natural bone is a special case, which has less mineral than most other biomineralized rigid biomaterials and therefore the bone can be remarkably tough [79]. The major advantage of hierarchical structuring is that the materials can be made multifunctional with increased adaptability and fracture toughness can be improved independently of other properties by optimization at different size levels. For example, stiffness is a property controlled at nanometer levels, whereas toughness (resistance to fracture) is controlled at micrometer to centimeter levels. Therefore, these two properties can be controlled independently such that biological ceramics can be as stiff as technical ceramics but much more durable [112]. As a result, the biological materials, which have risen from millions of years of evaluation, have been inspiring scientist and researchers over the last several decades aimed at discovering some of their structural “secrets” [113-120]. In the next section, the structure of nacre and crab carapace, which are studied extensively, will be reviewed in more detail.

2.3.2.1 The structure of the nacre

Nacre (also called mother of pearl) is an inorganic-organic composite material that is formed in the nature and it has been intensively studied because of its fascinating microstructure and relative simplicity as compared to other biological systems [41]. Its significance as a structural material comes from its remarkable mechanical properties, such as fracture toughness and strength, which are comparable or better at room temperature than those of some high-technology structural ceramics [116]. It is twice as hard and a thousand times as tough as its constituent phases [121]. Currey [122] was the first to describe the unusual toughness possessed by the structure of the nacre. The hierarchical structure of a typical nacreous shell is illustrated in Figure 2.14 (for the shell of red abalone, a marine gastropod Haliotis rufescens). The shell structure contains at least six levels of hierarchy, which contributes significantly to the mechanical properties of the material [79, 115, 123]. It is composed two layers (see Figure 2.14); the outer prismatic layer is made up of large crystals of rhombohedral calcite, which is a hard and brittle material. The inner layer (nacre) is composed of approximately 95% volume of aragonite (a crystallographic form of $CaCO_3$) and 5% volume of organic materials (proteins and polysaccharides) [116]. The calcitic (rhombohedral) and aragonitic (orthorhombic) isomorphs of $CaCO_3$ found in the prismatic and nacreous sections of red abalone are unique to this species and they are not encountered in geological or synthetic $CaCO_3$ [124]. At the lowest level, nacre consist of an organic layer having thickness of ~ 30 nm and proceeding with single crystals of the aragonite, which is in the shape of “bricks” with dimension of 0.5 vs. 10 μm as can be seen in Figure 2.14. The ordered brick-and-mortar arrangement of organic and inorganic nanolayers is suggested being the most essential strength and toughness determining structural feature of nacre [125]. There are many other studies that have been conducted in understanding the mechanism underlying the mechanical behavior of nacre and mimicking the structure of nacre [116, 121, 123, 125-129].

2.3.2.2 The structure of the crab carapace

Crabs are arthropods whose carapace or cuticle is composed of a mineralized brittle hard component (calcite) and a softer organic component, which is mainly chitin (see SEM image in Figure 2.15). Crab carapaces are complex structures showing hierarchical organization where initiation, growth, and orientation of calcite domains are controlled by organic intra-and extracellular elements [130]. The brittle component is organized in a helical pattern called a Bouligand structure and there are canals linking the inside to the outside of the shell as shown in Figure 2.15 [110]. These canals play a role in the transport of calcium ions. At higher magnification, crab cuticle consists of a chitin-protein mixture. There are cation-binding glycoproteins in the organic matrix and mineralization of calcium carbonate is initiated at these nucleation sites. The twisted fibrillar matrix of chitin develops screw dislocations and these defects favor crystal growth by introducing privilege sites for further crystalline units to grow [130].

2.4 Literature Review on Synthesis of Hydroxyapatite

Despite numerous attempts, there is still a strong need for synthetic bone substitution materials such as hydroxyapatite and its composites in clinical applications [54]. In general, calcium phosphate compounds can be synthesized either by wet [54, 131-135] or dry processes (solid-state reactions) [136, 137]. In the wet method, a calcium solution is mixed with a phosphate solution in order to form precipitates whereas in the dry method, the solid-phase reaction takes place between calcium and phosphate containing compounds at high temperatures. Furthermore, some other methods such as, vibro-milling from natural bone [138], solution spray drying [139], emulsion or micro-emulsion [140], microwave irradiation [141], sol-gel [142, 143], mechanochemical-hydrothermal [144, 145], and enzyme-catalyzed [146] synthesis of HAp have also emerged to control the powder morphology, size, and chemical composition.

Using wet-chemical methods, CaP ceramics with good crystallinity, physiological stability, and with the morphological characteristics resembling that of the hard tissues can be prepared. However, the physical, chemical, and mechanical properties of the final product usually depend on the specific method used in the synthesis [147]. In the following sections, literature on various wet-chemical methods will be reviewed. Although there are many synthesis methods available with varying degrees of overlap, only a few methods will be discussed in this report: chelate decomposition, urea decomposition, precipitation and hydrolysis of calcium phosphate precursors.

2.4.1 Chelate decomposition

The chelate decomposition method first was used in the studies where relatively larger-size particles were desired to study the crystallography of HAp [148, 149]. In this method, a chelating agent, usually a carboxylic acid is used to bind the calcium ions in a homogenous chemical reaction. A slow release of calcium ions from a calcium complex into a phosphate solution results in formation of CaP precipitates. Some common chelating agents are acetic acid, lactic acid, citric acid, tartaric acid, and ethylenediamine tetraacetic acid

(EDTA). Among them, EDTA is the most common one since it binds to Ca^{2+} much more strongly compared to other chelating agents.

Toriyama *et al.* [150] prepared CO_3HAp by a homogenous oxidative decomposition of calcium-EDTA chelates in a phosphate solution with hydrogen peroxide. Calcium nitrate (0.01 mol), diammonium hydrogen phosphate (0.006 mol), EDTA (0.012 mol) and 35% hydrogen peroxide (H_2O_2) were mixed and the solution was kept at 90 °C for 4h in a water bath to synthesize the CaP compound. When calcium and EDTA solutions are mixed, calcium ions will form complex with EDTA. Since practically all Ca^{2+} ions are tied by EDTA in the solution; no precipitation is formed when mixed with phosphate solution. Heating the solution in the presence of hydrogen peroxide results in decomposition of Ca-EDTA complex and slow release of Ca^{2+} from Ca-EDTA chelate. As the solution becomes supersaturated, apatite crystals nucleate and grow. Carbonate-containing HAp particles synthesized in this method consisted of hexagonal columnar crystals grown in the direction of the *c*-axis as revealed by SEM analysis.

Similarly, Fujishiro *et al.* [151] and Kandori *et al.* [152] synthesized HAp by a reaction of Ca-EDTA chelates and phosphate ions at 100-250 °C. Since they did not use H_2O_2 in the reaction medium, high temperatures were needed to decompose Ca-EDTA complex. Hydroxyapatite obtained in these studies incorporated carbonate in its structure and the morphology depended strongly on the experimental conditions.

Depending on the solution pH, the following reactions take place in the homogenous precipitation of hydroxyapatite in the $Ca(edta)^{2-}$ - Phosphate solution.

$$10Ca^{2+} + 6H_2PO_4^{-} + 14OH^{-} \xleftrightarrow{Kp} Ca_{10}(PO_4)_6(OH)_2 + 12H_2O \qquad (12)$$

$$10\,Ca^{2+} + 6\,HPO_4^{2-} + 8\,OH^- \xleftrightarrow{Kp} Ca_{10}(PO_4)_6(OH)_2 + 6\,H_2O \tag{13}$$

$$10\,Ca^{2+} + 6\,PO_4^{3-} + 2\,OH^- \xleftrightarrow{Kp} Ca_{10}(PO_4)_6(OH)_2 \tag{14}$$

$$Ca(edta)^{2-} \xleftrightarrow{Kd} Ca^{2+} + edta^{4-} \tag{15}$$

$$Ca(edta)^{2-} + H_2O \xleftrightarrow{Kd} Ca^{2+} + Hedta^{3-} + OH^- \tag{16}$$

$$Ca(edta)^{2-} + 2\,H_2O \xleftrightarrow{Kd} Ca^{2+} + H_2edta^{2-} + 2\,OH^- \tag{17}$$

$$Ca(edta)^{2-} + 3\,H_2O \xleftrightarrow{Kd} Ca^{2+} + H_3edta^- + 3\,OH^- \tag{18}$$

Figure 2.16 shows the concentration variation of EDTA ions with pH. For instance, at pH > 12 the dominant form is edta^{4-} in the solution and *Equation* 15 is more likely to take place.

In another interesting study, Shchukin *et al.* [153] have shown biomimetic synthesis of hydroxyapatite exclusively inside poly(allylamine)/poly(styrene sulfonate) polyelectrolyte capsules of micron scale. The authors employed a poly(allylamine hydrochloride)/PO_4^{3-} complex as a source of phosphate anions to capture calcium ions and make them react in the capsule volume. The deposition of hydroxyapatite was performed from alkali water solution containing $CaCl_2$ as illustrated in Figure 2.17. The authors suggested that these HAp composite capsules could find applications as medical agents for bone repairing and catalytic microreactors.

In 1998, Anabel Lopez-Macipe and colleagues [154] used citrate ions as the Ca-complexing agent. Their experiments were carried out by using solutions of 0.05 *M* $CaCl_2$, 0.03 *M* Na_2HPO_4 and 0.1 *M* Na_3(cit) (where cit^{3-} = $C_6H_8O_7^{3-}$). After heating to 100 ^{o}C in 30 min, they observed nano-sized (30-60 nm) and needle-like crystals of poorly crystalline HAp precipitation. In addition to these studies, synthesis of HAp with chelate decomposition has been also reported by others with varying success and/or detail [155-160].

2.4.2 Urea decomposition

Urea decomposition takes advantage of an increase in solution pH caused by production of ammonia (NH_3) during the thermal hydrolysis of urea. In addition, the urease enzyme can also be employed in the hydrolysis of urea. The advantage of this process is that the decomposition of urea can be accomplished at lower temperatures and enzyme is not consumed in the reaction [161]. The decomposition of urea by heat or urease takes place according to the following reactions:

$$(NH_2)_2CO + H_2O \xleftrightarrow{HEAT\ or\ UREASE} CO_2 + 2NH_3 \tag{19}$$

In aqueous solution NH_3 and CO_2 react with water according to;

$$NH_3 + H_2O \leftrightarrow NH_4^+ + OH^- \tag{20}$$

$$CO_2 + 2H_2O \leftrightarrow HCO_3^- + H_3O^+ \tag{21}$$

$$HCO_3^- + H_2O \leftrightarrow CO_3^{2-} + H_3O^+ \tag{22}$$

Homogenous calcium phosphate solutions are prepared at low pH (~ 2) where HAp is soluble (see Figure 2.1). Heating the solution in the presence of urea can gradually increase the solution pH to a value that HAp is insoluble. Since CO_2 is also produced during the decomposition of urea, the apatite would likely to incorporate CO_3 in the lattice.

Aizawa *et al.* [162, 163] synthesized calcium-deficient apatite fibers (CO_3HAp) by using urea decomposition method. Appropriate amounts of $Ca(NO_3)_2$ and $(NH_4)_2HPO_4$ and $(NH_2)_2CO$ were mixed and pH of the solution was adjusted to ~3 with addition of HNO_3 where HAp is not stable. By refluxing the solution at 90 ^oC for 72 h, the pH of the solution increased from ~3 to ~ 8. As the solution pH increases, HAp crystals nucleate and grow (HAp is the most stable CaP phase at pH ~ 8). The product obtained was calcium deficient carbonated HAp with rod-like morphology as shown in Figure 2.18.

In another study, Zhang *et al.* [164] used 0.167 *M* calcium ion solution and 0.1 *M* phosphate ion solutions with urea. The solution was refluxed at 85-90 ^{o}C for 70-120 h to produce HAp whiskers. The morphology of the HAp crystals were similar to the one observed by Aizawa *et al.* [162]. Similarly, Mortier *et al.* [165] also employed a homogenous precipitation method using urea to precipitate fibrous CO_3HAp from a solution of $Ca(NO_3)_2$ and $(NH_4)_2HPO_4$ at 120-150 ^{o}C.

Jokic *et al.* [166] synthesized nano-sized hydroxyapatite by the catalytic decomposition of urea and urease. The low crystalline carbonated hydroxyapatite was precipitated from an aqueous solution of $CaCl_2$, NaH_2PO_4, urea, and urease at temperatures between 30-40 ^{o}C. The authors also investigated the effect of temperature and ration of the reagents/urease concentrations on the size and morphology of the HAp crystals. It was found that the particle size decreases below 100 nm with decreasing the ratio of the concentrations of the reagents to the urease concentration.

2.4.3 Precipitation of HAp

Direct precipitation of HAp involves mixing of soluble reagents of calcium and phosphate at temperatures less than 100 ^{o}C. No modifiers are added to manipulate the chemical solution equilibria [167, 168].

Slosarczyk *et al.* [169] employed precipitation method to obtain CO_3HAp. In their experiments, $Ca(NO_3)_2{\cdot}4H_2O$ as calcium reagents and $(NH_4)_2HPO_4$ as phosphate source were used. Ammonium bicarbonate (NH_4HCO_3) was used as carbonate source. During synthesis, the pH of the reaction medium was kept ~11 using ammonium hydroxide solution. After aging for 24 h at room temperature CO_3HAp precipitates were obtained. Similarly, Donadel and coworkers [147] synthesized HAp from a solution containing 0.09 mol of $(NH_4)_2HPO_4$ and 0.152 mol of $Ca(NO_3)_2 \cdot 4H_2O$. The solution pH was adjusted by using NH_4OH. To precipitate HAp the prepared calcium phosphate solution was heated at 65 °C for 90 min under stirring. In addition, there are other reports on precipitation method to produce HAp [54, 167, 168, 170]. In all these investigations, depending on pH of the solution, hydroxyapatite was precipitated according to the $Equations\ 12, 13, and\ 14$. For instance, at high pH (>13) PO_4^{3-} ions are dominant in the solutions (see Figure 2.19) and so $Equation\ 14$ is more likely to take place to precipitate HAp.

In addition to studies above, Kokubo [171-173] reported for the first time that HAp can be synthesized by using simulated body fluid (SBF) with ion concentration (Na^+, 142.0; K^+, 5.0; Mg^{2+}, 1.5; Ca^{2+}, 2.5; Cl^-, 148.0; HCO_3^-, 4.2; HPO_4^{2-}, 1.0; SO_4^{2-}, 0.5 *mM*) nearly equal to those of human blood plasma. This method allows obtaining a carbonated hydroxyapatite with small crystallites and defective structure similar to apatite in bone. In a different study, Tas [174] prepared nano-sized HAp particles (~50 nm) from the calcium nitrate tetrahydrate and diammonium hydrogen phosphate salts dissolved in modified synthetic body fluid (SBF) solution at 37 °C and pH of 7.4. The author claimed that the significance of this study was the superior high-temperature stability of such ‘biomimetic’ HAp powders as compared to those reported in previous studies.

2.4.4 HAp synthesis via hydrolysis of CaP precursors

To synthesize hydroxyapatite, hydrolysis of calcium phosphate precursors can be employed by controlling the temperature or pH. The precursors have included anhydrous dicalcium phosphate (monetite, DCPA), dicalcium phosphate dihydrate (brushite, DCPD), α-tricalcium phosphate (α-TCP), amorphous calcium phosphate, calcium pyrophosphate treated at temperatures between 37 ^{o}C and 450 ^{o}C.

Liu *et al.* [175] precipitated HAp from the reaction of $CaHPO_4 \cdot 2H_2O$ (brushite) (0.5162 g) and $Ca(OH)_2$ (0.1482 g), which were dissolved in 40 mL deionized water. After preparing 40 mL solution of $CaHPO_4 \cdot 2H_2O$ and $Ca(OH)_2$, the pH of the solution was adjusted to about 9. Then the solution was held at 140 ^{o}C for 24 h to precipitate HAp. The corresponding hydrothermal reaction is as follows:

$$4Ca(OH)_2 + 6CaHPO_4 \cdot 2H_2O \rightarrow Ca_{10}(PO_4)_6(OH)_2 + 18H_2O \tag{23}$$

In a similar method, LeGeros *et al.* [176] obtained CO_3HAp powders from the hydrolysis of $CaHPO_4$ (monetite). The authors also investigated the effect of carbonate on the crystallinity and the morphology of the apatite crystallites. Monma and Kamiya [177] synthesized HAp from the hydrolysis of brushite. According to their results, HAp formed most rapidly at pH~8 and complete conversion was obtained within 2.5 h at 40 ^{o}C, 1 h at 60 ^{o}C, and only 5 min at 80 ^{o}C. The HAp precipitated was non-stoichiometric with Ca/P ratio < 1.60 and showed low crystallinity. Furthermore, Fulmer *et al.* [178] reported formation of calcium deficient hydroxyapatite at near-physiological temperature by reaction of tetracalcium phosphate, monocalcium phosphate monohydrated, and calcium hydroxide.

In general, HAp particles obtained from EDTA decomposition and urea decomposition methods tend to be bigger than those prepared by precipitation and hydrolysis of calcium phosphate precursor methods. The size and morphology of the HAp powders synthesized from chelate decomposition vary over a wide range at the micro-scale. The HAp particles produced by urea decomposition tend to have a greater size than those prepared by other methods. Similar to precipitation method, HAp particles obtained from hydrolysis of CaP precursors are typically on the nano-scale. Furthermore, in all of the methods described above and many others, the effect of the reagents, reagent concentration, solution pH and reaction temperature on HAp particle's morphology and composition were investigated [155].

2.5 Synthetic Attempts at Mimicking Bone Formation

Bone is an organic-inorganic nanocomposite and has been attractive as models for synthetic structural composites because of its unusual combinations of mechanical properties, such as strength, low stiffness, and high fracture toughness. Considering the nature of the interaction between mineral and organic components of the bone, in designing novel polymer-HAp nanocomposites, there are several important factors that are necessary to take into account, such as the choice of the polymer, the techniques for synthesizing the hydroxyapatite, and the intermolecular contacts formed upon interactions of these components [179]. Therefore it is important to find an organic substrate that can effectively induce HAp nucleation. In recent years, many attempts have been also carried out to investigate the nucleation of HAp on substrates with different functional groups.

2.5.1 HAp-polymer composites

Hartgerink *et al.* [180] reported on the use of self-assembly and mineralization to prepare a peptide-amphiphile (PA)/HAp nanocomposite material that recreates the structural orientation between collagen and hydroxyapatite observed in natural bone. The authors used a holey TEM grid on which PA nanofibers formed by self-assembly and then introduced dilute solutions of $CaCl_2$ and Na_2HPO_4 on both sides of the grid to form nano-size HAp crystals. The phosphorylated serine residue in the PA structure interacts strongly with calcium ions and helps direct mineralization of hydroxyapatite. The crystallographic *c* axes of hydroxyapatite were aligned with the long axes of the peptide-amphiphile fibers and this alignment was the same as that observed between collagen fibrils and hydroxyapatite crystals in the bone. Figure 2.20 shows TEM micrographs of the corresponding PA-HAp composite. Moreover, the authors recently discovered a system to cooperatively template HAp mineralization using 3D PA scaffold. The system employs the natural enzyme alkaline phosphatase, and a phosphorylated PA nanofiber gel matrix to template, in three dimensions, HAp nano-size crystals, with size, shape, and crystallographic orientation similar to the natural bone mineral [181].

Another approach to design polymer-HAp nanocomposites is to mimic the hierarchy of the collagen-crystal fibril network in the bone. Liao *et al.* [182] developed a new type of nanocomposite bone material, HAp/collagen/PLA, by using a biomimetic strategy. In their study, first a bone-like HAp/collagen composite was prepared and then this material was dissolved in a poly(lactic acid) (PLA) solution to form HAp/collagen/PLA nanocomposite, which contains approximately 12 wt% PLA. The reason of incorporation PLA in to the HAp/collagen nanocomposite was to improve the mechanical strength of the material. The authors described that the collagen molecules and nano-sized hydroxyapatite particles assembled into mineralized fibrils about 6 nm in diameter and about 300 nm long, which they then assembled into bundles for dispersion within the PLA matrix. The authors also claimed that HAp/collagen/PLA nanocomposite showed some features of natural bone both in main composition and hierarchy microstructure. The Figure 2.21 shows a schematic of the nano-to microscale hierarchical microstructure of the nanocomposite. Furthermore, the nano-composite was shown to be bioactive by the cell culture and animal model tests.

Gungormus *et al.* [183] performed in vitro experiments of calcium phosphate mineralization on hydroxyapatite-binding peptides. They studied the effects of different peptides with different affinities and structural properties on the mineralization of calcium phosphates. The implication of their research is that the hydroxyapatite-binding peptides may be used in the restoration or regeneration of hard tissues by controlling the formation of calcium phosphate biominerals.

Recently, Olszta *et al.* [34] tried to duplicate the most fundamental level of bone structure, the interpenetrating nanostructured architecture, by using the polymer-induced liquid-precursor (PILP) process. For that purpose, they chose a Cellagen® sponge (in order to mimic the organic matrix of the bone), which is a commercially available hemostatic sponge composed of reconstituted type I bovine collagen. It contains the 67 nm banding pattern indicating that is has assembled appropriately to match native type I collagen. The mineralization process was achieved by immersing Cellagen® sponge in a calcium phosphate solution of $CaCl_2$ and K_2HPO_4 at 37 °C and pH of 7.4. Furthermore, polyaspartic acid (polyAsp, a polymer process-directing agent) was also used in the mineralization process and it was suggested that this anionic polyAsp additive simply mimic the polyanionic character of the non-collagenous proteins in the organic matrix of bone. As a result of their in vitro experiments, the authors proposed that the nucleation of HAp crystals in mineralized collagenous tissues (bone and dentins) does not initially occur within hole zones, but rather a liquid-phase amorphous precursor is drawn into the collagen fibrils through capillary action, and upon solidification, the precursor crystallizes, causing the collagen fibrils embedded with nano-size platelets of HAp (see Figure 2.22). This liquid-phase precursor, analogous to the

PILP phase they showed in vitro, would be induced by polyanionic proteins found in non-collagenous proteins in the organic matrix of the bone.

Song and colleagues [184] employed the poly(2-hydroxyethyl methacrylate) (pHEMA) and the poly(2-hydroxyethyl methacrylamide) (pHEMAm) hydrogel scaffold as an organic template for nucleation and growth of CaP. They used the urea-mediated mineralization to form CaP on the hydrogel polymer surface. When urea decomposes, pH gradually increases and this causes the hydrolysis of surface 2-hydroxyethyl esters and the precipitation of HAp from the solution. A segment of pHEMA hydrogel was soaked in an acidic solution (pH 2.5-3.0) of HAp containing a high concentration of urea (2.0 *M*). Then, after heating from room temperature to 95 ^{o}C (within 2 h), the pH slowly increased to about 8. By allowing the mineralization to proceed for 12 h at 95 ^{o}C, approximately 7 μm CaP layer was formed over the entire pHEMA hydrogel surface (see Figure 2.23). The authors also applied the same mineralization technique to pHEMAm, a hydrogel that is not prone to side chain hydrolysis under the mineralization condition. In this case, loosely bound HAp and in lesser quantity was obtained on the polymer surface. From their study, it can be concluded that the hydrolysis of the hydroxyethyl esters side chains of pHEMA to the corresponding carboxylic acids, generating abundant Ca^{2+}-binding sites, plays a crucial role on the precipitation of HAp onto the pHEMA hydrogel scaffolds. Furthermore, in 2005, Song *et al.* [185] investigated the mineralization of HAp on the hydrogels functionalized with either carboxylate or hydroxyl ligands. Cross-linked polymethacrylamide and polymethacrylate hydrogels were functionalized with mineral-binding ligands and used to template the formation of hydroxyapatite using similar experimental procedure. Their findings show that both -COOH and -OH groups are capable of templating the growth of CaP.

Perkin *et al.* [186] employed self-assembled shell cross-linked poly(acrylic acid-b-isopropene) (PAA_{78}-b-PI_{97}) micelles or cross-linked PAA nanocages in aqueous solution as templates for the preparation of novel polymer-inorganic nanocapsules. They showed that the hybrid nanostructures were approximately 60 nm in diameter and consisted of spherical polymer nanoparticles or nanocages enclosed within a continuous 10-20 nm thick surface layer of amorphous calcium phosphate layer (see Figure 2.24). Their results also indicated the importance of functional groups in the biomineralization process. The specific interactions between PAA-sequestered Ca^{2+} ions and phosphate anions played an important role on the nucleation of CaP layer on the outer surface of polymers. Nucleation of calcium phosphate specifically in association with the polymer nanoparticles was facilitated by low supersaturation levels and by sequestration of Ca^{2+} ions within the carboxylate-rich PAA domains prior to addition of phosphate solution.

Li *et al.* [187] showed that a bone-bonding polymer known as Polyactive® is capable of inducing carbonated hydroxyapatite (CO_3HAp) formation in a simulated body fluid (SBF). Polyactive® is a block copolymer contains polyethylene oxide (PEO, hydrophilic) and polybutylene terephthalete (PBT, hydrophobic) groups. The authors produced 100 μm thick coatings of CO_3HAp after a 4-day incubation of a rectangular Polyactive® plate 60 x 30 x 1.5 mm in 100 mL of the simulated body fluid (see Figure 2.25). Their results confirmed that calcium phosphate formation was initiated by Polyactive®. The carboxyl groups (COOH) produced during the hydrolysis of Polyactive® play a crucial role in nucleating HAp, which is in agreement with studies of Kawashita and coworkers [188]. According to the hypothesis proposed by Li *et al.* [189], in the polymer gel, both calcium ions and phosphate groups are accumulated around COOH and COO^- groups through electrostatic forces and hydrogen bonds. The local increase of supersaturation induces the hydroxyapatite nucleation and both calcium and phosphate diffuse through the hydrogel, thus resulting in formation of HAp within the material. Furthermore, the PEO part of the polymer, which is hydrophilic, has a high affinity for calcium ions and this may cause calcium and phosphate ions move from the solution into the polymer for the growth of CO_3HAp [190].

Recently, Iwatsubo *et al.* [191] found a new method to construct HAp and polymer composites. A solution containing calcium and phosphate ions was supersaturated with polyacrylic acid (PAA) which also forms a polymer complex with a polyvinyl alcohol (PVA) substrate at the surface. The supersaturation with PAA was claimed because the solution without the PAA generated precipitation whereas with PAA, the solution was transparent for more than 2 weeks. The PVA film used as a substrate was soaked in a supersaturated solution that contains 5 *mM* $CaCl_2$, 3 *mM* $(NH_4)_2HPO_4$ and 0.139 *mM* in the repeating unit of PAA (MW 2000) at pH around 7. According to the authors, the heterogeneous nucleation took place at the surface layer of PVA/PAA complex formed on the substrate. Approximately 20 mg of HAp coating was obtained on the PVA film of radius 1 cm after 21 days in a 200 mL of supersaturated solution maintained at 30 ^oC. When a crosslinked film of a miscible blend of PVA/ PAA was used as the template, the film swelled in the supersaturated solution to form gel. In 13 days, 29 mg weight increase was reported, which corresponds to a 71 wt % HAp in the composite. According to the authors, the loose network of polymer chains enabled the diffusion of calcium, phosphate, and hydroxyl ions from the outside to the inside of the gel, which led to the high mineralization rate. As shown schematically in Figure 2.26, the polymer chains of the hydrogel would adsorb HPO_4^{2-} through hydrogen bonding. After the adsorption of HPO_4^{2-}, Ca^{2+} can be attracted within the polymer matrix by electrostatic interaction with HPO_4^{2-}. In addition to this, calcium ions can also be attracted to the polymer matrix by the electrostatic effect of the COO^- groups of PAA. Consequently, a hypercomplex of Ca^{2+}(PVA/HPO_4^{2-}/PAACa) can be formed, which is a precursor of the HAp-rich phase [17]. The authors claimed that the comparison of their mineralization process with the biomineralization process of HAp and $CaCO_3$ showed that the physicochemical mechanism of their mineralization process was similar to that in biological systems.

Kokubo [171] investigated the formation of biologically active bone-like apatite layer on organic polymers by a biomimetic method, which is based on the mechanism of formation of a bone-like apatite layer on the surfaces of CaO-SiO_2-based glasses and glass-ceramics in the living body. He employed simulated body fluid as explained in the previous sections to form HAp on the poly(ethylene terephthalate), poly(methyl methacrylate), polyether sulfone, polyamide 6 (Nylon 6), and polyethylene. The apatite formed in this process was represented by the general formula $Ca_{10-x}[(CO_3,HPO_4)_x(PO_4)_{6-x}(OH)_{2-x}]$. Kokubo concluded that if the apatite-polymer composites could be fabricated into a three-dimensional structure similar to natural bone, the resultant composite was expected to show analogous mechanical properties to those of natural bone as well as high bioactivity, and hence had great potential as bone-repairing materials

Many other groups have also investigated the preparation of bone-like materials with the use of organic substrates such as poly(acrylic acid), chitosan, acidic phosphoproteins, cellulose, chitin, and many others [192-201].

2.5.2 HAp-collagen composites

In a recent study, Kikuchi *et al.* [202] synthesized a HAp and collagen composite by a simultaneous titration precipitation method using $Ca(OH)_2$ and H_3PO_4 at 40 °C and pH around 8. The composite obtained showed a self-organized nanostructure similar to bone assembled by the chemical interaction between HAp and collage. In addition, similar to the bone, the *c*-axes of HAp nanocrystals (50-100 nm in size) were aligned along collagen fibers up to 20 μm in length. Furthermore, HAp-collagen composite was incorporated into the remodeling process of bone, resorbed by osteoclastic cells, and new bone was formed by osteoblasts after the resorption, as if the composite were grafted autologous bone. The authors reported that this high-performance bioactivity of the composite might result from its similarity of composition and nanostructure to bone. The composite exhibited a bending strength of 40 MPa and Young's modulus of 2.5 GPa. As a result, the authors suggested that this HAp-collagen composite could replace autologous bone graft materials.

Zhang *et al.* [203] has shown the fabrication of a composite with hierarchical structure by self-assembly of nanofibrils of mineralized collagen. HAp was precipitated on the collagen from a solution of $CaCl_2$ and NaH_2PO_4 at pH of around 7. The authors claimed that they demonstrated a new hierarchical self-assembly structure of collagen-hydroxyapatite composite for the first time by conventional and high-resolution transmission electron microscopy and HAp crystals were associated with collagen fibril surfaces (see Figure 2.27). HAp crystals grown on the surface of the collagen fibrils surrounded the surface of the collagen fibrils with their *c*-axes oriented along the longitudinal axes of the collagen fibrils, as seen in natural bone.

Wang *et al.* [204] employed a method to mimic biomineralization in the collagen. The mineralization process was achieved after immersing collagen samples in SBF at 37 ^oC for 5-45 h. They obtained large HAp crystals with diameter of 500-800 nm, which developed into flake like structure after 32 h immersion in SBF. According to authors, the carbonated

HAp nanocrystals are self-assembled and self-organized at the active nucleation sites of collagen matrix through covalent bonding. The nucleation was initiated as a heterogeneous reaction due to the ionic interaction of Ca^{2+} with the carboxylic site of the collagen. Then, PO_4^{3-} ion would accumulate at the calcium complexes and grew to the critical nucleation size, which then forms nano-sized calcium deficient CO_3HAp.

Numerous other studies have been conducted in synthesis of biocomposites composed of HAp and collagen that will not be reviewed here [205-209].

2.5.3 Use of self-assembled monolayers for templating HAp

Recently, Toworfe and coworkers [210] investigated the effect of surface functional groups on the nucleation and growth of calcium phosphates. For that purpose, the authors employed self-assembled monolayers (SAMs) to create amine ($–NH_2$), carboxyl (–COOH) and hydroxyl (–OH) functionalized surfaces by grafting 3-aminopropyltriethoxysilane, 3-triethoxysilylpropyl succinic anhydride, and glycidoxypropyl tri-methoxysilane, onto oxidized silicon wafers. Calcium phosphate was precipitated on the SAMs by immersing specimens in a simulated body fluid for 7 days at 37 ^{o}C. The authors demonstrated that the thickness of CaP coating is much higher for –OH and –COOH terminated surfaces (highest for –OH surface), suggesting that a hydroxylated or carboxylated surface enhances CaP nucleation and growth relative to aminated surfaces. Their results are not in agreement with most of the literature which state that COOH functional groups have a more powerful induction capability for the heterogeneous nucleation of HAp than that of OH functional groups. The Ca/P ratio on the –OH, –COOH and $–NH_2$ surfaces were found to be 1.66, 1.70 and 1.41, respectively. The low Ca/P ratio on the NH_2 surface may be due to the fact that the amine-terminated surface adsorbs more PO_4^{3-}. This is attributed to the inhibition of Ca^{2+}

adsorption on aminated surfaces under physiological conditions. This observation suggests that Ca^{2+} adsorption on a polymer surface is a crucial initial step in apatite formation.

Zhu *et al.* [211] studied HAp deposition onto positively charged surfaces (i.e., self-assembled monolayers (SAMs) terminated with NH_2 head groups) and negatively charged surfaces (i.e., OH-SAMs (weak) and COOH-SAMs (strong)) soaked at 50 ^{o}C in 1.5 SBF with pH 7.0-7.6 (stable supersaturated solution of SBF, with the concentrations of Ca^{2+} and PO_4^{3-} ions 1.5 times higher than those in SBF). Their results show that the solution conditions affect greatly the deposition of HAp on the charged surfaces. In a 1.5 SBF with pH < 7.4 negative surfaces with -COOH functional groups have a more powerful induction capability for the heterogeneous nucleation of HAp than that of OH functional groups, whereas nucleation was obviously prohibited on a positive surface (NH_2-SAM). Furthermore, they observed HAp deposition on the positive NH_2-SAM after the calcium phosphate particles had nucleated homogeneously in supersaturated solution (1.5 SBF, pH ≥7.4). The maximum amount of CaP formed on the COOH-SAM (pH 7.4), NH_2-SAM (pH 7.4 and pH 7.6) and OH-SAM (for the pH 7.4 solution) reached 120, 50 and16 μg, respectively. The reason for the more powerful HAp deposition ability of the COOH-SAM, compared to that of OH-SAM arises from the fact that they have different magnitudes of surface potential. However, there is no reasonable explanation from this point of view considering the NH_2-SAM, because heterogeneous nucleation of HAp on the positive surfaces is prohibited. According to authors, one possible explanation is that the deposition of HAp onto positively charged NH_2-SAM is due to the adhesion of the negatively charged HAp microparticles homogeneously formed in the solution. They suggested a two-stage mechanism to explain the interaction. Firstly, long-range electrostatic forces promote the adhesion of calcium phosphate microparticles onto the

NH_2-SAM. Then, chemical bonds (hydrogen bonds between the NH_3 head groups of the NH_2-SAM and the PO_4^{3-} ions in the HAp) form between the particles and the NH_2-SAM, which might favor strong adhesion.

In another study, Tanahashi *et al.* [212] also showed the apatite formation dependence on the surface functional groups. Self-assembled monolayers (SAMs) of alkanethiols having CH_3, PO_4H_2, COOH, $CONH_2$, OH, and NH_2 terminal groups formed on a gold surface via sulfur attachment were soaked in a simulated body fluid (SBF), at 37 °C for up to 40 days. The effect of the terminal functional groups on the calcium phosphate deposition was assessed using X-ray photo-electron spectroscopy and measuring the sample mass. Their results showed that the growth rate decreased in the order $PO_4H_2 > COOH \gg CONH_2 \approx OH > NH_2 \gg CH_3 \approx 0$. The results are in good agreement with the most of the literature that negatively charged surfaces act as potent substrates for apatite nucleation. According to Tanahashi *et al.* [212], the low apatite deposition on the NH_2-SAM surface may be attributable to the lack of complexation of Ca ion with the surface phosphate amino complex. The low apatite formation in the case of nonionic groups such as $CONH_2$ and OH was explained as follows: The calcium ion complexation with the $CONH_2$ and OH groups occurs via ionic-dipolar interaction which is a weak interaction compared with electrostatic interaction between Ca^{2+} and the negatively charged group. The ion-induced dipole interaction between the CH_3 and Ca^{2+}, which is the weakest of the interaction forces among those of the interactions given in Figure 2.28, causes little apatite formation induction in the case of CH_3-SAM.

In summary, extensive research has been undertaken into the deposition and growth of calcium phosphates, particularly hydroxyapatite on the polymeric substrates to mimic the bone formation and other natural materials that are inorganic-organic composites. Although enormous progress has been made in understanding the process of HAp biomineralization in natural bone, the bone formation under mild temperature, pressure and pH has not been completely replicated in the lab, due to our incomplete knowledge of the mineralization process. The development of bone-like composite materials with improved mechanical properties and enhanced biocompatibility is still a big challenge. Therefore, the ability to tailor synthetic nanocomposite materials that exhibit hierarchical order over multiple length scales opens up possibilities for bottom up approaches for designing novel inorganic-organic materials with properties similar to the bone. The attempts at synthesizing bone-like composites will not only make contribution towards the understanding of biomineralization process, but also lead to the development of new strategies for the fabrication of bone implant materials.

Table 2.1. Various calcium phosphate compounds with their atomic Ca/P ratios [23].

Compound and acronym	Ca/P	Formula
Hydroxyapatite (HAp)	1.67	$Ca_{10}(PO_4)_6(OH)_2$
Amorphous calcium phosphate	-	$Ca_{10-x}H_{2x}(PO_4)_6(OH)_2$
Brushite (Dicalcium phosphate dihydrate, DCPD)	1.0	$CaHPO_4 \cdot 2H_2O$
Monetite (Dicalcium phosphate anhydrous, DCPA)	1.0	$CaHPO_4$
Octacalcium phosphate (OCP)	1.33	$Ca_8H_2(PO_4)_6 \cdot 5H_2O$
α-Tricalcium phosphate (α-TCP)	1.5	α-$Ca_3(PO_4)_2$
β-Tricalcium phosphate (β-TCP)	1.5	β-$Ca_3(PO_4)_2$
Tetracalcium phosphate (TTCP)	2.0	$Ca_4(PO_4)_2O$
Calcium pyrophosphate (CPP)	1.0	$Ca_2P_2O_7$
Heptacalcium phosphate (HCP)	0.7	$Ca_7(P_5O_{16})_2$
Monocalcium phosphate monohydrate (MCPM)	0.5	$Ca(H_2PO_4) \cdot H_2O$

Table 2.2. The composition of human bone mineral (dry weight) [24, 57].

Major Composition		Trace Elements Concentration (μg/g dry weight)			
Component	Concentration (wt%)	Element	Range	Element	Range
Ca	34.8	Li	1-26	As	0.011
P	15.2	Be	0-4	Se	0.1-21
CO_3	7.4	B	2-4	Br	1-5
Na	0.9	Al	3-241	Rb	0.3-0.7
K	0.03	Si	3-40	Sr	75-150
Mg	0.72	S	0.69-1.83%[a]	Zr	0.3-6
Sr	0.05	Ti	0.1-2	Mo	0-0.1
Cl	0.13	V	0.04-8	Ag	1-19
F	0.03	Cr	0.1-6	Cd	1-8
P_2O_7	0.07	Mn	0.2-26	Sn	3-13
		Fe	3-120	Sb	0-3
		Co	0-0.4	Ba	20-5940
		Ni	2-18	Hg	0.012
		Cu	1-3860	Pb	10-50
		Zn	50-280	Rare earths	0.001-2.2

[a] weight percent

Table 2.3. Principle components of some structural biological composites [110].

	Mineral			Organic			
Biological composite	$CaCO_3$	Ca	CO_3HAp	Keratin	Collagen	Chitin	Other
Shells	x						x
Horns		x		x			
Bones			x		x		
Teeth			x				x
Bird Beaks		x		x			
Crustacean	x					x	x
Insect cuticle						x	x

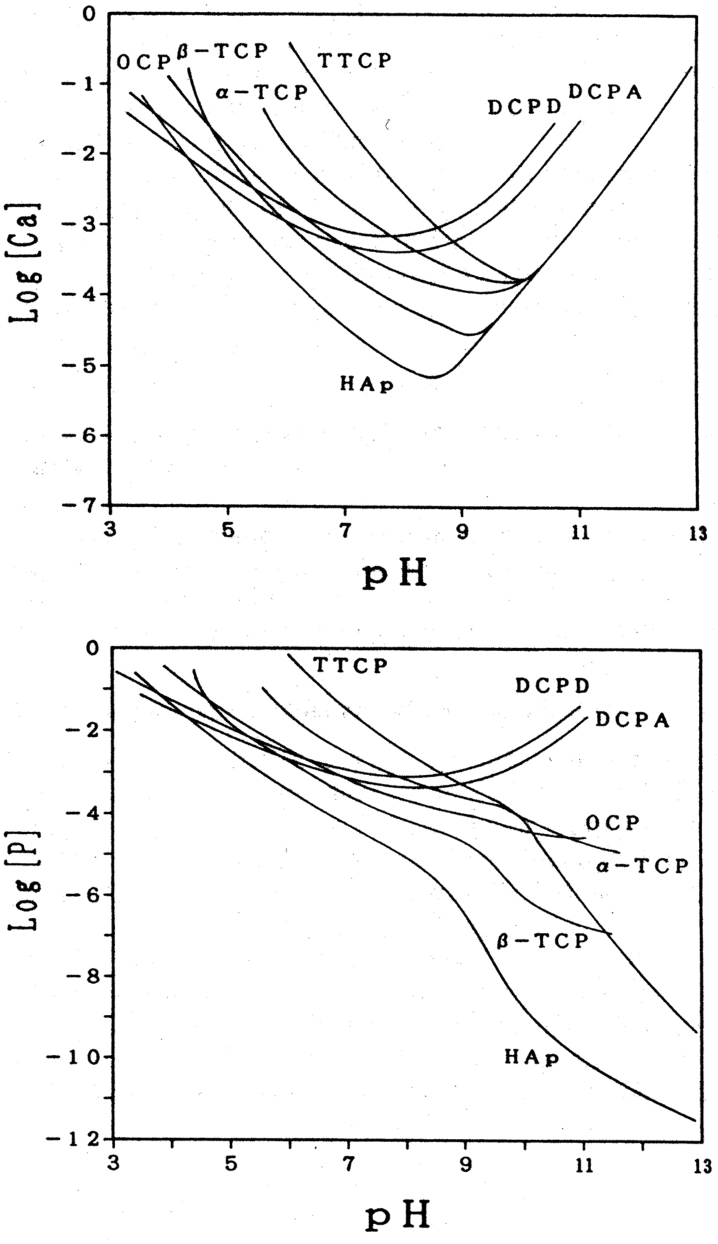

Figure 2.1. Solubility phase diagram for the ternary $Ca(OH)_2$-H_3PO_4-H_2O system at 37°C showing two logarithms of the concentrations of calcium and phosphate as a function of the pH in solution saturated with various salt in the solubility isotherm [213].

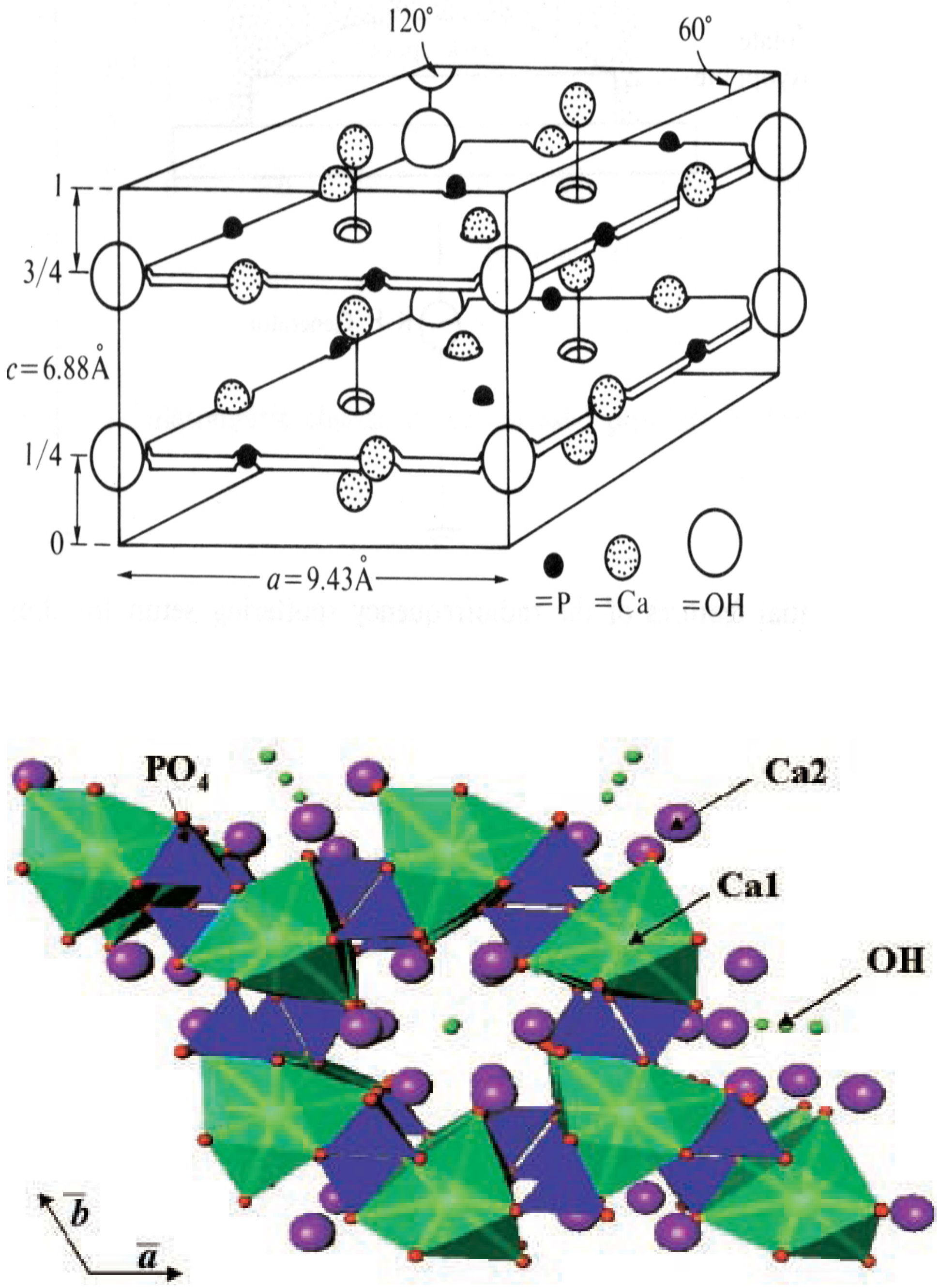

Figure 2.2. Structure of the hydroxyapatite (hexagonal, space group *P*63/*m*) [7, 10].

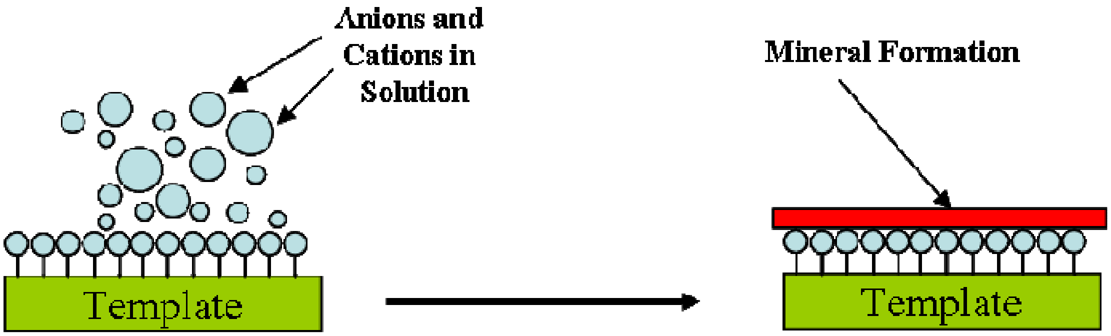

Figure 2.3. Formation of mineral coating on a template [214].

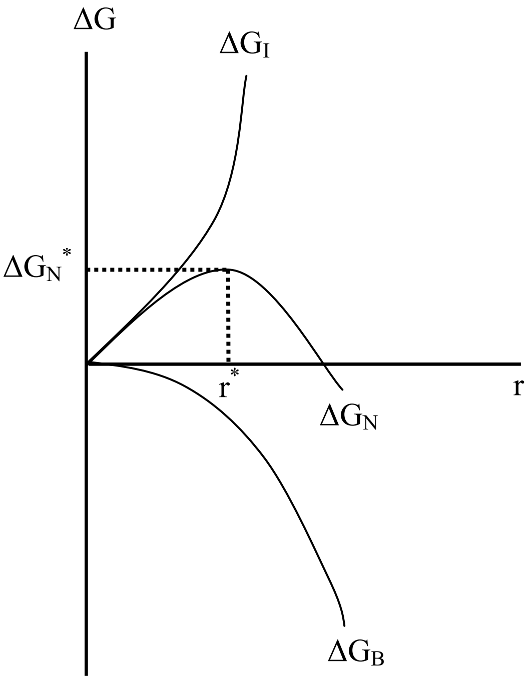

Figure 2.4. Free energy of nucleation (ΔG_N) as a function of cluster size (r).

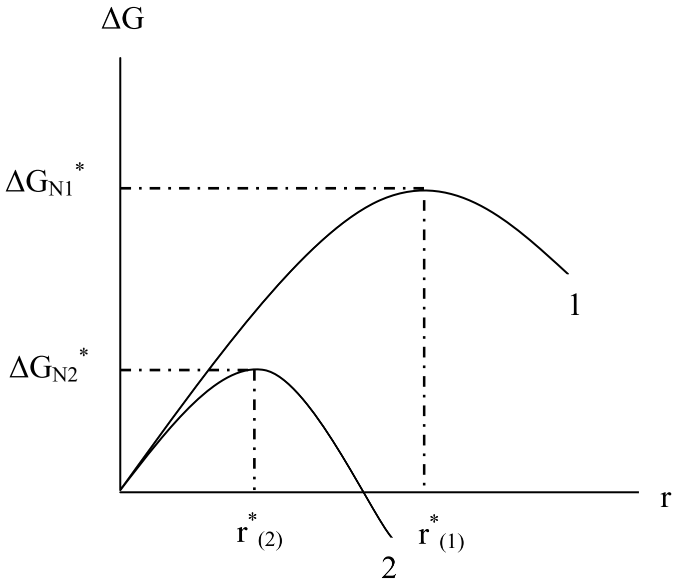

Figure 2.5. Free energy curves for nucleation in the absence (1) and presence (2) of an organic surface.

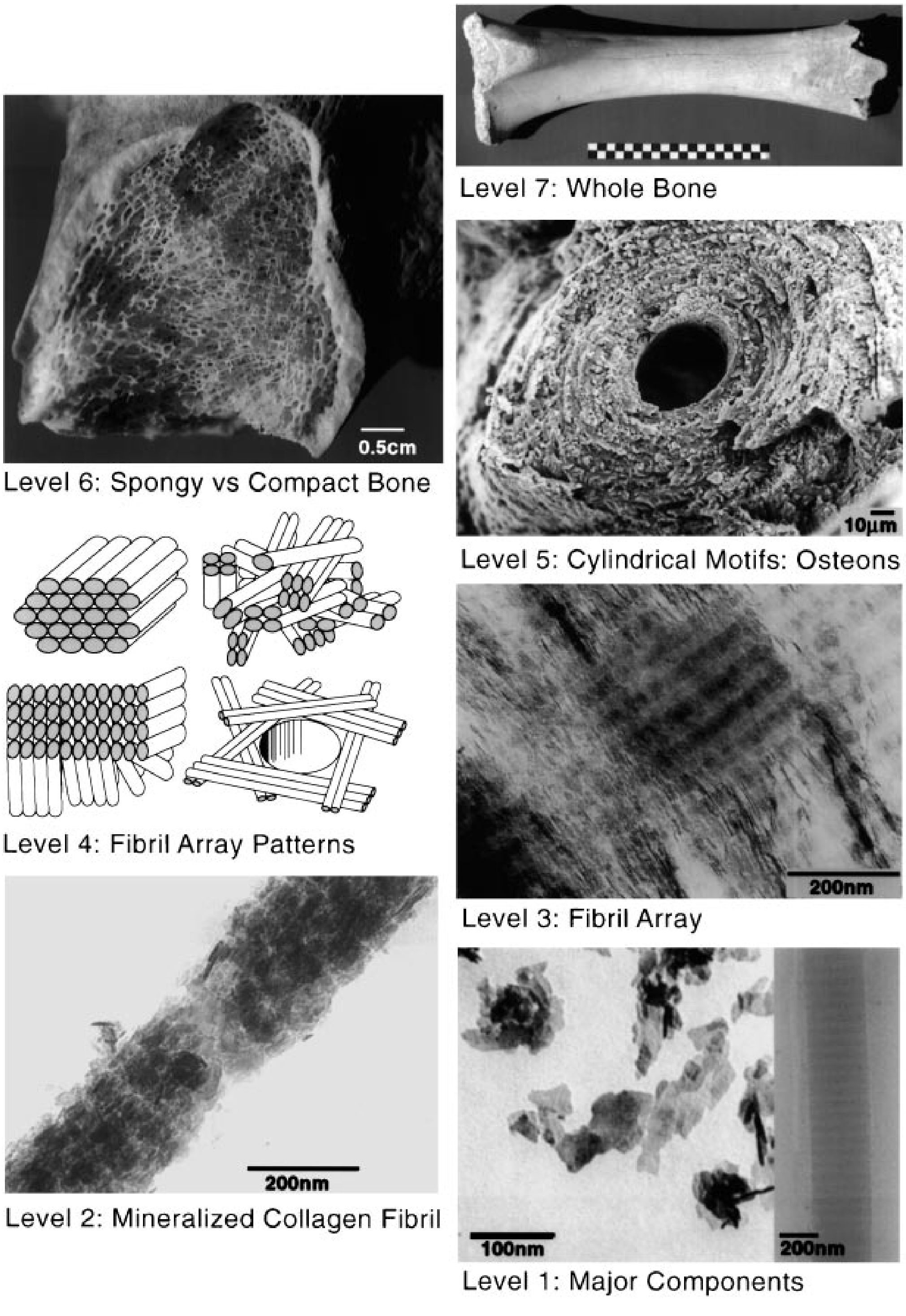

Level 7: Whole Bone

Level 6: Spongy vs Compact Bone

Level 5: Cylindrical Motifs: Osteons

Level 4: Fibril Array Patterns

Level 3: Fibril Array

Level 2: Mineralized Collagen Fibril

Level 1: Major Components

Figure 2.6. The seven hierarchical levels of organization found in the bone family of materials as reported by Weiner and Wagner [43].

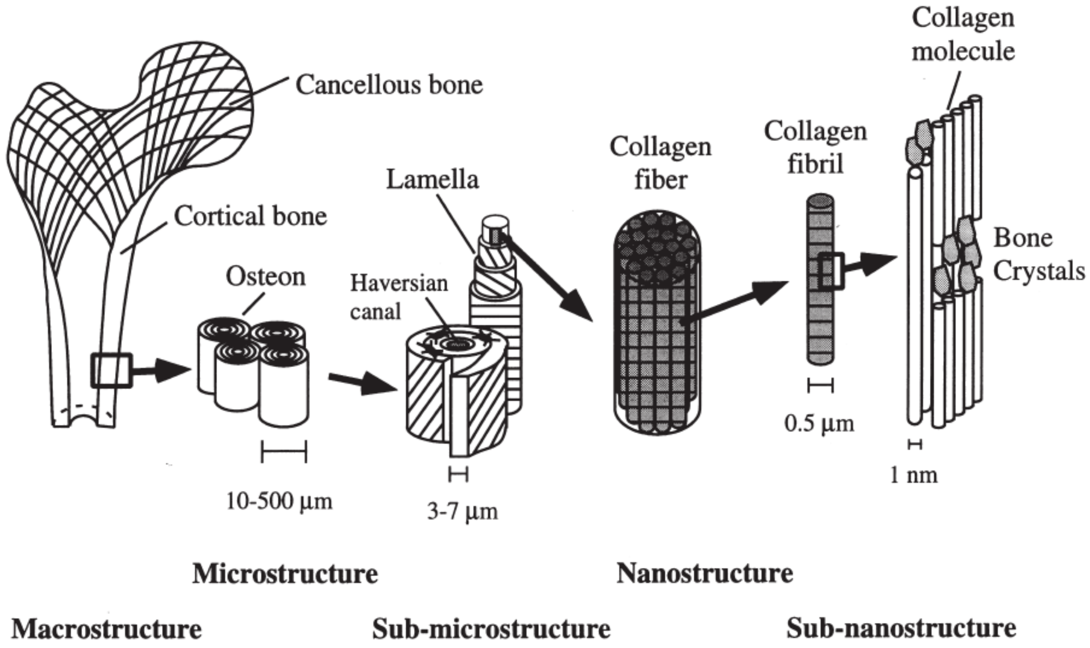

Figure 2.7. Hierarchical organization of bone as reported by Rho *et al.* [44].

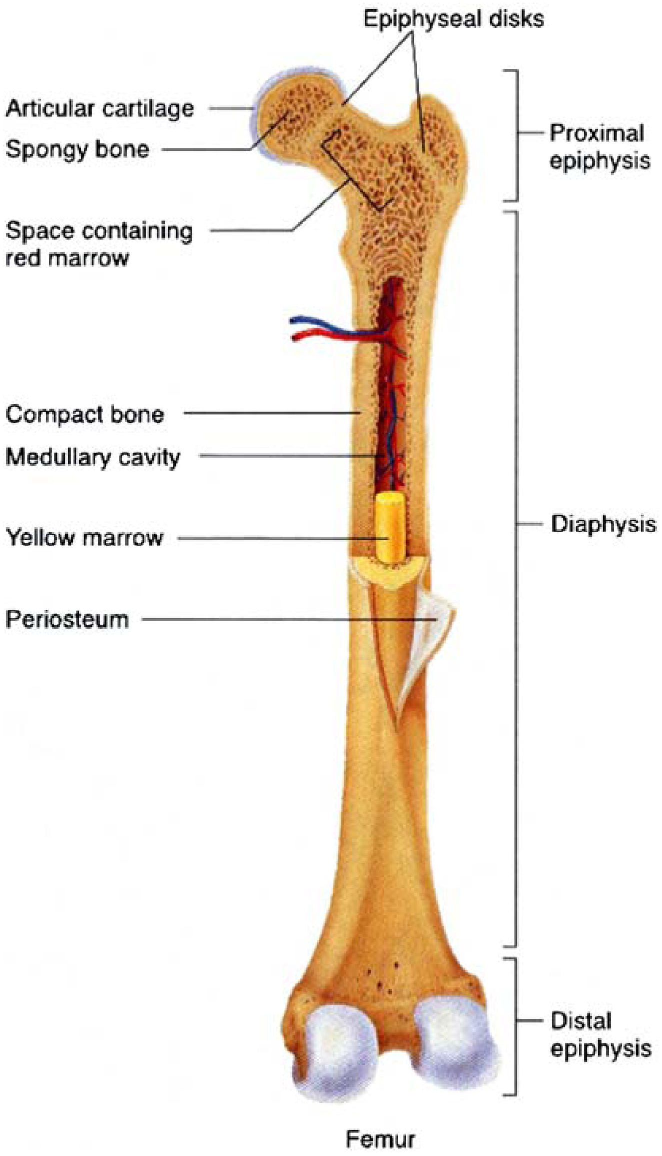

Figure 2.8. General structure of a mammalian bone [3].

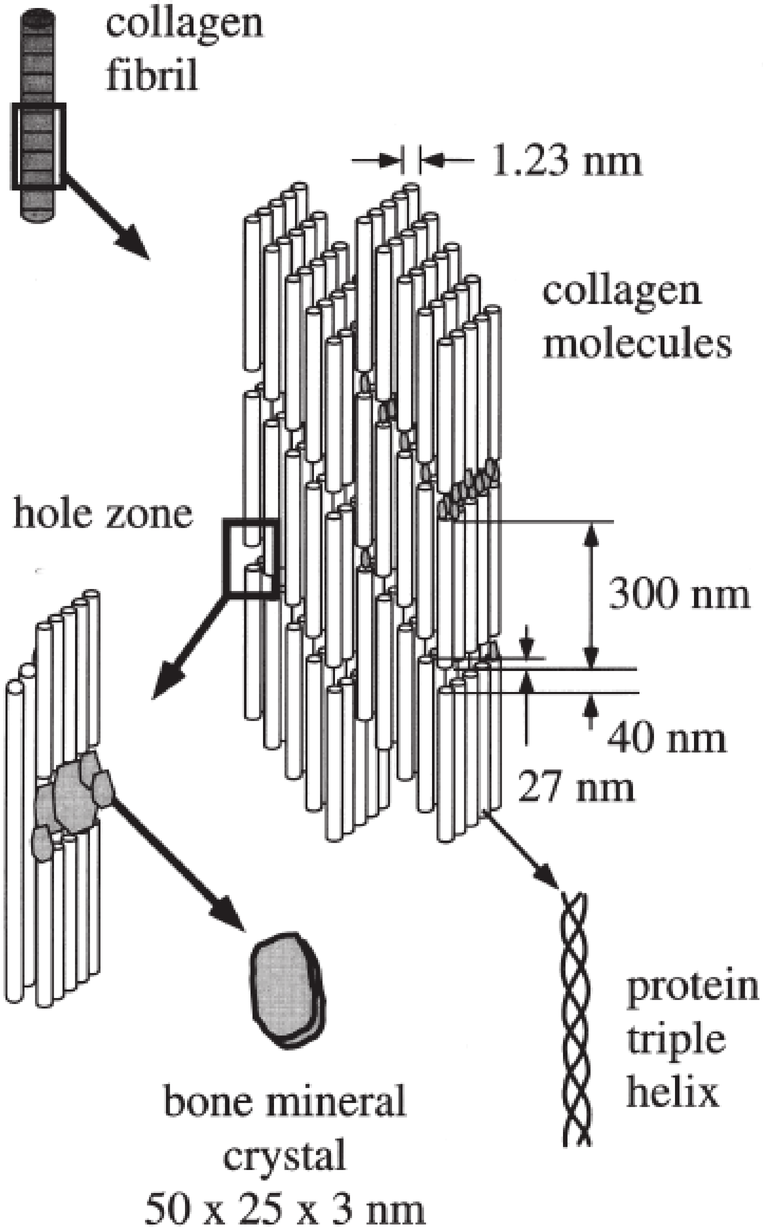

Figure 2.9. A schematic representation of the assembly of the collagen fibrils, triple helical molecule and bone crystals. The location of crystals is primarily in the hole zones of the collagen fibrils [44].

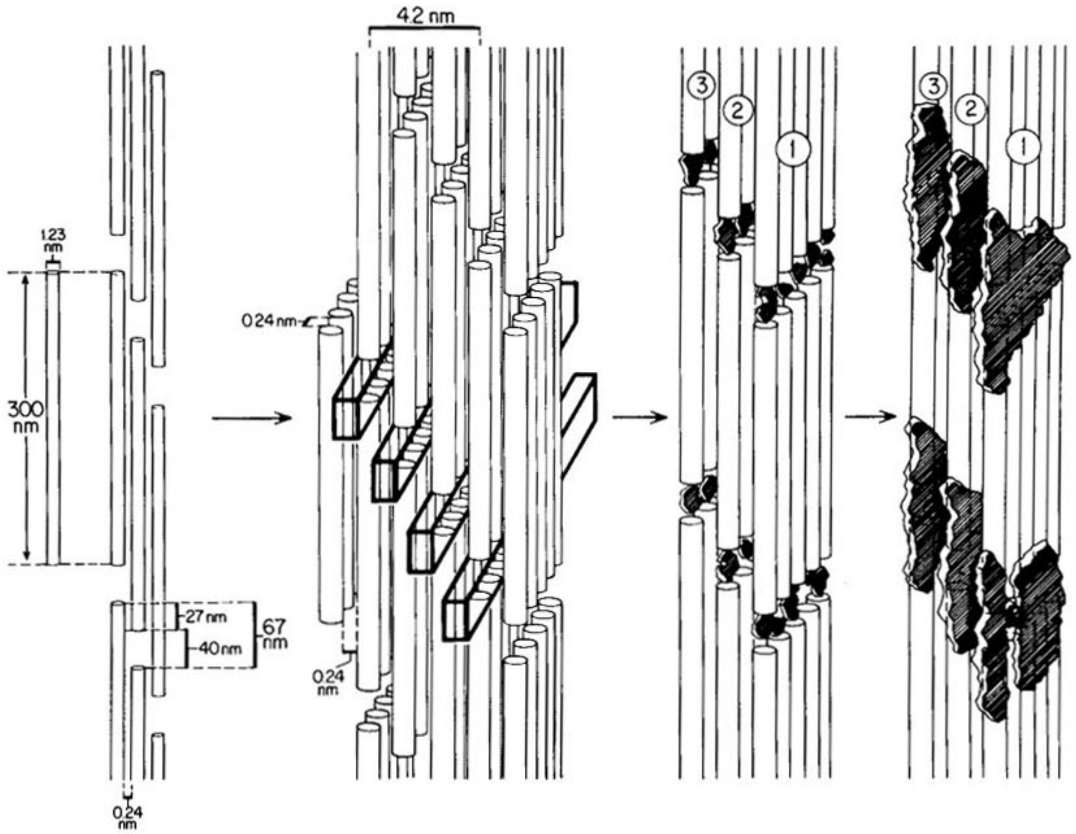

Figure 2.10. Schematic illustration showing the mineralization steps in the assembly of the 3D model of collagen fibrils. The plate-like nano-sized crystals are initially deposited in the hole zones between collagen fibrils and the crystallographic *c*-axes of the crystals is almost parallel to one another and to the long axis of the collagen fibrils. The growth of crystals in widthwise is not limited to single hole zones (the crystals may also occupy hole zones of the adjacent collagen molecules). If two crystals form in adjacent zones, they may fuse to create larger particles [78].

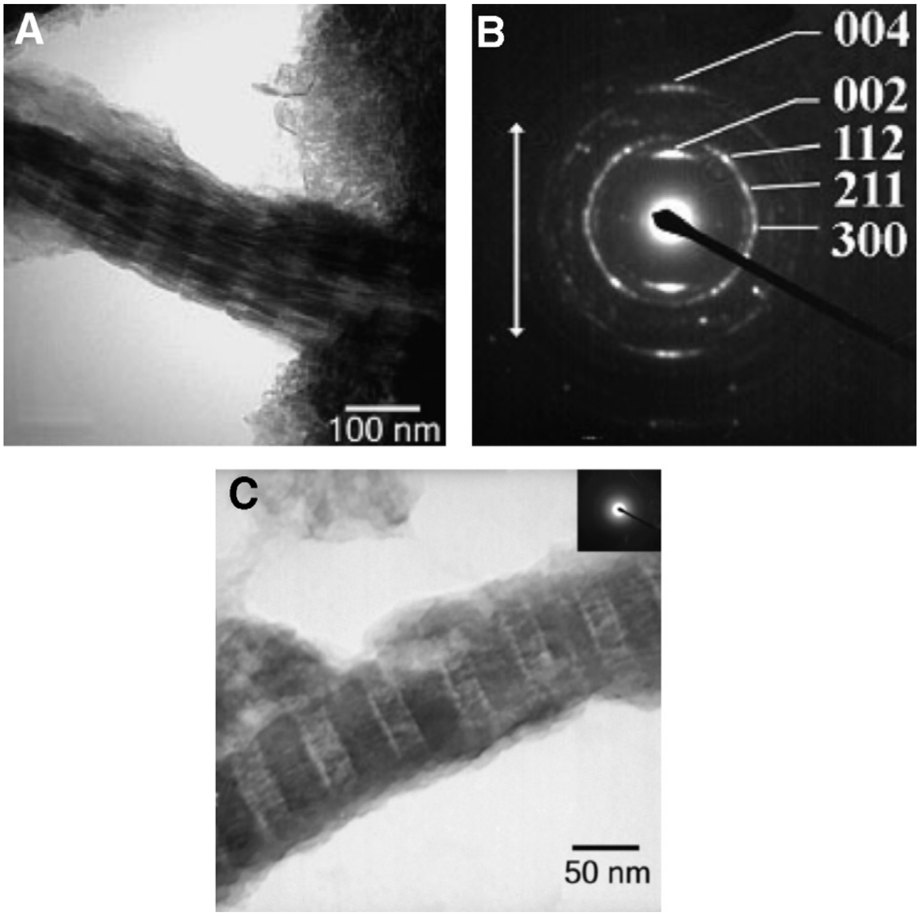

Figure 2.11. Electron images of equine cortical bone. (a) TEM bright field image demonstrating intrafibrillar mineralization of type I collagen fibrils in natural bone. The native banding pattern of type I collagen can be observed due to the infiltration of electron dense mineral (without any staining). The striated appearance results from hydroxyapatite platelets aligned parallel to the long axis of the collagen (b) Selected area electron diffraction (SAED) of a single fibril of crushed equine bone with the characteristic HAp diffraction rings. The arcing of the (002) and (004) planes, which are parallel to the long axis of the collagen fibrils (white arrow) is characteristic of bone. (c) TEM bright field image of an isolated collagen fibril showing the characteristic banding pattern of type I collagen [34].

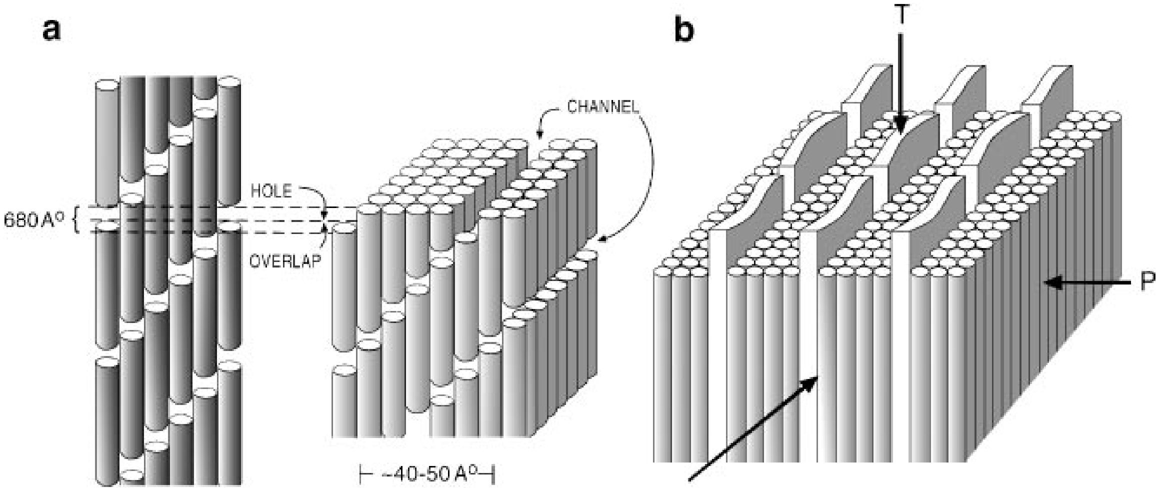

Figure 2.12. Diagramatic illustration (not drawn to scale) of the structure of type I collagen as demonstrated by Weiner and Wagner [43]. (a, left side) A 2-dimensional section through part of a 1.5 nm thick collagen fibril illustrating the staggered array model first reported by Hodge and Petruska [85]. (a, right side) A 3-dimensioanal perspective showing the alignment of the holes to form a channel or gaps. (b) A model showing the proposed location of the plate-like mineral crystals in the channels. The arrows in (b) show the three main symmetry directions. In parallel-fibered bone, T is in the plane transverse to the bone long axis and P is in the plane parallel to the natural outer surface of the bone.

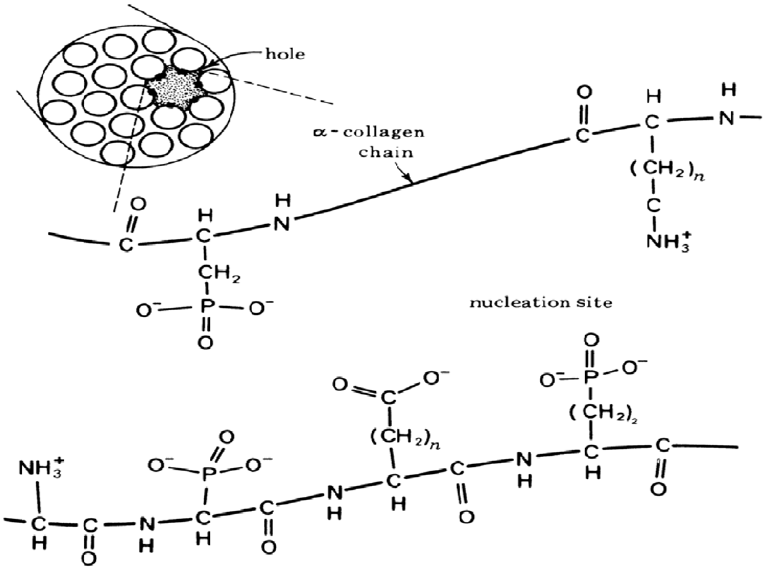

Figure 2.13. Schematic representation of a nucleation site in collagen fibril [82].

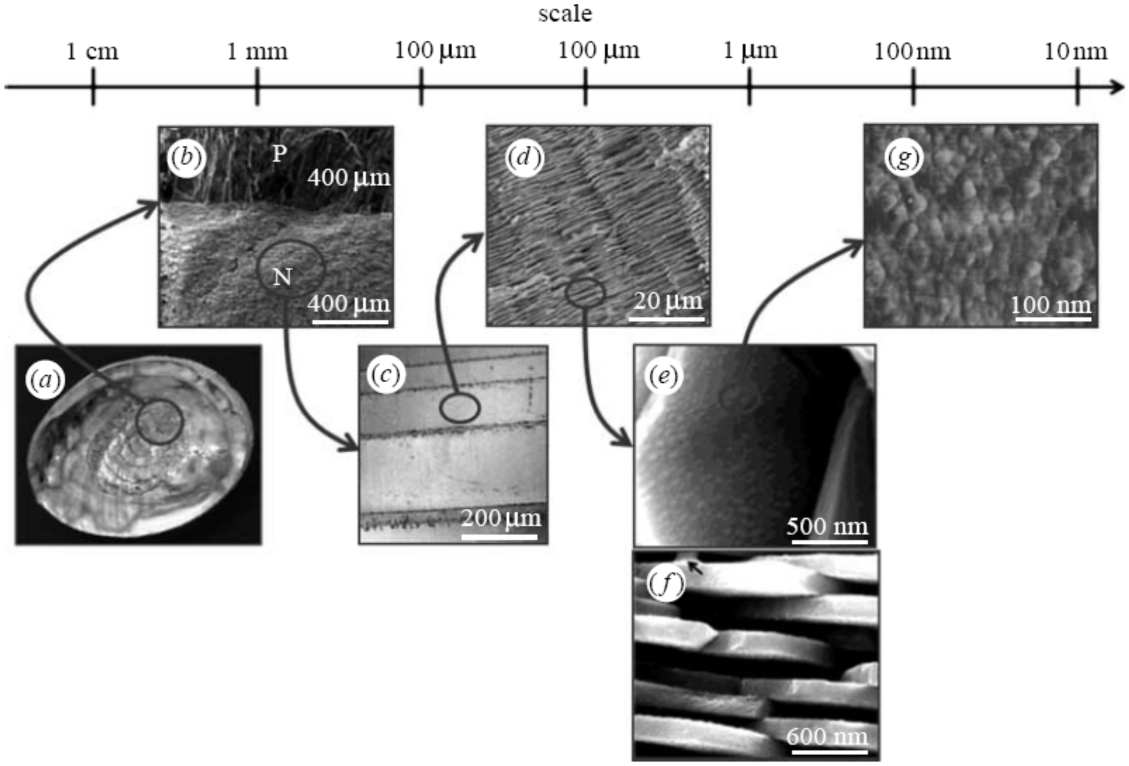

Figure 2.14. The hierarchical structure of nacre [115].

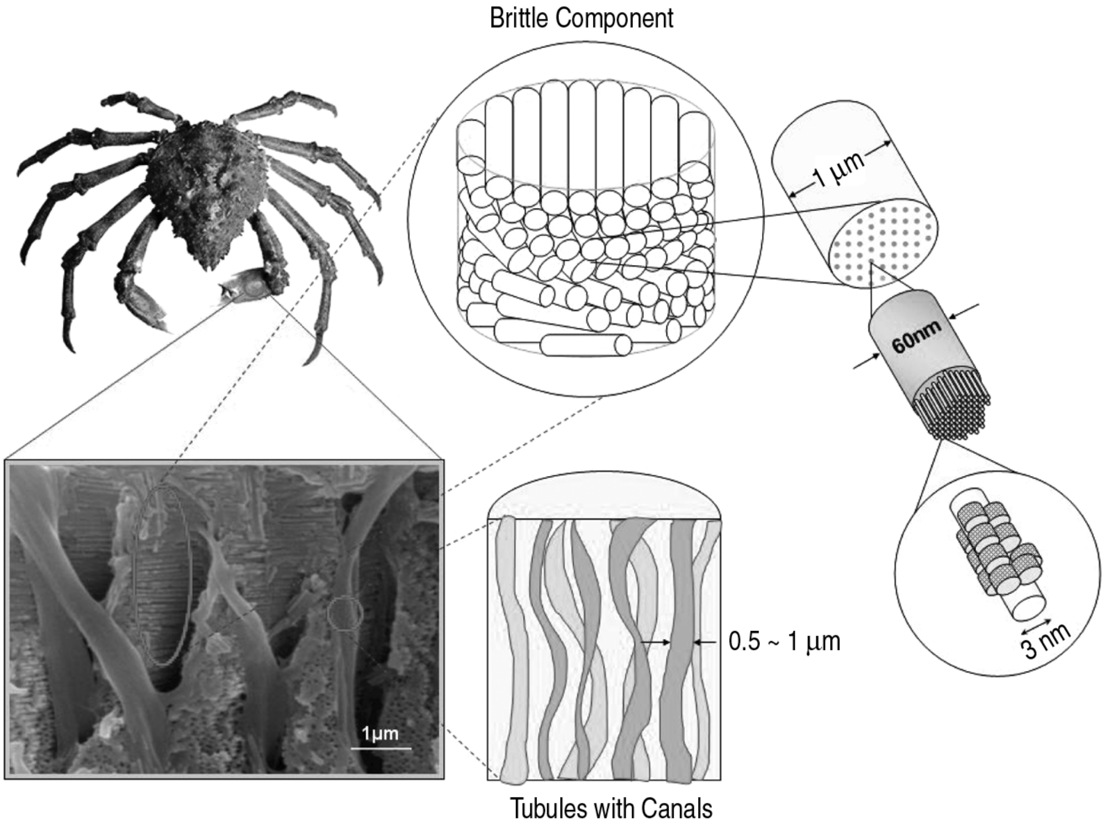

Figure 2.15. The hierarchy of spider crab structure [110].

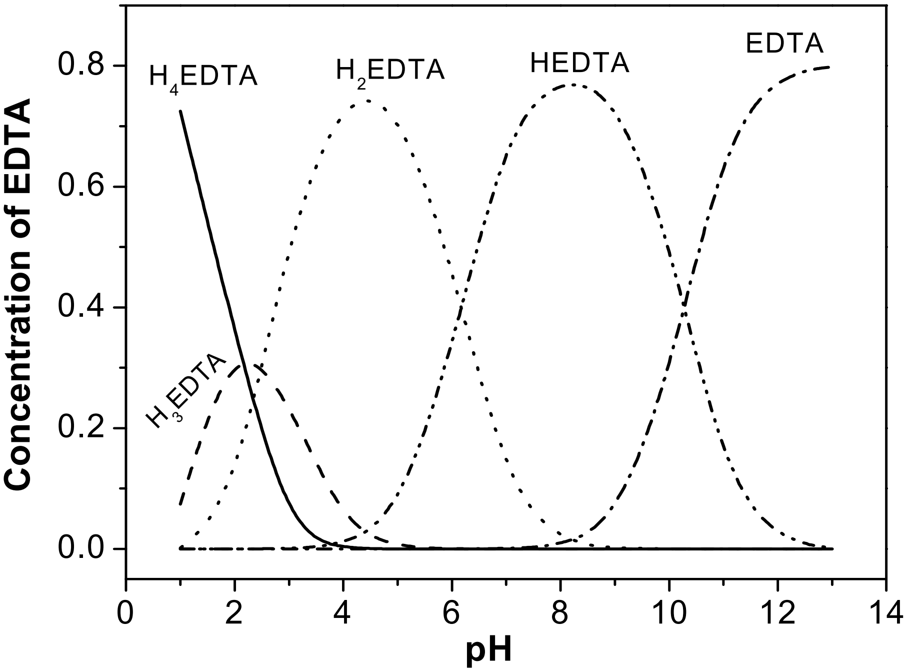

Figure 2.16. Concentration variation of EDTA with pH at room temperature.

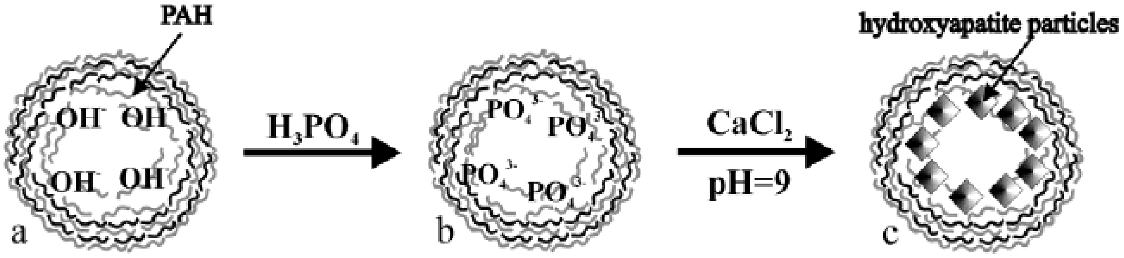

Figure 2.17. Schematic illustration of the hydroxyapatite synthesis inside polyelectrolyte capsules. (a) Poly(allylamine hydrochloride)/poly(styrene sulfonate) (PAH/PSS) capsules with positively charged PAH macromolecules inside are doped with OH$^-$ ions to ensure complete filling of the capsule volume with PO$_4^{3-}$ via performing a neutralization reaction. (b) The capsules are treated with H$_3$PO$_4$ to form PAH/ PO$_4^{3-}$ complex. (c) The polyelectrolyte capsules are washed and added to the solution containing CaCl$_2$ at pH 9 for 48 h to form hydroxyapatite particles [153].

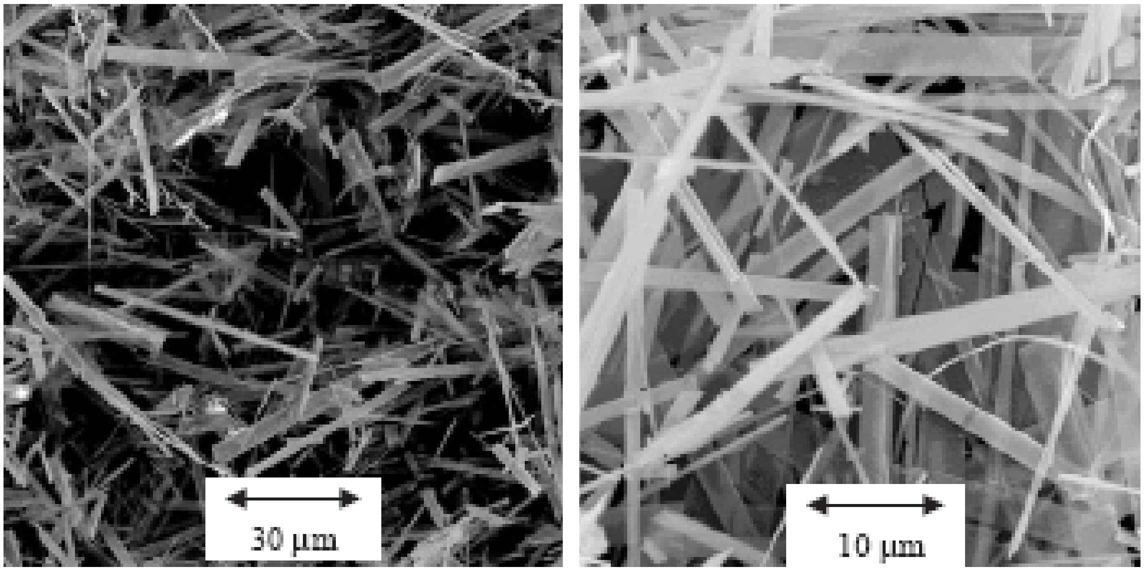

Figure 2.18. The morphology of the HAp crystals observed by Aizawa *et al.* [162, 163].

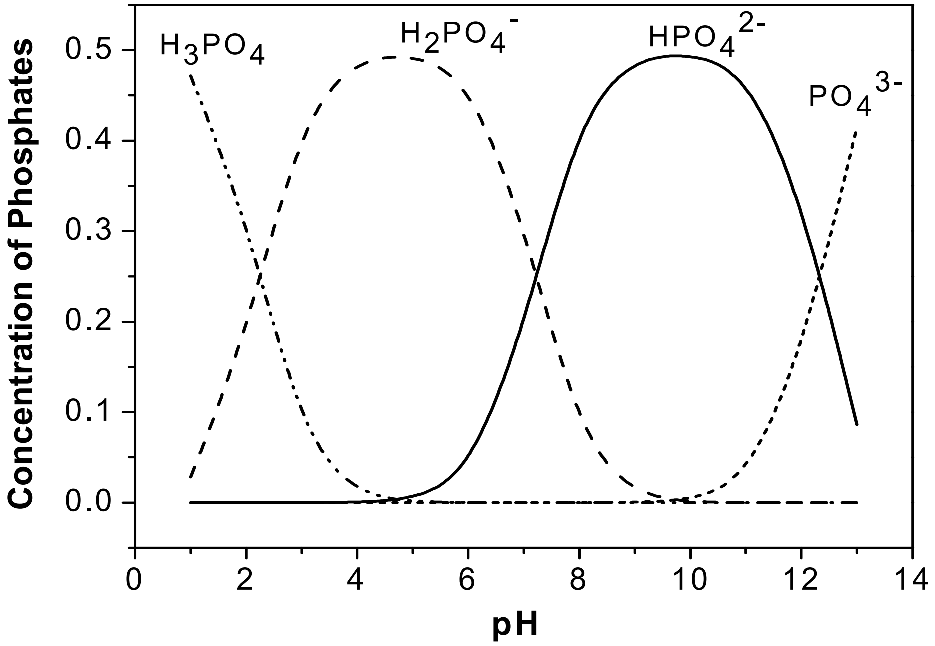

Figure 2.19. Concentration variation of phosphates with pH at room temperature.

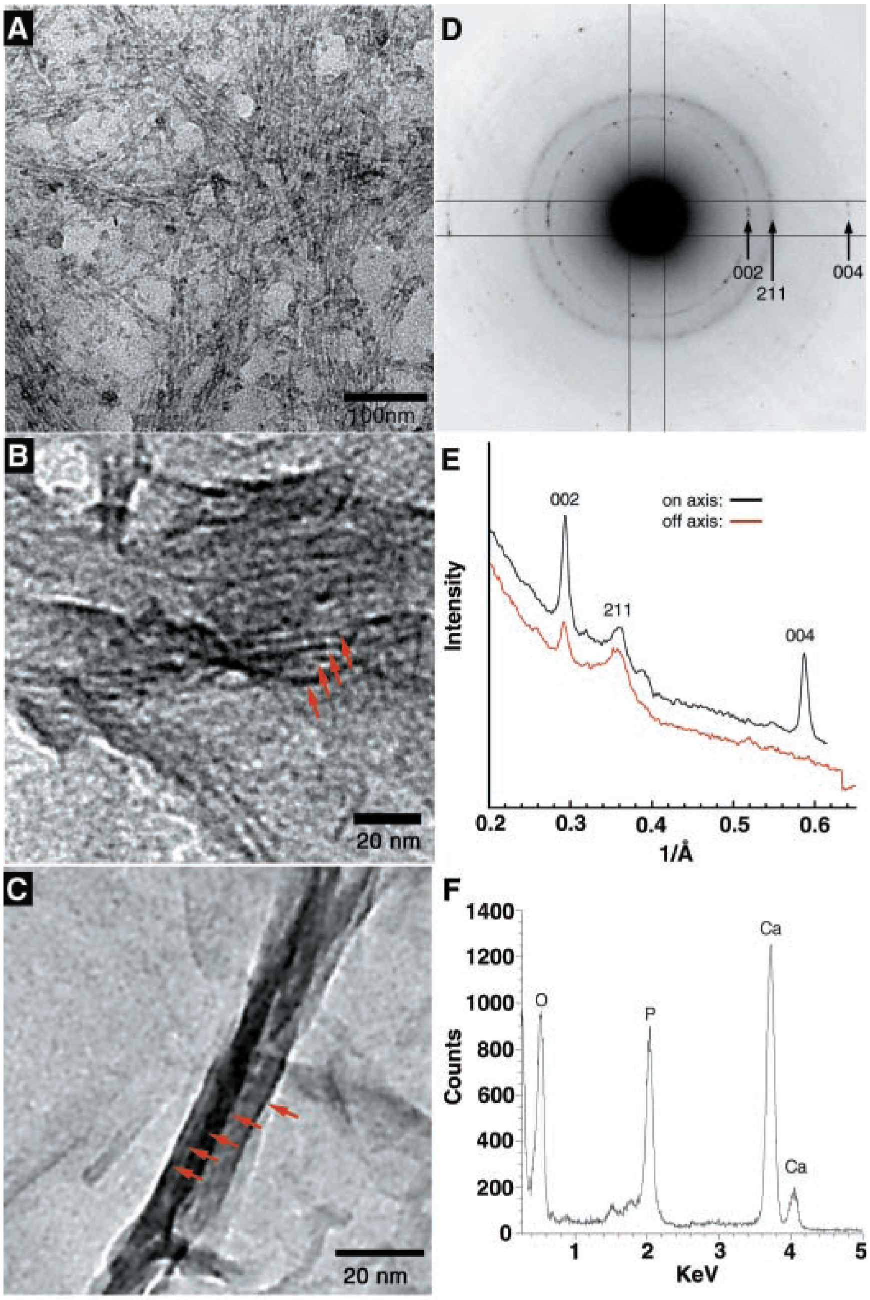

Figure 2.20. (a) TEM micrographs of the unstained, cross-linked peptide-amphiphile fibers treated for 10 min with $CaCl_2$ and Na_2HPO_4 solutions. (b) after 20 min, observation of HAp crystals in parallel arrays on some of the PA fibers (shown by arrows). (c) after 30 min, HAp particles (shown by arrows) completely cover PA fibers. (d) Electron diffraction pattern taken from TEM micrograph (c) shows (002) and (004) planes of HAp. (e) Plot of intensity vs. inverse Å reveals that (002) and (004) peaks of HAp are strongly enhanced along the PA fiber axis, which indicates preferential alignment of the HAp crystals with their *c*-axes along the long axis of the bundle. (f) EDS profile of the HAp crystals after 30 min (Ca/P ratio is approximately 1.7) [180].

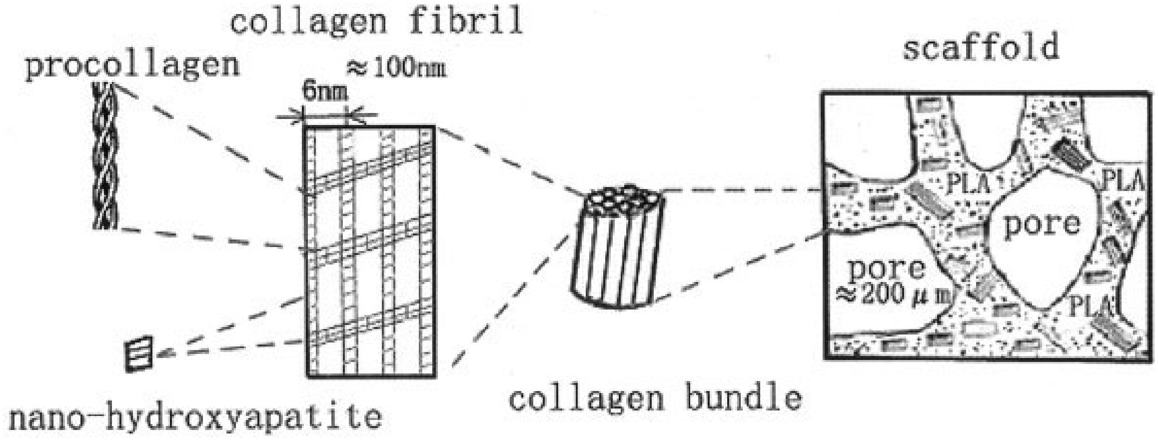

Figure 2.21. Hierarchical structure of the HAp/collagen/PLA nanocomposite, as described by Liao *et al.* [182]. The nano-sized hydroxyapatite crystals and collagen molecules assembled into mineralized fibril similar to natural bone. The mineralized fibrils then assemble into bundles and are uniformly distributed within a PLA matrix. The porous microstructure of this material is similar to that of cancellous bone.

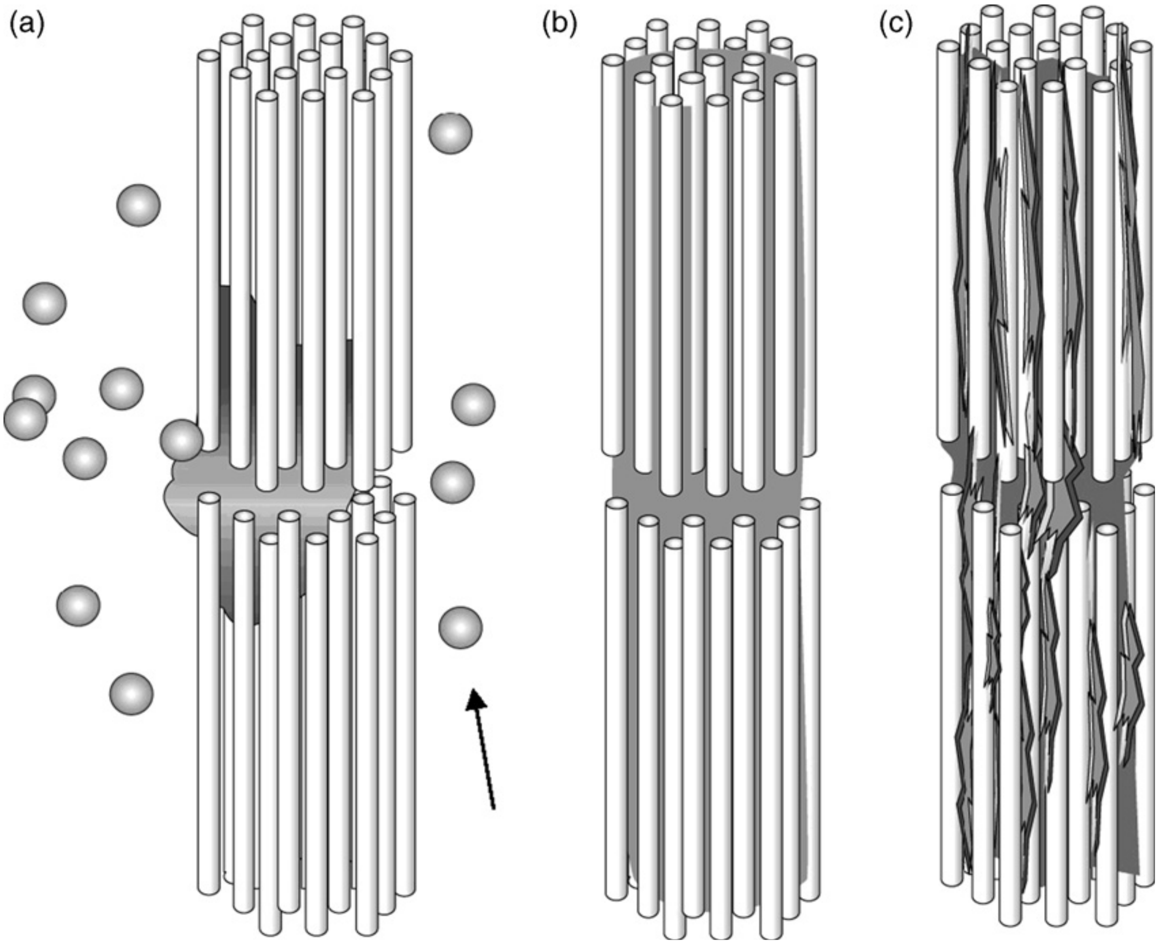

Figure 2.22. A schematic representation of the proposed mechanism of intrafibrillar mineralization of collagen. The picture shows the hole zone region of a collagen fibril within the aqueous mineralizing solution, which also contains the polymeric process-directing agent (polyaspartate). (a) Formation of highly hydrated amorphous calcium phosphate particles and incorporation of these particles into the hole zones and interstices of the collagen fibril by capillary action. (b) Solidification of amorphous mineral precursor as the hydration water is excluded. (c) Crystallization of the amorphous precursor mineral, which results in the collagen embedded with nano-sized crystal of HAp [34].

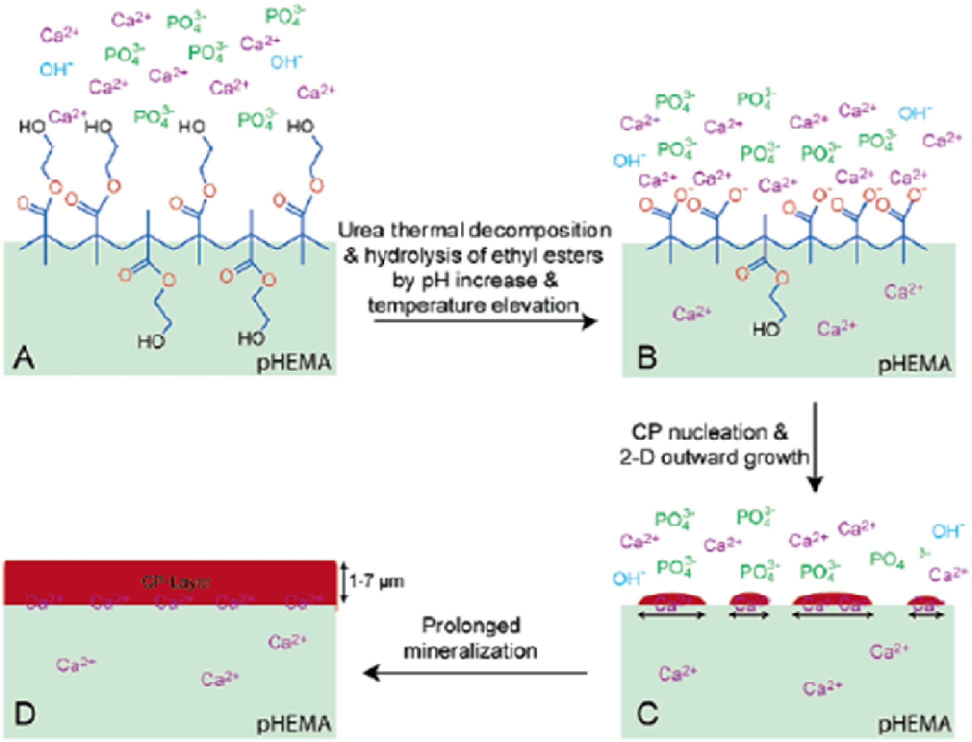

Figure 2.23. Mineralization of HAp onto the pHEMA hydrogel scaffolds with the thermal decomposition of urea [184].

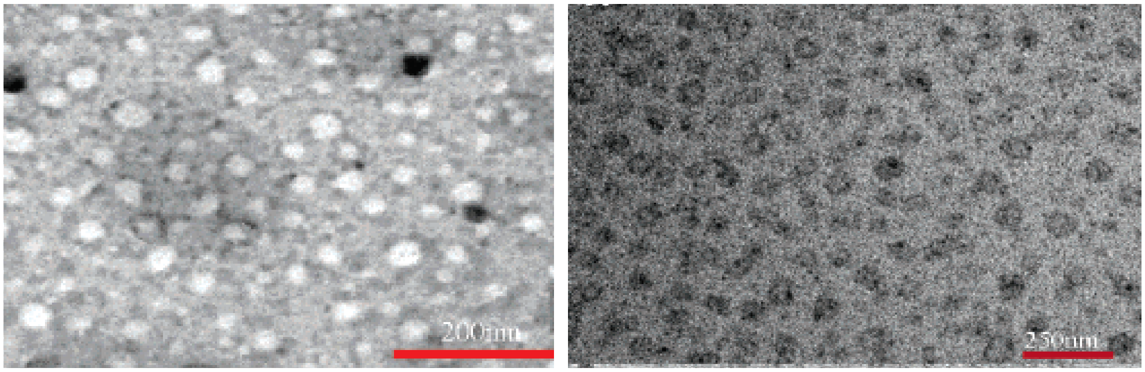

Figure 2.24. TEM micrographs of (left side) uranyl acetate stained sample of shell cross-linked PAA-b-PI micelles and (right side) unstained calcium phosphate mineralized shell cross-linked PAA-b-PI micelles [186].

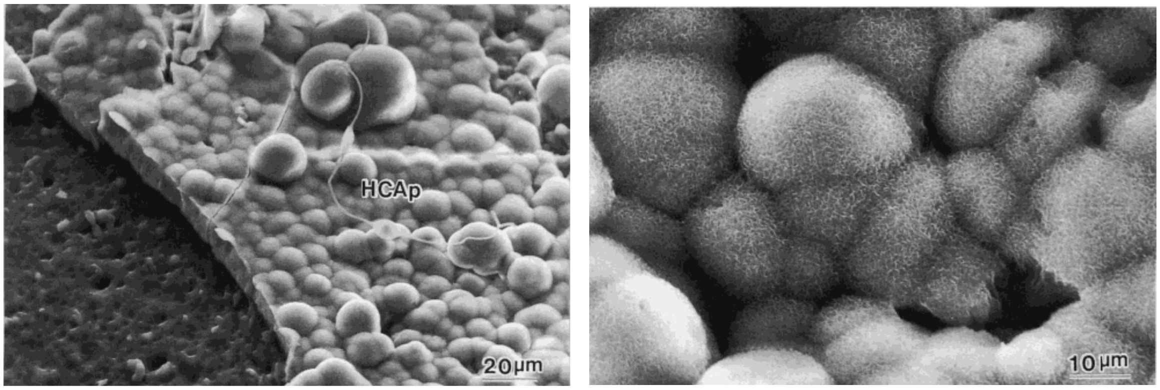

Figure 2.25. SEM micrographs at two magnifications of the CO_3HAp layer formed on the Polyactive® [187].

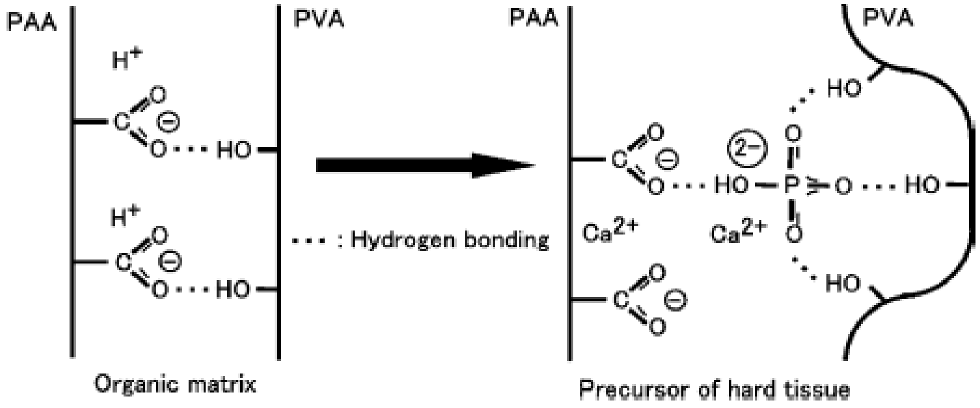

Figure 2.26. Schematic illustration of hypercomplex formation (right) via the polymer complex [17].

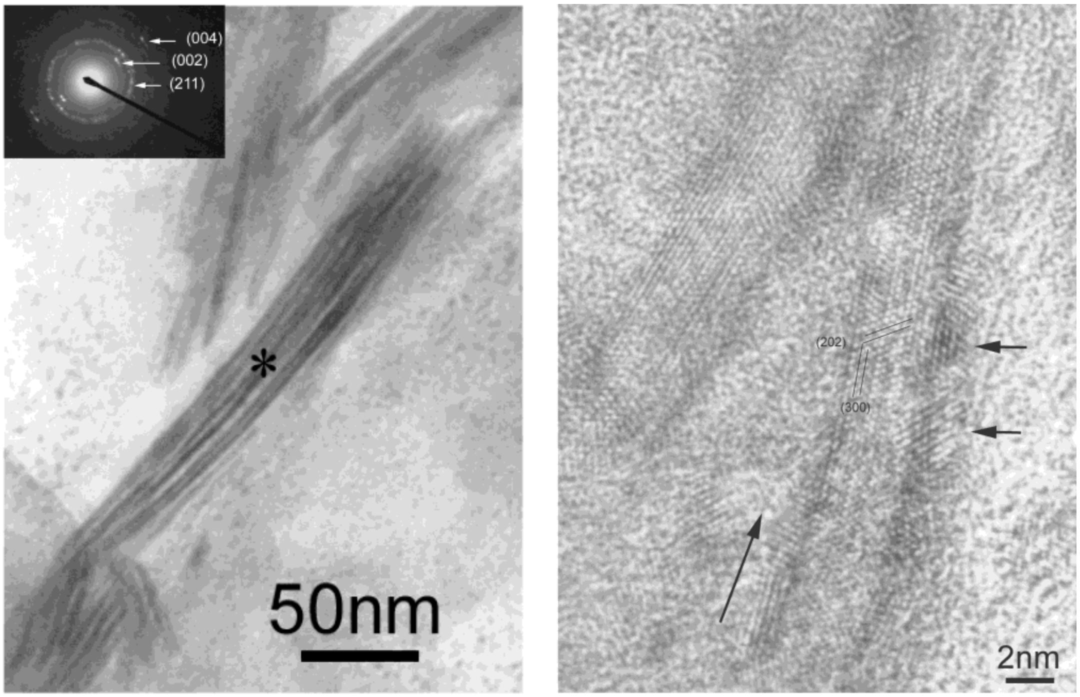

Figure 2.27. TEM micrograph (left side) of the mineralized collagen fibrils. Inset is the selected area electron diffraction pattern of the mineralized collagen fibrils taken from the region shown by asterisk. High resolution TEM image (right side) of mineralized collagen fibrils. Long arrow shows the longitude direction of collagen fibril. Two short arrows indicate the HAp nanocrystals [203].

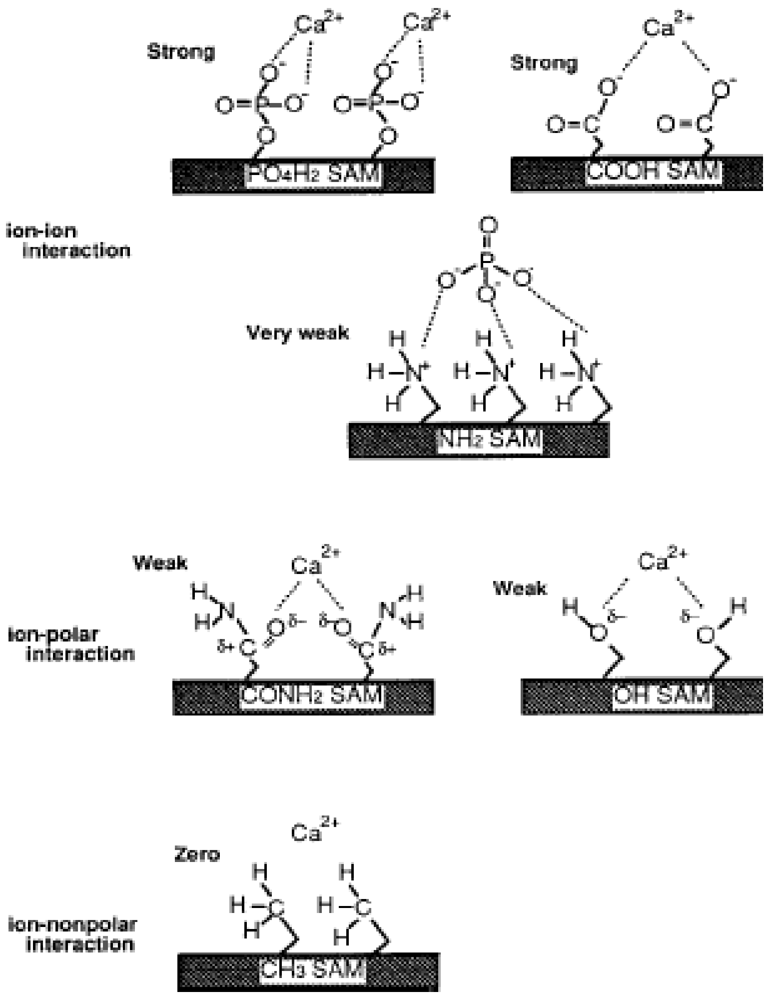

Figure 2.28. Various interaction modes between calcium and phosphate ions and surface functional groups as an initial step for apatite formation [212].

2.6 References

1. C. Rey, C. Combes, C. Drouet, and M.J. Glimcher. *Osteoporos Int.*, (2009).
2. M. Vallet-Regi. *Dalton Trans.*, (2006); p: 5211-5220.
3. S.V. Dorozhkin. *J. Mater. Sci.*, (2007); 42, p: 1061-1095.
4. Z. Amjad. *Calcium Phosphates in Biological and Industrial Systems,* (1998)*;* p: 1-515; Boston, Kluwer Academic Publishers.
5. L.L. Hench. *J. Am. Ceram. Soc.*, (1991); 74, p: 1487-1510.
6. H.B. Pan and B.W. Darvell. *Cryst. Growth Des.*, (2009); 9, p: 639-645.
7. J.C. Elliott. *Studies in Inorganic Chemistry: Structure and Chemistry of the Apatites and Other Calcium Orthophosphates,* (1994)*;* p; New York, Elsevier Science B.V.
8. L.L. Hench. *Biomaterials*, (1998); 19, p: 1419-1423.
9. L.L. Hench. *J. Am. Ceram. Soc.*, (1998); 81, p: 1705-1728.
10. M. Vallet-Regi. *J. Chem. Soc., Dalton Trans.*, (2001); p: 97-108.
11. S.C. Rizzi, D.J. Heath, A.G.A. Coombes, N. Bock, M. Textor, and S. Downes. *J. Biomed. Mater. Res.*, (2001); 55, p: 475-486.
12. K. Kato, Y. Eika, and Y. Ikada. *J. Biomed. Mater. Res.*, (1996); 32, p: 687-691.
13. J. Li, B. Fartash, and L. Hermansson. *Biomaterials*, (1995); 16, p: 417-422.
14. R. Labella, M. Braden, and S. Deb. *Biomaterials*, (1994); 15, p: 1197-1200.
15. Y. Abe, T. Kokubo, and T. Yamamuro. *J. Mater. Sci.: Mater. Med.*, (1990); 1, p: 233-238.
16. M. Wang, S. Deb, K.E. Tanner, and W. Bonfield. *Realising Their Commer. Potential, Eur. Conf. Compos. Mater., 7th*, (1996); 2, p: 455-460.
17. T. Iwatsubo, K. Sumaru, T. Kanamori, T. Shinbo, and T. Yamaguchi. *Biomacromolecules*, (2006); 7, p: 95-100.
18. D. Arcos, J. Rodriguez-Carvajal, and M. Vallet-Regi. *Solid State Sci.*, (2004); 6, p: 987-994.
19. F. Balas, J. Perez-Pariente, and M. Vallet-Regi. *J. Biomed. Mater. Res., Part A*, (2003); 66A, p: 364-375.
20. M. Vallet-Regi. *An. Quim. Int. Ed.*, (1997); 93, p: S6-S14.
21. J.C. Elliott, G. Bonel, and J.C. Trombe. *J. Appl. Crystallogr.*, (1980); 13, p: 618-621.
22. R.Z. LeGeros. *Monogr Oral Sci*, (1991); 15, p: 1-201.
23. M. Vallet-Regi and J.M. Gonzalez-Calbet. *Prog. Solid State Chem.*, (2004); 32, p: 1-31.
24. S.V. Dorozhkin and M. Epple. *Angew. Chem., Int. Ed.*, (2002); 41, p: 3130-3146.
25. A. Malsy and M. Bohner. *European Cells and Materials*, (2005); 10, p: 28.
26. L.C. Palmer, C.J. Newcomb, S.R. Kaltz, E.D. Spoerke, and S.I. Stupp. *Chem. Rev.*, (2008); 108, p: 4754-4783.
27. P. Calvert and P. Rieke. *Chem. Mater.*, (1996); 8, p: 1715-1727.
28. S. Mann. *Nature* (1988); 332, p: 119-124.
29. A.E. Nielsen. *Kinetics of Precipitation,* (1964)*;* p: 153 pp; New York, Macmillan.
30. A.A. Campbell, G.E. Fryxell, J.C. Linehan, and G.L. Graff. *J. Biomed. Mater. Res.*, (1996); 32, p: 111-118.
31. S. Mann. *Biomineralization Principles and Concepts in Bioinorganic Materials Chemistry,* (2001)*;* p: 1-198; New York, Oxford University Press.

32. S. Mann, D.D. Archibald, J.M. Didymus, T. Douglas, B.R. Heywood, F.C. Meldrum, and N.J. Reeves. *Science*, (1993); 261, p: 1286-1292.
33. I.M. Siegel. *All About Bone,* (1998)*;* p: 1-206; New York, Demos Medical Publishing, Inc.
34. M.J. Olszta, X. Cheng, S.S. Jee, R. Kumar, Y.-Y. Kim, M.J. Kaufman, E.P. Douglas, and L.B. Gower. *Mater. Sci. Eng., R*, (2007); 58, p: 77-116.
35. L.A. Heinz and S. Weiner. *On Biomineralization,* (1989)*;* p: 3-324; New York, Oxford University Press.
36. J. Currey. *The Mechanical Adaptations of Bones,* (1984)*;* p: 4-294; New Jersey, Princeton University Press.
37. R. Carola, P.J. Harley, and R.C. Noback. *Human Anatomy,* (1992)*;* p: 129-143; New York, McGraw-Hill, Inc.
38. M.L. Oyen. *MRS Bull.*, (2008); 33, p: 49-55.
39. D.A. Cameron. *Clin Orthop Relat Res*, (1963); 26, p: 199-228.
40. S.A. Wainwright, W.D. Biggs, J.D. Currey, and J.M. Gosline. *Mechanical Design in Organisms,* (1976)*;* p: 6-423; New York, John Wiley & Sons, Inc.
41. J.Z. Zhang, Z.-l. Wang, J. Liu, S. Chen, and G.-y. Liu. *Self-Assembled Nanostructures,* (2003)*;* p: 7-316; New York, Kluwer Academic/Plenum Publishers.
42. C.S. Cowin. *Bone Mechanics Handbook,* (2001)*;* p: 2-931; Boca Raton, CRC Press
43. S. Weiner and H.D. Wagner. *Annu. Rev. Mater. Sci.*, (1998); 28, p: 271-298.
44. J.Y. Rho, L. Kuhn-Spearing, and P. Zioupos. *Med Eng Phys*, (1998); 20, p: 92-102.
45. C. Gunn. *Bones and Joints,* (1996)*;* p: 1-167; New York, Churchill Livingstone.
46. R.K. Nalla, J.J. Kruzic, J.H. Kinney, and R.O. Ritchie. *Biomaterials*, (2005); 26, p: 217-231.
47. S.A. Reid. *Scanning Microsc*, (1987); 1, p: 579-597.
48. P.V. Hauschka and F.H. Wians, Jr. *Anat. Rec.*, (1989); 224, p: 180-188.
49. R.A. Robinson and S.R. Elliott. *J. Bone and Joint Surg.*, (1957); 39A, p: 167-188.
50. C. Burger, H.-w. Zhou, H. Wang, I. Sics, B.S. Hsiao, B. Chu, L. Graham, and M.J. Glimcher. *Biophys. J.*, (2008); 95, p: 1985-1992.
51. D.R. Simpson. *Clin Orthop Relat Res*, (1972); 86, p: 260-286.
52. R.Z. LeGeros. *Hydroxyapatite Relat. Mater.*, (1994); p: 3-28.
53. C. Rey. *Biomaterials*, (1990); 11, p: 13-15.
54. D. Tadic, F. Peters, and M. Epple. *Biomaterials*, (2002); 23, p: 2553-2559.
55. A.S. Posner. *Physiol. Rev.*, (1969); 49, p: 760-792.
56. F. Betts, N.C. Blumenthal, and A.S. Posner. *J. Cryst. Growth*, (1981); 53, p: 63-73.
57. F.C.M. Driessens and R.M.H. Verbeeck. *Biominerals,* (1990)*;* p: 1-428; Boca Raton, CRC Press.
58. R. Legros, N. Balmain, and G. Bonel. *Calcif. Tissue Int.*, (1987); 41, p: 137-144.
59. K. Schmidt-Rohr. *unpublished work.*, (2009).
60. C.K. Loong, C. Rey, L.T. Kuhn, C. Combes, Y. Wu, S.H. Chen, and M.J. Glimcher. *Bone*, (2000); 26, p: 599-602.
61. C. Rey, J.L. Miquel, L. Facchini, A.P. Legrand, and M.J. Glimcher. *Bone*, (1995); 16, p: 583-586.
62. D.G.A. Nelson and J.C. Barry. *Anat. Rec.*, (1989); 224, p: 265-276.
63. W.E. Brown, N. Eidelman, and B. Tomazic. *Adv Dent Res*, (1987); 1, p: 306-313.

64. R.A. Robinson. *J. Bone & Joint Surg.*, (1952); 34A, p: 389-435,476.
65. A. Rubin Matthew, I. Jasiuk, J. Taylor, J. Rubin, T. Ganey, and P. Apkarian Robert. *Bone*, (2003); 33, p: 270-282.
66. W.J. Landis, M.J. Song, A. Leith, L. McEwen, and B.F. McEwen. *J Struct Biol*, (1993); 110, p: 39-54.
67. W.J. Landis, K.J. Hodgens, J. Arena, M.J. Song, and B.F. McEwen. *Microsc Res Tech*, (1996); 33, p: 192-202.
68. S. Weiner and W. Traub. *FASEB J*, (1992); 6, p: 879-885.
69. S. Weiner and P.A. Price. *Calcif. Tissue Int.*, (1986); 39, p: 365-375.
70. M.J. Glimcher. *Dev. Biochem*, (1981); 22, p: 617-673.
71. X. Su, K. Sun, F.Z. Cui, and W.J. Landis. *Bone*, (2003); 32, p: 150-162.
72. S.J. Eppell, W. Tong, J.L. Katz, L. Kuhn, and M.J. Glimcher. *J Orthop Res*, (2001); 19, p: 1027-1034.
73. T. Hassenkam, E. Fantner Georg, A. Cutroni Jacqueline, C. Weaver James, E. Morse Daniel, and K. Hansma Paul. *Bone*, (2004); 35, p: 4-10.
74. P. Fratzl, N. Fratzl-Zelman, K. Klaushofer, G. Vogl, and K. Koller. *Calcif Tissue Int*, (1991); 48, p: 407-413.
75. P. Fratzl, M. Groschner, G. Vogl, H. Plenk, Jr., J. Eschberger, N. Fratzl-Zelman, K. Koller, and K. Klaushofer. *J Bone Miner Res*, (1992); 7, p: 329-334.
76. H.R. Wenk and F. Heidelbach. *Bone*, (1999); 24, p: 361-369.
77. W.J. Landis. *Phosphorus, Sulfur Silicon Relat. Elem.*, (1999); 144-146, p: 185-188.
78. W.J. Landis. *Gravit Space Biol Bull*, (1999); 12, p: 15-26.
79. J.D. Currey. *Science*, (2005); 309, p: 253-254.
80. W.F. Neuman and M.W. Neuman. *Chem. Rev.*, (1953); 53, p: 1-45.
81. W.E. Brown and L.C. Chow. *Annu. Rev. Mater. Sci.*, (1976); 6, p: 213-236.
82. M.J. Glimcher. *Philos. Trans. R. Soc. London, Ser. B*, (1984); 304, p: 479-508, 472 plates.
83. S. Lees. *Connect Tissue Res*, (1987); 16, p: 281-303.
84. A. Miller. *Philos. Trans. R. Soc. London, Ser. B*, (1984); 304, p: 455-477.
85. A.J. Hodge and J.A. Petruska. *Aspects Protein Struct., Proc. Symp., Madras*, (1963); p: 289-300.
86. E.P. Katz and S.-T. Li. *J. Mol. Biol.*, (1973); 80, p: 1-15.
87. R.A. Robinson and M.L. Watson. *Anat Rec*, (1952); 114, p: 383-409.
88. M. Yamauchi, E.P. Katz, K. Otsubo, K. Teraoka, and G.L. Mechanic. *Connect Tissue Res* (1989); 21, p: 159-167; discussion 168-159.
89. R.D.B. Fraser, T.P. MacRae, A. Miller, and E. Suzuki. *J. Mol. Biol.*, (1983); 167, p: 497-521.
90. S. Weiner and W. Traub. *FEBS Lett.*, (1986); 206, p: 262-266.
91. W. Traub, T. Arad, and S. Weiner. *Proc Natl Acad Sci U S A*, (1989); 86, p: 9822-9826.
92. M.J. Glimcher. *Biomaterials*, (1990); 11, p: 7-10.
93. S.E. Mergenhagen, G.R. Martin, A.A. Rizzo, D.N. Wright, and D.B. Scott. *Biochim Biophys Acta*, (1960); 43, p: 563-565.
94. P.D. Delmas, R.P. Tracy, B.L. Riggs, and K.G. Mann. *Calcif. Tissue Int.*, (1984); 36, p: 308-316.

95. A. Veis. *J Bone Miner Res*, (1993); 8 Suppl 2, p: S493-497.
96. A. Veis. *The Chemistry and Biology of Mineralized Connective Tissues,* (1981)*;* p: 5-680; New York, Elsevier.
97. J.D. Currey. *J Biomech*, (1990); 23, p: 837-844.
98. M.J. Glimcher. *Anat. Rec.*, (1989); 224, p: 139-153.
99. M.J. Glimcher. *Rev. Mod. Phys.*, (1959); 31, p: 359-393.
100. W.J. Landis, K.J. Hodgens, M.J. Song, J. Arena, S. Kiyonaga, M. Marko, C. Owen, and B.F. McEwen. *J. Struct. Biol.*, (1996); 117, p: 24-35.
101. S. Mann. *Biomimetic Materials Chemistry,* (1996)*;* p: 1-383; New York, John Wiley & Sons, Inc.
102. M.J. Glimcher. *Instr Course Lect*, (1987); 36, p: 49-69.
103. C. Berthet-Colominas, A. Miller, and S.W. White. *J. Mol. Biol.*, (1979); 134, p: 431-445.
104. B.F. McEwen, M.J. Song, and W.J. Landis. *J Comput Assist Microsc*, (1991); 3, p: 201-210.
105. S. Weiner and W. Traub. *Connect Tissue Res*, (1989); 21, p: 259-265.
106. M.E. Maitland and A.L. Arsenault. *Calcif. Tissue Int.*, (1991); 48, p: 341-352.
107. S.W. White, D.J.S. Hulmes, A. Miller, and P.A. Timmins. *Nature*, (1977); 266, p: 421-425.
108. I.A. Aksay, M. Trau, S. Manne, I. Honma, N. Yao, L. Zhou, P. Fenter, P.M. Eisenberger, and S.M. Gruner. *Science*, (1996); 273, p: 892-898.
109. H.A. Lowenstam. *Science*, (1981); 211, p: 1126-1131.
110. M.A. Meyers, A.Y.M. Lin, Y. Seki, P.-Y. Chen, B.K. Kad, and S. Bodde. *Congr. Anu. ABM*, (2006); 61st, p: 4310-4338.
111. *National Research Council, Hierarchical Structures in Biology as a Guide for New Materials Technology,* (1994)*;* p: 1-130; Washington, D.C., National Academy Press.
112. J.F.V. Vincent. *J. Mater. Res.*, (2008); 23, p: 3140-3147.
113. S. Weiner and L. Addadi. *J. Mater. Chem.*, (1997); 7, p: 689-702.
114. P.Y. Chen, A.Y.M. Lin, A.G. Stokes, Y. Seki, S.G. Bodde, J. McKittrick, and M.A. Meyers. *JOM*, (2008); 60, p: 23-32.
115. G.M. Luz and J.F. Mano. *Philos. Trans. R. Soc.*, (2009); 367, p: 1587-1605.
116. M. Sarikaya and A.I. Aksay. *Biomimetics: Design and Processing of Materials,* (1995)*;* p: 2-285; New York, American Institute of Physics Press.
117. J.L. Arias and M.S. Fernandez. *Mater. Charact.*, (2003); 50, p: 189-195.
118. E. Bauerlein. *Angew. Chem., Int. Ed.*, (2003); 42, p: 614-641.
119. S. Weiner, Y. Talmon, and W. Traub. *Int. J. Biol. Macromol.*, (1983); 5, p: 325-328.
120. C. Tamerler and M. Sarikaya. *MRS Bull.*, (2008); 33, p: 504-512.
121. A.P. Jackson, J.F.V. Vincent, and R.M. Turner. *J. Mater. Sci.*, (1990); 25, p: 3173-3178.
122. J.D. Currey. *Proc.R.Soc.Lond. B 4*, (1977); 196, p: 443-463.
123. F. Barthelat. *Philos. Trans. R. Soc., A: Mathematical, Physical & Engineering Sciences*, (2007); 365, p: 2907-2919.
124. M. Sarikaya, H. Fong, D.W. Frech, and R. Humbert. *Mater. Sci. Forum*, (1999); 293, p: 83-97.
125. Z. Tang, N.A. Kotov, S. Magonov, and B. Ozturk. *Nat. Mater.*, (2003); 2, p: 413-418.

126. G. Mayer. *Science*, (2005); 310, p: 1144-1147.
127. A. Sellinger, P.M. Weiss, N. Anh, Y. Lu, R.A. Assink, W. Gong, and C.J. Brinker. *Nature*, (1998); 394, p: 256-260.
128. G. Mayer and M. Sarikaya. *Exp. Mech.*, (2002); 42, p: 395-403.
129. L. Addadi and S. Weiner. *Nature*, (1997); 389, p: 912-913, 915.
130. M.-M. Giraud-Guille and E.B. Gervaise Mosser. *C.R.Palevol*, (2004); 3, p: 503-513.
131. M. Akao, H. Aoki, and K. Kato. *J. Mater. Sci.*, (1981); 16, p: 809-812.
132. M. Asada, Y. Miura, A. Osaka, K. Oukami, and S. Nakamura. *J. Mater. Sci.*, (1988); 23, p: 3202-3205.
133. A. Slosarczyk, E. Stobierska, Z. Paszkiewicz, and M. Gawlicki. *J. Am. Ceram. Soc.*, (1996); 79, p: 2539-2544.
134. J. Gomez-Morales, J. Torrent-Burgues, T. Boix, J. Fraile, and R. Rodriguez-Clemente. *Cryst. Res. Technol.*, (2001); 36, p: 15-26.
135. A.C. Tas and S.B. Bhaduri. *J. Am. Ceram. Soc.*, (2004); 87, p: 2195-2200.
136. R.M.H. Verbeeck, E.A.P. De Maeyer, and F.C.M. Driessens. *Inorg. Chem.*, (1995); 34, p: 2084-2088.
137. S.J. Joris and C.H. Amberg. *J. Phys. Chem.*, (1971); 75, p: 3172-3178.
138. A. Ruksudjarit, K. Pengpat, G. Rujijanagul, and T. Tunkasiri. *Adv. Mater. Res.*, (2008); 47-50, p: 797-800.
139. P. Luo and T.G. Nieh. *Mater. Sci. Eng., C*, (1995); C3, p: 75-78.
140. G.K. Lim, J. Wang, S.C. Ng, and L.M. Gan. *J. Mater. Chem.*, (1999); 9, p: 1635-1639.
141. A. Lak, M. Mazloumi, M.S. Mohajerani, S. Zanganeh, M.R. Shayegh, A. Kajbafvala, H. Arami, and S.K. Sadrnezhaad. *J. Am. Ceram. Soc.*, (2008); 91, p: 3580-3584.
142. T.A. Kuriakose, S.N. Kalkura, M. Palanichamy, D. Arivuoli, K. Dierks, G. Bocelli, and C. Betzel. *J. Cryst. Growth*, (2004); 263, p: 517-523.
143. M.H. Fathi and A. Hanifi. *Mater. Lett.*, (2007); 61, p: 3978-3983.
144. S.-H. Rhee. *Biomaterials*, (2002); 23, p: 1147-1152.
145. L. Suchanek Wojciech, P. Shuk, K. Byrappa, E. Riman Richard, S. TenHuisen Kevor, and F. Janas Victor. *Biomaterials*, (2002); 23, p: 699-710.
146. C. Hoffmann, C. Zollfrank, and G. Ziegler. *J. Mater. Sci.: Mater. Med.*, (2008); 19, p: 907-915.
147. K. Donadel, M.C.M. Laranjeira, V.L. Goncalves, V.T. Favere, J.C. de Lima, and L.H.M. Prates. *J. Am. Ceram. Soc.*, (2005); 88, p: 2230-2235.
148. D.R. Simpson. *Amer. Mineral.*, (1968); 53, p: 432-444.
149. R. Zapanta-LeGeros, O.R. Trautz, J.P. LeGeros, and E. Klein. *Science*, (1967); 155, p: 1409-1411.
150. M. Toriyama, Y. Kawamoto, T. Suzuki, Y. Yokogawa, K. Nishizawa, F. Nagata, and M.R. Mucalo. *J. Mater. Sci. Lett.*, (1996); 15, p: 179-181.
151. Y. Fujishiro, H. Yabuki, K. Kawamura, and T. Sato. *J. Chem. Technol. Biotechnol.*, (1993); 57, p: 349-353.
152. K. Kandori, N. Horigami, A. Yasukawa, and T. Ishikawa. *J. Am. Ceram. Soc.*, (1997); 80, p: 1157-1164.
153. D.G. Shchukin, G.B. Sukhorukov, and H. Moehwald. *Chem. Mater.*, (2003); 15, p: 3947-3950.

154. A. Lopez-Macipe, J. Gomez-Morales, and R. Rodriguez-Clemente. *Adv. Mater.*, (1998); 10, p: 49-53.
155. R.K. Roeder, G.L. Converse, H. Leng, and W. Yue. *J. Am. Ceram. Soc.*, (2006); 89, p: 2096-2104.
156. M. Yoshimura, H. Suda, K. Okamoto, and K. Ioku. *J. Mater. Sci.*, (1994); 29, p: 3399-3402.
157. N. Asaoka, H. Suda, and M. Yoshimura. *Nippon Kagaku Kaishi*, (1995); p: 25-29.
158. S. Suzuki, M. Ohgaki, M. Ichiyanagi, and M. Ozawa. *J. Mater. Sci. Lett.*, (1998); 17, p: 381-383.
159. D. Janackovic, I. Jankovic, R. Petrovic, L. Kostic-Gvozdenovic, S. Milonjic, and D. Uskokovic. *Key Eng. Mater.*, (2003); 240-242, p: 437-440.
160. I. Bogdanoviciene, A. Beganskiene, K. Tonsuaadu, J. Glaser, H.J. Meyer, and A. Kareiva. *Mater. Res. Bull.*, (2006); 41, p: 1754-1762.
161. A.C. Tas, P.J. Majewski, and F. Aldinger. *J. Am. Ceram. Soc.*, (2002); 85, p: 1414-1420.
162. M. Aizawa, A.E. Porter, S.M. Best, and W. Bonfield. *Biomaterials*, (2005); 26, p: 3427-3433.
163. M. Aizawa, H. Ueno, K. Itatani, and I. Okada. *J. Eur. Ceram. Soc.*, (2006); 26, p: 501-507.
164. H. Zhang, Y. Yan, Y. Wang, and S. Li. *Adv. Eng. Mater.*, (2002); 4, p: 916-919.
165. A. Mortier, J. Lemaitre, L. Rodrique, and P.G. Rouxhet. *J. Solid State Chem.*, (1989); 78, p: 215-219.
166. B. Jokic, D. Tanaskovic, I. Jankovic-Castvan, S. Drmanic, R. Petrovic, and D. Janackovic. *J. Mater. Res.*, (2007); 22, p: 1156-1161.
167. A. Barroug, J. Lemaitre, and P.G. Rouxhet. *J. Alloys Compd.*, (1992); 188, p: 152-156.
168. K. Ishikawa, E.D. Eanes, and M.S. Tung. *J. Dent. Res.*, (1994); 73, p: 1462-1469.
169. A. Slosarczyk, Z. Paszkiewicz, and C. Paluszkiewicz. *J. Mol. Struct.*, (2005); 744-747, p: 657-661.
170. T. Iizuka and A. Nozuma. *J. Ceram. Soc. Jpn.*, (1998); 106, p: 820-823.
171. T. Kokubo. *Thermochim. Acta.*, (1996); 280/281, p: 479-490.
172. T. Kokubo, S. Ito, Z.T. Huang, T. Hayashi, S. Sakka, T. Kitsugi, and T. Yamamuro. *J. Biomed. Mater. Res.*, (1990); 24, p: 331-343.
173. T. Kokubo. *J. Non-Cryst. Solids*, (1990); 120, p: 138-151.
174. A.C. Tas. *Biomaterials*, (2000); 21, p: 1429-1438.
175. J. Liu, X. Ye, H. Wang, M. Zhu, B. Wang, and H. Yan. *Ceram. Int.*, (2003); 29, p: 629-633.
176. R.Z. LeGeros, J.P. LeGeros, O.R. Trautz, and W.P. Shirra. *Advan. X-Ray Anal.*, (1971); 14, p: 57-66.
177. H. Monma and T. Kamiya. *J. Mater. Sci.*, (1987); 22, p: 4247-4250.
178. M.T. Fulmer, R.I. Martin, and P.W. Brown. *J. Mater. Sci.: Mater. Med.*, (1992); 3, p: 299-305.
179. R. Bhowmik, K.S. Katti, and D. Katti. *Polymer*, (2007); 48, p: 664-674.
180. J.D. Hartgerink, E. Beniash, and S.I. Stupp. *Science*, (2001); 294, p: 1684-1688.
181. E.D. Spoerke, S.G. Anthony, and S.I. Stupp. *Adv. Mater.*, (2009); 21, p: 425-430.

182. S.S. Liao, F.Z. Cui, W. Zhang, and Q.L. Feng. *J. Biomed. Mater. Res., Part B*, (2004); 69B, p: 158-165.
183. M. Gungormus, H. Fong, I.W. Kim, J.S. Evans, C. Tamerler, and M. Sarikaya. *Biomacromolecules*, (2008); 9, p: 966-973.
184. J. Song, E. Saiz, and C.R. Bertozzi. *J. Am. Chem. Soc.*, (2003); 125, p: 1236-1243.
185. J. Song, V. Malathong, and C.R. Bertozzi. *J. Am. Chem. Soc.*, (2005); 127, p: 3366-3372.
186. K.K. Perkin, J.L. Turner, K.L. Wooley, and S. Mann. *Nano Lett.*, (2005); 5, p: 1457-1461.
187. P. Li, D. Bakker, and C.A. van Blitterswijk. *J. Biomed. Mater. Res.*, (1997); 34, p: 79-86.
188. M. Kawashita, M. Nakao, M. Minoda, T. Miyamoto, H.M. Kim, T. Kokubo, and T. Nakamura. *Key Eng. Mater.*, (2001); 192-195, p: 697-700.
189. P. Li, C. Ohtsuki, T. Kokubo, K. Nakanishi, N. Soga, and K. de Groot. *J. Biomed. Mater. Res.*, (1994); 28, p: 7-15.
190. R.F. Hamon, A.S. Khan, and A. Chow. *Talanta*, (1982); 29, p: 313-326.
191. T. Iwatsubo, S.P. Kusumocahyo, T. Kanamori, and T. Shinbo. *J. Appl. Polym. Sci.*, (2006); 100, p: 1465-1470.
192. Y.E. Greish, J.L. Sturgeon, A. Singh, N.R. Krogman, A.H. Touny, S. Sethuraman, L.S. Nair, C.T. Laurencin, H.R. Allcock, and P.W. Brown. *J. Mater. Sci.: Mater. Med.*, (2008); 19, p: 3153-3160.
193. A.K. Khripunov, Y.G. Baklagina, V.A. Sinyaev, E.S. Shustikova, B.A. Paramanov, D.P. Romanov, R.Y. Smyslov, and A.A. Tkachenko. *Glass Phys. Chem.*, (2008); 34, p: 192-200.
194. Q. Hu, B. Li, M. Wang, and J. Shen. *Biomaterials*, (2004); 25, p: 779-785.
195. V.M. Rusu, C.-H. Ng, M. Wilke, B. Tiersch, P. Fratzl, and M.G. Peter. *Biomaterials*, (2005); 26, p: 5414-5426.
196. M.C. Gutierrez, M. Jobbagy, M.L. Ferrer, and F. del Monte. *Chem. Mater.*, (2008); 20, p: 11-13.
197. G. He, T. Dahl, A. Veis, and A. George. *Nat. Mater.*, (2003); 2, p: 552-558.
198. T. Taguchi, M. Shiraogawa, A. Kishida, and M. Akashi. *J. Biomater. Sci., Polym. Ed.*, (1999); 10, p: 19-32.
199. K. Furuichi, Y. Oaki, H. Ichimiya, J. Komotori, and H. Imai. *Sci. Technol. Adv. Mater.*, (2006); 7, p: 219-225.
200. Y. Yokogawa, J.P. Reyes, M.R. Mucalo, M. Toriyama, Y. Kawamoto, T. Suzuki, K. Nishizawa, F. Nagata, and T. Kamayama. *J. Mater. Sci.: Mater. Med.*, (1997); 8, p: 407-412.
201. M. Antonietti, M. Breulmann, C.G. Goltner, H. Colfen, K.K.W. Wong, D. Walsh, and S. Mann. *Chem. Eur. J.*, (1998); 4, p: 2493-2500.
202. M. Kikuchi, S. Itoh, S. Ichinose, K. Shinomiya, and J. Tanaka. *Biomaterials*, (2001); 22, p: 1705-1711.
203. W. Zhang, S.S. Liao, and F.Z. Cui. *Chem. Mater.*, (2003); 15, p: 3221-3226.
204. Y. Wang, C. Yang, X. Chen, and N. Zhao. *Adv. Eng. Mater.*, (2006); 8, p: 97-100.
205. E. Sachlos, D. Gotora, and J.T. Czernuszka. *Tissue Eng.*, (2006); 12, p: 2479-2487.

206. M. Kikuchi, T. Ikoma, S. Itoh, H.N. Matsumoto, Y. Koyama, K. Takakuda, K. Shinomiya, and J. Tanaka. *Compos. Sci. Technol.*, (2004); 64, p: 819-825.
207. S. Liao, F. Watari, M. Uo, S. Ohkawa, K. Tamura, W. Wang, and F. Cui. *J. Biomed. Mater. Res., Part B*, (2005); 74B, p: 817-821.
208. L.F. Sukhodub, C. Moseke, L.B. Sukhodub, B. Sulkio-Cleff, V.Y. Maleev, M.A. Semenov, E.G. Bereznyak, and T.V. Bolbukh. *J. Mol. Struct.*, (2004); 704, p: 53-58.
209. J.-H. Bradt, M. Mertig, A. Teresiak, and W. Pompe. *Chem. Mater.*, (1999); 11, p: 2694-2701.
210. G.K. Toworfe, R.J. Composto, I.M. Shapiro, and P. Ducheyne. *Biomaterials*, (2005); 27, p: 631-642.
211. P. Zhu, Y. Masuda, T. Yonezawa, and K. Koumoto. *J. Am. Ceram. Soc.*, (2003); 86, p: 782-790.
212. M. Tanahashi and T. Matsuda. *J. Biomed. Mater. Res.*, (1997); 34, p: 305-315.
213. H. Oonishi and K. Oomamiuda. *Degradation/resorption in bioactive ceramics in orthopedics. Handbook of Biomaterial Properties,* (1998)*;* p: 406-419; London, Chapman&Hall.
214. D.L. Wheeler, A.A. Campbell, G.L. Graff, and G.J. Miller. *J. Biomed. Mater. Res.*, (1997); 34, p: 539-543.

CHAPTER 3. RESEARCH OBJECTIVES

The main purpose of this thesis study was to develop organic-inorganic nanocomposites that mimic the structure of the natural materials, particularly the structure of the bone. We used self-assembling thermo-reversibly gelling anionic and zwitterionic pentablock copolymers as a template for the formation of calcium phosphate phases. Subsequently, the same block copolymers conjugated to hydroxyapatite nucleating peptides were also employed as templates to better control the precipitation of hydroxyapatite nanoparticles. Even though the inorganic fraction in the nanocomposites was increased to about 40 wt%, it was still significantly lower than that seen in nature (65 wt%). One of the reason was the high polymer concentration (~30 wt%) needed for the polymer-inorganic gel formation in these block copolymer systems. To overcome this limitation, we employed diblock copolypeptides that form gels at very low concentrations (~ 4.0 wt%). Consequently, we developed a novel diblock copolypetide-HAp nanocomposite system with a maximum inorganic content of approximately 55 wt%. This approach is similar to nature where protein templates commonly control the nucleation and growth of the inorganic nanoparticles in biological systems such as bone. All these self-assembled nanocomposite systems were characterized extensively by small-angle x-ray and neutron scattering (SAXS/SANS), XRD, NMR, TEM, TGA, and FTIR methods. This was a collaborative project and the work is presented in Chapters 6, 7, and 8 in different manuscripts. In addition, this work would also serve as a guide for the future directions of this project, where the focus will be on the development of polymer-zirconia nanocomposites for the energy related purposes.

Having great similarity to the hard tissues in human body, the study of calcium phosphates has gained considerable attention in recent years especially for the repair of hard and soft skeletal tissues. Mimicking the formation of calcium phosphates similar to that in natural hard tissues contributes significantly to the development of new bone implant materials. It is well known that bone mineral is carbonated hydroxyapatite (CO_3HAp) with approximately 6 wt% carbonate incorporated in the HAp structure. In this regard, we synthesized a bone-like apatite by using a chelate decomposition method. In this study, we investigated the effect of experimental parameters on the carbonate incorporation and how the carbonate substitution alters the lattice parameters. Later, using this chelate decomposition method we deposited CO_3HAp on the poly(methylmethacrylate) (PMMA) surfaces. Several characterization methods such as XRD, FTIR, SEM, EDS, TGA, and elemental analysis were employed to analyze CO_3HAp powders and PMMA-CO_3HAp composite system. These studies were covered in Chapters 4 and 5 in two different manuscripts.

CHAPTER 4. EFFECT OF pH ON THE CARBONATE INCORPORATION INTO THE HYDROXYAPATITE PREPARED BY AN OXIDATIVE DECOMPOSITION OF CALCIUM-EDTA CHELATE

A paper published in *The Journal of American Ceramic Society*

J. Am. Ceram. Soc., 2008, 91(1), 77-82

Yusuf Yusufoglu[a] and Mufit Akinc[b]

4.1 Abstract

In this study, the carbonate incorporation into the hydroxyapatite (HAp) lattice under various pH conditions was investigated. Crystalline-sodium and carbonate-containing calcium HAp ($NaCO_3HAp$) powders were prepared using an oxidative decomposition of calcium-EDTA chelates in a sodium phosphate solution with hydrogen peroxide. The powders obtained were characterized by X-ray diffraction, infrared spectroscopy, thermal gravimetric analysis, scanning electron microscopy, energy-dispersive X-ray spectroscopy, and elemental analysis. Depending on pH, spherical particles approximately 3.5 μm in diameter or hexagonal prismatic particles measuring 3–9 μm in length were obtained. Various characterization techniques showed that the precipitates were a single-phase $NaCO_3HAp$. The carbonate content and the lattice parameters of the HAp were a function of solution pH. Maximum carbonate incorporated into the HAp lattice was at pH=10, corresponding to lattice parameters of a = 0.93880 nm and c = 0.69070 nm. Furthermore, spectroscopic analyses indicate that the as-prepared samples are B-type carbonated HAp, in

which carbonate ions occupy the phosphate sites. After heat treatment at 965 ^{o}C, most of the carbonate is removed from the HAp lattice.

[a,b] Ames Laboratory and Department of Materials Science and Engineering, Iowa State University, Ames, IA 50011.

[a] Primary researcher and author

[b] Author for correspondence

4.2 Introduction

Having excellent biocompatibility and nontoxicity, calcium phosphate bioceramics have found many applications as biomaterials, particularly for hard tissue regeneration [1]. Among the variety of calcium phosphates, hydroxyapatite (HAp) has been studied extensively by medical and material science communities because of its chemical and biological similarity to the mineral phase of bones and teeth [2]. HAp has a hexagonal structure with space group $P6_3/m$ and lattice parameters $a = b = 9.4225$ Å and $c = 6.8850$ [3]. Furthermore, synthetic HAp has a stoichiometric formula of $Ca_{10}(PO_4)_6(OH)_2$ and it is the most stable calcium phosphate compound at $7 < pH < 11$. However, biological apatites do not have a pure or stoichiometric HAp. The atomic arrangement of HAp makes it possible for large deviations from its ideal composition and a fraction of the lattice ions are replaced by other ions, especially CO_3^{2-}, and, to a lesser extent, by Na^+, K^+, Mg^{2+}, Fe^{2+}, Cl^-, and F^- [4]. The carbonate content of apatite in the natural bone is approximately 7.4 wt%. Dentin and enamel also contain nearly 5.6 and 3.5 wt% CO_3^{2-} in HAp lattice, respectively. The carbonate ions can substitute for hydroxyl (called A type) or phosphate (called B type) sites and sometimes both sites may be occupied simultaneously (called AB type). Biological apatites are mainly B-type carbonated HAp (CO_3HAp) [5, 6].

Incorporation of CO_3^{2-} in to the HAp lattice influences the crystal structure, stability, surface charge, solubility and biological reactivity of the apatite. It was found that CO_3HAp ceramics have higher resorption rates than that of pure HAp, resulting in faster bone regeneration. Carbonated minerals are likely to have higher osteoconductivity and faster bioresorption [7, 8]. Furthermore, incorporation of CO_3 groups into the HAp lattice improves the mechanical strength and is used as *in situ*-hardened bone fillers or screw fixations [9-11]. As a result, carbonated HAp seems to be more biocompatible and it is actually desirable over pure HAp for bioresorbable implants.

Suchanek *et al*. [12] prepared CO_3HAp and NaCO_3HAp powders via a heterogeneous reaction between $Ca(OH)_2/CaCO_3/Na_2CO_3$ and an $(NH_4)_2HPO_4$ aqueous solution using the mechanochemical-hydrothermal route. In that study, crystalline CO_3HAp and NaCO_3HAp powders were synthesized at room temperature with carbonate concentration ranging between 0.8 and 12 wt%. Kinoshita *et al.* [13] used a homogenous precipitation method using urea (H_2NCONH_2) to precipitate CO_3HAp from a solution of $Ca(NO_3)_2$ and $(NH_4)_2HPO_4$ at 80°-100°C. Urea decomposition at elevated temperature yields NH_3 and CO_3^{2-} to precipitate CO_3HAp. Toriyama *et al.* [14] also prepared CO_3HAp by an oxidative decomposition of calcium-ethylene diamine tetra acetic acid dihydrate (Ca-EDTA) chelates in a phosphate solution with hydrogen peroxide. De Maeyer *et al.* [15] obtained a NaCO_3HAp precipitate from the hydrolysis of $CaHPO_4$ in Na_2CO_3 solution under homogenous precipitation conditions. The precipitates were well-crystalline B-type carbonated apatites with a carbonate content ranging from 8 to 20 wt%.

In the present study, NaCO_3HAp powders were prepared by a homogenous method similar to the one that reported by Toriyama *et al.*, [14] who reported that CO_3HAp can be synthesized by an oxidative decomposition method of a calcium-EDTA chelate. However, little evidence was given for the CO_3 occupancy in the HAp lattice, the role of solution pH in the level of CO_3 substitution, and how the CO_3 incorporation alters the lattice parameters. The purpose of this study is to elucidate the role pH plays on the incorporation of CO_3 into the HAp lattice and its effect on lattice parameters.

4.3 Experimental Procedure

All the chemicals used in this study were obtained from Fisher Scientific (Fair Lawn, NJ) and were of laboratory grade and purity. Sodium-containing CO_3HAp powders at seven different pH values (6.2, 7.1, 8.2, 9.0, 10.0, 10.5 and 11.0) were synthesized by a homogenous method similar to one used by Toriyama *et al.* [14]. In this method, a Ca-EDTA chelate was decomposed by H_2O_2 in a solution containing phosphate ions.

A Ca-EDTA solution was prepared by mixing 10.0 mL aqueous solution of 1.0M $Ca(NO_3)_2$ with 96.00 mL solution of 0.125M di sodium salt of ethylene diamine tetra acetic acid dihydrate (Na_2EDTA) and 24.0 mL solution of 0.25M Na_3PO_4 was added. Then, 25.0 mL of 30% H_2O_2 (to obtain a molar ratio of H_2O_2 / EDTA = 21) was added. Once all the reactants were added, the solution pH was adjusted with sodium hydroxide (NaOH) addition. The clear solution was placed in a water bath at 70 ^{o}C for 24 h. The precipitates formed were filtered on a Buchner funnel and washed with distilled water. Finally, the resulting powder was heated at 50 ^{o}C for approximately 10 min to evaporate the excess water.

The X-ray diffraction (XRD) patterns of the powders were obtained with Cu$K\alpha$ radiation (XDS-2000, Scintag Inc., Cupertino, CA) operating at 45kV and 40mA, and the scanning rate was 0.75^{o}/min with a sampling interval of 0.03^{o} over a range of $10 \leq 2\theta \leq 60^{o}$. Phase analysis was performed using the ICDD database and the Scintag DMSNT search

/match software. The lattice parameters were determined by using the general structure analysis system (GSAS), a Rietveld profile-analysis [16].

The CO_3^{2-} content in the as-prepared samples is estimated from the lattice parameters using the method described by LeGeros [17]. Because the *a* axis is more sensitive to structural changes [18], the CO_3^{2-} content will be estimated by using the *a* lattice parameters. LeGeros [17] offered the following empirical expression relating the *a* lattice parameter to the carbonate content:

$$a\ (\text{nm}) = (0.9442 \pm 0.0014) - (6.3 \pm 1.0) \times 10^{-4}\ [\text{wt\%}CO_3^{2-}] \qquad (1)$$

FTIR scans were obtained using a Bruker spectrometer (Bruker IFS-66v, Bruker Optics Inc., Billerica, MA) using a 1.0 wt% sample in KBr pellets in the range of 400-4000 cm^{-1} with a 4 cm^{-1} resolution averaging 32 scans. The carbonate content was estimated from the infrared spectra by comparing the extinction coefficient (*E*) of the 1415 cm^{-1} (CO_3^{2-}) to that of 575 cm^{-1} (PO_4^{3-}) peak. The empirical relation offered by Featherstone *et al.* [19] allows estimation of CO_3^{2-} content to better than ± 10%:

$$\text{wt\% } CO_3^{2-} = 16.1\ (E_{1415} / E_{575}) - 0.2 \qquad (2)$$

Thermogravimetric analyses were carried out by TA 2950 with high-resolution option (Hi-Res™ thermogravimetric analyses (TGA) 2950, TA Instruments Inc., New Castle, DE). Hi-Res™ TGA is based on adjusting the heating rate during weight loss in order to improve separation between closely occurring decomposition events and therefore, the approach with Hi-Res™ TGA allows very high heating rates to be used in regions where no weight changes are occurring while avoiding transition temperature overshoot. A resolution setting of one will produce a TGA scan at 50°C/min that roughly approximates the resolution obtained by a constant heating rate scan at 20°C/min. In this study, approximately 20 mg samples were heated from room temperature to 965°C in a 100 mL/min flowing air with an initial heating rate of 40°C/min and a resolution setting of five. On a conventional TGA constant heating experiment, this heating rate corresponds to lower than 20°C/min.

Scanning electron microscopy (Hitachi S-2460N, Hitachi, Tokyo, Japan) in conjunction with energy-dispersive X-ray spectroscopy (EDS) was used to determine the morphology and chemistry of the powders. Loose powders were affixed to carbon stubs with a double-stick carbon tape and coated with approximately 15 nm of gold (Au). For the EDS analysis, as-prepared powders were embedded in epoxy and then polished to reveal cross sections and to provide a known sample geometry. The polished samples were coated with approximately 15 nm of carbon. EDS was performed using Oxford Instruments (Oxon, U.K.) "ISIS" X-ray system equipped with a Si(Li) light-element detector using an accelerating voltage of 12 kV. Images were collected using backscattered electron imaging mode. Multiple spectra were collected for each sample, and the amount of Na was estimated from the EDS spectra using Oxford's SEMQuant application.

The carbonate content was quantitatively determined as carbon using a CHN/S elemental analyzer (PE 2400 Series II, Perkin-Elmer, Ann Arbor, MI) and four runs were performed for each sample. The relative uncertainty in CO_3^{2-} calculated from carbon amount was approximately 5%. Additionally, the quantitative analysis of calcium and phosphorous was performed with inductively coupled plasma mass spectrometry (ThermoFinnigan ELEMENT I ICP-MS, Thermo Fisher Scientific Inc., Bremen, Germany). For this purpose, approximately 0.002 g sample was dissolved in 5 mL of HNO_3 and then 0.1 mL of this solution was diluted up to 500 mL. Three runs were performed for each sample.

4.4 Results and Discussion

(1) XRD

Figure 4.1 shows the XRD pattern of the as-prepared powders and pure HAp (Standard Reference Material® 2910). All observed peaks can be assigned to HAp with reference to ICCD (# 9-432 and Standard Reference Material® 2910) and Si standard. This is consistent with the phases predicted by the calcium phosphate pH - concentration equilibrium diagram, as well as with those that Toriyama *et al.* [14], and Kandori and colleaugues [3, 20] observed, who report that the most stable calcium phosphate phase is HAp at pH >6. Although all of the observed peaks can be assigned to pure HAp, most of the peaks are shifted, reflecting a change in unit cell dimensions due to CO_3^{2-} and Na^+ substitutions.

Broadening of the most intense peaks around $2\theta \approx 32^o$, especially at pH = 10 and 10.5, is due to carbonate substitution, which increases the lattice disorder. Broadening of the peaks was more pronounced at pH = 10, in agreement with maximum incorporation of carbonate into the HAp lattice, which occurs around pH = 10.

Because the as-precipitated powders contain large but undetermined amounts of bulk and lattice water (as indicated by FTIR and TGA data), it introduces significant uncertainty into the lattice constant determinations. As adsorbed water is eliminated by 120°C and the lattice water by 400°C, the powders were heated to 400°C to eliminate the lattice water [3]. The relationship between lattice parameters and pH is illustrated in Figure 4.2. While the lattice parameter of the *a*-axis decreases, that of the *c* axis increases up to pH = 10. Above pH = 10, the trend is reversed.

A number of studies reported that the *a* axis decreases as the carbonate content increases for the B-type carbonated HAp [15, 17, 21]. The amount of carbonate incorporated into the HAp lattice was estimated by using the expression given by LeGeros [17] and the results are given in Figure 4.3 (indicated by the solid curve), which shows the variation of carbonate content (in wt%) with pH as determined by several independent methods. Although the values show some variation in absolute carbonate content, they follow the same trend. It appears that as the pH increases, the carbonate content reaches a maximum around pH ~ 10.

The XRD patterns of selected samples heat treated at 965°C are shown in Figure 4.4. Two significant observations can be made in comparison with XRD patterns of as-prepared powders. First, the HAp peaks sharpen due to decomposition of CO_3^{2-} and there is improved crystallinity with the high temperature heat treatment. Second, β-$Ca_3(PO_4)_2$ (β-TCP) appears for the powders prepared in near-neutral solutions ($6 \leq$ pH ≤ 9). Carbonated apatite powders with a sub-stoichiometric atomic Ca/P ratio (Ca-def HAp) of 1.4 to 1.6, as is the case for these samples (see Table 4.1), have been known to form β-TCP when heated to 950ºC [3, 12, 14, 22, 23].

$$\text{Ca-def HAp} \rightarrow x\, Ca_{10}(PO_4)_6(OH)_2 + y\, \beta\text{-}Ca_3(PO_4)_2 + CO_2 + H_2O \qquad (3)$$

β-TCP formation is not observed for powders prepared at pH ≥ 10, because they have Ca/P > 1.6. Furthermore, CaO peaks are observed for the powder prepared at pH = 10 (with high Ca/P), which is in agreement with the literature [3, 12, 22].

(2) Infrared Spectroscopy

Figure 4.5 shows the FTIR spectra of the as-prepared powders and the standard HAp sample (Standard Reference Material® 2910). The absorption peaks observed for the precipitates show that these are typical spectra for the carbonated HAp [12, 15, 18, 24-27], confirming that the precipitates obtained are CO_3-containing HAp. Theoretically, four vibrational modes are expected for the phosphate ions in the HAp spectra. Pure HAp shows phosphate peaks at 965 cm^{-1} (a single intense band), 470 cm^{-1}, between 1050-1095 cm^{-1} and 565-602-635 cm^{-1} (three sites) for ν_1, ν_2, ν_3, and ν_4, respectively. For our as-prepared powders, these peaks appear at 964 cm^{-1}, 467 cm^{-1}, 1046 cm^{-1} (a single intense band) and 562-606 cm^{-1} (two sites). The peaks at 562-606 cm^{-1} range (see Figure 4.5) assigned for ν_4 phosphate bands are well separated and is an indicator of high degree of crystallinity [12, 15, 28]. Broad absorption bands observed around 3450 and 1630 cm^{-1} are due to incorporated water molecules [12, 15, 24, 29]. The intensity of peak at 1630 cm^{-1} decreases as pH increases, suggesting that as pH increases, the amount of water incorporated decreases. TGA results support this conclusion because the weight loss between 25° and 400 °C, which is related to the loss of adsorbed and lattice water, decreases as pH increases. The sharp peak at 3570 cm^{-1} is assigned to hydroxyl stretching and is clearly visible only in pure HAp spectra. In the spectra of the as-prepared powders, this peak is masked by broad H_2O absorptions (see Figure 4.5).

The absorption bands observed at 871 and 1418-1470 cm^{-1} are due to carbonate group and the positions of these peaks determine the substitution environment of the CO_3^{2-}. Three vibrational modes were reported for carbonate ions, ν_1, ν_2, and ν_{3a} and ν_{3b}. The ν_1 band is not observed in the FTIR spectrum as it overlaps with the strong ν_3 PO_4^{3-} band but it can be seen at 1108 cm^{-1} in the Raman spectrum [3]. There are two substitution sites for CO_3^{2-} in the apatite lattice: type A substitution (CO_3^{2-} substitutes for OH^-), in which ν_2, ν_{3a}, and ν_{3b} bands show up at 880, 1458 and 1546 cm^{-1}, respectively. For B-type substitution (CO_3^{2-} substitutes for PO_4^{3-}), ν_2, ν_{3a}, and ν_{3b} shifted downward and were observed at 871, 1420, and 1475 cm^{-1}, respectively [3, 15, 22, 24, 25, 30].

For the powders prepared in this study, the carbonate ν_2, $\nu_{3a,}$ and ν_{3b} bands appear at 871, 1418, 1470 cm^{-1}, respectively, confirming that the as-prepared powders are mainly B-type carbonated HAp. It is also worth noting that the relative intensities of the CO_3^{2-} bands (871 cm^{-1} and 1418-1470 cm^{-1}) increase with pH, with a maximum intensity observed at pH 10 (see Figure 4.5). As it was explained earlier, the carbonate content at different pH was also estimated from infrared (IR) analysis by using Eq. (2) and illustrated in Figure 4.3. The results are in good agreement with the one obtained from XRD (lattice parameter experiments).

Heat treatment of powders at 400°C practically eliminates the broad water absorption bands around 3450 and 1630 cm^{-1} (see Figures 4.5 and 4.6), suggesting that most of the water is removed. Further, small OH^- peaks at 3570 cm^{-1} and 630 cm^{-1} emerge after water is removed. The additional band at 2350 cm^{-1} that appears for samples prepared at moderate pH is due to ν_3 of molecular CO_2, and the appearance of this band could not be associated with any particular characteristic of the minerals [3].

Figure 4.7 illustrates the spectra of the powders after heat treatment at 965°C in air. For the most part, the carbonate bands at 871 cm^{-1} and 1418-1470 cm^{-1} are diminished. However, for the powders prepared at high pH, small carbonate peaks at 1418-1470 cm^{-1} are still present, implying that a small amount of carbonate still remain even after heat treatment at 965°C.

The bands around 750 and 2020 cm^{-1}, as seen in some of the as-prepared samples, could be attributed to the ν_2 and ν_3 modes of the $[N\text{-}C\text{-}N]^{2-}$ ions, respectively [3, 31]. Elliott [3] reported that the synthetic CO_3HAp prepared from ammonium salts contained small amounts of nitrogen (typically 0.1 wt %), leading to the formation of the $[N\text{-}C\text{-}N]^{2-}$ by a reaction between retained NH_4^+ and CO_3^{2-} after heating to 900°C [3, 32, 33]. Similarly, our samples may contain small amounts of nitrogen due to the decomposition of EDTA and this may cause the formation of the $[N\text{-}C\text{-}N]^{2-}$ upon heating to 965°C. Furthermore, for the powders prepared at pH>9, which have high Ca/P ratio, additional peaks are observed at around 3650 cm^{-1}. These peaks might arise from different states of OH groups or from the formation of $CaCN_2$ [31]. It has been reported that the CO_3HAp samples with an atomic Ca/P ratio higher than 1.67 will form CaO in air at temperatures 950°C or higher [22]. Then, CaO may further react with NH_3 and C (which may come from the decomposition of EDTA) to form $CaCN_2$ [31].

(3) Elemental Analysis of the As-Prepared Powders

The elemental analysis of the as-prepared powders is given in Table 4.1. The results imply that the precipitates are sodium-containing carbonated HAp ($NaCO_3HAp$). Data illustrate that the PO_4^{3-} content decreases as CO_3^{2-} increases, indicating that carbonate ions might be substituting for PO_4^{3-} to form B-type carbonated HAp (see Figure 4.8).

The variation of carbonate content was determined by several independent methods as illustrated in Figure 4.3, and they are in agreement with the chemical analysis results that the maximum amount of carbonate incorporation occurs at pH 10. The data clearly shows that carbonate content increases as pH increases, reaching a maximum at pH 10 and decreases at pH>10. Moreover, the highest Ca/P ratio is also obtained at pH 10.

(3) SEM of the As-Prepared Powders

The morphology of the as-prepared samples is shown in Figure 4.9. At low pH values (i.e., at pH 6.2 and 8.2), plate-like primary particles agglomerate into the spherulites (Figures

4.9(a) and (b)). This type of morphology is common in apatite with atomic Ca/P ratios lower than 1.67 as is the case in our study [14].

At higher pH (i.e., 10 and 10.5) the morphology changed into needle-like hexagonal, prismatic particles just like Busch *et al.* [34] observed. According to Toriyama *et al.*, [14] this morphology results from slow precipitation of HAp. Slow dissociation of the Ca-EDTA complex results in slow release of Ca^{2+}, which in turn results in slow precipitation of HAp.

(5) Thermogravimetric Analysis

Figure 4.10 shows TGA of the as-prepared samples along with pure HAp for comparison. All of the samples show a significant weight loss from 25° to 400°C and this could be related to the loss of adsorbed and lattice water [3, 12, 18]. This is in agreement with the IR results (Figures 4.5 and 4.6). Weight loss observed between 600° and 965°C is due to the decomposition of carbonate, with evolution of CO_2 gas. For CO_3HAp, CO_2 loss in air usually starts around 600°C and is completed at 900°-1000°C depending on the heating rate and composition [3, 18, 23, 35].

The carbonate contents of the precipitated powders were estimated by assuming that the weight loss between 600° and 965°C is primarily due to evolution of CO_2 as a result of CO_3^{2-} decomposition and given in Figure 4.3. The precipitate obtained at pH = 10 contains the highest carbonate content and is consistent with the XRD, IR, and elemental analysis results. A slightly higher carbonate content estimated from TGA may be due to residual lattice water or other impurities that may be evolving in this temperature regime.

Elliott [3] reported a widely accepted chemical formula for NaCO_3HAp as $Ca_{10-x}Na_{2x/3}(PO_4)_{6-x}(CO_3)_x(H_2O)_x(OH)_{2-x/3}$, where $0 \le x \le 3$, corresponding to the theoretical solubility limit of carbonate in HAp of 22.27 wt%. According to the author, for every CO_3^{2-}

substituting for PO_4^{3-}, the charge balance is maintained by substituting a Na^+ for Ca^{2+} and removing one-third NaOH to create vacancies. In our study, even though it was not intended to investigate the mechanism of the substitution, it can be said that the charge balance for PO_4^{3-} substitution with CO_3^{2-} is maintained partially by substituting a Na^+ for Ca^{2+} as reported by Elliott [3]. The CO_3 contents estimated from four different characterization methods are given in Figure 4.3 and all are within the theoretical solubility limit of carbonate in HAp lattice.

(6) Mechanism of Carbonate Insertion

The formation of the $NaCO_3HAp$ is due to the generation of CO_2 through the decomposition of EDTA. Hydrogen peroxide (H_2O_2) plays a crucial role on the decomposition of EDTA. (H_2O_2) is an acid ($pK_a = 11.6$) and dissociates into H_2O_2 anion (HO_2^-), which is a strong nucleophil

$$H_2O_2 \leftrightarrow HO_2^- + H^+ \tag{4}$$

Gilbert and Glewe suggested that the decomposition pathway for EDTA starts with a HO_2^- attack to C-N bonds of EDTA and the C-N bonds of intermediate compounds are further attacked by HO_2^- to form carbonate and nitrate ions [36, 37]. The amount of carbonate formed depends on the extent of EDTA decomposition. The more the EDTA decomposed, the more the carbonate likely to be inserted into the HAp lattice.

Under acidic conditions, decomposition of EDTA with H_2O_2 is slow because it is very stable at low pH. Looking at Eq. (3) at low pH values, $[HO_2^-]$ is lower, resulting in relatively lower EDTA decomposition. On the other extreme, HO_2^- might be scavenged by OH^- at pH >10. Because HO_2^- react with OH^- ions in alkaline solutions [37, 38], this may provide a plausible explanation reduction in carbonate content of the powders synthesized at pH>10. Moreover, hydroxyl ions may compete with carbonate at a high pH and this may provide another explanation for that reduction in carbonate content above pH 10. In addition, a H_2O_2 anion might also be scavenged when excessive H_2O_2 is used [39].

4.5 Conclusions

In this study, the effect of solution pH on the incorporation of carbonate into the apatite lattice during homogeneous precipitation of HAp by the decomposition of Ca-EDTA with H_2O_2 was investigated. The carbonate content was estimated from elemental analysis, XRD, IR and TGA. The results from each technique show good agreement, at least semi-quantitatively. The amount of carbonate in the apatite lattice increases as pH increases from 6.2 to a maximum at pH = 10 before decreasing as the pH is further increased. The increase in the carbonate content of the HAp was attributed to more extensive decomposition of EDTA and hence increased carbonate formation as pH increases. The decrease in the carbonate content above pH = 10 is believed to be due to consumption of reactive HO_2^- by OH^- ions. The maximum amount of carbonate appears to form at pH $\approx$ 10, resulting in maximum carbonate insertion into the apatite lattice. Incorporation of carbonate correlates with lattice parameter change, namely lattice constant *a* decreases, while *c* increases with carbonate content of the apatite. Furthermore, both elemental analysis and IR results show that the as-prepared powders are B-type carbonated HAp, carbonate substituting predominantly to phosphate sites.

4.6 Acknowledgments

Ames Laboratory is operated for the U.S. Department of Energy by Iowa State University under contract No. DE-AC02-07CH11358. This research was supported by the

Department of Energy. We wish to thank Warren Straszheim for assisting with the SEM experiments and helpful discussions, and Josh Messerly for the ICP analysis.

Table 4.1. Elemental analysis results and atomic Ca/P ratios of the as-prepared powders.

	Weight % (1)					
pH	Ca (2)	PO_4 (2)	Na (3)	CO_3 (4)	Atomic (Ca+Na)/P	Atomic Ca/P
6.2	32.2	52.2	1.2	2.87	1.55	1.46
7.1	31.9	51.1	1.4	3.21	1.59	1.48
8.2	31.3	50.4	1.4	3.66	1.58	1.47
9.0	31.3	49.7	1.2	3.94	1.59	1.49
10.0	34.1	45.9	1.4	6.95	1.89	1.76
10.5	33.8	47.6	1.3	4.58	1.79	1.68
11.0	35.4	50.5	1.3	3.60	1.77	1.66

(1) Presumably majority of the balance is hydroxyl and lattice water.
(2) Obtained from ICP analysis.
(3) Obtained from EDS analysis.
(4) Calculated from Carbon determined using a CHN/S elemental analyzer.

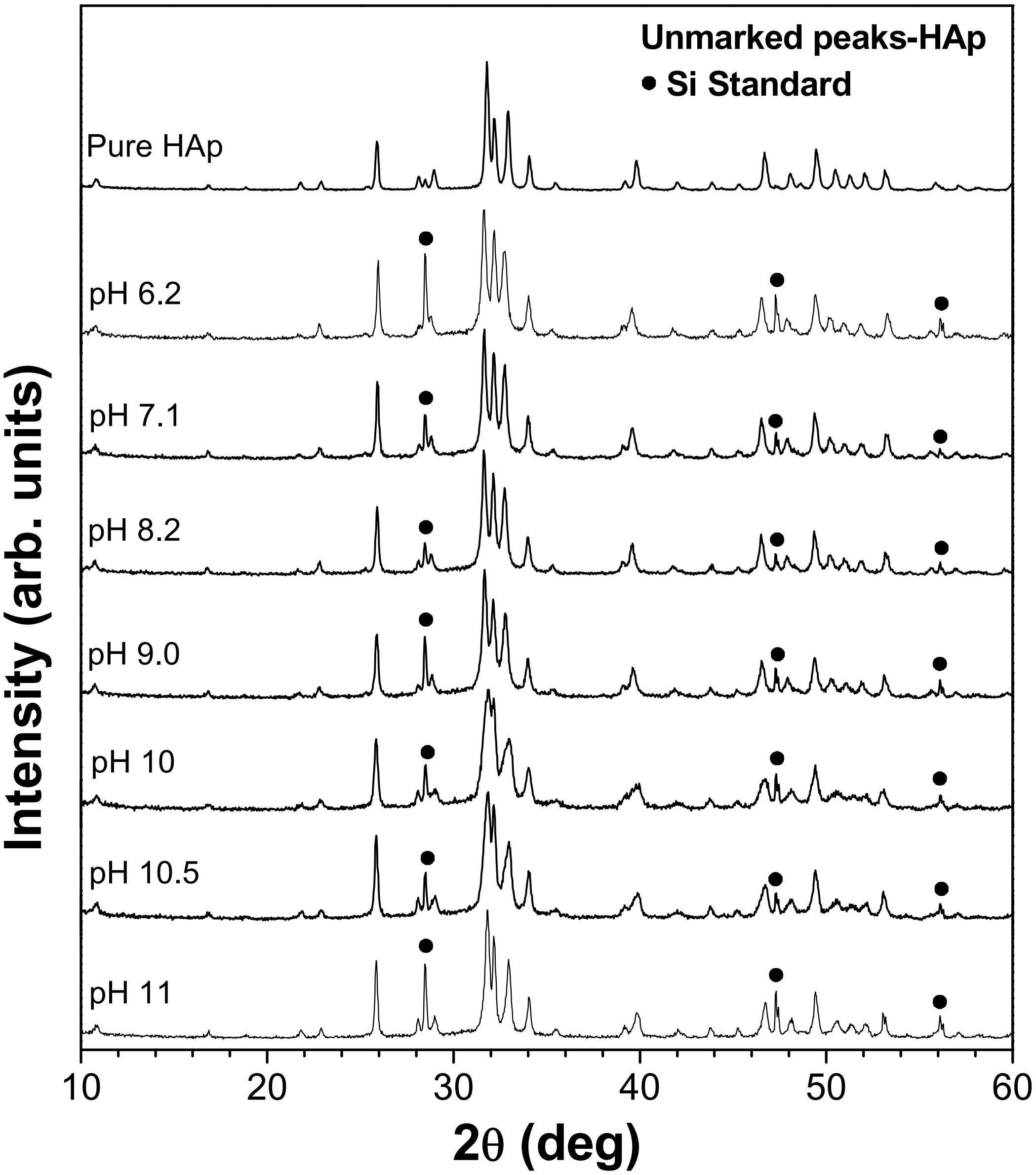

Figure 4.1. X-ray diffraction patterns of the as-prepared powders and pure HAp. The Si peak intensity varies as its fraction varies for each sample.

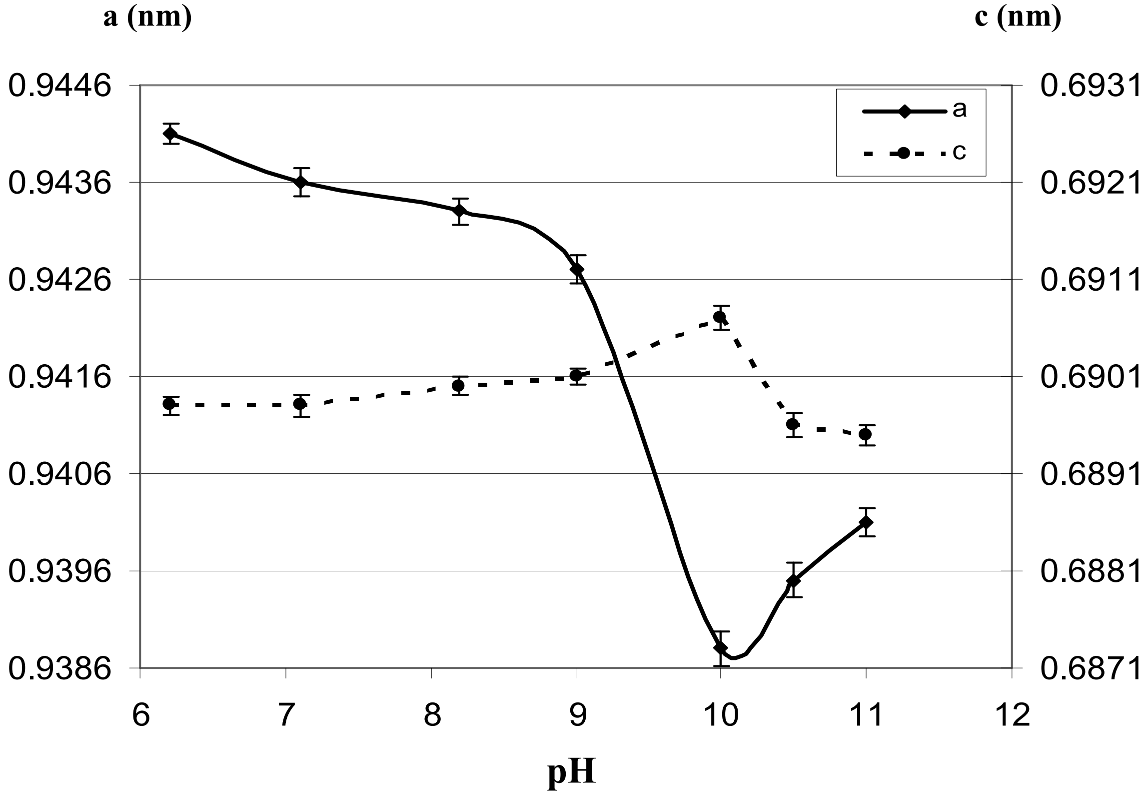

Figure 4.2. Variation of lattice parameters with pH. The lattice parameter *a* decreases up to pH = 10 and then increases, while the lattice parameter *c* shows opposite trend, i.e., shows a maximum at about pH = 10.

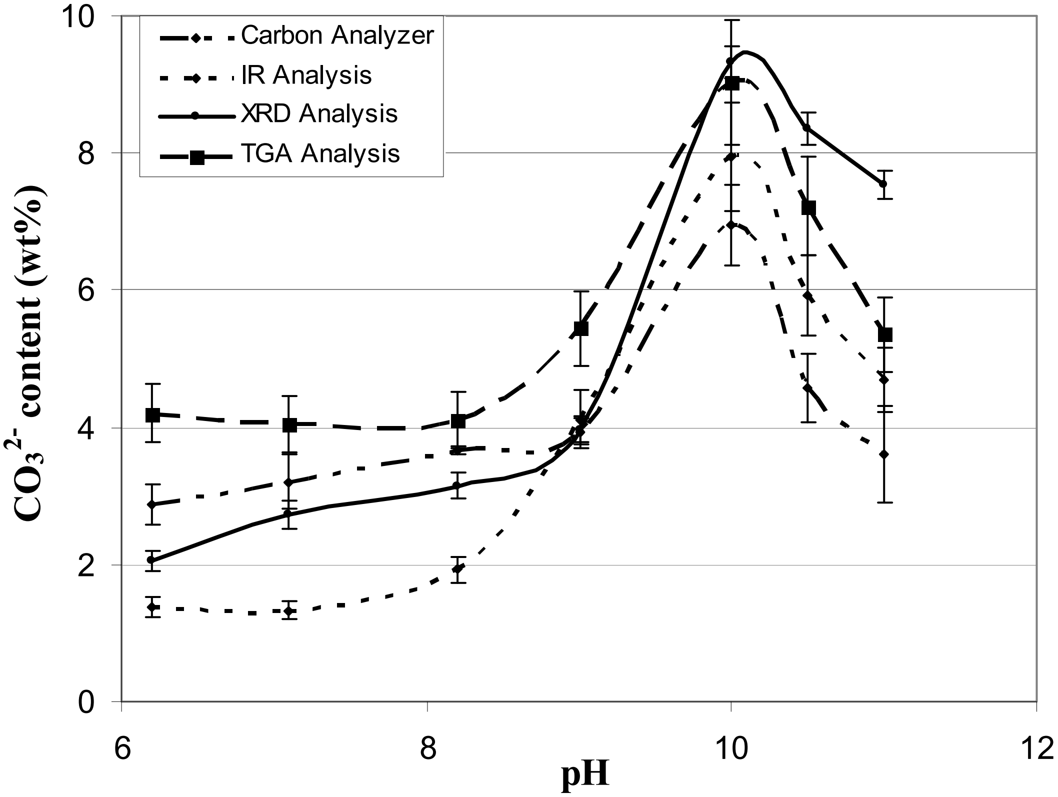

Figure 4.3. Relationship between CO_3^{2-} content and solution pH as determined by carbon analyzer, X-ray diffraction (XRD) (lattice parameter experiments), infrared (IR), and thermal gravimetric analysis (TGA).

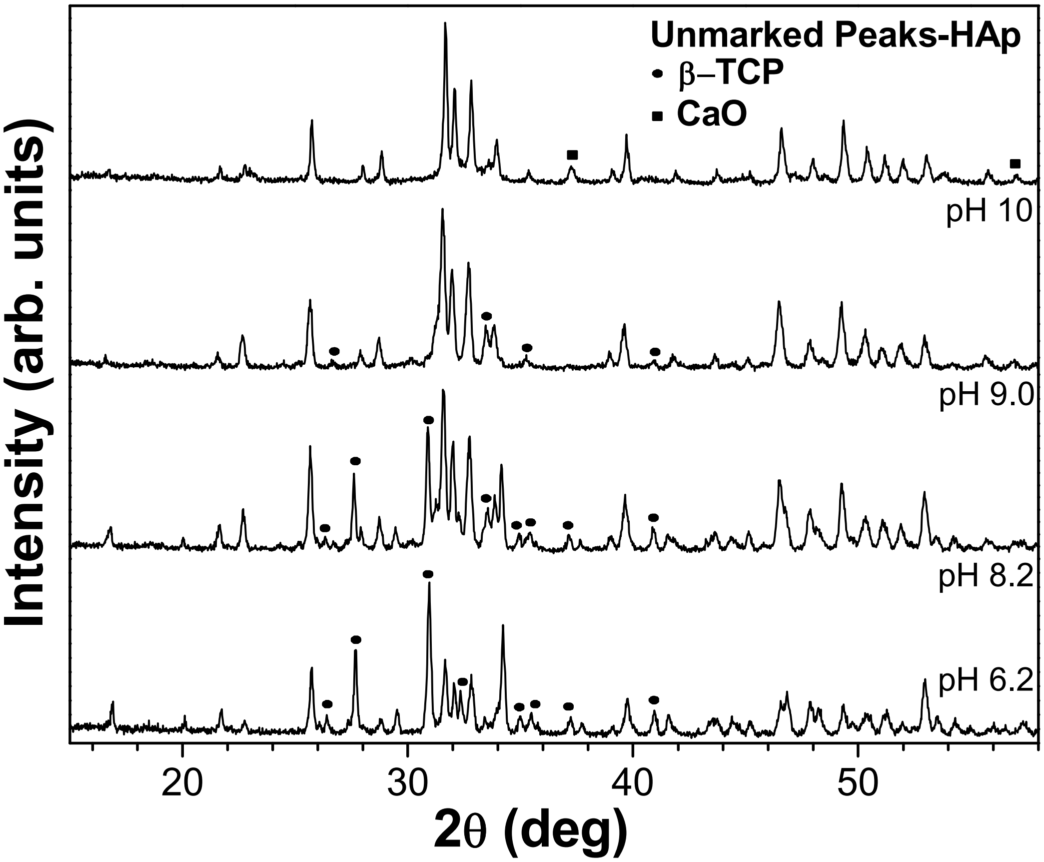

Figure 4.4. X-ray diffraction patterns of the powders heated at 965°C.

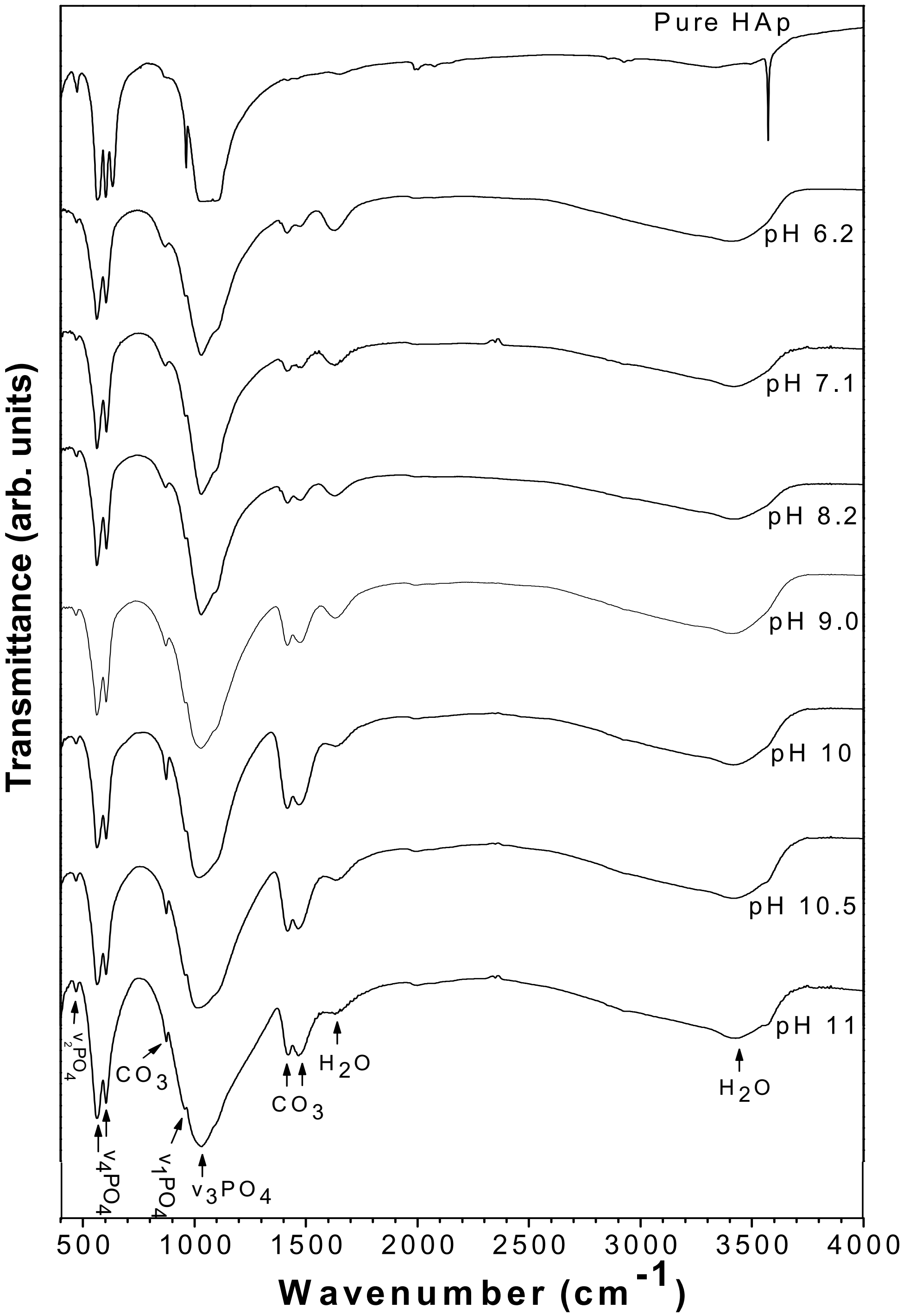

Figure 4.5. FTIR spectra of the as-prepared powders and pure hydroxyapatite (HAp) (Standard Reference Material® 2910).

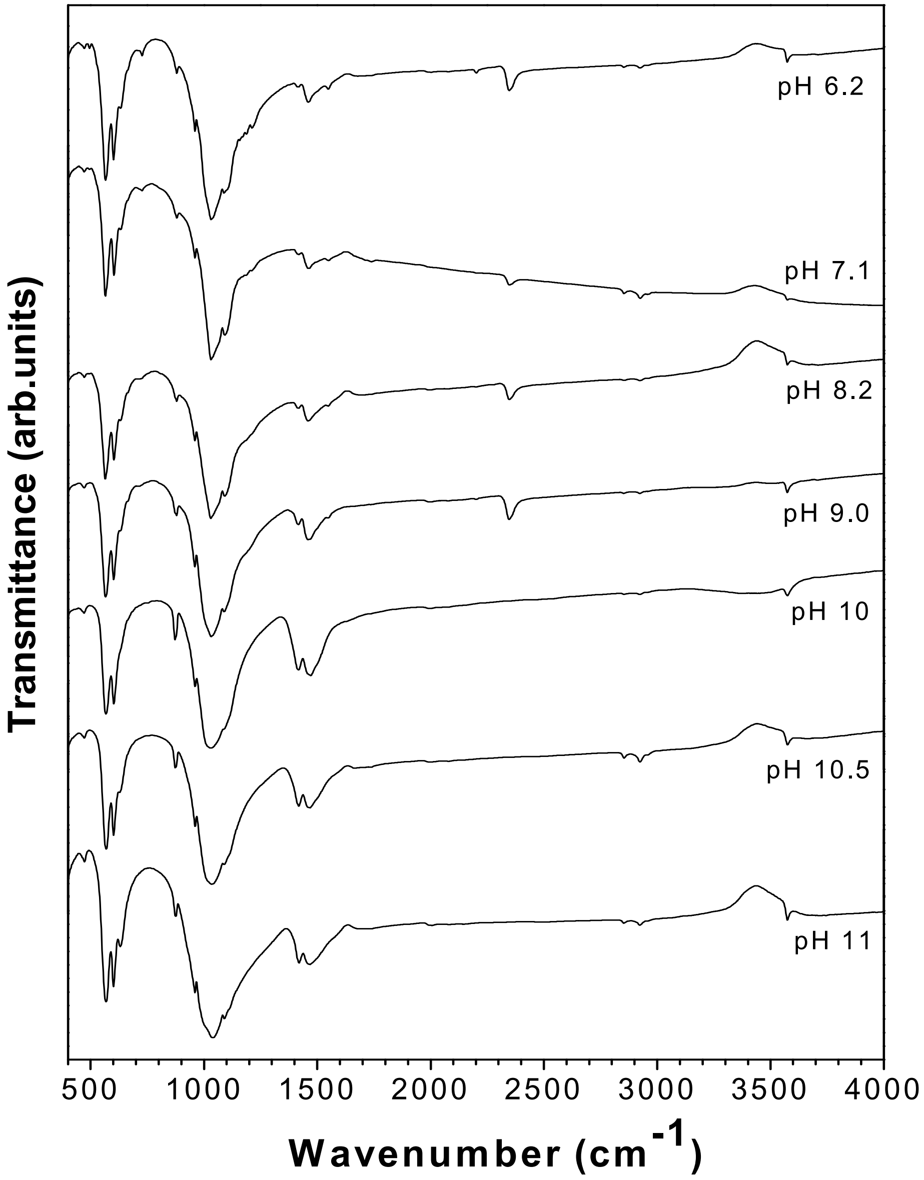

Figure 4.6. FTIR spectra of the as-prepared powders heated to 400°C. *Note,* the broad peaks associated with molecular water around 3450 and 1630 cm^{-1} disappear, and a sharp peak due to hydroxide at 3570 cm^{-1} appears.

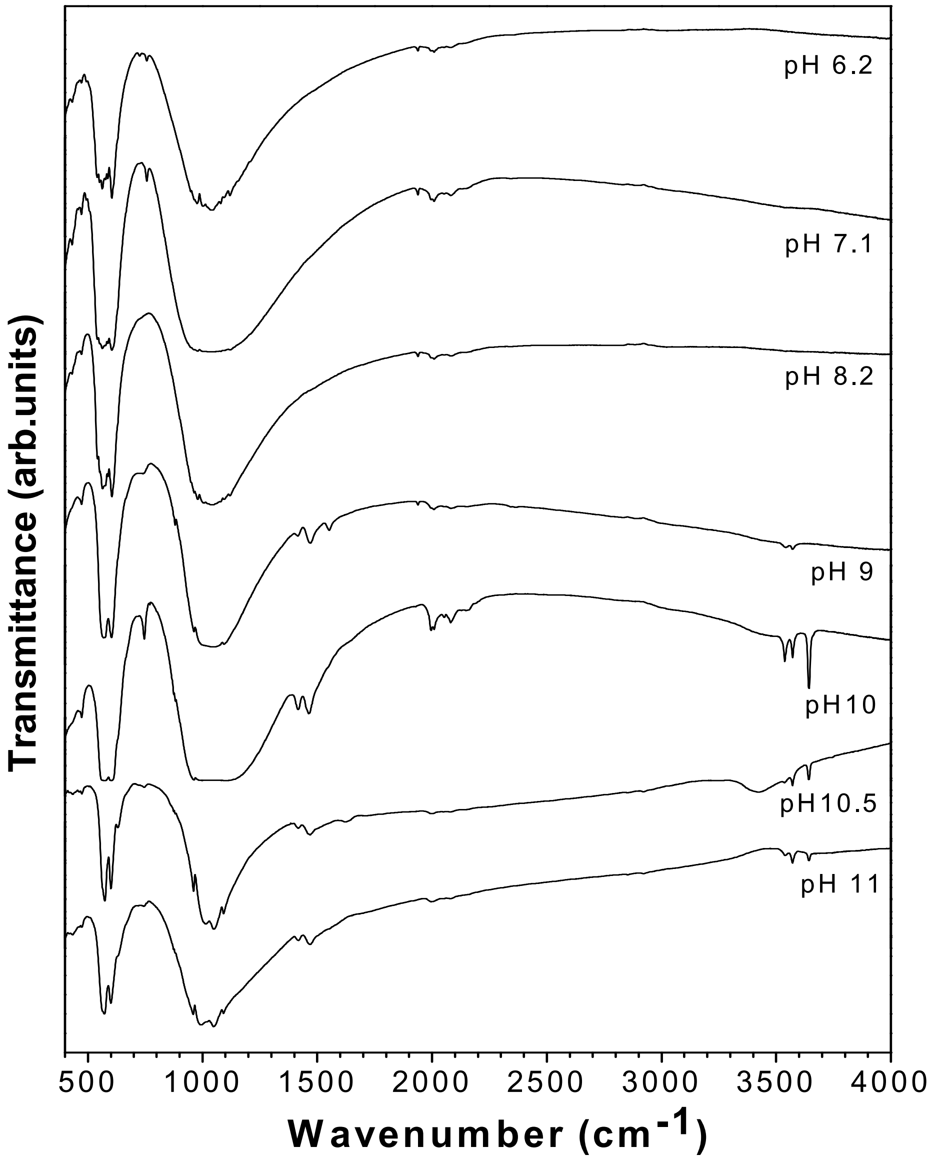

Figure 4.7. FTIR spectra of the as-prepared powders heated at 965°C.

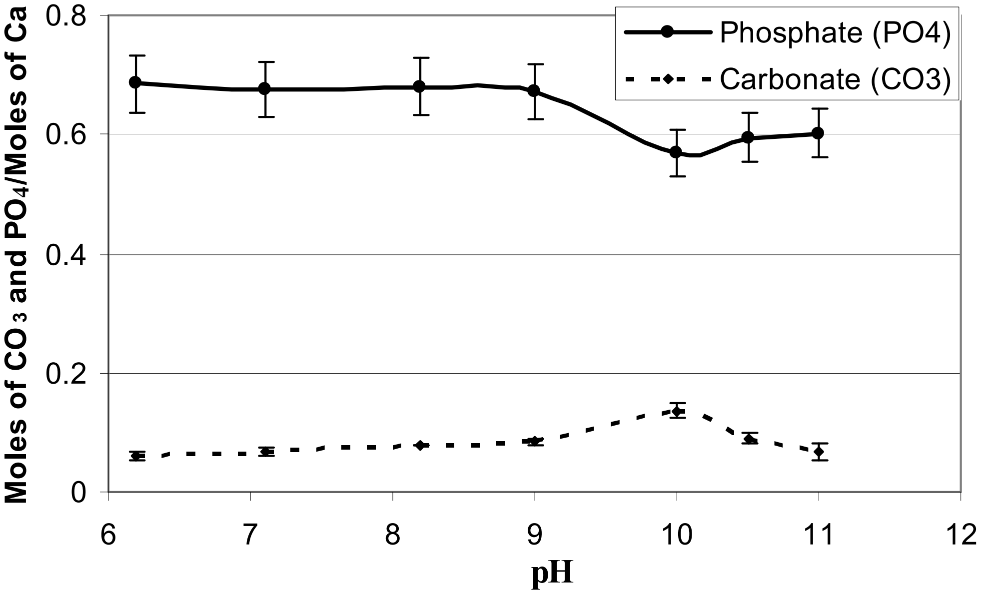

Figure 4.8. Variation of phosphate and carbonate content as a function of pH.

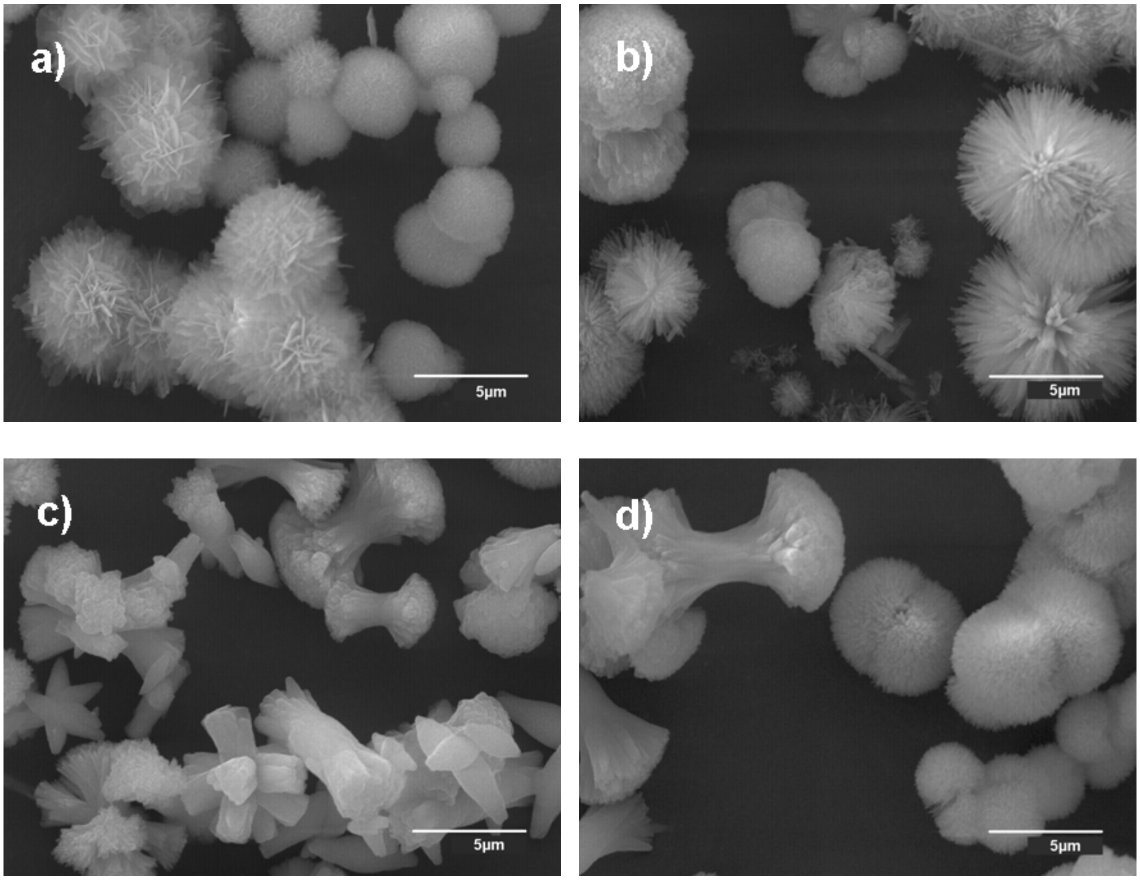

Figure 4.9. Scanning electron microscopy images of the as-prepared powders. *Note* that the plate-like and needle-like primary crystallites radiate from a nucleus to form spherulitic particles, while prismatic crystallites at higher pH grow and branch out at both ends to form a "double-cauliflower" shape, and eventually into double-spherulite-shaped particles (Figure 4.9 indicates various pH values, (a) pH = 6.2, (b) pH = 8.2, (c) pH = 10.0, (d) pH = 10.5).

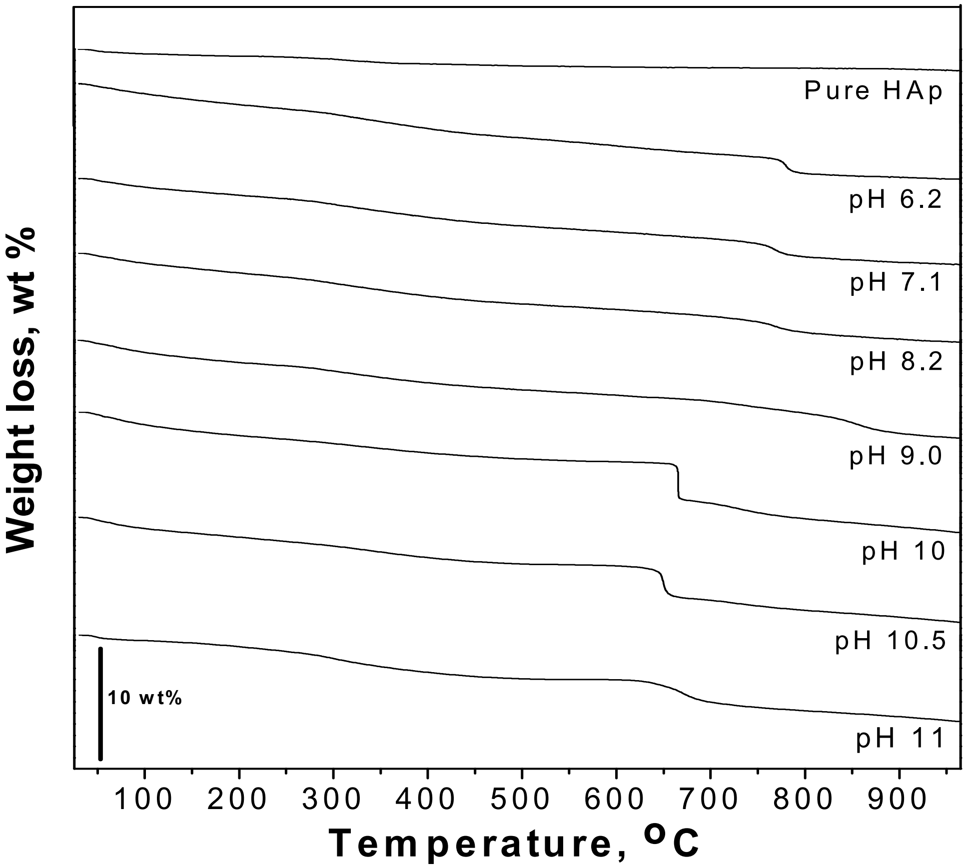

Figure 4.10. Thermal gravimetric analysis plots of $NaCO_3HAp$ and pure HAp powders heated in air. Weight loss for pure HAp is much less than carbonated powders as expected. Sharp weight loss for pH = 10 and 10.5 at about 650°C coincides with the highest carbonate content observed for these samples and might be associated with CO_2 evolution.

4.7 References

1. S.V. Dorozhkin and M. Epple. *Angewandte Chemie, International Edition*, (2002); 41, p: 3130-3146.
2. H. Aoki. *Japan Association of Apatite Science*, (1991); p: 1-214.
3. J.C. Elliott. *Studies in Inorganic Chemistry Volume 18: Structure and Chemistry of the Apatites and Other Calcium Orthophosphates,* (1994)*;* p: 10-404.
4. Z. LeGeros Racquel. *Clinical orthopaedics and related research*, (2002); p: 81-98.
5. R.Z. LeGeros. *Monographs in oral science*, (1991); 15, p: 1-201.
6. C. Rey, V. Renugopalakrishnan, B. Collins, and M.J. Glimcher. *Calcified Tissue International*, (1991); 49, p: 251-258.
7. E. Landi, G. Celotti, G. Logroscino, and A. Tampieri. *Journal of the European Ceramic Society*, (2003); 23, p: 2931-2937.
8. Y. Doi, H. Iwanaga, T. Shibutani, Y. Moriwaki, and Y. Iwayama. *Journal of Biomedical Materials Research*, (1999); 47, p: 424-433.
9. R. Murugan, S. Ramakrishna, and K.P. Rao. *Materials Letters*, (2006); 60, p: 2844-2847.
10. T.A. Schildhauer, A.P. Bennett, T.M. Wright, J.M. Lane, and P.F. O'Leary. *Journal of orthopaedic research* (1999); 17, p: 67-72.
11. J.C. Lotz, S.S. Hu, D.F. Chiu, M. Yu, O. Colliou, and R.D. Poser. *Spine*, (1997); 22, p: 2716-2723.
12. W.L. Suchanek, P. Shuk, K. Byrappa, R.E. Riman, K.S. TenHuisen, and V.F. Janas. *Biomaterials*, (2001); 23, p: 699-710.
13. M. Kinoshita, K. Itatani, S. Nakamura, and A. Kishioka. *Gypsum & Lime*, (1990); 227, p: 207-215.
14. M. Toriyama, Y. Kawamoto, T. Suzuki, Y. Yokogawa, K. Nishizawa, F. Nagata, and M.R. Mucalo. *Journal of Materials Science Letters*, (1996); 15, p: 179-181.
15. E.A.P. De Maeyer, R.M.H. Verbeeck, and D.E. Naessens. *Inorganic Chemistry*, (1993); 32, p: 5709-5714.
16. R.B. VonDreele and A.C. Larson. (2004); p.
17. R.Z. LeGeros. *Nature* (1965); 206, p: 403-404.
18. J.D. Layani, I. Mayer, and F.J. Cuisinier. *Journal of inorganic biochemistry*, (2000); 81, p: 57-63.
19. J.D.B. Featherstone, S. Pearson, and R.Z. LeGeros. *Caries Research*, (1984); 18, p: 63-66.
20. K. Kandori, N. Horigami, A. Yasukawa, and T. Ishikawa. *Journal of the American Ceramic Society*, (1997); 80, p: 1157-1164.
21. S. Peroos, Z. Du, and N.H. de Leeuw. *Biomaterials*, (2006); 27, p: 2150-2161.
22. J. Barralet, J.C. Knowles, S. Best, and W. Bonfield. *Journal of materials science. Materials in medicine*, (2002); 13, p: 529-533.
23. S. Meejoo, W. Maneeprakorn, and P. Winotai. *Thermochimica Acta*, (2006); 447, p: 115-120.
24. G. Xu, I.A. Aksay, and J.T. Groves. *Journal of the American Chemical Society*, (2001); 123, p: 2196-2203.

25. M. Aizawa, H. Ueno, K. Itatani, and I. Okada. *Journal of the European Ceramic Society*, (2006); 26, p: 501-507.
26. H. El Feki, J.M. Savariault, A.B. Salah, and M. Jemal. *Solid State Sciences*, (2000); 2, p: 577-586.
27. R.V. Santos and R.N. Clayton. *American Mineralogist*, (1995); 80, p: 336-344.
28. I. Rehman and W. Bonfield. *Journal of materials science. Materials in medicine*, (1997); 8, p: 1-4.
29. V. Jokanovic, D. Izvonar, M.D. Dramicanin, B. Jokanovic, V. Zivojinovic, D. Markovic, and B. Dacic. *Journal of Materials Science: Materials in Medicine*, (2006); 17, p: 539-546.
30. A. Slosarczyk, Z. Paszkiewicz, and C. Paluszkiewicz. *Journal of Molecular Structure*, (2005); 744-747, p: 657-661.
31. S. Habelitz, L. Pascual, and A. Duran. *Journal of the European Ceramic Society*, (1999); 19, p: 2685-2694.
32. S.E.P. Dowker and J.C. Elliott. *Calcified Tissue International*, (1979); 29, p: 177-178.
33. S.E.P. Dowker and J.C. Elliott. *Journal of Solid State Chemistry*, (1983); 49, p: 334-340.
34. S. Busch, H. Dolhaine, A. DuChesne, S. Heinz, O. Hochrein, F. Laeri, O. Podebrad, U. Vietze, T. Weiland, and R. Kniep. *European Journal of Inorganic Chemistry*, (1999); p: 1644-1653.
35. Z. Zyman, D. Rokhmistrov, I. Ivanov, and M. Epple. *Materialwissenschaft und Werkstofftechnik*, (2006); 37, p: 530-532.
36. E. Gilbert and S. Hoffmann-Glewe. *Water Research*, (1990); 24, p: 39-44.
37. Y. Ku, L.-S. Wang, and Y.-S. Shen. *Journal of Hazardous Materials*, (1998); 60, p: 41-55.
38. R. Venkatadri and R.W. Peters. *Hazardous Waste & Hazardous Materials*, (1993); 10, p: 107-149.
39. B.A. Weir, D.W. Sundstrom, and H.E. Klei. *Hazardous Waste & Hazardous Materials*, (1987); 4, p: 165-176.

CHAPTER 5. DEPOSITION OF CARBONATED HYDROXYAPATITE (CO_3HAp) ON POLY(METHYLMETHACRYLATE) SURFACES BY DECOMPOSITION OF CALCIUM-EDTA CHELATE

A paper published in *The Journal of American Ceramic Society*

J. Am. Ceram. Soc., 2008, 91(10), 3147-3153

Yusuf Yusufoglu[a] and Mufit Akinc[b]

5.1 Abstract

Inspired from the nature, the development of organic-inorganic composites between polymers and hydroxyapatite (HAp) has been investigated extensively. In this study, bone-like apatite (carbonated hydroxyapatite, CO_3HAp) was precipitated on poly-methylmethacrylate (PMMA) films by the oxidative decomposition of Ca-EDTA (calcium-ethylenediamine tetraacetate) chelates. Corona-treated PMMA films were soaked in a Ca-EDTA-PO_4-H_2O_2 solution and aged at 63°C and pH ~ 9 for times ranging from 1 to 24 h. Apatite formed on PMMA films was characterized by X-ray diffraction, Fourier transform infrared (FTIR), Scanning electron microscope, energy-dispersive X-ray spectroscopy, and carbon analysis. The apatite was found to be CO_3HAp with Ca/P atomic ratio ranging between 1.3 and 1.9. Elemental analyses indicated that the carbonate content of the apatite phase was around 6.5 wt% after 24 h of aging time. Lattice parameters were estimated using a Rietveld profile-analysis and found to be a = 0.9438 nm and c = 0.6901 nm. Furthermore, FTIR spectra indicated that the apatite deposited on PMMA was B-type CO_3HAp, in which

carbonate ions occupy the phosphate sites. In the first 3 h of aging, isolated rod-like HAp particles were observed. With time, the needle-like crystallites radiate from a nucleus to form double-spherulite shape particles. The crystallites grew into a continuous layer with a thickness of ~15 μm after 24-h aging. The adhesive strength between the PMMA substrate and the apatite layer was determined to be around 1.7 MPa.

[a,b] Ames Laboratory and Department of Materials Science and Engineering, Iowa State University, Ames, IA 50011.
[a] Primary researcher and author
[b] Author for correspondence

5.2 Introduction

The development of organic-inorganic composite materials similar to those produced by nature has received a considerable attention. Bones, dentine, eggshell and the shell of marine mollusks are some examples of highly complex organic-inorganic hybrid materials produced in nature. Compared to synthetic counterparts, natural hybrid materials have superior mechanical properties and are synthesized under milder conditions [1]. The organic component of the biomaterial imparts toughness and it serves as a template for nucleation of inorganic phase. For example, during the bone formation the collagen (organic matrix) provides sites for nucleation of calcium-deficient carbonated hydroxyapatite (CO_3HAp) (inorganic phase). The CO_3HAp accounts for 65 wt% of the total bone mass with the remaining being the organic collagen and water [2]. In general, bone-bonding implants are produced by the application of CO_3HA ceramics in the form of either bulk or coating [3, 4]. The synthetic CO_3HAp has been used as a bioactive inorganic component because of its chemical and biological similarity to the mineral phase of bone [5]. Insertion of CO_3^{2-} to the

HAp lattice alters the stability, surface charge, solubility, and biological reactivity of the apatite [6, 7]. It was shown that CO_3HAp has higher osteoconductivity and resorption rates than that of pure HAp, resulting in faster bone regeneration [8]. Moreover, carbonate incorporation into the HAp structure improves mechanical strength and is used as *in situ*-hardened bone fillers or screw fixations [9, 10]. In general, the studies in the literature imply that CO_3HAp is more biocompatible and it is actually desirable over pure HAp as bioresorbable implant.

Deposition of apatite on polymeric substrates has been investigated extensively not only for understanding the fundamental mechanism of biomineralization, but also for the design and development of novel materials suitable for prosthetic medical applications [11]. Sato *et al.* [12] investigated the formation of apatite on the poly-methylmethacrylate (PMMA) which was surface-treated by applying plasma discharge or alkaline solution. The PMMA films were soaked in a simulated body fluid (SBF) at 36.5 ^{o}C for 7 days and apatite was formed on the substrate. They reported that the adhesion strength of apatite to the organic polymer substrate was approximately 4.5 MPa and this method was promising for developing hard and soft tissue implants with high bioactivity. Casaletto *et al.* [13] also studied the HAp coating on PMMA substrates by immersing the PMMA films in a SBF with ion concentrations nearly 1.5 times to those of human blood plasma. They reported that good quality HAp coatings with approximately 2 μm thickness can be obtained on PMMA films by the biomimetic method. Similarly, Liu *et al*. [14] investigated the apatite deposition on PMMA and other polymeric substrates. In their study, PMMA was pretreated with ultraviolet (UV) light, and then subjected to a SBF with ion concentrations nearly equal to those of human body plasma at 36.5 ^{o}C. Their results indicated that a dense and uniform layer of highly bioactive apatite can be formed in arbitrary thickness on PMMA with adhesive strength of around 5 MPa. In another study, Varma *et al.* [15] investigated *in vitro* nucleation of calcium phosphate phase over functionalized PMMA films. The PMMA films were treated with a methanol solution of sodium hydroxide (NaOH) and adenosine triphosphate solution before immersing in a SBF solution for calcium phosphate nucleation. Furthermore, Li *et al.* [16] showed that a bone-bonding polymer known as Polyactive® (a polyester-type polymer which is a block copolymer composed of a polyethylene oxide soft segment and a polybutylene terephthalate hard segment) is capable of inducing CO_3HAp formation in SBF. They produced 100-µm-thick coatings of CO_3HAp after 4 days of aging. Miyazaki *et al.* [17] precipitated HAp on polyamide films containing carboxyl groups after exposing to a solution 1.5 times SBF concentration. They showed that polyamide film acts as an effective substrate for apatite formation. Formation of apatite on various polar polymeric substrates was also reported by others [11, 18-22].

In our previous study, it was shown that CO_3HAp can be synthesized by a homogenous oxidative decomposition of calcium-ethylenediaminetetraacetic acid (Ca-EDTA) chelate in a phosphate solution containing hydrogen peroxide (H_2O_2) [23]. It was shown that the carbonate content of the apatite increases with the solution pH and reaches a maximum value of around 7 wt% at $\mathrm{pH} \approx 10$.

By using the same method, we report the formation of CO_3HAp on corona-treated PMMA films. PMMA is a self-curing cement and is the current standard for cement-held prostheses which gives immediate structural support [24]. Furthermore, PMMA materials have been used as a cement to secure orthopedic implants to the skeleton [25, 26]. However, the clinical use of PMMA has some restrictions. PMMA cements are inert materials and

PMMA does not form chemical bond to bone and therefore it does not induce bone formation [24, 27]. One solution to overcome this deficiency is to coat PMMA with CO_3HAp, which has been proven to induce bone formation and has been used in various implant applications [28, 29].

In an effort to imitate the formation of natural bone, the PMMA films were used as a template for the precipitation of CO_3HAp on the polymeric surfaces from aqueous solutions. The purpose of this study was to investigate the formation and characteristics of the CO_3HAp on the PMMA films by a homogenous precipitation method similar to the one that was used in our previous paper [23]. The coating was characterized using X-ray diffractometer (XRD), Fourier transform infrared (FTIR), Scanning electron microscope (SEM), energy-dispersive X-ray spectroscopy (EDS), and carbon analysis. The strength of CO_3HAp and the PMMA film interface was also measured.

5.3 Experimental Procedure

All chemicals used in this study were obtained from Fisher Scientific (Fair Lawn, NJ) and are laboratory grade and purity. The 0.05-mm-thick PMMA films were corona treated by electrical discharge at 2.5 J/cm^2 each side by 3M Company (St. Paul, MN). After corona treatment, the surface of the PMMA film is rendered chemically more reactive.

A Ca-EDTA solution was prepared by mixing 200 mL aqueous solution of 0.5*M* $Ca(NO_3)_2 \cdot 2H_2O$ with 38 g ethylenediaminetetraacetic acid disodium salt dihydrate ($Na_2EDTA \cdot 2H_2O$) to which 120 mL solution of 0.5*M* $Na_3PO_4 \cdot 12H_2O$ was added. Then, approximately 300 mL of 30% H_2O_2 solution was added and the solution pH was adjusted to pH ~ 9 with NaOH. Once all the reactants are added and pH of the solution is adjusted, 3 cm x 3 cm corona-treated PMMA films were aged in 90 mL of the above solution for time intervals ranging from 1 to 24 h at 63°C in a water bath. Because practically all the Ca^{2+} ions are tied by EDTA in the solution, no precipitate is formed when Ca-EDTA solution is mixed with phosphate solution. Heating the solution in the presence of H_2O_2 results in a slow decomposition of Ca-EDTA complex and releasing Ca^{2+} into the solution. As the solution becomes saturated, the calcium phosphate crystals nucleate and grow on the PMMA film, and also in the bulk solution. After the specified time intervals, HAp-coated PMMA films were taken out from the solution and rinsed out with distilled water to remove the excess solution and the loosely bound apatite.

The structure of the calcium phosphate coating was determined with a powder XRD (XDS-2000, Scintag Inc., Cupertino, CA) using Cu$K\alpha$ radiation and operating at 45kV and 40mA. The scanning rate was 0.75° /min with a sampling interval of 0.03° over a range of $10^\circ \leq 2\theta \leq 60^\circ$. Phase analysis was performed using the ICDD (The International Centre for Diffraction Data) database and the Scintag DMSNT (Diffraction Management System for NT) search /match software. Furthermore, the general structure analysis system, a Rietveld profile-analysis, was used to determine the lattice parameters [30]. The CO_3^{2-} content deposited on PMMA films is estimated from the lattice parameters using the empirical expression given by LeGeros [31]. Because *a*-axis is more sensitive to structural changes [32, 33], CO_3^{2-} content is estimated from the *a* lattice parameter:

$$a\ (\text{nm}) = 0.9456 - (5.3 \times 10^{-4})\ (\text{wt }\%CO_3^{2-}) \qquad (1)$$

The FTIR spectra were obtained using a Bruker spectrometer (Bruker IFS-66v, Bruker Optics Inc., Billerica, MA) in the range of 400-4000 cm^{-1} with a 4 cm^{-1} resolution and averaging 32 scans. For the FTIR analysis, the HAp coatings were carefully scraped from the PMMA surface, ground and pressed into KBr pellets containing approximately 1 wt%

sample. The carbonate content was estimated from the infrared spectra by comparing the extinction coefficient (E) of the CO_3^{2-} at about 1415 cm^{-1} with that of the PO_4^{3-} at about 575 cm^{-1} (Eq. (2)). The extinction coefficients were calculated from the measurements of baseline transmittance (T_2) and peak transmittance (T_1) using the relationship $E = \log(T_2/T_1)$. The empirical relation offered by Featherstone *et al.* [34] allows estimation of CO_3^{2-} content to better than ±10%:

$$\text{wt \% } CO_3^{2-} = 16.1\ (E_{1415}/E_{575}) - 0.2 \qquad (2)$$

SEM (JEOL, JSM-5910LV, Tokyo, Japan) in conjunction with (EDS) was used to ascertain the morphology and chemical constituents of the coating operating at an accelerating voltage of 10 kV. In addition, the coating thickness was also estimated from the cross sections. CO_3HAp-coated PMMA films were embedded in epoxy and polished to reveal cross sections and to provide a known sample geometry. The polished samples were coated with approximately 15 nm of carbon. For the EDS measurements, pure HAp (standard reference material® 2910) was used as standard with the measured Ca/P ratio of 1.7, which is very close to stoichiometric value of pure HAp (1.67). Moreover, at least 5 measurements were taken for samples in the EDS experiments.

The carbonate content was also quantitatively determined as carbon using a CHN/S elemental analyzer (PE 2400 Series II, Perkin-Elmer, Ann Arbor, MI) and three runs were performed for each sample. The relative uncertainty in CO_3^{2-} was around 5 %. Furthermore, calcium phosphate formation was followed by recording the mass changes in the PMMA films at regular intervals.

The adhesive strength of the apatite layer to the PMMA film was measured using Instron-5569 testing machine (Instron Inc., Canton, MA) at a crosshead speed of 1 mm/min until the fracture occurred between the apatite and the PMMA substrate. PMMA film with hydroxyapatite layer on both sides was glued to circular studs on each side with two-part epoxy (Miller-Stephenson Epoxy 907). An average of 10 measurements was taken.

5.4 Results and Discussion

The mass difference between the coated and uncoated PMMA films was used to estimate the amount of apatite deposited, and it is given in Figure 5.1. The extent of deposition on PMMA films increases with time and shows a significant increase after several hours of aging time. In contrast, the films soaked in the distilled water under the similar conditions did not show any significant mass gain in 24 h. The mass gain correlates well with the pH decrease (see Figure 5.1).

Depending on the solution pH, precipitation of hydroxyapatite (HAp, $Ca_{10}(PO_4)_6(OH)_2$) may proceed according to the Eq.(3) with the equilibrium constant of K ≈ 1×10^{13} as reported by Fujishiro *et al.* [35]:

$$Ca^{2+} + 3/5\,HPO_4^{2-} + 4/5\,OH^- \xleftrightarrow{K_P} 1/10\,Ca_{10}(PO_4)_6(OH)_2 + 3/5\,H_2O \qquad (3)$$

Because PO_4^{3-} is a conjugate base of the weak acid H_3PO_4, the concentration of various phosphate species vary with pH. Figure 5.2 shows concentration of phosphate ions as a function of pH, which was constructed by using Mathcad® 11 software.

During the aging, pH of the solution decreases from 9 to about 7.1 as OH^- ions are consumed according to the HAp formation reaction (Eq. (3)). The decrease in pH is faster in the first 15 h, and slows down as it approaches 24 h. With the exception of first several hours, which correspond to undersaturated solution, the amount of HAp formed and decrease in pH show similar trends.

The X-ray diffraction patterns of apatite-coated PMMA films with increasing aging time and pure HAp (standard reference material® 2910) are illustrated in Figure 5.3. The characteristic HAp peaks appear after 3 h of aging (no diffraction peaks were observed before 3 h). The samples aged for 6 h show characteristic HAp peaks and a large background of amorphous PMMA film, in agreement with the mass of HAp measured (see Figure 5.1). The number of peaks and the peak intensities increased with aging time. For instance, the intensity of the (211) and (300) peaks increased with aging time in good agreement with SEM observations as the number and size of HAp particles increase with aging time. After 15 h, well developed HAp peaks were observed (see Figure 5.3). This agrees well with the phases predicted by the calcium phosphate pH - concentration equilibrium diagram [36, 37], as well as with those of Yusufoglu and Akinc [23]. Furthermore, Dorozhkin [5] showed that HAp is the most stable calcium phosphate phase at $7 \leq \text{pH} \leq 11$. Even though all of the observed peaks can be assigned to HAp with reference to ICCD (# 9-432) and standard reference material® 2910, some of the peaks are shifted reflecting a change in unit cell dimensions, which is believed to be due to CO_3^{2-} incorporation. Furthermore, HAp precipitated on PMMA films shows a higher $I_{(300)}/I_{(211)}$ than that of pure HAp, indicating the preferred orientation on PMMA film consistent with Fujishiro *et al.*'s findings who synthesized HAp on various substrates via hydrothermal reactions [35, 38].

Figure 5.4 shows the variation of lattice parameters with aging time. Because the most intense peaks of the apatite appear after 6 h, the lattice constants were calculated for only long aging times. Pure HAp has lattice parameters a = 9.4225 Å and c = 6.8850 Å [33] and it is well established observation that a-axis decreases, while c-axis increases for the B-type CO_3 substitution where CO_3^{2-} substitutes for PO_4^{3-} [6, 37, 39, 40]. Even though the trend in the lattice parameters is in good agreement with the literature, it shows a systematic underestimation in the carbonate amount (calculated from the *a* lattice parameters using Eq. (1)) compared with the results obtained from FTIR analysis and elemental carbon analyses. The amount of carbonate estimated using Eq. (1) was found to be approximately 0.8, 3.1 and 3.4 wt% for aging times of 6h, 15h and 24h., respectively. This discrepancy may be attributed to the presence of water in apatite structure, which was clearly observed in the FTIR spectra (see Figure 5.5). Elliott reported in detail that incorporation of water molecules into the apatite structure might cause considerable increase in the *a* lattice parameters due to the substitution for OH^- in the HAp structure which results in the *a*-axis parameter increase [37]. Although, the amount of CO_3 was underestimated from the lattice parameters, the behavior of lattice parameters has shown that deposited apatite is B-type CO_3HAp which agrees well with FTIR and EDS findings.

The FTIR spectra of HAp formed on PMMA at several aging times and pure HAp (standard reference material® 2910) are given in Figure 5.5. The observed absorption peaks correspond to CO_3HAp[6, 9, 41-43]. The phosphate bands of HAp are observed at $\nu_1 = 965$ cm^{-1} (a single intense band), $\nu_2 = 470$ cm^{-1}, $\nu_3 = 1050\text{-}1095$ cm^{-1}, and $\nu_4 = 565\text{-}602\text{-}635$ cm^{-1} (three sites) [6, 9, 44]. The phosphate peaks at $\nu_4 = 565\text{-}610$ cm^{-1} and $\nu_3 = 1045$ cm^{-1} appeared after 1 h of aging time. The other adsorption bands of phosphate at $\nu_2 = 470$ cm^{-1} and $\nu_1 = 960$ cm^{-1} were more apparent after 2 h. The broad absorption bands at around 3430 and 1620 cm^{-1} are due to the incorporated water molecules [37, 43, 45].

The peaks at 871 and 1416-1475 cm^{-1} are assigned to CO_3^{2-} and their intensity increases with aging time reaching a maximum at 24 h. The amount of carbonate content for different aging times was estimated from infrared (IR) analysis using Eq. (2) and illustrated in Figure 5.7. Neither carbonate peaks, nor water bands were observed in the IR spectra of pure HAp (Standard Reference Material® 2910) (see Figure 5.5), confirming that the apatite precipitated on PMMA films was hydrated CO_3HAp.

Carbonate can substitute for either PO_4^{3-} or OH^- sites in biological HAp. If CO_3^{2-} substitutes for OH^- ions (A-type CO_3HAp), the CO_3^{2-} bands appear at 880 (ν_2), 1458 (ν_{3a}) and 1546 (ν_{3b}) cm^{-1}. However, if it substitutes for PO_4^{3-} (B-type CO_3HAp) the CO_3^{2-} bands shift downward appearing at 871 (ν_2), 1420 (ν_{3a}) and 1475 (ν_{3b}) cm^{-1} [6, 7, 37, 43, 45, 46]. In the apatite precipitated on PMMA films, the carbonate ν_2, ν_{3a} and ν_{3b} peaks are observed at 871, 1418, 1475 cm^{-1}, respectively, indicating mainly B-type CO_3HAp formation. Nevertheless, possibility of some CO_3^{2-} substitution on the OH^- sites may not be completely excluded.

The SEM micrographs of HAp formed on PMMA films at various aging times are illustrated in Figure 5.6. Micrographs clearly indicate that the formation of the HAp on PMMA films depends largely on the aging time. HAp first forms as 1μm long rod-like particles, then grow into approximately 5 μm long rod-like particles (the inset in Figures 5.6(a) and (b)), and finally a “twin-cauliflower” like morphology appear at later stages. These “twin-cauliflower” particles grow to form a spherical shape (see Figure 5.6(e)). This unique morphology was also reported by Busch *et al.* [47]. After 6 h of aging, HAp particles grow into a continuous layer, and the whole PMMA surface was covered with particles after 15 h. This is in good agreement with the gravimetric analysis, which showed a significant increase in sample weight after 6 h of aging (see Figure 5.1). The change in the morphology with time may be attributed to the change in pH and/or concentration of other ions with time.

The chemical composition of the HAp formed on PMMA film was analyzed by EDS and it showed Ca, P, and Na. Sodium is probably incorporated from the reagent Na_2EDTA

and/or NaOH used to raise the initial pH of the solution. For up to 6 h, two types of particles with Ca/P =1.3 and 1.7 were detected. The particles with Ca/P = 1.3 correspond to octa calcium phosphate (OCP: $Ca_8H_2(PO_4)_6{\cdot}5H_2O$), and 1.7 is in close agreement with the atomic ratio of 1.67 for stoichiometric HAp. Because OCP is believed to be a precursor in the crystallization of bone-like apatite (CO_3HAp) [48-51], it is conceivable that the coating was initially a mixture of OCP and HAp which transforms to HAp via dissolution/reprecipitation mechanism [51-54]. For instance, Elliot [37] reported that transformation of OCP to HAp takes place through one of the following reactions:

$$Ca_8H_2(PO_4)_6{\cdot}5H_2O + 2\,Ca^{2+} \rightarrow Ca_{10}(PO_4)_6(OH)_2 + 3\,H_2O + 4\,H^{+} \qquad (4)$$

$$5\,Ca_8H_2(PO_4)_6{\cdot}5H_2O \rightarrow 4\,Ca_{10}(PO_4)_6(OH)_2 + 6\,H_3PO_4 + 17\,H_2O \qquad (5)$$

The diffraction peaks of OCP were not assigned with certainty in the Figure 5.3. Because the standard powder XRD patterns of HAp and OCP are very similar in the 2θ range of 20-40^{o} [55], the peaks observed in Figure 5.3 for aging times up to 6 h can be assigned to either HAp or OCP, which is consistent with EDS results. Because the limiting ion at the initial stages of the precipitation is Ca^{2+} (Ca^{2+} ions are released by slow decomposition of Ca-EDTA) it is reasonable to form calcium phosphate phases with lower Ca/P (OCP) which might transform to HAp with time as shown in Eq. (4). The variation in pH with aging time (see Figure 5.1) was also consistent with the EDS results. The gradual decrease in pH to a steady state value can be related to the gradual transformation of OCP to HAp, as reported by Graham and Brown [56].

Chickerur *et al.* [40] showed that when OCP hydrolyzes in the presence of carbonate, it incorporates CO_3 in type B sites. Furthermore, a similar trend does not exist for HAp synthesized under conditions where OCP could not be a precursor [54]. For aging times 15 and 24 h, Ca/P = 1.8 and 1.9 were measured, respectively. The observed molar Ca/P ratios were higher than the one for the stoichiometric HAp (1.67) due to substitution of CO_3^{2-} for PO_4^{3-}.

The amount of carbonate was also estimated from the elemental analysis using a CHN/S analyzer and shown in Figure 5.7 along with carbonate content estimated from FTIR spectra using Eq. (2). The trends are similar but FTIR data consistently predicts somewhat lower carbonate content than carbon analysis. It is believed that the carbon analysis represents the carbonate content of the precipitated HAp more accurately. The carbonate content increased from approximately 4.5 wt% to 6.5 wt% as aging time increases from 1 h to 24 h, which lies within the range 4-8 wt% of carbonate contents reported for the adult human bone [8, 57].

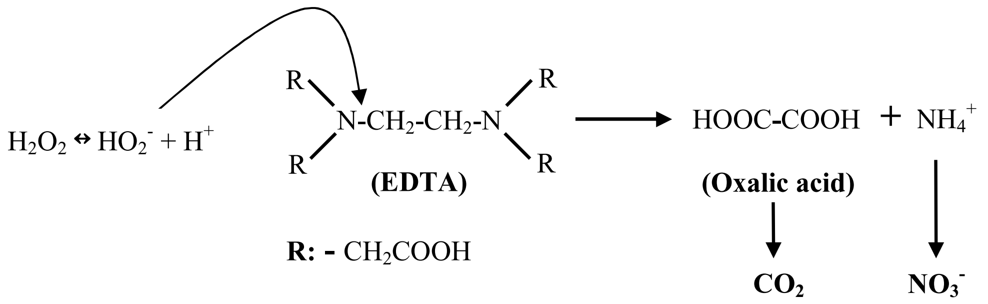

(6)

The source of carbonate in the precipitated HAp is believed to be due to decomposition of EDTA (Eq. (6)). H_2O_2 plays a crucial role on the decomposition of EDTA. H_2O_2 is a weak acid (pK_a=11.6) and dissociates to H_2O_2 anion (HO_2^-), which is a strong nucleophil (Eq. (7)).

$$H_2O_2 \leftrightarrow HO_2^- + H^+ \qquad (7)$$

Gilbert and Glewe suggested that the decomposition pathway for EDTA starts with

HO_2^- attack to C-N bonds of EDTA and the C-N bonds of intermediate compounds are further attacked by HO_2^- to form carbonate and nitrate ions (Eq. (6)) [58, 59]. The amount of carbonate formed depends on the extent of EDTA decomposition. The more EDTA is decomposed, the more carbonate is likely to be inserted into the HAp lattice. Increased concentration of carbonate ion with time agrees well with the observed higher carbonate insertion into HAp structure with time.

The film thickness was measured from the SEM cross sections of the coatings. Figure 5.8 shows the cross sections of apatite deposited on PMMA films at 15 and 24 h. Because continuous coatings were obtained at $t \geq 15$ h, thickness values are meaningful for only long aging times. Approximately 10 and 15-µm-thick HAp was observed after 15 and 24 h, respectively. When we calculate the volume of the apatite from the observed thickness for different aging times and assume 40%-50 % porosity, the estimated coating mass corroborates well with the results obtained from mass measurements shown in Figure 5.1.

The adhesive strength of HAp/PMMA interface was measured to be 1.67 (±0.12) MPa. Tanahashi *et al.* [21] and Kokubo [22] reported adhesive strength of 1.06 MPa for HAp formed on PMMA substrate by using SBF. Although the exact nature of the higher adhesion strength observed in the present study is not known, it may be surmised that the carbonate content of HAp or corona activation of PMMA may play a role in enhanced adhesion strength.

5.5 Conclusions

By using the homogenous oxidative decomposition of Ca-EDTA chelate in a phosphate solution containing H_2O_2, we accomplished the formation of continuous bone-like apatite (CO_3HAp) with a fairly strong adhesion on the corona-treated PMMA films. Our work mimics the biological mineralization in that the organic phase (PMMA) serves as a template for nucleation and growth of CO_3HAp. The deposition on PMMA films increases with the increasing aging time. Approximately 15-µm-thick continuous HAp layer was formed on the PMMA film after 24 h of aging. Elemental analysis and FTIR results illustrated that the deposited apatite was CO_3HAp with a maximum carbonate content of approximately 6.5 wt% observed at 24 h aging time. Furthermore, XRD studies have shown that the lattice parameter a decreased while c increased with carbonate insertion into the structure reaching the values of $a = 0.9438$ nm and $c = 0.6901$ after 24 h, which is a characteristic for B-type carbonate substitution. The FTIR spectra also indicated that the apatite was B-type CO_3HAp. The adhesive strength of the CO_3HAp/PMMA interface was measured to be approximately 1.7 MPa. In conclusion, we believe that this work will contribute to gaining insight into how biomaterials mimic calcium phosphate deposition when implanted at defect bone sites.

5.6 Acknowledgments

This work was supported by the U.S. Department of Energy under contract number DE-AC02-07CH11358. We wish to thank Louis Charles for assisting and helpful discussion with the adhesive strength measurement experiments.

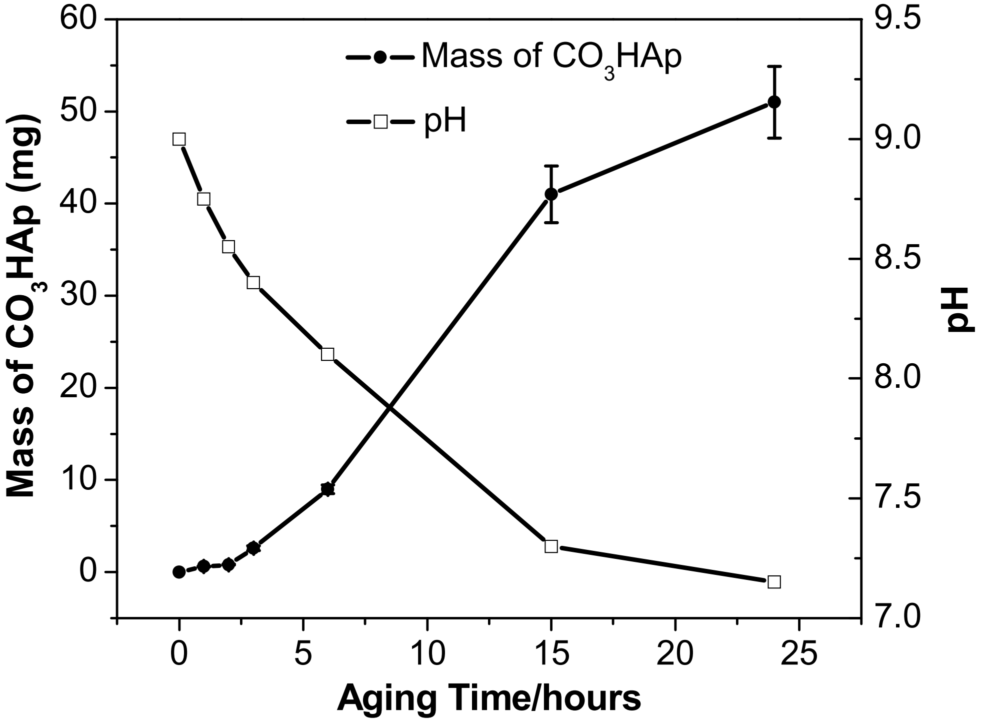

Figure 5.1. Carbonated hydroxyapatite formed on the poly(methylmethacrylate) film and the change in pH with aging time. Note there is an induction period until sufficient calcium-ethylenediamine tetraacetate decomposes to reach saturation concentration for precipitation.

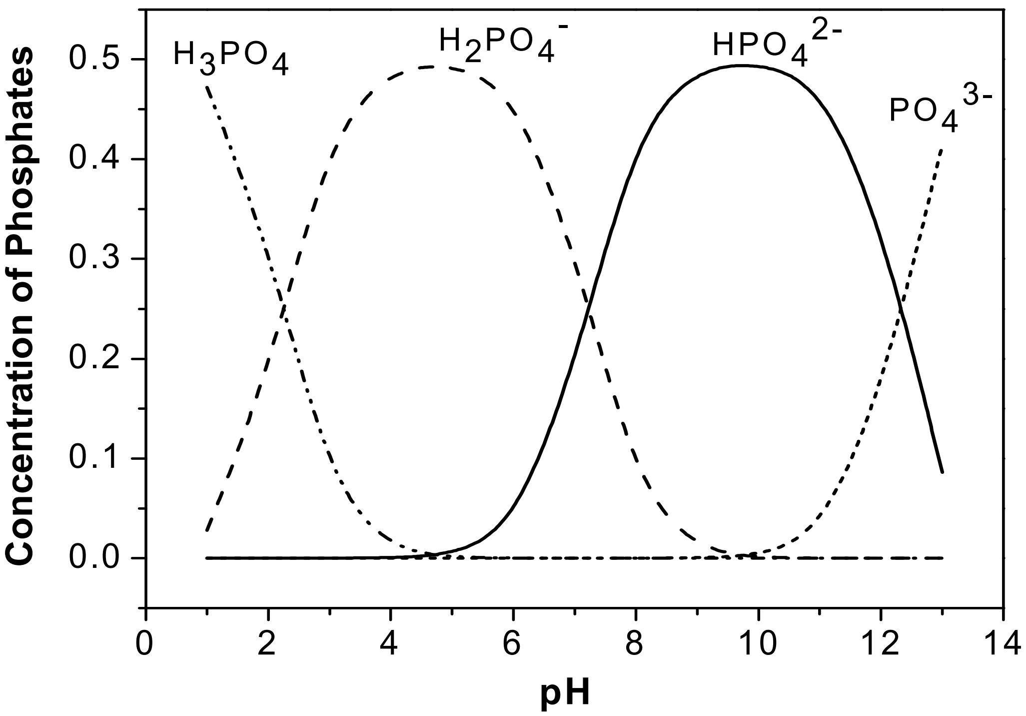

Figure 5.2. Concentration variation of phosphates with pH at room temperature.

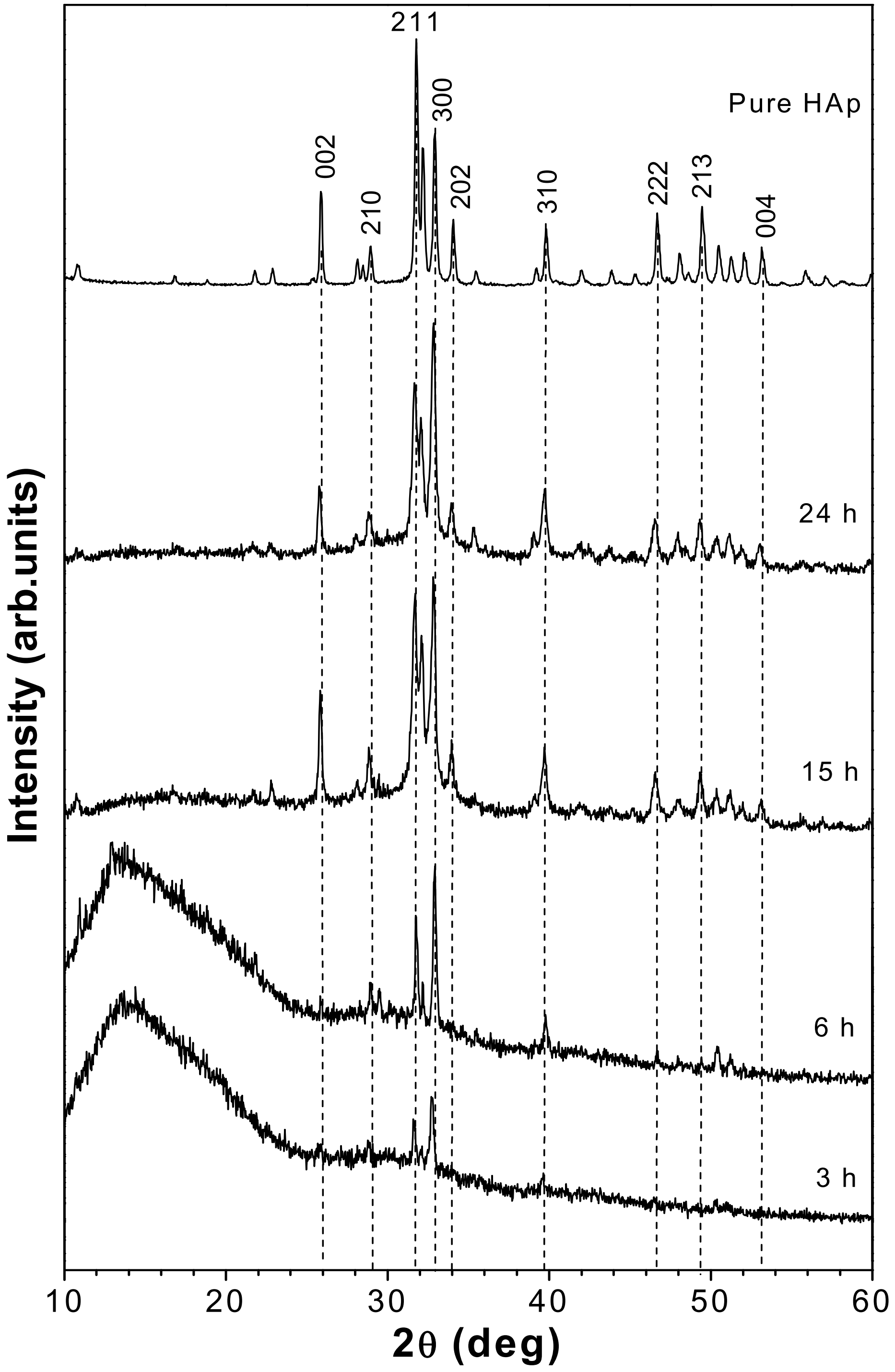

Figure 5.3. X-ray diffraction patterns of pure hydroxyapatite (standard reference material® 2910) and apatite deposited poly(methylmethacrylate) films after various aging times.

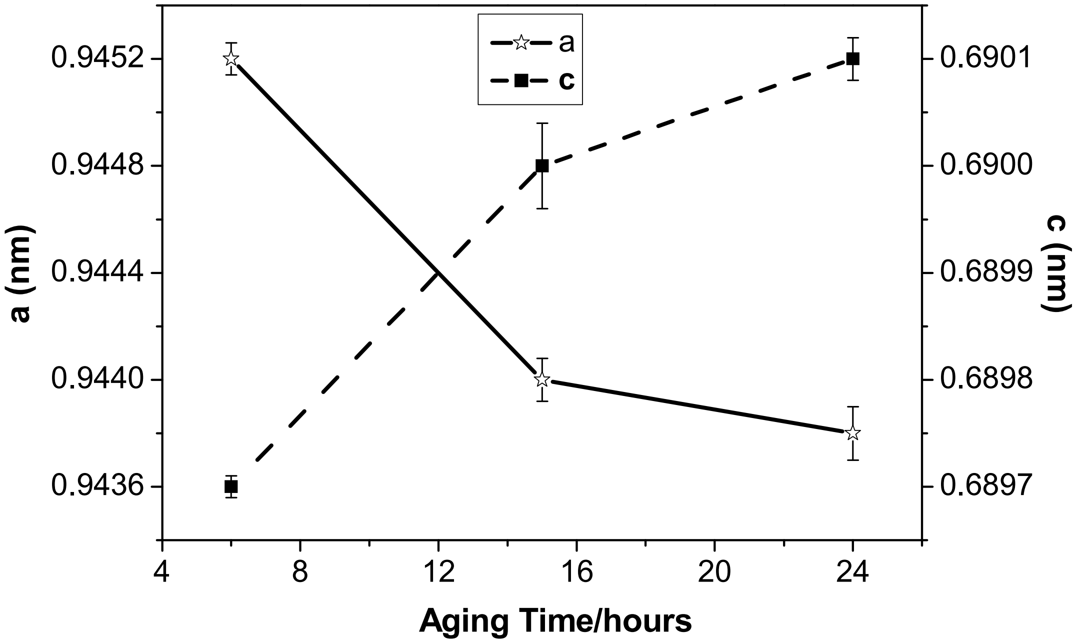

Figure 5.4. Variation of lattice parameters with aging time. The lattice parameter *a* decreases, while the lattice parameter *c* shows opposite trend.

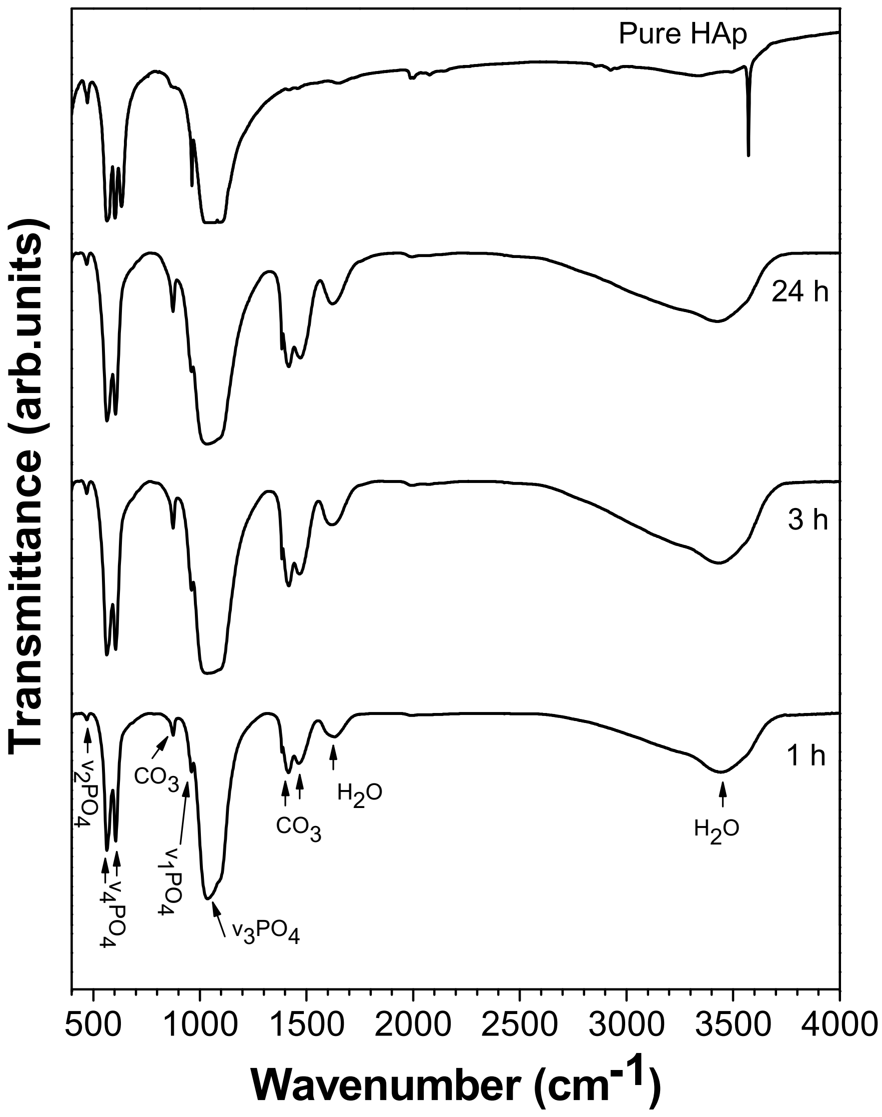

Figure 5.5. Fourier transform infrared spectra of the hydroxyapatite (HAp) formed on poly(methylmethacrylate) films at several aging times and pure HAp (standard reference material® 2910).

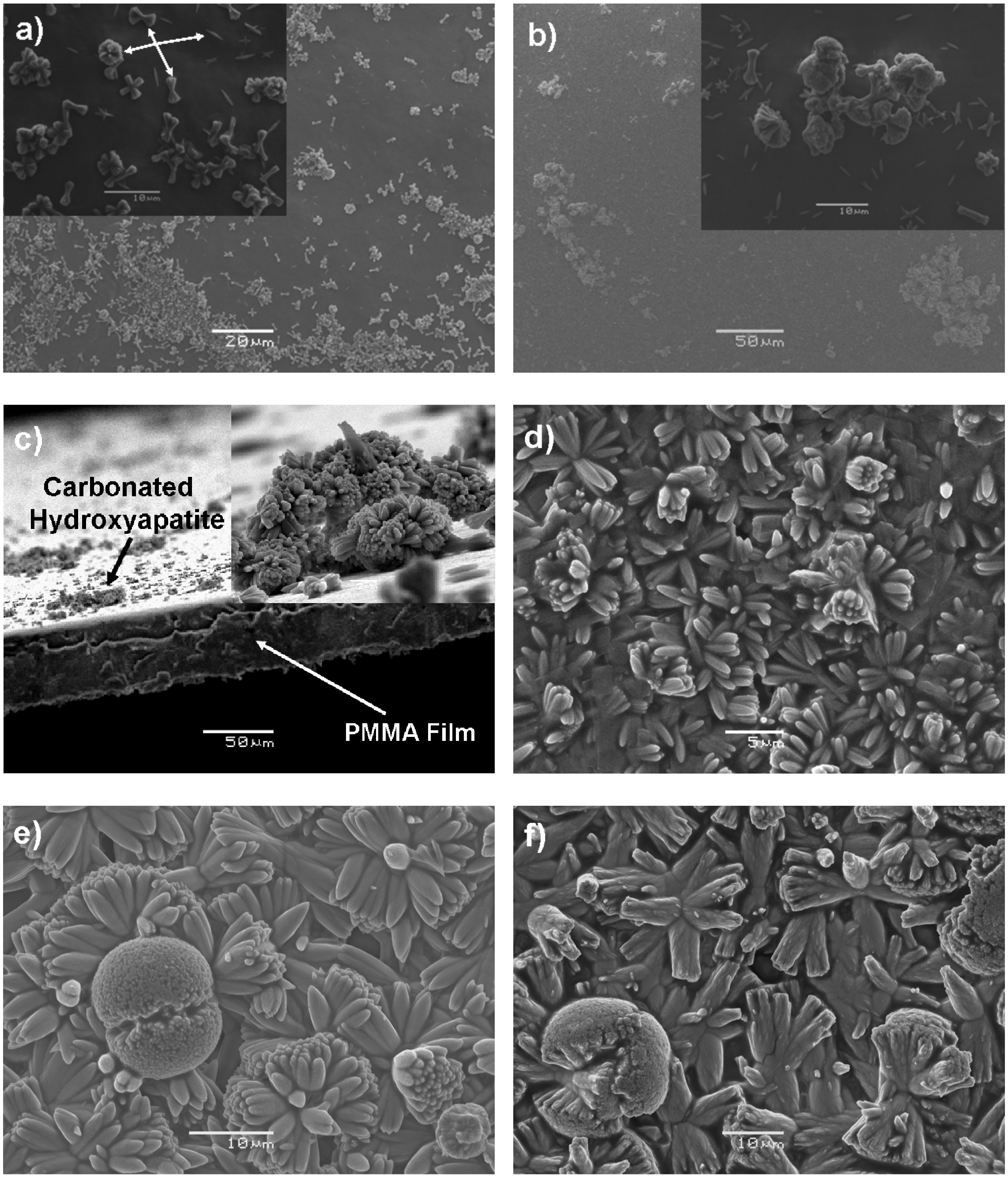

Figure 5.6. Scanning electron microscope images of the surfaces of poly-methylmethacrylate (PMMA) films coated with apatite for aging times of (a) 1 h, (b) 2 h, (c) 3 h, (d) 6 h, (e) 15 h, and (f) 24 h.

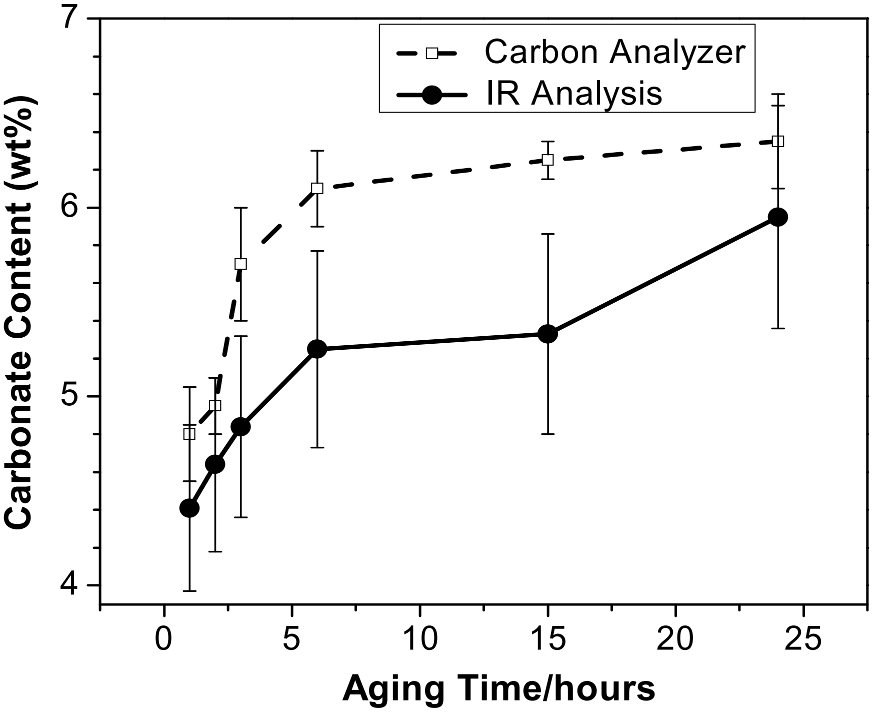

Figure 5.7. Carbonate content as a function of aging time which is determined by a carbon analyzer and infrared (IR) analysis by using Eq. (2).

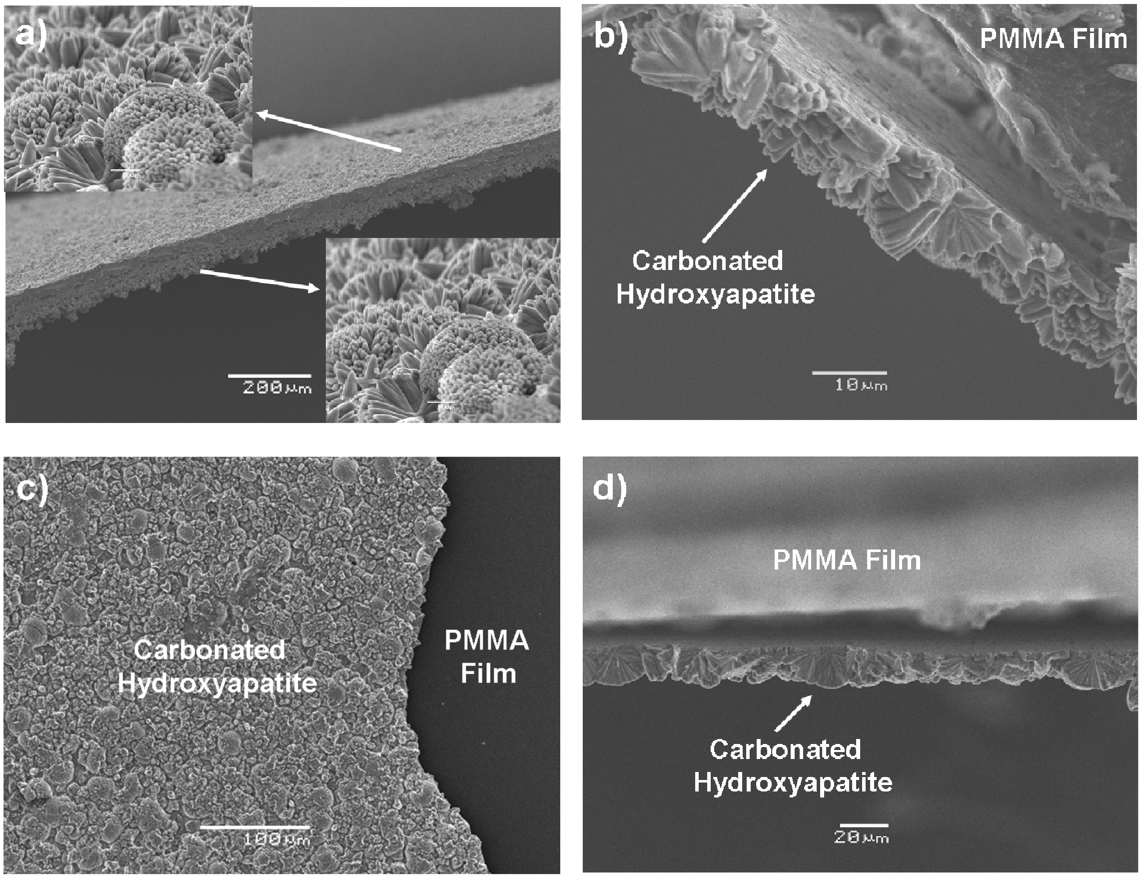

Figure 5.8. Scanning electron microscope images of the cross sections of apatite coating on poly(methylmethacrylate) (PMMA) films for aging times of (a,b) 15 h, and (c,d) 24 h.

5.7 References

1. K. Naka and Y. Chujo. *Chemistry of Materials*, (2001); 13, p: 3245-3259.
2. M. Vallet-Regi. *Dalton transactions*, (2006); p: 5211-5220.
3. M. Jarcho. *Clinical Orthopaedics and Related Research*, (1981); 157, p: 259-278.
4. R.G.T. Geesink, K. De Groot, and C.P.A.T. Klein. *Clinical Orthopaedics and Related Research*, (1987); 225, p: 147-170.
5. S.V. Dorozhkin. *Journal of Materials Science*, (2007); 42, p: 1061-1095.
6. E.A.P. De Maeyer, R.M.H. Verbeeck, and D.E. Naessens. *Inorganic Chemistry*, (1993); 32, p: 5709-5714.
7. A. Slosarczyk, Z. Paszkiewicz, and C. Paluszkiewicz. *Journal of Molecular Structure*, (2005); 744-747, p: 657-661.
8. E. Landi, G. Celotti, G. Logroscino, and A. Tampieri. *Journal of the European Ceramic Society*, (2003); 23, p: 2931-2937.
9. W.L. Suchanek, P. Shuk, K. Byrappa, R.E. Riman, K.S. TenHuisen, and V.F. Janas. *Biomaterials*, (2001); 23, p: 699-710.
10. J.C. Lotz, S.S. Hu, D.F. Chiu, M. Yu, O. Colliou, and R.D. Poser. *Spine*, (1997); 22, p: 2716-2723.
11. E. Dalas and A. Chrissanthopoulos. *Journal of Crystal Growth*, (2003); 255, p: 163-169.
12. K. Sato, D. Onodera, M. Hibino, and T. Yao. *Key Engineering Materials*, (2006); 309-311, p: 771-774.
13. M.P. Casaletto, S. Kaciulis, G. Mattogno, A. Mezzi, L. Ambrosio, and F. Branda. *Surface and Interface Analysis*, (2002); 34, p: 45-49.
14. G.J. Liu, F. Miyaji, T. Kokubo, H. Takadama, T. Nakamura, and A. Murakami. *Journal of Materials Science: Materials in Medicine*, (1998); 9, p: 285-290.
15. H.K. Varma, K. Sreenivasan, Y. Yokogawa, and A. Hosumi. *Biomaterials*, (2003); 24, p: 297-303.
16. P. Li, D. Bakker, and C.A. van Blitterswijk. *Journal of Biomedical Materials Research*, (1997); 34, p: 79-86.
17. T. Miyazaki, C. Ohtsuki, Y. Akioka, M. Tanihara, J. Nakao, Y. Sakaguchi, and S. Konagaya. *Journal of materials science. Materials in medicine*, (2003); 14, p: 569-574.
18. Y. Chen, A.F.T. Mak, J. Li, M. Wang, and A.W.T. Shum. *Journal of Biomedical Materials Research, Part B: Applied Biomaterials*, (2005); 73B, p: 68-76.
19. T. Iwatsubo, S.P. Kusumocahyo, T. Kanamori, and T. Shinbo. *Journal of Applied Polymer Science*, (2006); 100, p: 1465-1470.
20. F. Branda, A. Costantini, G. Luciani, G. Laudisio, L. Ambrosio, and L. Rimondini. *Key Engineering Materials*, (2001); 192-195, p: 127-130.
21. M. Tanahashi, T. Yao, T. Kokubo, M. Minoda, T. Miyamoto, T. Nakamura, and T. Yamamuro. *Journal of the American Ceramic Society*, (1994); 77, p: 2805-2808.
22. T. Kokubo. *Thermochimica Acta*, (1996); 280/281, p: 479-490.
23. Y. Yusufoglu and M. Akinc. *Journal of the American Ceramic Society*, (2008); 91, p: 77-82.

24. M.J. Dalby, L. Di Silvio, E.J. Harper, and W. Bonfield. *Journal of Materials Science: Materials in Medicine*, (1999); 10, p: 793-796.
25. M. Jager and A. Wilke. *Journal of Biomaterials Science Polymer edition*, (2003); 14, p: 1283-1298.
26. M. Ohgaki and K. Yamashita. *Journal of the American Ceramic Society*, (2003); 86, p: 1440-1442.
27. M. Moursi Amr, V. Winnard Alissa, L. Winnard Phillip, J. Lannutti John, and R. Seghi Robert. *Biomaterials*, (2002); 23, p: 133-144.
28. R.M. Meffert. *Current opinion in periodontology*, (1997); 4, p: 104-108.
29. T.W. Bauer and J. Schils. *Skeletal radiology*, (1999); 28, p: 423-432.
30. R.B. VonDreele and A.C. Larson. (2004); p.
31. R.Z. LeGeros. *Nature* (1965); 206, p: 403-404.
32. J.D. Layani, I. Mayer, and F.J. Cuisinier. *Journal of inorganic biochemistry*, (2000); 81, p: 57-63.
33. R. Astala and M.J. Stott. *Chemistry of Materials*, (2005); 17, p: 4125-4133.
34. J.D.B. Featherstone, S. Pearson, and R.Z. LeGeros. *Caries Research*, (1984); 18, p: 63-66.
35. Y. Fujishiro, A. Fujimoto, T. Sato, and A. Okuwaki. *Journal of Colloid and Interface Science*, (1995); 173, p: 119-127.
36. H. Oonishi and K. Oomamiuda. *Degradation/resorption in bioactive ceramics in orthopedics Handbook of Biomaterial Properties*, (1998); p: 406-419.
37. J.C. Elliott. *Amsterdam-London-New York-Tokyo, Elsevier*, (1994); p: 10-404.
38. Y. Fujishiro, S. Uchida, and T. Sato. *Bioceramics, Proceedings of the International Symposium on Ceramics in Medicine*, (1999); 12, p: 141-144.
39. S. Peroos, Z. Du, and N.H. de Leeuw. *Biomaterials*, (2006); 27, p: 2150-2161.
40. N.S. Chickerur, M.S. Tung, and W.E. Brown. *Calcified Tissue International*, (1980); 32, p: 55-62.
41. B. Feng, J.Y. Chen, S.K. Qi, L. He, J.Z. Zhao, and X.D. Zhang. *Biomaterials*, (2001); 23, p: 173-179.
42. W.L. Murphy and D.J. Mooney. *Journal of the American Chemical Society*, (2002); 124, p: 1910-1917.
43. S.V. Dorozhkin. *Journal of the American Ceramic Society*, (2007); 90, p: 244-249.
44. I. Rehman and W. Bonfield. *Journal of materials science. Materials in medicine*, (1997); 8, p: 1-4.
45. G. Xu, I.A. Aksay, and J.T. Groves. *Journal of the American Chemical Society*, (2001); 123, p: 2196-2203.
46. M. Aizawa, H. Ueno, K. Itatani, and I. Okada. *Journal of the European Ceramic Society*, (2006); 26, p: 501-507.
47. S. Busch, H. Dolhaine, A. DuChesne, S. Heinz, O. Hochrein, F. Laeri, O. Podebrad, U. Vietze, T. Weiland, and R. Kniep. *European Journal of Inorganic Chemistry*, (1999); p: 1644-1653.
48. L. Jonasova, A. Muller Frank, A. Helebrant, J. Strnad, and P. Greil. *Biomaterials*, (2004); 25, p: 1187-1194.
49. M. Tanahashi and T. Matsuda. *Journal of Biomedical Materials Research*, (1997); 34, p: 305-315.

50. M. Iijima, H. Kamemizu, N. Wakamatsu, T. Goto, Y. Doi, and Y. Moriwaki. *Journal of Crystal Growth*, (1997); 181, p: 70-78.
51. M.S. Johnsson and G.H. Nancollas. *Crit Rev Oral Biol Med*, (1992); 3, p: 61-82.
52. A.A. Campbell, G.E. Fryxell, J.C. Linehan, and G.L. Graff. *Journal of Biomedical Materials Research*, (1996); 32, p: 111-118.
53. R. Xin, Y. Leng, and N. Wang. *Journal of Crystal Growth*, (2006); 289, p: 339-344.
54. W.E. Brown, N. Eidelman, and B. Tomazic. *Adv Dent Res* (1987); 1, p: 306-313.
55. X. Lu and Y. Leng. *Biomaterials*, (2004); 25, p: 1779-1786.
56. S. Graham and P.W. Brown. *Journal of Crystal Growth*, (1996); 165, p: 106-115.
57. I. Hofmann, L. Mueller, P. Greil, and F.A. Mueller. *Journal of the American Ceramic Society*, (2007); 90, p: 821-824.
58. E. Gilbert and S. Hoffmann-Glewe. *Water Research*, (1990); 24, p: 39-44.
59. Y. Ku, L.-S. Wang, and Y.-S. Shen. *Journal of Hazardous Materials*, (1998); 60, p: 41-55.

CHAPTER 6. SYNTHESIS AND CHARACTERIZATION OF IONIC BLOCK COPOLYMER TEMPLATED CALCIUM PHOSPHATE NANOCOMPOSITES

A paper published in *Chemistry of Materials*

Chem. Mater., 2008, 20, 5922-5932

M. Kanapathipillai[a+], Y.Yusufoglu[a+], A. Rawal[a], Y.-Y. Hu[a], C.-T. Lo[b], P. Thiyagarajan[b], Y.E. Kalay[a], M. Akinc[a], S. Mallapragada[a], K. Schmidt-Rohr[a-]

6.1 Abstract

Self-assembling thermo-reversibly gelling anionic and zwitterionic pentablock copolymers were used as templates for precipitation of calcium phosphate nanostructures, controlling their size and ordered structural arrangement. Calcium and phosphate ions were dissolved in a block-copolymer micellar dispersion at low temperatures. Aging at ambient temperature produced inorganic nanoparticles, presumably nucleated by ionic interactions. The self-assembled nanocomposites were characterized by small-angle X-ray and neutron scattering (SAXS/SANS), nuclear magnetic resonance (NMR), thermogravimetric analysis (TGA), and transmission electron microscopy (TEM). ^{1}H-^{31}P NMR with ^{1}H spin diffusion from polymer to phosphate proved the formation of nanocomposites, with inorganic particle sizes from ~2 nm, characterized by ^{1}H-^{31}P dipolar couplings, to >100 nm. TEM analysis showed polymer micelles surrounded by calcium phosphate. SAXS attested that a significant fraction of the calcium phosphate was templated by the polymer micelles. SANS data indicated that the order of the polymer was enhanced by the inorganic phase. The nanocomposite gels exhibited higher moduli than the neat polymer gels. The calcium phosphate was characterized by TGA, X-ray diffraction, high-resolution TEM, and various NMR techniques. An unusual crystalline phase with ≥2 chemically and ≥3 magnetically inequivalent HPO_4^{2-} ions was observed with the zwitterionic copolymer, highlighting the influence of the polymer on the calcium phosphate crystallization. The inorganic fraction of the nanocomposite was around 30 wt% of the dried hydrogel. Thus, a significant fraction of calcium phosphate has been templated by the tailored self-assembling ionic block copolymers, providing a bottom-up approach to nanocomposite synthesis.

[+] Primary researchers and both authors contributed equally to the work
[a] Ames Laboratory, Iowa State University, Ames, IA 50011
[b] Argonne National Laboratory, 9700 S. Cass Ave, Argonne, IL 60439
[-] Author for correspondence

6.2 Introduction

In most examples of successful templating of polymer-ceramic composites, the polymer-inorganic phase interaction is limited to the surface of the polymer and restricts the systematic study of the effects that variables such as ionic interaction, relative size and concentration of polymer have on templating and nanocrystal formation [1-4]. One method to create nanocomposites and also to expand its applicability to the creation of three-dimensional macroscale structures is the dispersion of already synthesized particles or ionic solutions into the structured matrix [4, 5]. But nanoparticle aggregation, high viscosity of the nanostructured materials, and incompatibility of the particle surface and ionic solutions with the polymers limit the use of these types of templating methods [5]. We have demonstrated that these problems can be circumvented by the use of self-assembling thermo-reversible block copolymer gels that can facilitate a bottom-up approach for inorganic nanocomposite synthesis [6]. Although successful templating was achieved by this approach, the percentage of inorganic precipitate in the final nanocomposite was low (~15 wt%), compared to about 70 wt% seen in nature [7].

In the bone formation process, collagen fibrils are formed by self-assembly of collagen triple helices and hydroxyapatite (HAp) crystals grow within these fibrils [8]. During the HAp crystal growth, the acidic macromolecules such as glycoproteins that are attached to the collagen scaffold play important templating roles. Glycoproteins are covalently linked to polysaccharide side chains that often contain sulfate and carboxylate residues, and these functional groups serve as binding sites for Ca^{2+} ions [9]. To mimic natural nanocomposites better, the ionic interactions between the organic-inorganic interfaces need to be enhanced. Tanahashi *et al.* [10] have shown using self-assembled monolayers that anionic polymers template better compared to cationic or nonionic polar polymers, and further, ionic blocks containing, for instance, carboxylate groups or phosphobetaines are ideal for calcium phosphate precipitation. Other studies have also indicated that carboxyl groups not only provide a site for heterogeneous nucleation of apatite but also contribute to a tight adhesion of the apatite layer to polymer films [11]. Moreover, Spanos and co-workers [12] synthesized a novel composite with 9% HAp and 91% polymer by weight made of a biocompatible synthetic polymer (sulphonated polysulfone) and HAp by the precipitation of calcium phosphate phase in aqueous suspensions of the polymer particles.

Theoretical results using molecular dynamics simulations [13] have established general conditions for successful nanotemplating methods. It has been shown, for instance, that polymers with end-group functionalized blocks with a specific affinity for the inorganic components provide a successful templating strategy [14]. In this respect, block copolymers containing blocks of sulfobetaines, which are analogues to phosphobetaines, and blocks of acrylic acids, which contain carboxylate groups, are good choices for polymer templates in biomimetic mineralization. Further, it is believed that the interactions of acrylic-acid carboxylate groups with Ca^{2+} ions mimic those of the carboxylate groups in bone [15]. Hence, many mineralization studies have focused on poly(acrylic acid)-based templates for surface mineralization studies [15-17]. However, to enable hierarchical self-assembly of nanocomposites, copolymers that can self-assemble in three dimensions at multiple length scales in the presence of the inorganic phase need to be synthesized and investigated.

As hierarchically assembling copolymer templates, we have synthesized pentablock copolymers consisting of central triblock PEO_{100}-PPO_{65}-PEO_{100} Pluronic F127 copolymers modified with zwitterionic or anionic terminal blocks. The zwitterionic pentablock copolymers contain polysulfobetaine side chains, with an isoelectric point (*iep*) value of about 6.3. This polymer is ionic over a wide range of $pH \approx 2 - 11$. The anionic pentablock copolymer, on the other hand, contains acrylic acid blocks and imparts pH sensitivity above pH ~ 6. In addition to the ionic nature, the thermo-reversible ordering behavior of these polymers and their water solubility make them ideal templating materials for formation of nanocomposites. Here we study the influence of ionic moieties of the polymer template on the formation of inorganic nanocomposites by self-assembly of thermo-reversible ionic block-copolymer gel structures, a bottom-up approach that has been reported by us with cationic and Pluronic block-copolymer gels [6]. Further, along with other characterization methods, we present nuclear magnetic resonance (NMR), scattering, and electron microscopy results that support the structural picture of the polymer-inorganic nanocomposite superstructure.

6.3 Materials and Methods

All materials used were obtained from either Sigma Aldrich or Fisher Scientific and were of laboratory grade and purity.

Pentablock copolymer synthesis. Ionic pentablock copolymers were synthesized by atom transfer radical polymerization (ATRP). First, a cationic pentablock copolymer with poly(diethylaminoethylmethacrylate) (PDEAEM) side chains was synthesized by ATRP as described earlier [18]. This was followed by betanization of the tertiary amine groups of the side chains with propanesultone, to form the zwitterionic pentablock copolymer (PentaPZ). Its structure is shown in Scheme 6.1. In a typical reaction, pentablock polymer (6 g, 0.03 mmol) and 1, 3-propanesultone (30 g, 0.3 mmol) were dissolved in dry THF. The mixture was then reacted at 40 ^{o}C under argon for 2 days with continuous stirring. The reaction mixture was then precipitated with diethyl ether and vacuum-dried.

The structure of the anionic pentablock copolymer (PentaPAA) is shown in Scheme 6.2. For its synthesis, first the Pluronic macroinitiator was prepared as reported previously [18]. Difunctional Pluronic macroinitiator (8 g, 0.06 mmol), copper bromide (0.1885 g, 0.06 mmol), and toluene (50 mL) were added to a flask, and the solution was mixed well by stirring for 15 min. A small amount of copper was added to the reaction to enhance the stability of the Cu(I)/Cu(II) equilibrium. The flask was purged with Argon for 5 min. Tert-butyl acrylate (2.8 g, 2.1 mmol) and N-ppm ligand (0.37 g, 0.12 mmol) were added using a syringe. The mixture was freeze-pumped/thawed three times. The reaction was then carried out at 65 ºC in an oil bath overnight. The reaction mixture was then diluted in methylene chloride, passed through a short alumina column to remove the copper catalyst, and was rotary-evaporated. The remaining mixture was reprecipitated in *n*-heptane and dried under vacuum. Finally, the synthesized acrylate polymer was hydrolyzed with THF and trifluoro acetic acid (TFA) (20% v/v) mixture by stirring overnight. The mixture was precipitated in *n*-heptane and the acrylic acid polymer was isolated after vacuum-drying.

Pentablock Copolymer Characterization. Solution NMR measurements were performed on a Varian VXR400 spectrometer, GPC measurements using PLgel columns from Polymer Laboratories, to determine the composition and molecular weights, respectively, of the block copolymers. Simple tube inversion was used to find the gelation temperature. Titration measurements were carried out using a Corning 313 pH-temperature meter at room temperature to find the pK_a and *iep* values, and differential scanning calorimetry (DSC) in a thermal analysis DSC instrument Q 20 was used to find the critical micellization temperatures of the copolymer solutions. Details on these measurements are given in the supporting information (see Appendix A).

Pentablock-Calcium Phosphate Nanocomposite Synthesis. The calcium phosphate-polymer nanocomposite gel was synthesized using soluble calcium and phosphate salts, along the lines of the following reaction:

$$Ca(NO_3)_2 + (NH_4)_2HPO_4 + 2H_2O \rightarrow CaHPO_4{\cdot}2H_2O + 2(NH_4)NO_3 \qquad (1)$$

The following procedure was used: 2.9 g PentaPAA copolymer was mixed with 5.0 mL of 4.0 M $Ca(NO_3)_2$ in 25 *mM* tris-HCl solution. This solution was kept refrigerated overnight (at ~1 ^oC). Then, 3.0 mL of 4.0 *M* $(NH_4)_2HPO_4$ in 25 *mM* tris-HCl solution was added. The polymer content of the mixture was approximately 27% by weight. The mixture was allowed to equilibrate for 1.5 days in the refrigerator. Then the sample was aged at room temperature for 2 days, resulting in a hydrogel sample at pH ≈ 5 (this sample is referred to as PentaPAA27-5). A similar procedure was followed to obtain PentaPAA36-5, where the numbers 36 and 5 again refer to wt% of the polymer and pH of the gel, respectively. For the zwitterionic PentaPZ copolymer, an organic-inorganic hydrogel with a polymer concentration of approximately 46 wt% (PentaPZ46-5) was produced in a similar fashion.

Characterization Methods. Various experiments were performed to study the structural features of the polymer-based nanocomposite. Solid-state NMR can prove nanocomposite formation and provide information regarding the size of inorganic nanoparticles as well as their composition. SAXS and SANS can determine the ordering in the gels; due to the large electron-density contrast between the organic and inorganic components, SAXS has a higher sensitivity on the structure of the inorganic phase while SANS probes mainly the structure of the polymer phase by utilizing the large contrast between ^{1}H and ^{2}H in the polymer and D_2O, respectively [5]. TEM analysis illustrates the size of the precipitated nanosize calcium phosphate particles and helps characterize them. XRD was used to identify the crystalline phases of the inorganic component. TGA measurements yielded the percentage of inorganic material in the nanocomposite. Details of the experimental parameters and the sample preparation for these techniques can be found in the supporting information (see Appendix A).

Thermogravimetric analysis (TGA) was performed with a Perkin-Elmer thermogravimetric analyzer (Perkin-Elmer, TGA 7, Downers Grove, IL). Scanning transmission electron microscopy (STEM) images were captured on a JEOL 1200EX II (Japan Electron Optic Laboratories, Peabody, MA) and FEI-Tecnai G^2-F20 (FEI Inc., Hillsboro, OR) scanning transmission electron microscope equipped with an energy dispersive X-ray spectrometer EDX (EDX Inc., Mahwah, NJ). The latter instrument was also used for high resolution TEM examination. Wide-angle X-ray diffraction patterns were obtained using a Θ-Θ X-ray diffractometer (Scintag, XDS-2000, Cupertino, CA) operating at 45 kV. SAXS measurements were performed at the 12-ID beam line at the Advanced Photon Source in Argonne National Laboratory, while SANS measurements were carried out using the time-of-flight small-angle neutron diffractometer (SAND) at IPNS at Argonne National Laboratory. Solid-state NMR experiments were run using a Bruker DSX400 spectrometer (Bruker-Biospin, Rheinstetten, Germany) at 400 MHz for ^{1}H and 162 MHz for ^{31}P. Rheological experiments were carried out using an ARES rheometer (TA Instruments, New Castle, DE).

6.4 Results and Discussion

Polymer Characterization. The molecular weight of the cationic $PDEAEM_5$-PluronicF127-$PDEAEM_5$ pentablock copolymer, synthesized by ATRP, was 14,570 by GPC with a narrow molecular weight distribution (PDI < 1.1). The cationic pentablock copolymer was subsequently betanized with 1,3-propanesultone in dry THF to give the PentaPZ zwitterionic polymer and the composition verified by solution NMR. The molecular weight of the PentaPAA polymer was 17538 with a narrow molecular weight distribution (PDI < 1.2).

These PentaPZ and PentaPAA copolymers exhibit micellization (see supporting information in Appendix A) and thermo-reversible gelation due to the PPO block (Figure 6.1 and Figure S1, supporting information in Appendix A) and impart pH-dependent solubility due to their ionic blocks. The zwitterionic pentablock copolymer exhibits pH sensitivity over a wide pH range from pH ≈ 2-11 due to the sulfobetaine blocks, with an isoelectric point around pH 6.3, where the concentrations of positive and negative charges are equal. The anionic pentablock copolymer, on the other hand, is hydrophilic above its *pKa* (6.3) due to the acrylic acid side chains.

Formation of Organic-Inorganic Nanocomposites. The thermogravimetric analysis of the CaP/hydrogel samples (see Figure S2, supporting information) showed approximately 30 wt% inorganic for the dried hydrogels. These inorganic fractions are significantly larger than in our previous studies of calcium phosphate formation on cationic and polar templates, [6] which yielded 6 or 15 wt% of inorganic component. The TGA results given are based on the mass of the dried hydrogel at ~200 °C as 100%.

NMR Proof of Nanocomposite Formation. Figure 6.2 shows ^{31}P solid-state NMR spectra (thin lines) of the PentaPAA27-5, PentaPAA36-5 and PentaPZ46-5 nanocomposites and three related model compounds. The thick lines are the corresponding spectra of the nonprotonated phosphate (PO_4^{3-}) components, obtained after recoupling of the $^{31}P\{^1H\}$ dipolar interaction for two rotation periods. Based on their chemical shifts, the peaks in Figure 6.2b can be tentatively assigned to brushite (large peak) and hydroxyapatite [19]. The spectra of the other samples contain several components that will be discussed below. The one-dimensional ^{31}P NMR spectra shown in Figures 6.2a-c confirm that solid phosphates are present in the samples, but do not reveal whether they are part of nanocomposites. This can be achieved instead by two-dimensional ^1H-^{31}P heteronuclear correlation NMR experiments with ^1H spin diffusion, where cross peaks between polymer protons and inorganic phosphate prove the intimate contact between the organic and inorganic phases that is the characteristic of nanocomposites [20, 21].

Such cross peaks are not observed at short spin-diffusion times, where the phosphate "sees" only the nearest protons, i.e., those in the inorganic phase. In a nanocomposite, the polymer proton peaks appear within tens to hundreds of milliseconds of spin diffusion. The corresponding dramatic change in the heteronuclear correlation spectra is indeed observed in PentaPAA36-5; see Figure 6.3. Figure 6.3a shows contour plots of the 2D spectra for 0.05 ms, 5 ms, and 50 ms. Cross sections along the ^1H dimension, taken at 2.5 ppm in the ^{31}P dimension, are shown in Figure 6.3b. Within 50 ms, the polymer proton (OCH_2 and CH_3) peaks have become completely dominant.

The spectra of Figure 6.3 were acquired without homonuclear decoupling in the ^1H dimension, which makes the experiment simple to run (analogous to a WISE experiment with hypercomplex data acquisition) [22]. Homonuclear decoupling is not necessary here since the high mobility of the PPO and of parts of the PEO blocks results in sharp ^1H peaks. The application of this method to PentaPAA27-5, see Figure 6.3c and 6.3d, highlights the advantage of detecting the sharp polymer peaks, even when they are small, on the background of the broader proton peaks of the inorganic phases. In this material, the polymer peaks are observed at the main 1.4 ppm ^{31}P peak only after much longer spin-diffusion times than those in PentaPAA36-5, indicating larger domain sizes of the brushite component. In contrast, Figure 6.3d shows that the hydroxyapatite component resonating near 2.8 ppm in the ^{31}P dimension undergoes fast spin diffusion from the polymer, within 50 ms, but its signal is weak and noisy due to relatively inefficient cross polarization of its nonprotonated PO_4^{3-} groups.

The protons with the strongest homonuclear dipolar couplings are not visible in the "WISE" spectra of Figure 6.3, due to their dipolar broadenings by many tens of ppm. This potential limitation is eliminated in ^1H-^{31}P HetCor experiments with ^1H homonuclear decoupling [20, 21]. Figure 6.4 demonstrates how, in PentaPAA36-5, the signals of a relatively small brushite component, with strong dipolar couplings between waters of crystallization and POH protons, become visible in this version of the experiment. The sharpness of the peaks in both dimensions highlights the crystalline order of this component. In the cross section at the ^{31}P position of the brushite peak, 1.4 ppm, spin diffusion from the polymer is observed, but it is not complete within 50 ms, as witnessed by the remaining HPO_4 peak at 11 ppm still seen after 50 ms. Application of the experiment with homonuclear decoupling to PentaPZ46-5 shows only slow spin diffusion from the polymer to the ^{31}P sites with sharp peaks (see Figure S4 in the supporting information given in Appendix A), but the low broad component centered at –1.8 ppm, which in spite of its low peak height accounts for 66% of the phosphate, exhibits close contact with the polymer.

For samples with spin-diffusion equilibration within 50 ms, a safe upper limit of 100 nm for the size of the domains can be estimated from the spin-diffusion analysis, as outlined in the Supporting Information. However, the accuracy of this approach is limited in the present systems since important parameters, such as the diffusion coefficients, are not known with sufficient accuracy or are difficult to include in spin-diffusion simulations, such as different proton densities in the organic and inorganic components. Quantifying the thickness of the smaller inorganic particles by ^{31}P{^{1}H} HARDSHIP NMR and the supramolecular structure by SAXS, with component fractions and domain-size estimates from NMR, is a more promising approach, taken below.

Domain Thickness from ^{31}P{^{1}H} HARDSHIP NMR. The ^{1}H spin-diffusion method requires that there are protons within the inorganic phase, at a significant concentration. If that is not the case, for instance in hydroxyapatite, we can use a complementary method based on the strongly distance-dependent dipolar couplings between ^{31}P in the nanoparticles and ^{1}H in the polymer matrix. The couplings of ^{31}P to dispersed protons within the inorganic phase, which would interfere with this approach if simple $^{31}P\{^{1}H\}$ REDOR [23] was used, are refocused in the recently introduced $^{31}P\{^{1}H\}$ HARDSHIP method [24]. The HARDSHIP dephasing curve reflects the surface-to-volume ratio of the inorganic phase, with an accuracy that is significantly greater than that of ^{1}H spin diffusion in nanocomposites. $^{31}P\{^{1}H\}$ HARDSHIP dephasing in plates of 4 nm thickness or spheres of 12 nm diameter can be observed quite easily [24].

Figure 6.5a shows $^{31}P\{^{1}H\}$ HARDSHIP dephasing of hydroxyapatite in PentaPAA27-5 measured at 13 kHz MAS with the optimum HARDSHIP pulse sequence [24]. The dephasing can be fit by assuming layers of 1.8 nm thickness or spheres of 6 nm diameter. The dephasing of the major component in PentaPAA36-5, Figure 6.5b, yields a similar result but with a larger uncertainty due to the relatively short T_{2H} of the protons within the inorganic component, which requires a significant correction of the simulation curves at longer recoupling times [24]. Experiments on brushite, $CaHPO_4 \cdot 2H_2O$, showed that due to its high proton density, the homonuclear dipolar couplings are too strong and the T_{2H} is too short for HARDSHIP to work well.

SAXS and SANS: Evidence of Templating. SAXS and SANS provide direct information on the morphology and ordering of structures in the gels and nanocomposites. In SANS, the contrast is due to the nuclear scattering length difference between the D_2O and the polymer/inorganic phase. As shown in Figure 6.6a, the self-assembled zwitterionic PentaPZ46-5 copolymer gels both with and without calcium phosphate display distinct first-order diffraction peaks in SANS data. The second-order peak position in relation to the first order peak (Q*) in the neat polymer gel clearly indicates hexagonal close packing of cylinders in the ordering of micelles. However, in the case of the nanocomposite gel, the first-order diffraction peak broadens, making the second-order peak less visible, presumably due to disorder introduced by the templating of calcium phosphate on the polymer phase.

The SAXS data in Figure 6.6b show similar diffraction peaks both without and with calcium phosphate. The peak intensity is greatly increased in the composite, which proves that a significant fraction of the high-electron density inorganic phase is templated by the block copolymer micelles and thus enhances their structure factor. The diffraction peaks are observed at Q/Q* values of $1, \sqrt{3}, \sqrt{7}, \sqrt{12}$, indicating hexagonal close packing of rod-like polymer micelles consistent with the SANS data. With use of the Q* value for the gels with cylinder phase the lattice spacing $d = (4/3)^{½} (2\pi/Q^*)$ can be determined. Furthermore, in the low Q region of the SAXS data the scattering intensity I(Q) varies as $Q^{-1.5}$, suggesting that both the neat and the nanocomposite gels have rod-like structures, in agreement with the TEM data below.

The lattice spacings (the characteristic distance between the centers of the cylinders) from the SANS data of the neat and the calcium phosphate templated PentaPZ46-5 polymer gels were around 18.5 nm, indicating little effect of the inorganic component on the superstructure. This may be due to the relatively small inorganic volume fraction in the nanocomposite. Similar trends were observed in the SANS data for PentaPAA27-5 (see Figures 6.6c and d) and PentaPAA36-5 (see Figure 6.6e and f) polymer-gel nanocomposites. However, in contrast to the PentaPZ46-5 gels, the PentaPAA gels exhibit sharper peaks in the SANS patterns, indicating a higher level of ordering. Further, the PentaPAA36-5 neat polymer show diffraction peaks at Q/Q* values of 1, $\sqrt{3}$, 2, $\sqrt{8}$, indicating FCC packing of spherical polymer micelles consistent with the SAXS and TEM data. With the use of the Q* value for the gels with FCC structure, the lattice spacing $d = 2\pi/Q^*$ can be determined. The *d*-spacings in the gel structures of PentaPAA27-5 and PentaPAA36-5 are around 16 nm, but there was a slight reduction in the *d*-spacing in the presence of calcium phosphate when compared to the neat polymers. In the case of PentaPAA27-5 the polymer phase has ionic character and the broadening of the peak in the SANS pattern for the neat polymer gel might be due to electrostatic repulsion between the micelles, leading to a looser packing of particles. The sharper peaks in the presence of calcium phosphate might be due to charge neutralization in the PentaPAA gels, leading to more ordered dense packing.

The SAXS data show relatively low intensity for the neat PentaPAA polymer gels due to low X-ray contrast between polymer and water. In the presence of the inorganic component, higher scattering intensity was again observed for PentaPAA36-5 with a scattering peak corresponding to a *d*-spacing of ~15 nm, proving templating of calcium phosphate on the polymer micelles. Furthermore, the SAXS curves of both PentaPAA nanocomposites show power-law scattering with a higher exponent (~4) in the low Q region. This suggests the presence of larger inorganic aggregates with 3-dimensional morphology. The higher power-law exponent in the case of PentaPAA27-5 when compared to PentaPAA36-5 suggests the presence of larger calcium phosphate aggregates in the former, in agreement with the NMR data. It is interesting to note that the small-angle upturn in the SAXS curves could be attributed not just to larger particles but alternatively to a superstructure of the mineralized micelles, such as 0.2 μm diameter aggregates. The TEM data show that larger inorganic particles are indeed present. The dried nanocomposite gel sample exhibits SAXS patterns similar to those of the gel samples. However, a small shift in the scattering patterns toward larger Q-values (smaller spacings) was observed, which is expected due to the removal of water.

TEM. Transmission electron micrographs of 5 wt% PentaPAA and PentaPZ polymers prepared by diluting the neat gels in deionized water (see Figures 6.7a and 6.8a) revealed approximately 15 nm diameter spheroidal micelles, in agreement with the SAXS and SANS results and our previous studies [6]. Figure 6.7b shows a TEM image of PentaPAA36-5 nanocomposite gel diluted to 5 wt% polymer. According to STEM-EDX measurements, both calcium and phosphate (dark regions in Figure 6.7b) are present around the micelles. Further images are shown in Figure S6 of the supporting information in Appendix A. The atomic ratio of calcium to phosphorus for PentaPAA27-5 was found to be about 1, quite close to that of brushite (Ca/P=1) and in agreement with XRD and NMR. For PentaPAA36-5, in addition to regions with Ca/P=1, some areas with a Ca/P ratio of 1.9 were also observed, indicating there is another calcium phosphate phase other than brushite, consistent with NMR. Further, Figure 6.7c shows a TEM micrograph of plate-like calcium phosphate crystallites collected from the bottom of the redissolved polymer in PentaPAA36-5, consistent with the larger calcium phosphate particles inferred from spin-diffusion NMR. The inorganic coating of some of the micelles can be seen more clearly in Figure 6.7d, which displays a high-angle annular dark field (HAADF) image of PentaPAA27-5.

Figure 6.8 illustrates TEM micrographs of PentaPZ polymer PentaPZ46-5 nanocomposite. The neat polymer (5 wt% in deionized water) revealed the typical ~15 nm diameter spherical micelles (Figure 6.8a). By contrast, the morphology observed for the PentaPZ46-5 nanocomposite is quite different (see Figures 6.8b-d), exhibiting rod-like calcium phosphate nanoparticles. The presence of Ca and P was confirmed by STEM-EDX and the atomic Ca/P ratio was found to be around 1.0 for PentaPZ46-5.

XRD Analysis. Figure 6.9 shows the X-ray diffraction patterns of the hydrogel and vacuum-dried hydrogel samples, respectively. As seen from Figure 6.9b, the X-ray diffraction pattern of PentaPAA27-5 revealed the typical reflections for crystalline synthetic brushite ($CaHPO_4 \cdot 2H_2O$) (ICDD card #09-0077). XRD of PentaPAA36-5 showed only broad reflections, indicating that the calcium phosphate phase might be amorphous, nanocrystalline, or a minor volume fraction compared to the polymer (Figure 6.9c). Moreover, the characteristic peaks of natural brushite (ICDD card #11-0293), a mineral normally only found in caves [25], were observed for PentaPZ46-5, shown in Figure 6.9a, and this is similar to our previous results with PDEAEM-modified Pluronic F127 pentablock gel composite as templates [6].

After vacuum-drying of the hydrogel samples, the natural brushite peaks disappeared for PentaPZ46-5, while weak HAp peaks appeared in addition to synthetic brushite peaks for PentaPAA27-5 (see Figures 6.9d and 6.9e), in agreement with NMR. Further, sharp peaks of brushite and sodium calcium hydrogen phosphate were observed for PentaPAA36-5 after drying (see Figure 6.9f). With use of the Scherrer equation, brushite crystal sizes of > 40 nm and > 45 nm were estimated from the widths of the Bragg peaks for the vacuum-dried PentaPAA36-5 and PentaPAA27-5, respectively.

HRTEM. The characteristics of the crystalline calcium phosphate phases in the hydrogel samples were investigated using high-resolution transmission electron microscopy (HRTEM), as shown in Figure 6.10. Nanocrystalline particles within the amorphous polymer matrix are clearly seen from the HRTEM images (marked by arrows in parts (a), (c) and (d) of Figure 6.10). The insets in Figure 6.10b-d show fast Fourier transform (FFT) patterns of the full area of the HRTEM images. Arrows on the FFT pattern indicate the diffracted intensity from the nanocrystals within the amorphous polymer matrix. The measured lattice spacing for PentaPAA36-5 in Figure 6.10b is in good agreement with the distance between (041) planes in synthetic brushite (compared with ICDD card #09-0077), consistent with XRD and NMR of PentaPAA36-5. Figure 6.10c presents a HRTEM image of PentaPZ46-5 and the lower inset in Figure 6.10c shows the filtered inverse-FFT image of an isolated nanocrystal, calculated by masking all but the spots shown by arrows in the FFT pattern. Although the existence of crystalline phases in the diluted PentaPZ46-5 hydrogel was confirmed by HRTEM, these nanocrystals could not be identified as one of the calcium phosphate phases with certainty since the measured lattice spacings did not show any characteristic low index planes. The HRTEM micrograph in Figure 6.10d confirms the existence of nanocrystalline brushite in PentaPAA27-5, in agreement with XRD and NMR. The FFT pattern of the nanocrystal shown in the upper inset agrees well with the [100] zone axis of brushite phase.

The size of the nanocrystals detected by HRTEM is on the order of 5-10 nm, which is smaller than the value estimated from XRD. However, it should be noted that HRTEM is sampling a very small volume of the specimen compared to XRD and NMR techniques. Moreover, HRTEM requires a specimen thickness of <50 nm and features contained within the field of view. Therefore, the probability of imaging smaller-than-average nanocrystals is high in HRTEM observations.

NMR Characterization of Calcium Phosphates. Based on ^{31}P NMR peak positions [19, 26] and phosphate protonation (Figure 6.2), the ^{31}P spectrum of PentaPAA27-5 can be assigned to brushite (large peak at 1.4 ppm) and hydroxyapatite (broader band at 2.8 ppm). The assignment is confirmed by the proton peak positions in their ^{1}H-^{31}P spectra without spin diffusion (bottom traces in Figures 6.3c and d): The OH^{-} proton of HAp is detected near 0.5 ppm, while the relatively sharp signals near 11 ppm agrees with that of HPO_4 in brushite from the literature [27]. In ^{1}H-^{31}P HetCor spectra with homonuclear decoupling, the 6.5-ppm ^{1}H signal of waters of crystallization in brushite [27] is also detected. This is fully consistent with the XRD analysis of this sample (see Figure 6.9). Deconvolution of the ^{31}P NMR signal yields a brushite:HAp phosphate ratio of 71:29, with a 5% disordered component counted in the 71% brushite.

The NMR analysis of the two other samples is not so straightforward. Therefore, we have identified further observables, such as the protonation of the phosphates and the number of inequivalent phosphates in the asymmetric unit cell.

HPO_4 versus PO_4 ions. Protonation of the phosphate ions was probed by NMR using simple $^{31}P\{^{1}H\}$ gated decoupling with recoupling for a maximum of two rotation periods. Figure 6.2 compares spectra after 0 (thin line) and $2t_r$ (thick line) of $^{31}P\{^{1}H\}$ recoupling, while Figure S5 in the supporting information (see Appendix A) shows a plot of the peak intensity with recoupling time. The fast signal decay of the sharp peaks in parts (a) and (c) of Figure 6.2 shows that a large fraction of phosphates in PentaPAA36-5 and PentaPZ46-5 are protonated (HPO_4^{2-}). Much slower dephasing is observed in Figure 6.2b, g for the 2.8 ppm signal in PentaPAA27-5, confirming its assignment to hydroxyapatite, and for the broad peak in PentaPZ46-5 centered at –1.5 ppm. The broad signal of PentaPAA36-5 decays with an intermediate rate. The dephasing thus also provides for spectral editing of overlapping signals in all three nanocomposite samples; see Figures 6.2a-c.

Number of Inequivalent Sites from NMR. The spectra of PentaPAA36-5 and PentaPZ46-5 show multiple peaks or shoulders, which might arise from different phases or from different sites in the unit cell of one phase. To distinguish these two situations, we performed ^{31}P 2D exchange experiments with ^{31}P spin diffusion in the mixing time of 2 s, which allows for equilibration on the 2 nm scale. Figure 6.11a shows such a 2D spectrum for PentaPZ46-5. Pronounced cross peaks between the two relatively sharp resonances prove that they belong to sites within one unit cell. The larger area of the left peak and its circular diagonal peak after spin diffusion suggests that these are actually two unresolved peaks, giving a total of three chemically inequivalent sites. The broad band centered on -2 ppm in the DP spectrum (top trace above Figure 6.11a) is not observed in this 2D spectrum due to its short ^{31}P T_1 relaxation time of less than 2 s. The different T_1 relaxation times in themselves prove that the ^{31}P associated with the broad band and the two sharp peaks are not within spin-diffusion contact, i.e., not in the same phase.

^{31}P 2D exchange spectra of PentaPAA36-5 are shown in Figure 6.11b and 6.11c. After a spin-diffusion time of 0.1 s, Figure 6.11b, a diagonal ridge is still visible because the magnetization has not yet equilibrated locally. The ridge has disappeared after 2 s, and ^{31}P spin diffusion between the broad bands with maxima near 1.2 and 4.8 ppm is observed. The difference in the two cross sections displayed above Figure 6.11c shows that the sharp peak at 1.9 ppm corresponds to a phase (crystalline brushite) separate from the major component producing the broad double-peaked intensity.

The number of orientationally inequivalent sites can be estimated by ^{31}P CODEX NMR with ^{31}P spin diffusion. In this experiment, a stimulated echo is detected under magic-angle spinning with recoupling of the chemical-shift anisotropy before and after a mixing time for spin diffusion. For sufficiently long dephasing/rephasing and mixing times, only magnetization remaining on the original ^{31}P site, or on magnetically equivalent sites, contribute to the stimulated echo. In a crystal with Z inequivalent sites in the asymmetric unit cell, the signal thus decays from 1 to 1/Z [28]. Figure 6.12 compares the long-time with the full initial intensity for the three nanocomposite and three model calcium phosphates. The normalized final intensities S/S_0 are plotted in Figure 6.12b. For the model compounds, they mostly match the 1/Z values expected from the known crystal structures. The 1/Z values for PentaPZ46-5 between 1/3 and 1/4 are significantly lower than those for $Ca(H_2PO_4)_2$, confirming that these are different crystal structures in spite of their relatively similar 1D spectra.

6.5 Conclusions

Synopsis of structural findings. Table 6.1 summarizes the results of the composition and other properties of the inorganic components of the nanocomposites obtained from NMR and XRD.

PentaPAA36-5 contains crystalline brushite and a partially disordered phosphate component at a molar ratio of 12:88. The latter has particles of < 2 nm thickness in close proximity with the polymer micelles, while the brushite crystallites are larger.

PentaPAA27-5 contains brushite and hydroxyapatite at a phosphate molar ratio of 71:29, as clearly shown by XRD and various NMR experiments. A 5% disordered HPO_4^{2-} component is counted in the 71% brushite; it might be a surface layer of the nanocrystals. The hydroxyapatite forms a ~1.8 nm thick crystalline partial coating of the polymer micelles, while the brushite is present as larger nanocrystals. While we have found that neat brushite quickly converts into the more stable, dehydrated monetite, the brushite in the nanocomposite appears to be stabilized.

PentaPZ46-5 contains amorphous PO_4^{3-} and crystalline HPO_4^{2-} phosphates at a 66:34 ratio, which have been separated spectroscopically based on their different rates of dephasing in gated-decoupling and in ^{31}P T_1 relaxation experiments (Figures 6.2c and 6.11a). The majority amorphous component has been templated by the polymer micelles, while the crystalline component forms crystallites of >50 nm width. The crystalline calcium phosphate contains at least two, probably three chemically inequivalent and at least three magnetically inequivalent HPO_4^{2-} ions, but it has not been assigned to a specific modification yet; it is not a sodium calcium phosphate since the sodium concentration in this sample (PentaPZ46-5) is particularly low. XRD does not show many distinctive peaks to help with the assignment. It is reasonable to propose that this unusual phosphate phase has been nucleated by the zwitterionic polymer, highlighting the influence of the polymer end block on the calcium phosphate crystallization.

6.6 Acknowledgments

This work was supported by the U.S. Department of Energy under contract number DE-AC02-07CH11358. This work benefited from the use of IPNS and APS, funded by the U.S. DOE, Office of Science, and Office of Basic Energy Science under contract DE-AC02-06CH11357. We wish to thank Matthew J. Kramer for helpful discussion of the TEM results.

Supporting Information Available. Details on the experimental techniques and associated sample preparation, further materials characterization, and additional NMR as well as TEM data are given in the supporting information in the Appendix A.

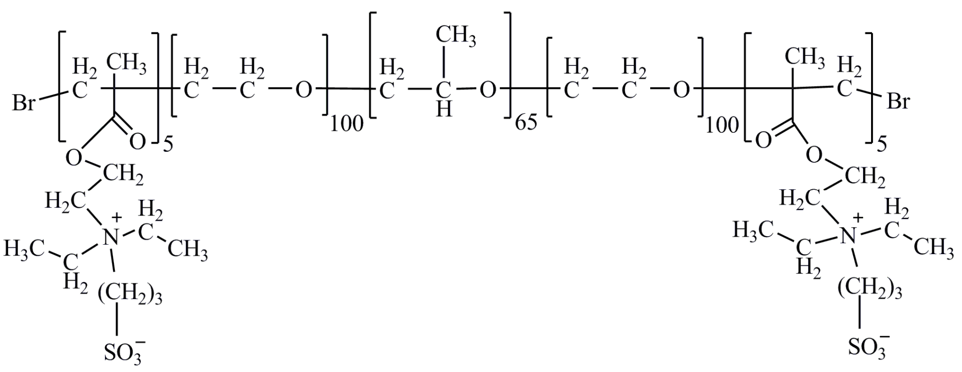

Scheme 6.1. Structure of the zwitterionic pentablock copolymer (PentaPZ).

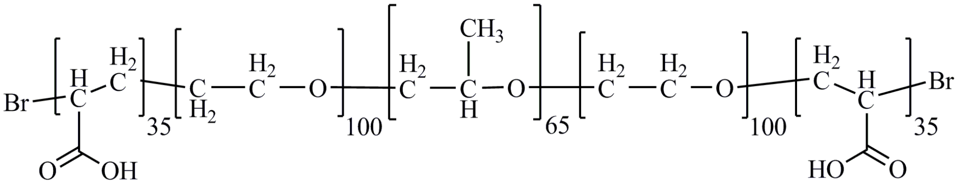

Scheme 6.2. Structure of the anionic pentablock copolymer (PentaPAA).

Table 6.1. Parameters of the synthesized materials from solid-state NMR results and the corresponding NMR methods used.

Sample	NMR method				
	inorganic fractions (^{31}P DP) ±3%		inorganic protons and their concentration (WISE & HETCOR)	inequiv. phosphates in unit cell (CODEX)	thickness *d* (WISE, HETCOR & HARDSHIP)
PentaPAA 36-5	partly disordered	88%	sparse HPO_4 low conc.	unknown	*d* = 1.6 nm
	brushite $(HPO_4)^{2-}$	12%	HPO_4 andH_2O high conc.	2	*d* ≥ 20 nm
PentaPAA 27-5	HAp $(PO_4)^{3-}$	29%	OH^-, H_2O, and HPO_4 low conc.	6	*d* = 1.8 nm
	brushite $(HPO_4)^{2-}$	71%	HPO_4 and H_2O high conc.	2	50 nm < *d* < 1μm
PentaPZ 46-5	disordered $(PO_4)^{3-}$	66%	H_2O low conc.	N/A	*d* < 20 nm
	crystalline $(HPO_4)^{2-}$	34%	H_2O and HPO_4 high conc.	3 or 4	50 nm < *d* < 1μm

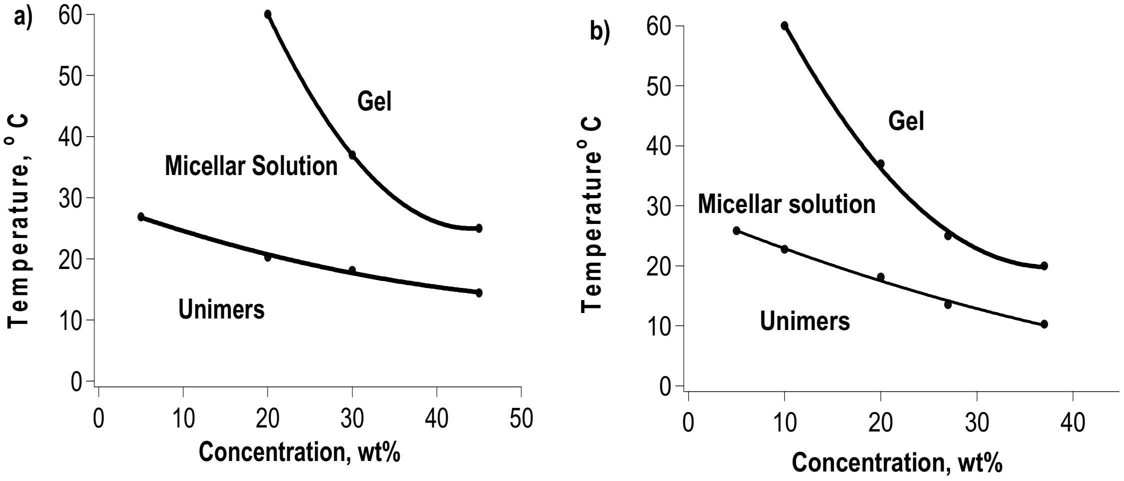

Figure 6.1. Phase diagrams of (a) PentaPZ (Mn, 15000), (b) PentaPAA (Mn 17538, PDI 1.196) pentablock copolymers obtained from DSC thermographs and simple gel inversion.

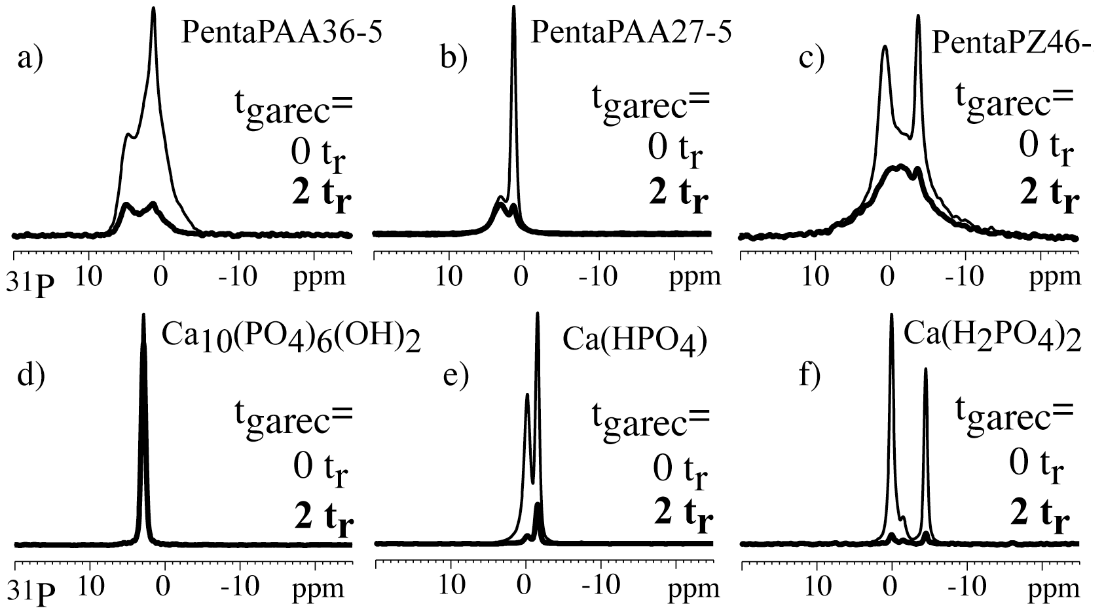

Figure 6.2. ^{31}P MAS NMR spectra (with direct polarization) of the synthesized polymer-calcium phosphate composites and model compounds (thin lines). Corresponding spectra with two rotation periods of ^{1}H-^{31}P recoupling are also shown (thick lines). (a) PentaPAA36-5; (b) PentaPAA27-5; (c) PentaPZ46-5; (d) hydroxyapatite; (e) monetite; (f) calcium dihydrogen phosphate. Spinning frequency: 7 kHz.

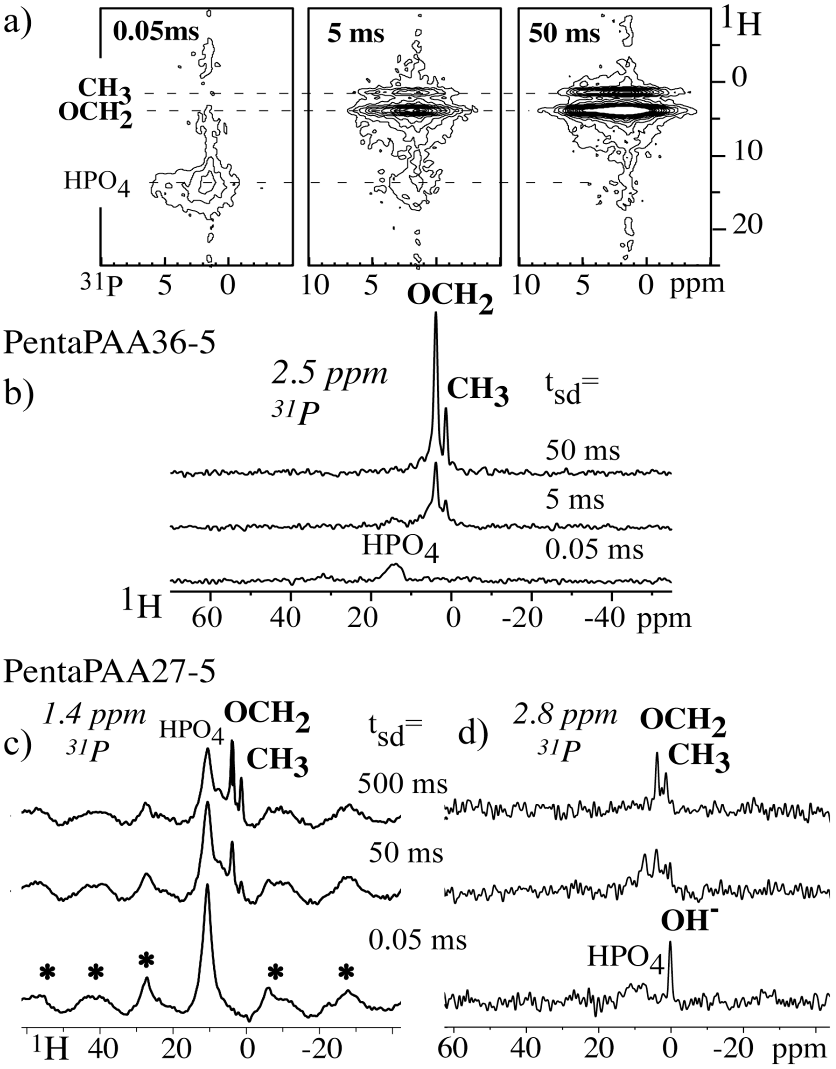

Figure 6.3. (a) 2D "WISE" ^{1}H-^{31}P NMR spectra of PentaPAA36-5 with spin diffusion mixing time (t_{sd}) of 0.05, 5, and 50 ms. (b) Cross sections from the 2D spectra in (a) at 2.5 ppm ^{31}P. (c, d) Cross sections from 2D "WISE" spectra of PentaPAA27-5 with spin diffusion mixing times of 0.05, 50, and 500 ms, taken (c) at 1.4 ppm ^{31}P (spinning sidebands are marked by asterisks in the bottom trace) and (d) at 2.8 ppm ^{31}P.

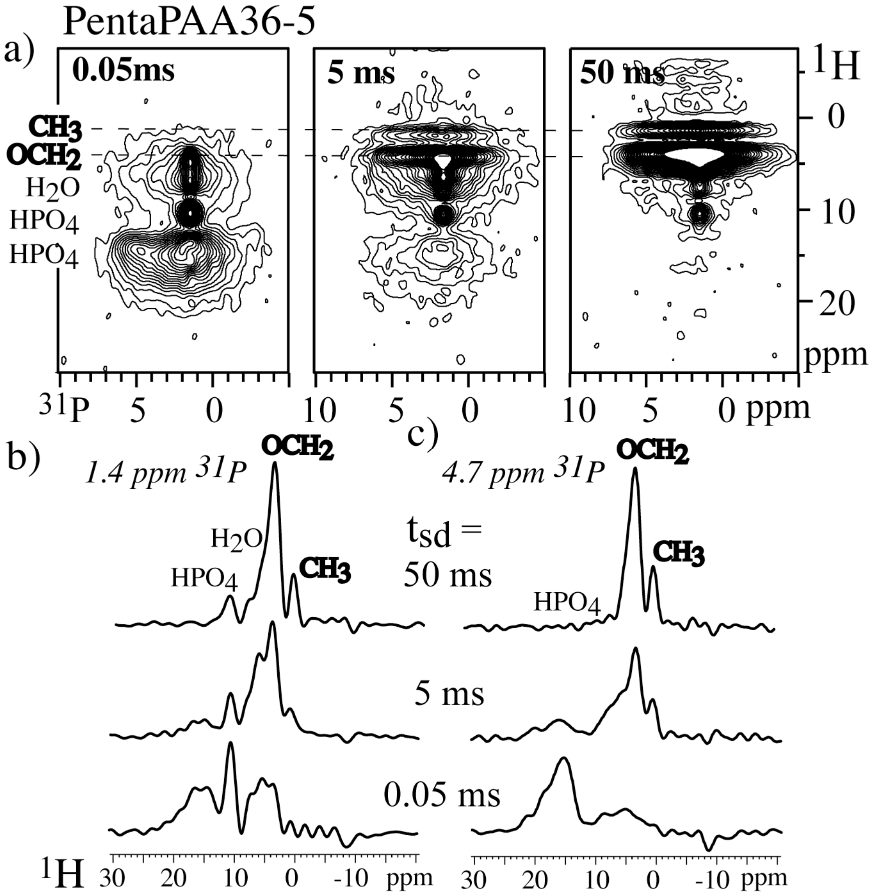

Figure 6.4. (a) Series of 2D ^{1}H-^{31}P HETCOR NMR spectra of PentaPAA36-5 with spin diffusion mixing time of 0.05, 5, and 50 ms. (b) and (c) are cross sections of the 2D spectra at 1.4 and 4.7 ppm ^{31}P, revealing different ^{1}H environments.

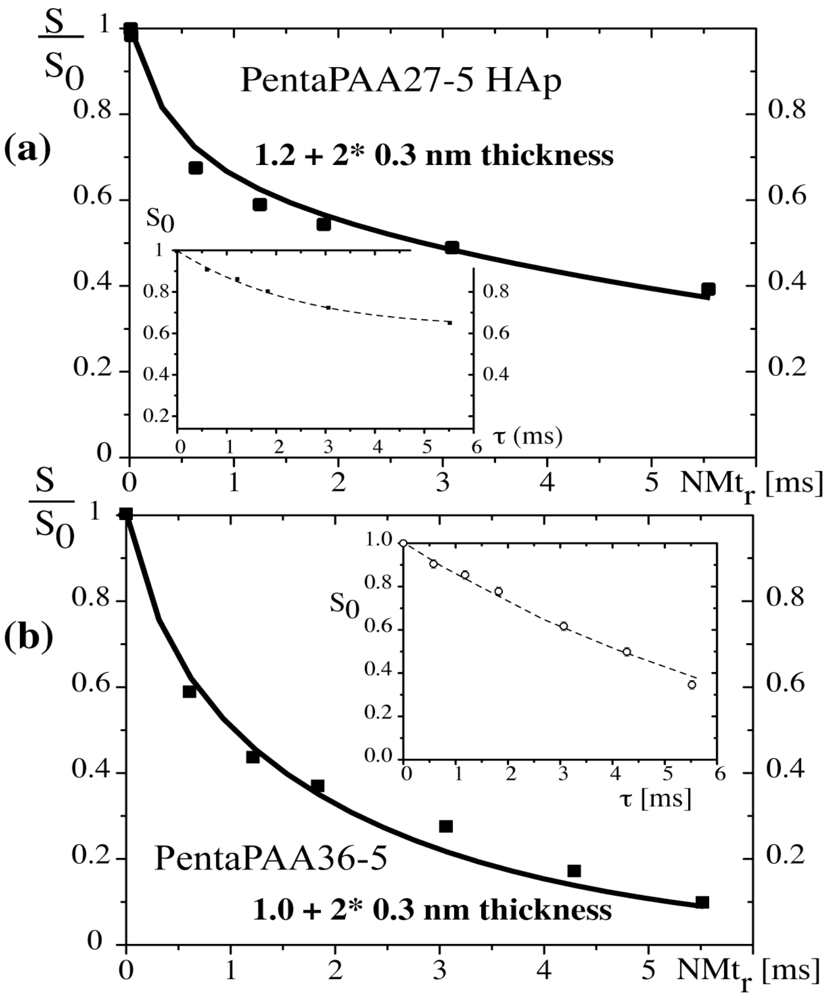

Figure 6.5. $^{31}P\{^{1}H\}$ HARDSHIP NMR dephasing of (a) PentaPAA27-5 at 2.8 ppm ^{31}P and (b) PentaPAA36-5 at 4.5 ppm ^{31}P. Recycle delay: 100 s. Spinning frequency: 13 kHz. Mt_r = 0.15 ms. The inset shows the S_0 decay under ^{1}H decoupling.

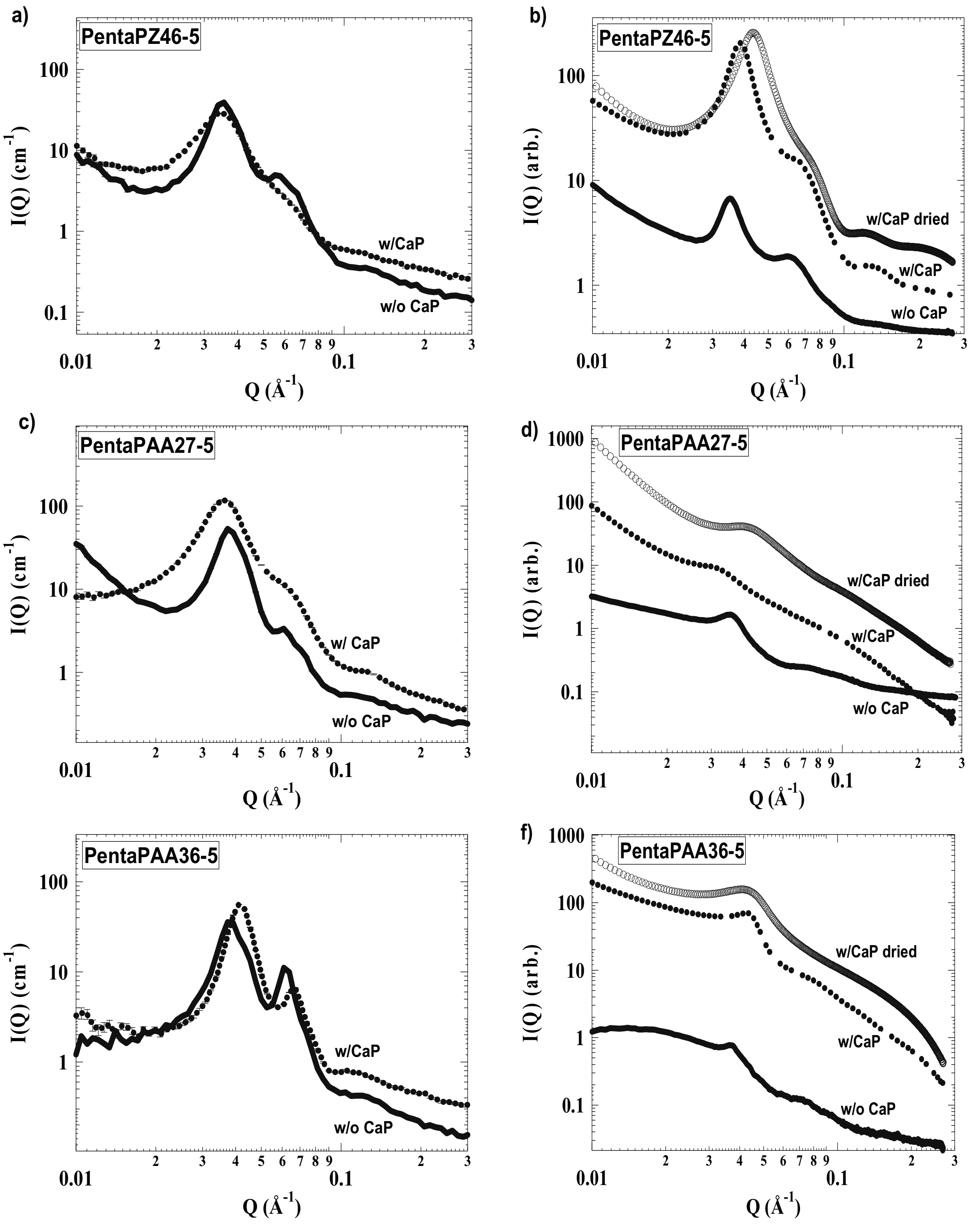

Figure 6.6. SANS and SAXS data of the three nanocomposites: (a) SANS and (b) SAXS of PentaPZ46-5 polymer-inorganic nanocomposites gels at pH 5.0; (c) SANS and (d) SAXS of PentaPAA27-5 polymer nanocomposite gels; (e) SANS and (f) SAXS of PentaPAA36-5 polymer-inorganic nanocomposites gels.

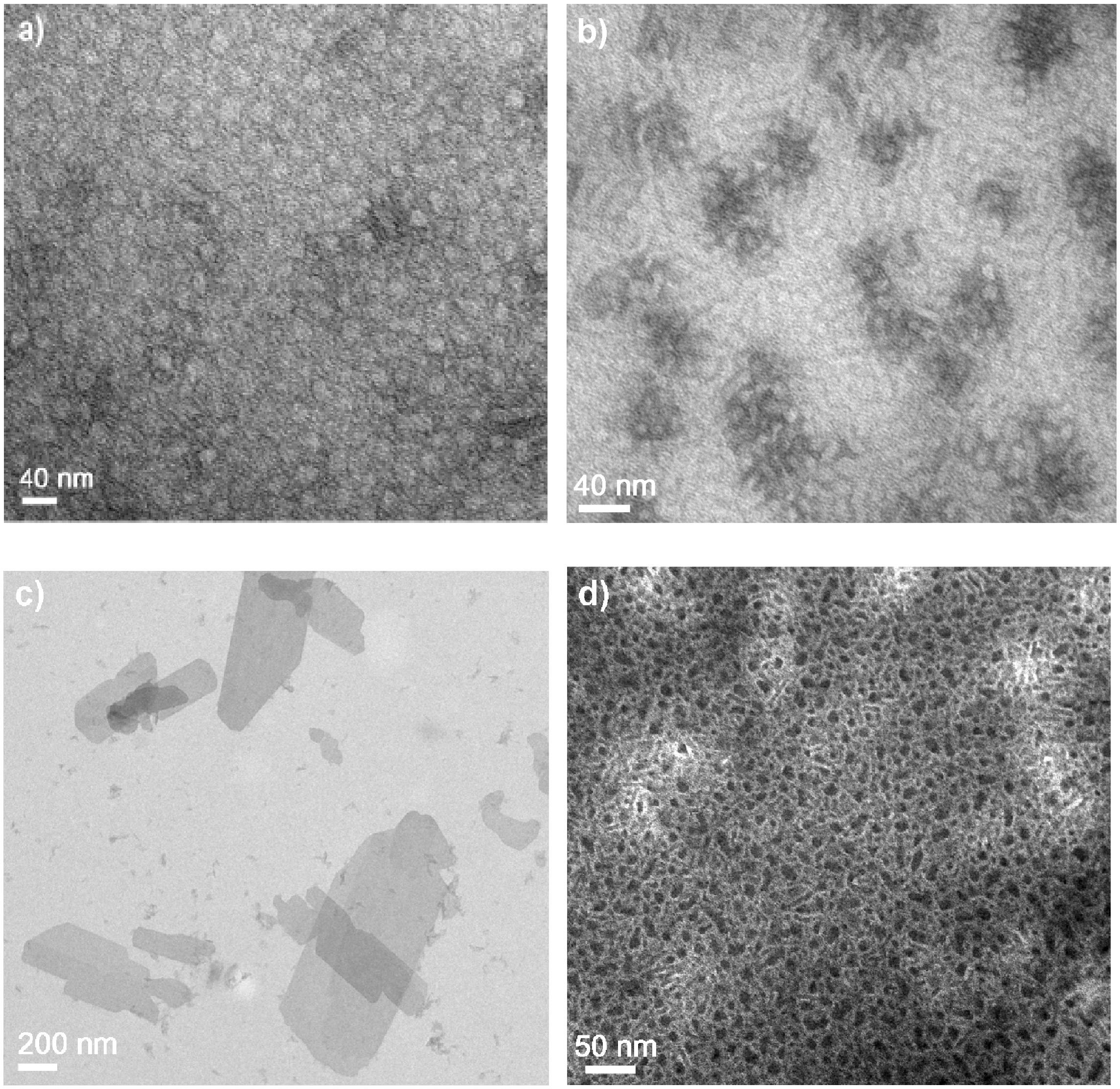

Figure 6.7. Transmission electron micrographs of stained (a) 5 wt% PentaPAA polymer prepared in deionized water, (b) PentaPAA36-5 nanocomposite deposited from a suspension diluted to 5 wt% polymer, (c) crystallites collected from the bottom of the vial containing the diluted PentaPAA36-5 material, and (d) high-angle annular dark field (HAADF) image of PentaPAA27-5 sample. Dark spots: polymer.

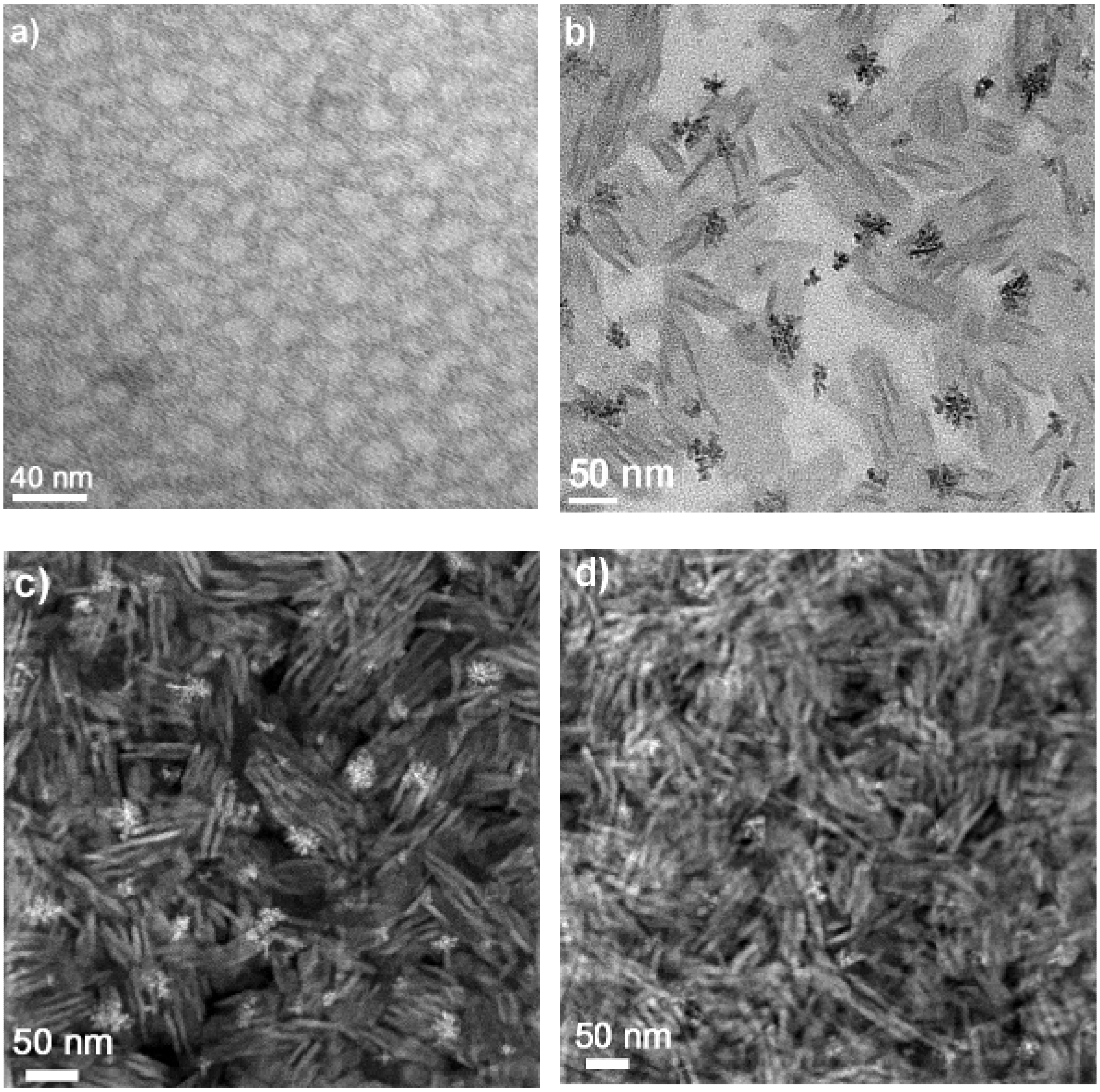

Figure 6.8. Transmission electron micrographs of stained (a) 5 wt% PentaPZ polymer prepared in deionized water, (b) PentaPZ46-5 nanocomposite deposited from a suspension diluted to 5 wt% polymer, and (c, d) HAADF images of the same sample.

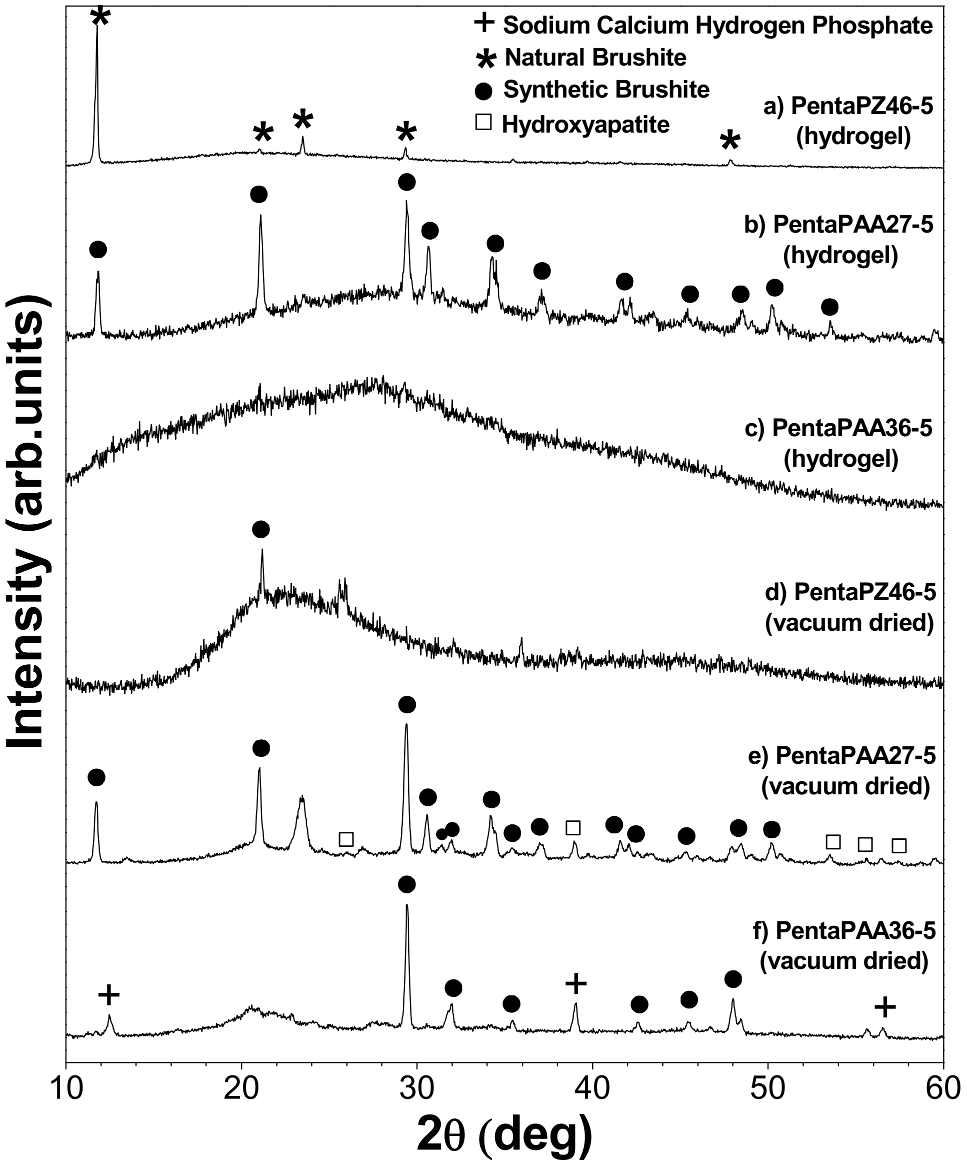

Figure 6.9. X-ray diffraction patterns of as-prepared hydrogel/calcium phosphate nanocomposites and vacuum-dried PentaPZ46-5, PentaPAA27-5, and PentaPAA36-5.

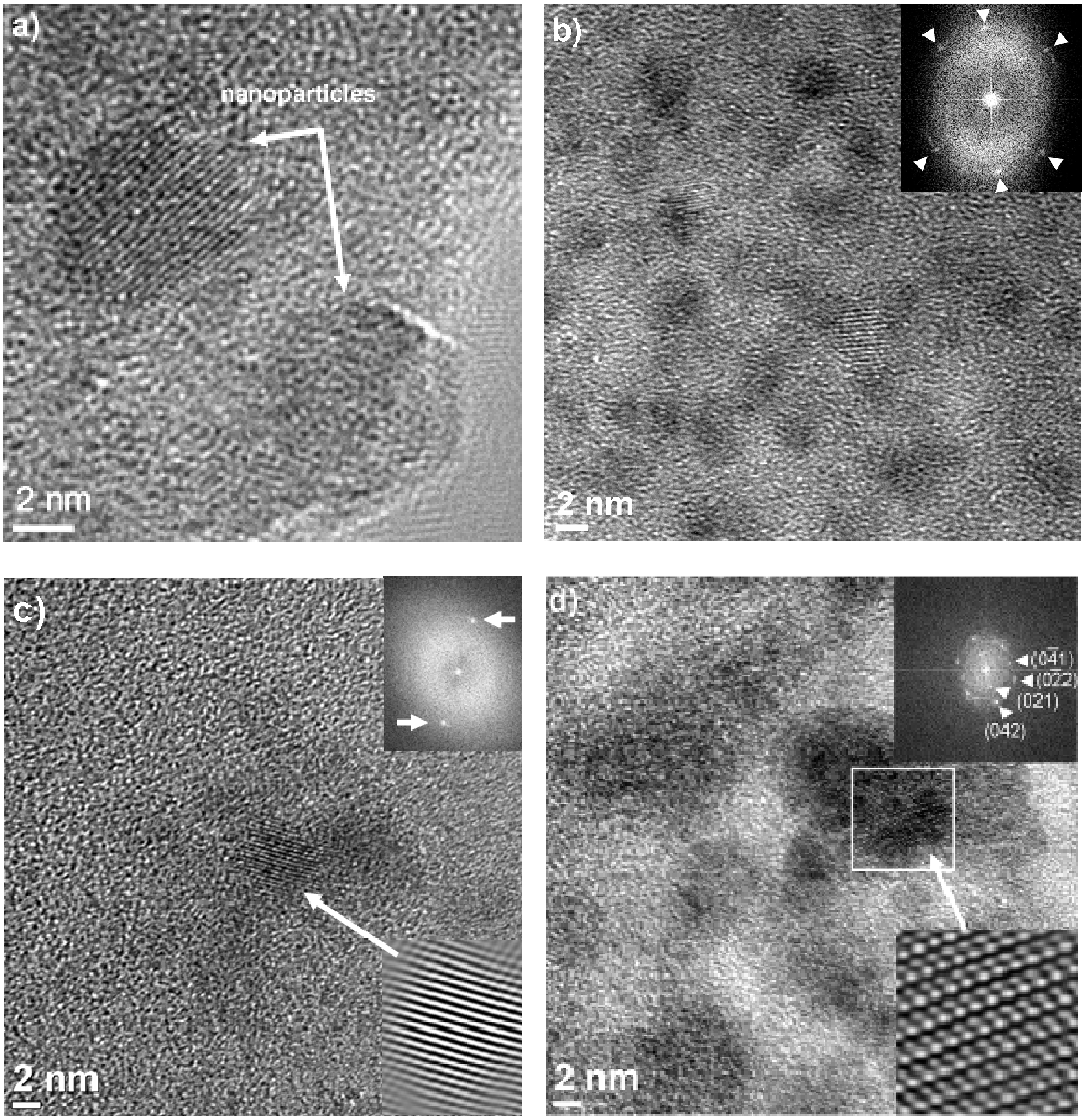

Figure 6.10. HRTEM images of (a, b) PentaPAA36-5, (c) PentaPZ46-5, and (d) PentaPAA27-5. The upper and lower insets show the FFT patterns and filtered inverse-FFT images, respectively. While nanocrystalline brushite was determined to be present in PentaPAA36-5, the type of calcium phosphate phase was not identified with certainty for PentaPZ46-5. The existence of brushite in PentaPAA27-5 was confirmed from the analysis of Figure 10d.

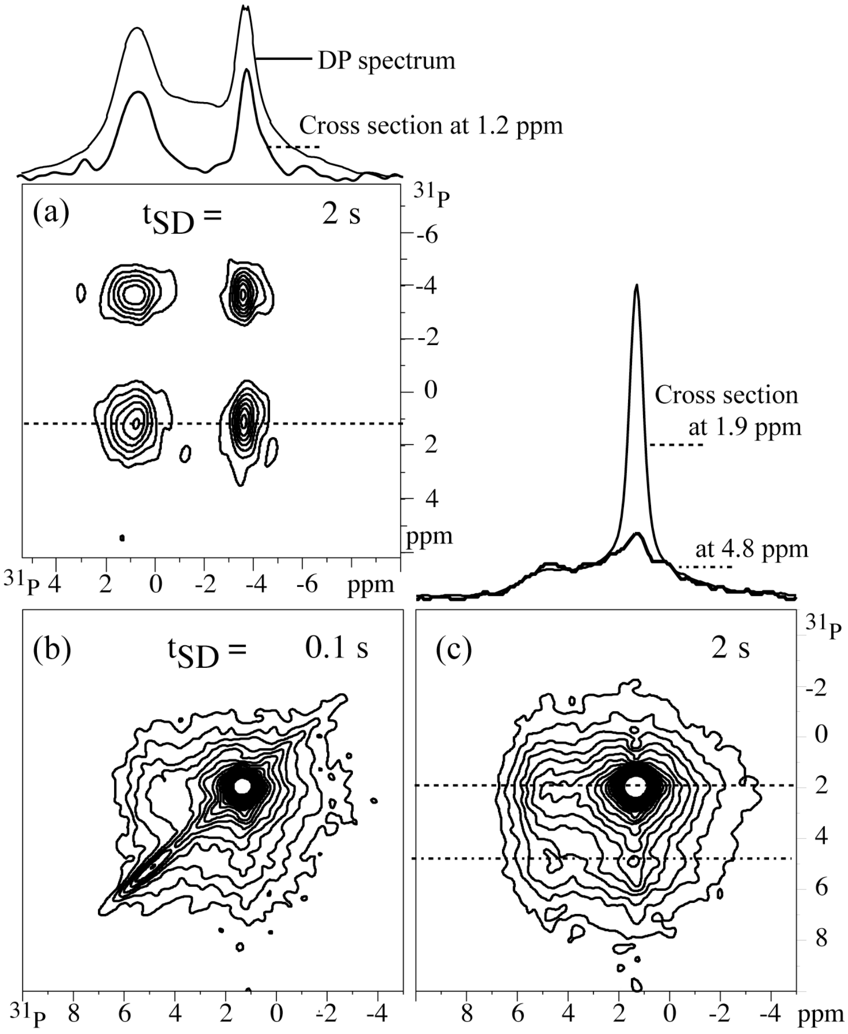

Figure 6.11. ^{31}P two-dimensional exchange NMR spectra of (a) PentaPZ46-5, mixing time 2 s, (b) PentaPAA36-5, mixing time 100 ms, (c) PentaPAA36-5, mixing time 2 s. Spinning frequency: 6.5 kHz. The 1D spectra shown on top of (a) are the regular DP ^{31}P MAS spectrum and a cross section from the 2D exchange spectra at 1.2 ppm ^{31}P as indicated. The 1D spectra on top of (c) are cross sections from the data set of PentaPAA36-5 at 1.9 and 4.8 ppm ^{31}P as indicated.

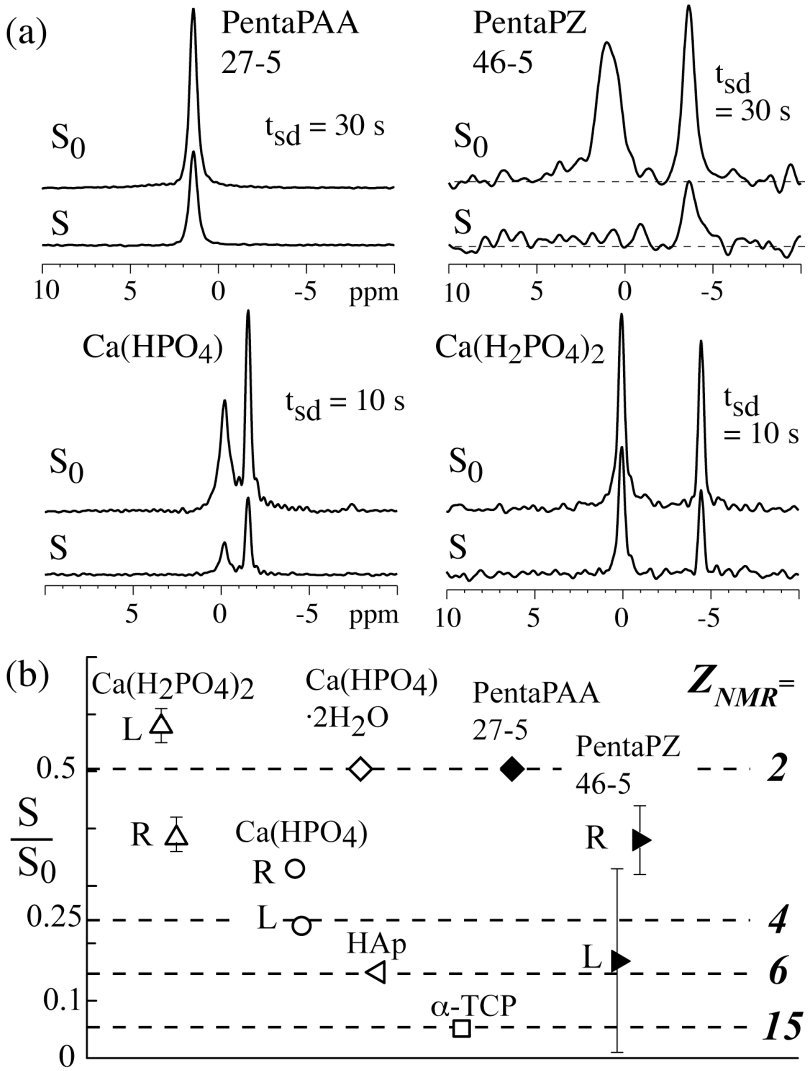

Figure 6.12. Determination of the number of magnetically inequivalent sites in the crystalline calcium phosphates by ^{31}P CODEX NMR with 10 or 30 s ^{31}P spin diffusion. (a) Spectra after spin exchange (S) compared with reference spectra (S_0). (b) Plot of S/S_0 for the three nanocomposites and several model compounds. L: left peak; R: right peak.

6.7 References

1. J. Song, E. Saiz, and C.R. Bertozzi. *J. Eur. Ceram. Soc.*, (2003); 23, p: 2905-2919.
2. J. Song, V. Malathong, and C.R. Bertozzi. *J. Am. Chem. Soc.*, (2005); 127, p: 3366-3372.
3. V.M. Rusu, C.-H. Ng, M. Wilke, B. Tiersch, P. Fratzl, and M.G. Peter. *Biomaterials*, (2005); 26, p: 5414-5426.
4. D.C. Pozzo, K.R. Hollabaugh, and L.M. Walker. *J. Rheol.(N.Y.)*, (2005); 49, p: 759-782.
5. D.C. Pozzo and L.M. Walker. *Colloids Surf., A*, (2007); 294, p: 117-129.
6. D. Enlow, A. Rawal, M. Kanapathipillai, K. Schmidt-Rohr, S. Mallapragada, C.T. Lo, P. Thiyagarajan, and M. Akinc. *J. Mater. Chem.*, (2007); 17, p: 1570-1578.
7. C. Du, F.Z. Cui, W. Zhang, Q.L. Feng, X.D. Zhu, and K. De Groot. *J. Biomed. Mater. Res.*, (2000); 50, p: 518-527.
8. J.D. Hartgerink, E. Beniash, and S.I. Stupp. *Science*, (2001); 294, p: 1684-1688.
9. S. Mann. *Principles and Concepts in Bioinorganic Materials Chemistry*, (2001); p: 240 pp.
10. M. Tanahashi and T. Matsuda. *J. Biomed. Mater. Res.*, (1997); 34, p: 305-315.
11. T. Miyazaki, C. Ohtsuki, Y. Akioka, M. Tanihara, J. Nakao, Y. Sakaguchi, and S. Konagaya. *J. Mater. Sci.: Mater. Med.*, (2003); 14, p: 569-574.
12. N. Spanos, V. Deimede, and P.G. Koutsoukos. *Biomaterials*, (2001); 23, p: 947-953.
13. J.A. Anderson and A. Travesset. *Macromolecules*, (2006); 39, p: 5143-5151.
14. C.D. Knorowski, J.A. Anderson, and A. Travesset. *Phys. Rev. Lett.*, (2008); submitted, p.
15. N. Barbani, L. Lazzeri, C. Cristallini, M.G. Cascone, G. Polacco, and G. Pizzirani. *J. Appl. Polym. Sci.*, (1999); 72, p: 971-976.
16. T. Iwatsubo, S.P. Kusumocahyo, T. Kanamori, and T. Shinbo. *J. Appl. Polym. Sci.*, (2006); 100, p: 1465-1470.
17. T. Iwatsubo, K. Sumaru, T. Kanamori, T. Shinbo, and T. Yamaguchi. *Biomacromolecules*, (2006); 7, p: 95-100.
18. M.D. Determan, J.P. Cox, S. Seifert, P. Thiyagarajan, and S.K. Mallapragada. *Polymer*, (2005); 46, p: 6933-6946.
19. W.P. Rothwell, J.S. Waugh, and J.P. Yesinowski. *J. Am. Chem. Soc.*, (1980); 102, p: 2637-2643.
20. S.S. Hou, F.L. Beyer, and K. Schmidt-Rohr. *Solid State Nucl. Magn. Reson.*, (2002); 22, p: 110-127.
21. S.S. Hou, T.J. Bonagamba, F.L. Beyer, P.H. Madison, and K. Schmidt-Rohr. *Macromolecules*, (2003); 36, p: 2769-2776.
22. K. Schmidt-Rohr. *Macromolecules*, (1992); 25, p: 3273-3277.
23. T. Gullion and J. Schaefer. *JMR*, (1989); 81, p: 196-200.
24. K. Schmidt-Rohr, A. Rawal, and X.-W. Fang. *J. Phys. Chem.*, (2007); 126, p: 054701.
25. J.W. Murray and R.V. Dietrich. *Am. Mineral.*, (1956); 41, p: 616-626.
26. W. Kolodziejski. *Top. Curr. Chem.*, (2004); 246, p: 235-270.
27. J.P. Yesinowski and H. Eckert. *J. Am. Chem. Soc.*, (1987); 109, p: 6274-6282.

28. D. Reichert, T.J. Bonagamba, and K. Schmidt-Rohr. *J. Magn. Reson.*, (2001); 151, p: 129-135.

CHAPTER 7. BIOINSPIRED SYNTHESIS OF SELF-ASSEMBLED CALCIUM PHOSPHATE NANOCOMPOSITES USING BLOCK COPOLYMER-PEPTIDE CONJUGATES

A paper published in *The Journal of Materials Research*

J. Mater. Res., 2008, 23(12), 3196-3212

Yusuf Yusufoglu[a,+], Yanyan Hu[a,+], Mathumai Kanapathipillai[a], Matthew Kramer[a], Yunus E. Kalay[a], P. Thiyagarajan[b], Mufit Akinc[a], Klaus Schmidt-Rohr[a], and
Surya Mallapragada[a-]

7.1 Abstract

Thermoreversibly gelling block copolymers conjugated to hydroxyapatite-nucleating peptides were used to template the growth of inorganic calcium phosphate in aqueous solutions. Nuclear magnetic resonance (NMR), Fourier transform infrared (FTIR), transmission electron microscopy, x-ray diffraction, and small-angle scattering were used to characterize these samples and confirm that the peptides promoted the growth of hydroxyapatite as the inorganic phase. Three different polymer templates were used with varying charges on the polymer chains (nonionic, anionic, and zwitterionic), to investigate the role of charge on mineralization. All of the polymer-inorganic solutions exhibited thermoreversible gelation above room temperature. Nanocomposite formation was confirmed by solid-state NMR, and several methods identified the inorganic component as hydroxyapatite. Small angle x-ray scattering and electron microscopy showed thin, elongated crystallites. Thermogravimetric analysis showed an inorganic content of 30-45 wt% (based

on the mass of the dried gel at ~ 200 °C). Our work offers routes for bioinspired bottom-up approaches for the development of novel, self-assembling, injectable nanocomposite biomaterials for potential orthopedic applications.

[+] Primary researchers and both authors contributed equally to the work

[a] Ames Laboratory, Iowa State University, Ames, IA 50011

[b] Argonne National Laboratory, 9700 S. Cass Ave, Argonne, IL 60439

[-] Author for correspondence

7.2 Introduction

Tremendous literature has appeared in recent years to explore ways to mimic biomineralization [1-4] and to understand the mechanism(s) involved in it with proteins, enzymatic biocatalysts, and other biopolymers [5-9]. Numerous studies have appeared on the in vitro synthesis and characterization of biominerals including calcium phosphate, calcium carbonate and silica [10-15]. All of these studies have focused on templating at the nanoscale or at the macroscale, but mostly only on the surface.

Controlling the structure at the molecular level as well as impressing hierarchical order over multiple-length scales as seen commonly in nature is a formidable challenge that has not been achieved yet, but significant progress is being made in these directions. Polymer templating has the advantage of molecular-level control and a promise to extend to the macroscale by hierarchical ordering. Our recent work has shown that synthetic block copolymers that undergo self assembly at multiple length scales can serve as effective templates for precipitation of calcium phosphates on nanoscale micelles, which can self-assemble further into macroscale gels and solids [16]. This is one of the first approaches for bottom-up design of macroscale composites with hierarchical order down to the nanoscale completely by self-assembly. However, the use of polymer templates alone does not provide biological specificity for controlled growth of the inorganic phase. Therefore, here we report the synthesis of thermoreversibly self-assembling polymer templates with attached hydroxyapatite-nucleating peptides [17], which were used to control the biomineralization process and to form polymer-hydroxyapatite nanocomposites completely by self-assembly. These novel systems that transition from liquid to solid at physiological temperatures could form the basis for injectable nanocomposites for orthopedic repair, such as in bone or cartilage defects. Characterization of the nanostructure and composition of the bioinspired nanocomposites remains a challenge. We report the use of a variety of complementary techniques including solid-state nuclear magnetic resonance (NMR), small-angle scattering, and transmission electron microscopy to elucidate the structure and composition of these bioinspired materials.

7.3 Materials and Methods

The hydroxyapatite-nucleating peptide (DSKSDSSKSESDSS), with a molecular weight of 1445 Da and theoretical pI of 4.23, was synthesized by Genscript Corporation (Piscataway, NJ), with a purity of ~ 95% and used as obtained. All other materials used were obtained from either Sigma-Aldrich (St. Louis, MO) or Fisher Scientific (Fairlawn, NJ) and were of high purity.

Synthesis and Characterization of Block Copolymers and Their Conjugates

A. Polymer synthesis method and scheme

Pluronic F127 [poly(ethyelene oxide)-b-poly(propylene oxide)-b-poly(ethylene oxide)] with a molecular weight of 12,600 (BASF Corp., Florham Park, NJ) was used to synthesize Pluronic-based anionic (PentaPAA) (M_n = 17,458, PDI 1.14) and zwitterionic

(PentaPZ) (M_n = 15,100, PDI 1.17) pentablock copolymers using an atom transfer radical polymerization (ATRP) technique as previously reported [18, 19]. These polymers are shown in Scheme 7.1. The Pluronic and PentaPZ end groups were modified to obtain carboxyl end groups as described below. The Pluronic and the two pentablock copolymers were then conjugated with the hydroxyapatite binding peptide using *N*-hydroxyl succinimide (NHS) chemistry [20, 21]. The peptide copolymer conjugation schemes used are shown below.

B. Pluronic end group modification (Scheme 7.2)

The hydroxyl end groups of Pluronic were converted to carboxyl groups by treating with succinic anhydride in pyridine as reported in the literature [22]. In short, Pluronic (32 g, 2.5 mmol) and succinic anhydride (1g, 10 mmol) were dissolved in pyridine (100 mL) and the reaction was carried out at 40 °C for 24 h. The mixture was then precipitated in diethyl ether, dissolved in toluene and reprecipitated in diethyl ether. The product was then dried under vacuum.

C. PentaPZ end group modification (Scheme 7.3)

The transformation of bromine end functional PentaPZ into azide end-functional PentaPZ was adopted from literature [23]. In short, the bromine end functionalized pentablock (15,100 g. mol $^{-1}$, 5.4 g, 0.36 mmol), sodium azide (234 mg, 3.6 mmol), and dimethyl formamide (15 mL) were added in a flask and stirred well. The mixture was reacted for 24 h at 50°C. After that, the azide- functionalized pentablock was precipitated in *n*-hexane, filtered and dried under reduced pressure. Click coupling was used to convert the azide end-functionalized PentaPZ to carboxyl-functionalized end group as reported previously in literature [20, 23]. In a round-bottom flask, azide- functionalized PentaPZ (1.65g, 0.11 mmol), copper bromide (47 mg, 0.33 mmol), and Nppm-ligand (99 mg, 0.66mmol) were added. After capping the flask with septum, the mixture was purged with argon for a couple of minutes. Degassed THF (4 mL) was then added into the mixture. Pentynoic acid (64.8 mg, 0.66 mmol) was added through a microsyringe. The mixture was then stirred overnight at room temperature. The carboxyl-functionalized PentaPZ was precipitated in *n*-hexane, filtered, and dried under vacuum.

D. Polymer-peptide conjugate synthesis (Scheme 7.4)

The carboxyl-terminated Pluronic or PentaPZ, or the acrylic groups of PentaPAA polymers were esterified with NHS as reported in literature [21]. To a round-bottom flask connected with an argon line and bubbler, Pluronic/PentaPZ/PentaPAA (0.128 mmol), 0.0792 g of *N,N'*-dicyclohexylcarbodiimide (3 X excess, 0.384 mol), 0.0442 g of NHS (3 X excess, 0.384 mol), and 8 mL of dichloromethane were added. The reaction was carried out at room temperature for 24 h. The reaction mixture was then filtered and precipitated in cold diethyl ether. The NHS attachment was verified by ^{1}HNMR with ester peak ar approximately 2.7 ppm.

The NHS-functionalized polymer was then conjugated with the hydroxyapatite binding peptide as described in the literature [21]. NHS polymer (1.5 g) was added to a solution of 12 mg of peptide in 50 mL of PBS (pH 7.4) with stirring at room temperature. After 4 hours, an additional 1.5 g of NHS-polymer was added to the mixture. The reaction was maintained at room temperature for 24 h. A small amount of the reacted mixture was then lyophilized, and the conjugation efficiency was determined using reverse-phase, high pressure liquid chromatography (RP-HPLC). The rest of the reaction mixture was dialyzed against water using a cellulose ester membrane with a molecular weight cutoff of 3500 (Spectrum Labs, Rancho Dominguez, CA) for 48 h to remove the uncoupled peptide. The polymer-peptide solution was then lyophilized, a pure white powder was obtained, and the peptide attachment was then qualitatively characterized with ^{1}H NMR.

The thermoreversible gelation behavior of the polymers was studied by simple gel inversion. A gradient RP-HPLC method was used to measure the conjugation efficiency of the peptide to the polymer. A Schimadzu C-18 analytical column (5 µm, 4.6x 250 mm) was used. A flow rate of 1 mL/min was used for the gradient elution with the mobile phases of 0.05% TFA in acetonitrile (solution A) and 0.065% TFA in 100% water (solution B). The mobile phase was run as follows: (i) 5% A for the first 0.01 min; (ii) 25% for the next 24.99 min; (iii) 100% A for the last 5 min (total run 30 min). The polymer-peptide conjugate was injected to the system, and the unreacted peptide was detected using the UV detector at 220 nm. The concentrations of the unreacted peptide were then calculated using the calibration curve obtained for the pure peptide using the same method. Amount of conjugated peptide was then found by subtracting the unreacted peptide from the initial added peptide to the polymer-peptide conjugation reaction.

E. Block copolymer: Calcium phosphate nanocomposite synthesis

The following procedure was used to obtain calcium phosphate (CaP)-block copolymer nanocomposite hydrogel samples: 1.2 g copolymer-peptide conjugate obtained by attaching peptide blocks to Pluronic F127 (designated as Pluronic-Pep) and 1.2 g of pure Pluronic F127 were mixed with 5.0 mL of $CaCl_2$ solution (4.0 *M*). The calcium containing polymer-peptide solution was kept in a refrigerator (at $T \approx 1\ ^{o}C$) for 2 days. Then, 3.0 mL of $(NH_4)_2HPO_4$ solution (4.0 *M*) was added and kept in refrigerator for another 2 days before aging at room temperature for 2 days to form a hydrogel nanocomposite containing approximately 22 wt% polymer-peptide. The pH of the hydrogel sample was maintained at ~

8 by adding 6 *M* NaOH solution. The sample is referred to as Pluronic-Pep22-8, where the numbers 22 and 8 refer to wt% of the polymer-peptide conjugate and pH of the gel, respectively.

To prepare other CaP/hydrogel samples, a similar procedure was followed using appropriate amounts of tri-block Pluronic F127, PentaPAA and PentaPZ with peptide groups attached (designated as Pluronic, PentaPAA-Pep and PentaPZ-Pep, respectively). Finally, Pluronic30-8, PentaPAA-Pep30-8 and PentaPZ-Pep45-8 hydrogel samples were prepared, where the first (30, 30, 45) and second numbers (8) refer to polymer content and pH of the gel, respectively. In addition, hydroxyapatite (HAp) precipitated from an aqueous solution of $CaCl_2$ and $(NH_4)_2HPO_4$ at pH ~ 8, and polymer hydrogels prepared in deionized water were used as control samples in the present study. The formation of HAp in CaP/polymer hydrogels is believed to take place along the following chemical reaction:

$$10\,CaCl_2 + 6\,(NH_4)_2HPO_4 + 2\,H_2O \rightarrow Ca_{10}(PO_4)_6(OH)_2 + 12\,(NH_4)Cl + 8HCl$$

F. Characterization

Calcium phosphate nanocomposite samples were analyzed by various characterization methods: x-ray diffraction (XRD), Fourier transform infrared spectroscopy (FTIR), thermogravimetric analysis (TGA), bright-field (BF) transmission electron microscopy (TEM), scanning transmission electron microscopy (STEM) using a high angle annular dark field (HAADF) detector, high-resolution TEM (HRTEM), and selected-area electron diffraction (SAED). Moreover, the atomic Ca/P ratio was also monitored by energy-dispersive spectroscopy (EDS) in the STEM-EDX.

The phase composition and crystallinity of the samples were assessed by using a theta-theta x-ray diffractometer (XDS-2000; Scintag, Cupertino, CA) and operating at 45 kV and 40 mA. The scanning rate was 0.60°/min, with a sampling interval of 0.02° over a range of $10^{o} \leq 2\theta \leq 60^{o}$. To minimize drying, hydrogel XRD samples were analyzed immediately following preparation. Scintag DMSNT search/match software and the ICDD 2007 database were used for the phase analysis. FTIR spectra were recorded with a Bruker spectrometer (Bruker IFS-66v; Bruker Optics Inc., Billerica, MA) over 400-4000 cm^{-1} with a 4 cm^{-1} resolution and averaging 32 scans. For the FTIR analysis, vacuum-dried samples were pressed into KBr pellets containing approximately 1 wt% sample. The content of inorganic phase (HAp) in the nanocomposites was estimated from thermogravimetric analysis (TGA) performed with a Perkin Elmer thermo gravimetric analyzer (PerkinElmer, Downers Grove, IL). Approximately 60 mg of the gel sample was heated in flowing air. The sample was heated to 50 °C, held at this temperature for 1 min, then ramped to 120 °C at a rate of 5.00 °C/min, and to 600 °C at rate of 10.00 °C/min.

G. Solid-state NMR

Solid-state NMR experiments were performed using a Bruker DSX400 spectrometer (Bruker-Biospin, Rheinstetten, Germany) at 400 MHz for ^{1}H and 162 MHz for ^{31}P. A Bruker 4-mm double resonance magic-angle spinning (MAS) probehead was used for 6.5-kHz and 7-kHz MAS ^{31}P or ^{1}H – ^{31}P experiments. The 90° pulse lengths were 5 μs for ^{1}H and 4 μs for ^{31}P. The direct-polarization experiments were carried out with recycle delays of 100 s at 7 kHz MAS. The 2D ^{1}H-^{31}P correlation experiments without homonuclear decoupling, using the wideline separation (WISE) NMR pulse sequence with hypercomplex data acquisition, were carried out with 256 20-μs t_1 increments and 5-s recycle delays. 2D ^{1}H-^{31}P heteronuclear correlation (HetCor) NMR experiments were carried out with 100 44-μs t_1 increments and 15-s recycle delays. Lee-Goldburg cross polarization (LGCP) was used for polarization transfer from ^{1}H to ^{31}P in both “WISE” [24] and HetCor experiments with contact times of 0.7 and 0.5 ms, respectively. Two-pulse phase-modulation (TPPM) was used for ^{1}H-^{31}P dipolar decoupling. The hydroxide proton peak at 0.18 ppm and ^{31}P peak at 2.8 ppm of NIST hydroxyapatite were used as secondary chemical shift references to calibrate the ^{1}H and ^{31}P chemical shifts, respectively. All NMR experiments were carried out at ambient temperature.

H. Scattering

Small-angle x-ray scattering (SAXS) experiments were performed at the 12-ID beam line at the Advanced Photon Source (APS) in Argonne National Laboratory to elucidate the structure of the polymer-peptide gel nanocomposites. By using 12 keV x-rays (λ = 1.035 Å) the data were collected at 1-s exposure with a 15 x 15 cm^2 CCD detector at a sample-to-detector distance of 2 m to measure the scattered intensity, and the transmitted intensity was measured using a photodiode buried in the beam stop. The measured 2D data for the gel samples sandwiched between kapton tapes were corrected, azimuthally averaged and the scattering data was expressed as a function of Q (4π sin θ/λ), where 2θ is the scattering angle. To complement the SAXS data that has higher sensitivity for the inorganic phase, small-angle neutron scattering (SANS) was used to highlight the structural features of the copolymer phase in the nanocomposite gels as the neutron-scattering contrast for the polymer phase, when in a deuterated solvent, is much higher than the inorganic phase. To increase the scattering contrast of the copolymer the gel samples were prepared in D_2O, and the pH was adjusted to 8 by using DCl and NaOD. The samples were sealed in quartz cylindrical cells with a 2-mm path length, and the experiments were performed using the time-of-flight SAND instrument at the Intense Pulsed Neutron Source (IPNS) at the Argonne National laboratory that yielded data in a Q range of 0.008 to 1 $Å^{-1}$ in a single measurement. The scattering data were corrected following the routine procedures and the $I(Q)$ was placed on an absolute scale in the units of cm^{-1}.

I. Electron Microscopy

TEM, STEM, HRTEM, SAED, and STEM-EDS analysis were performed with a FEI-Tecnai G^2-F20 (FEI Inc., Hillsboro, OR) scanning transmission electron microscope equipped with EDS (EDAX Inc., Mahwah, NJ) using a CCD camera and Digital Micrograph Software (Gatan, Pleasanton, CA). For the STEM analysis, the copolymer and nanocomposite gel samples were diluted with deionized water to obtain 5.0 wt% polymer solutions. Approximately 50 μL of the aqueous sample was placed onto a Formvar-coated copper grid, and the excess solution was wicked away. A negative contrast stain consists of 1% ammonium molybdate or phosphotungstic acid at pH ~ 8 was applied. Phosphotungstic acid was used for control samples only (polymer gels without any CaP), whereas ammonium molybdate was used for calcium phosphate nanocomposites. After applying the stain, the excess solution was wicked and allowed to dry.

7.4 Results and Discussion

A. Polymer characterization

The polymer-peptide attachment was qualitatively characterized using ^{1}H solution NMR. Compared with the spectra of the polymer alone, the additional peaks between 1-2.5 ppm corresponding to the peptide protons compared to the polymer alone ^{1}H NMR spectra confirmed the conjugation of the peptide to the polymer. The conjugation efficiency was determined by subtracting the amount of unreacted peptide measured by RP-HPLC and UV detection from that of the initial amount of peptide used for the conjugation. In the case of

Pluronic, the conjugation efficiency was found to be around 19.8%, whereas it was found to be around 26.6% and 22.9%, for PentaPAA and PentaPZ, respectively.

B. Structure and Composition of the Inorganic Phase

The x-ray diffraction patterns of the as prepared CaP/hydrogel samples and pure HAp (Standard Reference Material® 2910) are shown in Figure 7.1. All of the observed peaks can be assigned to HAp with reference to ICCD (JCPDS 9–432) and pure HAp (Standard Reference Material® 2910) as predicted by the calcium phosphate pH–concentration diagram [25, 26], and experimentally shown by Yusufoglu and Akinc [27], with the exception of one very weak peak at $2\theta = 11.7^o$ for PentaPZ-Pep45-8. Since brushite is believed to be a precursor in the precipitation of HAp [28, 29], and has its most intense peak at $2\theta = 11.7^o$ (JCPDS 9-0077), we surmise that this weak peak is likely from brushite.

As seen in Figure 7.1, all CaP/hydrogel nanocomposite XRD patterns exhibit similar features and show a broad peak at approximately $2\theta = 32^o$ and $2\theta = 26^o$, very similar to the XRD patterns of natural human bone and dentine [30, 31]. The broad peak at about $2\theta = 32^o$ is a composite band resulting from three of the most intense peaks of HAp [(211), (112), and (300) planes]. Moreover, the broad peaks are indicative of nanocrystalline or/and poorly crystalline nature of the HAp, and the broad background is possibly due to amorphous polymer matrix. Furthermore, HAp/hydrogel samples were vacuum dried and, the polymer was removed by dissolving in deionized water at ~1 °C. The XRD diffraction patterns of the vacuum-dried gel nanocomposite and polymer-free samples are illustrated in Figures 7.2 and 7.3, respectively. HAp precipitated in the absence of polymer is also included in Figure 7.3. The XRD patterns of vacuum-dried samples showed that some HAp reflections were absent. This is believed to be due to the preferential orientation of HAp crystallites in the polymer matrix during vacuum drying or sample preparation for XRD analysis. Furthermore, vacuum-dried polymer solutions prepared in deionized water (control samples) were also analyzed by XRD (data not shown). The diffraction peaks observed in Figure 7.2 at $2\theta \sim 19.5^o$ and $2\theta \sim 23.5^o$ were ascribed to polymer crystals formed during vacuum drying. The XRD patterns of samples with polymer removed after vacuum drying (designated as "washed" samples) are shown in Figure 7.3. The XRD patterns of the washed samples are similar to those of as-prepared CaP/hydrogel samples, with the exception that they are of higher intensity and also contain additional peaks that can all be assigned to HAp. In addition, comparison of the XRD results in Figures 7.2 and 7.3 supports the conclusion that vacuum drying may cause preferential orientation of HAp crystals in the polymer matrix.

To further characterize the HAp/hydrogel nanocomposite samples, FTIR analysis was performed, as illustrated in Figures 7.4 and 7.5.

The differences between hydrogel prepared in calcium phosphate solutions and in deionized water as well as pure HAp (Standard Reference Material® 2910) spectrum can be seen in Figure 7.4. The FTIR spectra in the present study were carefully compared with those reported earlier [32-34] and pure HAp (Figures 7.4 and 7.5). Pure HAp shows phosphate peaks at 965 cm^{-1}, 470 cm^{-1}, between 1050-1095 cm^{-1} and 565-602-635 cm^{-1} (three sites) for ν_1, ν_2, ν_3, and ν_4, respectively. For our vacuum-dried nanocomposite samples, these peaks appear at around 961 cm^{-1}, 454 cm^{-1}, 1038 cm^{-1} and 566-601 cm^{-1} (two sites). Infrared spectroscopy analysis showed major phosphate peaks, confirming the formation of HAp in the nanocomposites. Furthermore, the bands at around 1410 and 1460 cm^{-1} might be ascribed to CO_3 [35, 36]. However, in the presence of polymer, CO_3 peaks cannot be assigned with certainty because of the strong C-H and COO^- bands (from the polymer) in the same spectral regions. Possible assignments of all adsorption bands in Figures 7.4 and 7.5 are listed in Table 7.1. Because some of the CO_3 and PO_4 absorption bands overlap with the polymer-related peaks (C-H and C-O bands), FTIR analysis was also performed for the nanocomposite samples with the polymer removed (designated as "washed samples"). The spectra of the washed samples as well as HAp precipitated from an aqueous solution without any polymer were shown in Figures 7.5. The observed absorption peaks correspond to HAp [25, 27, 37, 38].

When the HAp was precipitated without any polymer under the same experimental conditions, small bands assigned to CO_3 were detected approximately 873, 1410 and 1465 cm^{-1}, as seen in Figure 7.5. The positions of these peaks indicate that the CO_3 groups may have been incorporated into the HAp crystal structure and replaced PO_4 [27, 33, 35, 39, 40]. Carbonate substitution most probably arises from the ion exchange with dissolved CO_2 from the atmosphere during the dissolution, stirring and reaction processes. However, further work is required to elucidate the source of CO_2 and the exact mechanism of substitution, which are not the focus of the present study. Even though the samples were dried under vacuum, a broad water peak was observed at approximately 3400 cm^{-1} that suggests that HAp binds water. This broad H_2O band from 3600 to 3100 cm^{-1} dominates both spectra in Figures 7.4 and 7.5, masking the OH peak of HAp in this region.

Moreover, as seen from Figure 7.5, after extracting the polymer by washing the vacuum-dried samples, all the PO_4-related peaks can be observed more clearly. The phosphate bands were generally broader, probably because of the small crystallite sizes. From the general view of FTIR analysis, it can be concluded that the mineral phase is HAp in the synthesized CaP/nanocomposite samples, which is consistent with XRD and NMR results.

As-prepared CaP/hydrogel nanocomposite samples were subjected to thermogravimetric analysis to determine the actual content of the mineral phase, which is confirmed to be HAp from various characterization methods in the present study (see Figure 7.6). Mainly three ranges of mass loss can be assigned to thermogravimetric analysis of the gel samples [30, 41, 42]. Removal of physically and chemically adsorbed water and possibly lattice water takes place from room temperature to approximately 200 ^{o}C. Weight loss related to the pyrolysis of the polymer is observed between 200 and 400 ^{o}C. At approximately 400 ^{o}C, only the inorganic phase (HAp) remains. If HAp has some incorporated carbonate in the form of carbonated apatite, there will be a weight loss above 400 ^{o}C due to the CO_3 removal from the HAp structure [25, 27, 41, 42]. A slight mass loss between the temperature range of 400-600 ^{o}C (see Figure 7.6) possibly corresponds to the decarboxylation of the HAp, releasing $CO_{2(g)}$, which is consistent with the findings from FTIR analysis. Pure HAp is stable up to 1200^{o}C and decomposition of HAp is not expected under our experimental conditions [25, 43]. Therefore, TGA makes it possible to determine the mineral content in the nanocomposites. The analysis of Figure 7.6 showed significant inorganic fractions, approximately 45 wt% for Pluronic-Pep22-8, 40 wt% for PentaPAA-Pep30-8, 35 wt% for Pluronic30-8, and 30 wt% for PentaPZ-Pep45-8. The inorganic content estimated from TGA results are based on the mass of the dried hydrogel at ~200 ^{o}C as 100%, and the results are in good agreement with the theoretically calculated values. In general, the inorganic content in the present study is significantly larger than the 6-15 wt% observed in our previous studies of calcium phosphate formation on cationic and polar templates [16] without hydroxyapatite-binding peptides.

C. NMR identification of phosphates

Figure 7.7 shows direct polarization (DP) and cross-polarization (CP) ^{31}P NMR spectra of Pluronic30-8, Pluronic-Pep22-8, PentaPAA-Pep30-8, and PentaPZ-Pep45-8. For all samples except PentaPZ-Pep45-8, the spectra show only one resolved band. Its position agrees with the 3-ppm chemical shift of hydroxyapatite [44], though the linewidth is larger than for ideal hydroxyapatite. For PentaPZ-Pep45-8, the CP spectrum shows two peaks, see Figure 7.7(h). Whereas the broad component is again hydroxyapatite, the sharp peak can be tentatively assigned to brushite, based on its chemical shift [44]. The quantitative DP ^{31}P NMR spectrum of PentaPZ-Pep45-8 indicates that brushite is only a minor component, compared to hydroxyapatite. For all samples, the DP and CP spectra showed similar features, but the lines in the CP spectra are broader. The likely reason is an enhanced contribution of signals from HPO_4^{2-} ions and PO_4^{3-} hydrogen bonded to H_2O in the CP spectrum.

These tentative assignments of the ^{31}P resonances are confirmed by the proton peak positions in 2D ^{1}H- ^{31}P correlation spectra without spin diffusion [Figures 7.8(a), 7.9(a), and 7.10(a)]. The OH^- proton of hydroxyapatite is detected around 0.2 ppm, while the broad signal near 7 ppm is consistent with H_2O hydrogen bonded to PO_4^{3-}, and the even broader band around 12 ppm must be assigned to HPO_4^{2-}. For PentaPZ-Pep45-8, the 6.5- and 10-ppm ^{1}H signals of the sharp 1.4 ppm ^{31}P peak agree with those of H_2O and HPO_4^{2-}, respectively, in brushite from the literature [45].

D. NMR evidence of the nanocomposite formation

The formation of nanocomposites can be proved by 2D ^{1}H-^{31}P heteronuclear correlation NMR experiments with ^{1}H spin diffusion, where the presence of cross-peaks between polymer protons and inorganic phosphate within a few tens of milliseconds proves the intimate contact between organic and inorganic phases that is characteristic of nanocomposites [16, 46]. Figure 7.8(a) shows a series of 2D HetCor ^{1}H-^{31}P spectra of PentaPAA-Pep30-8 with spin diffusion mixing times of 0.05, 50, and 500 ms. Cross-sections along the ^{1}H dimension, taken at 3.4 ppm in the ^{31}P dimension, are shown in Figure 7.8(b). First, only OH^- signals in the inorganic phase and a broad band of H-bonded H_2O appear. Within 50 ms, the polymer proton peaks (CH_3 and OCH_2) show up, and become completely dominant after 500 ms of spin diffusion; this proves the formation of a nanocomposite. Given the small proton concentration in hydroxyapatite, spin diffusion is relatively slow. The inorganic particles must be less than 10-nm thick, based on comparisons with spin diffusion in bone, where the inorganic crystals are ~ 3-nm thick.

A series of 2D HetCor ^{1}H-^{31}P spectra of PentaPZ-Pep45-8 and cross sections at HAp and brushite resonances are shown in Figure 7.9. Again, equilibration is observed within 500 ms for the HAp component, whereas the brushite cross-sections change little. This shows that the HAp is part of a nanocomposite, while brushite forms larger crystals. The heteronuclear correlation experiment can also be performed with homonuclear ^{1}H decoupling in the ω_1 dimension, using a pulse sequence closely resembling that of WISE NMR [24]. This version of the experiment is simpler, requires less radio-frequency irradiation, provides unscaled ^{1}H chemical shifts, and may yield higher resolution for mobile segments such as those of the Pluronic blocks. A series of "WISE" ^{1}H-^{31}P spectra of Pluronic-Pep22-8 are shown in Figure 7.10. The OH^- and polymer OCH_2 and CH_3 peaks are well resolved, and the formation of a nanocomposite is easily proven. Similar series of spectra were obtained for Pluronic30-8, PentaPAA-Pep30-8, and the HAp component in PentaPZ-Pep45-8, confirming nanocomposite formation in these materials.

E. Nanostructures of organic and inorganic phases from SAXS/SANS

By virtue of drastically different interaction of neutrons and x-rays with matter, SANS and SAXS serve as excellent complementary tools to investigate the nanostructural features in multicomponent hybrid polymer/inorganic nanocomposites. The complementarity can be clearly seen in Figure 7.11 wherein the SANS and SAXS profiles of the neat and corresponding nanocomposite gels are quite different. Whereas the SANS data of both the polymer and the nanocomposite gel samples look similar and exhibit peaks, the SAXS data show peaks only for the neat polymer, but power-law scattering for the nanocomposites due to the major contribution of the inorganic phase in the later. The reason for this is that the SAXS signals of nanocomposites are over 3 orders of magnitude higher than the neat polymers. In the SAXS data, we observe signatures for the average size of the inorganic nanocrystals in the high Q region and power-law scattering in the low Q region, representing their shape and correlations in the polymer matrix. In general, the power-law exponent in the low Q region suggests the connectivity between the fundamental particles, the size of which can be derived from the scattering intensity in the high Q region. The absolute value of the power-law exponent in the low Q will assume values in the vicinity of 1, 2, and 3 for the 1D (rod), 2D (sheet), and 3D morphologies, at $QR_g >> 1$, where R_g is the radius of gyration of whole particle. In the case of mass fractal objects, the absolute value of the power-law exponent becomes a noninteger in the range of 1 to 3, the larger the exponent value the denser the distribution of the fundamental particles in the matrix. Although real space images would aid the proper interpretation of the small-angle scattering data, modified Guinier analyses for the cross-sectional dimensions help to resolve between a mass fractal object versus a rod when the power-law exponent has a value in the vicinity of 1 and a sheet when it has a value around 2. We will use these ideas in the interpretation of the SAXS data below.

For the neat Pluronic gel, both the SANS [(Figure 7.11(a)] and the SAXS [(Figure 7.11(b)) data show diffraction peaks at Q/Q* values of $1, \sqrt{3}, 2, \textit{and } \sqrt{8}$ corresponding to the FCC packing of spherical micelles. The presence of peaks in the SANS data at similar repeat distances for the gels of the neat copolymers and the corresponding nanocomposites indicate that the growth of the inorganic phase has little effect on the long-range order and morphologies of the polymer phase. This is consistent with the fact that crystals that nucleate in the interstitial regions will grow around the polymer phase and get connected. The SANS data of the Pluronic30-8 and Pluronic-Pep22-8 nanocomposites clearly show power-law scattering in the low Q regions due to the presence of inorganic structures in addition to the peaks associated with the polymer morphology. For the PentaPAA system, the SANS data for both the neat polymer and the nanocomposite gels [(Figure 7.11(c)) show BCC ordering with d-spacing around 16 nm, and the nanocomposite exhibits power-law scattering in a small low Q region. The SANS data for the PentaPZ-Pep samples indicate a HCPC structure corresponding to the diffraction peaks at Q/Q* values of $1, \sqrt{3}, \sqrt{7}, \textit{and } \sqrt{12}$ for the neat polymer as well as the nanocomposite samples, with the d-spacing of 20 nm. In this case, the upturn in the low Q region was less pronounced when compared to the other composites.

Based on its high sensitivity for the inorganic phase, we use SAXS data to evaluate nanostructural features in the nanocomposites. The I(Q) curves of these nanocomposite samples are similar to those of bone [47]. In the case of Pluronic30-8 [(Figure 7.11(b)], the characteristic length scale of inorganic phase is ~ 4.86 nm and a $Q^{-2.183}$ power-law scattering in the low Q region. On the other hand, for the Pluronic-Pep22-8 gel, the characteristic length scale of inorganic phase is ~ 3.26 nm, which is significantly smaller, and a $Q^{-1.926}$ power-law scattering in the low Q region. The power-law scattering in the vicinity of 2 implies that the whole particle has a sheet-like morphology, which is consistent with the TEM of the nanocomposites presented later. Although we cannot determine the largest dimension of the sheet-like objects within the limited Q range of the small angle scattering data, we can use the modified Guinier analysis for a sheet-like morphology by plotting $\ln(Q^2.I)$ versus Q^2 and fitting a straight line in a Q region where $Q_{max}.T < 0.28$, where T is the average thickness of the sheet-like particles. The thicknesses of the sheet-like objects in Pluronic30-8 and Pluronic-Pep22-8 gels fall in the range of 4 to 5 nm. For a given block copolymer, we also observe that the nanocomposite with the peptides exhibits higher scattering intensity than that without the peptide, suggesting that the peptide may have some influence in enhancing the growth and nucleation of the inorganic during the nanocomposite formation. These results are consistent with the higher inorganic content measured for the peptide containing nanocomposites. Figure 7.11(d) shows the SAXS data for the neat PentaPAA-peptide and the corresponding nanocomposite. Consistent with the SANS data, the neat polymer shows several peaks for a highly ordered BCC phase with diffraction peaks at Q/Q* values of $1, \sqrt{2}, \sqrt{3}, \textit{and}\ 2$, whereas the nanocomposite exhibits the presence of nanocrystals with an average characteristic scale of ~ 3 nm and a $Q^{-2.565}$ power law scattering. In contrast to the observations for the Pluronic and PentaPAA systems, the neat PentaPZ gel [(Figure 7.11(f)] shows only weak peaks in the SAXS data. This discrepancy could be due to the potential for the samples on kapton tape to dry during the SAXS measurement, whereas the samples for the SANS measurement were contained in sealed quartz cells. The PentaPZ-Pep45-8 nanocomposite shows the presence of nanocrystals with an average length scale ~ 3.6 nm and a $Q^{-2.165}$ power-law scattering in the low Q region. Modified Guinier analysis of these nanocomposites revealed a thickness in the range of 4 nm.

In summary, SANS and SAXS data clearly show that both the polymer and the nanocomposite structures have long-range order with nanometer-size morphology. This is in good agreement with NMR data, where it was found that the polymer and inorganic are in close contact and in the nanometer-size range. Furthermore, the conjugated peptide with the polymer does significantly enhance the growth and nucleation of the inorganic compared to the polymer templates without the peptide.

Scanning transmission electron micrographs (STEM) of 5 wt% Pluronic, Pluronic-Pep, PentaPAA-Pep, and PentaPZ-Pep prepared in deionized water are illustrated in Figure 7.12. As seen from the STEM data in Figure 7.12, PentaPZ-Pep polymer solution revealed rod-like structures, whereas all other polymers showed spherical micelles, in agreement with the SAXS and SANS results. The electron beam damage of the polymer precludes the size determination of the spherical micelles by STEM. However, SAXS and SANS revealed that the micelles were approximately 15 nm in diameter, which is also consistent with our previous studies [16].

Extensive TEM studies were performed on the HAp nanocomposite samples and all micrographs are illustrated in Figures 7.13 and 7.14. The Figure 7.13 shows bright-field (BF) TEM images and corresponding SAED patterns of the HAp/hydrogel nanocomposite samples diluted to 5 wt% polymers with deionized water. In addition, HAp synthesized from an aqueous solution without any polymer added and a HAADF image of Pluronic-Pep22-8 is also shown in Figure 7.13. The Figure 7.13(a) reveals that HAp in Pluronic30-8 nanocomposite consists of thin, elongated plate-like crystals with a mean length and width of about 110 and 20 nm, respectively. HAp nanocrystals of PentaPAA-Pep30-8 are also of plate-like shape but with shorter mean length and irregular edges [Figure 7.13(b)]. This morphology is very similar to the apatite crystals from the mid-diaphyses of a 19-week-old human fetal femur [48]. Furthermore, the morphology of the Pluronic-Pep22-8 nanocomposite is quite similar to that observed for the Pluronic30-8. Although the nanocrystals appear to be more needle-like for Pluronic-Pep22-8 in Figure 7. 13(c), the apparent elongated crystals are actually plate-like but curled and viewed edge-on as seen from the HAADF image shown in Figure 7.13(d). It seems that curled plate-like nanocrystals appear to be needle-like when tilted and viewed on edge [Figure 7.13(d)]. The variable morphology of the nanocrystals is difficult to describe and they vary from ~ 30–80 nm in length and ~ 10–25 nm in width. Figure 7.13(e) reveals the morphology of HAp nanocrystals in PentaPZ-Pep45-8, which is also similar to other HAp nanocomposite samples. In general, the morphology of HAp nanocomposites observed in the present study is quite similar to those of various other HAp nanocomposites seen in the literature [33, 34]. However, the morphology of the HAp crystals synthesized without any polymer [(Figure 7.13(f)] looks significantly different than the one observed for HAp/hydrogel nanocomposite samples. The Figure 7.13(f) shows that HAp nanocrystals in polymer-free sample resulted in bulk precipitation of plate-like crystals. It appears that in the presence of the polymers, the morphology of HAp nanocrystals is more elongated plate-like than the one without any polymer.

The upper insets in Figure 7.13 demonstrate SAED patterns of HAp/hydrogel nanocomposites and HAp synthesized without any polymer (polymer-free sample). SAED patterns with prominent diffraction rings clearly reveal a well-formed polycrystalline phase. Furthermore, the diffraction rings are all associated with HAp (JCPDS 9–432), and corresponding planes of HAp are indexed in the insets of Figure 7.13. The findings from the SAED patterns are consistent with those obtained from the XRD study. Although the SAED pattern of polymer-free sample [(Figure 7.13(f)] shows clearly distinct spots, they did not form well defined rings, with the exception of the (211) plane of HAp as shown in (see Figure 7.13(f). However, the SAED patterns of HAp nanocomposites showed strong small spots forming well-defined rings, which indicates the preferential alignment of nanocrystals.

In Figure 7.14, HRTEM micrographs showing nanocrystals surrounded by amorphous phase (polymer) also confirm the existence of the HAp phase in the nanocomposites. The upper right and lower insets in Figure 7.14 illustrate the FFT pattern and filtered inverse-FFT image, respectively. The FFT pattern of the nanocrystals shown in the upper right inset was closely related to the FFT pattern of hydroxyapatite phase observed along the $[2\bar{1}0]$ zone axis for Pluronic30-8, PentaPAA-Pep30-8, PentaPZ-Pep45-8 and along the [021] zone axis for Pluronic-Pep22-8. Moreover, the upper left insets of Figure 7.14 show HRTEM images taken from different regions. All HRTEM images in Figure 7.14 demonstrate that the crystal lattice planes are well aligned, albeit with some defects. The crystal planes of HAp determined in these images were indexed by comparing the measured *d* spacings and interplanar angles with the calculated values of HAp (JCPDS 9–432). The results from HRTEM agree well with those obtained from XRD and SAED. The diffraction peaks of all crystal planes determined from HRTEM analysis are also present in the XRD and SAED patterns of the nanocomposites. Furthermore, the upper left insets in Figure 7.14 show clearly columnar growth morphology and HRTEM images of plate-like crystals in longitudinal sections reveal a lattice spacing of ~ 3.4 Å, corresponding to the interplanar spacing of (002) planes for hexagonal HAp (see Figure 7.14). This is evidence of the fact that the growth of the elongated plate-like nanocrystals occurs along the c-axis direction of HAp. As can be seen from the XRD diffraction patterns in Figure 7.1, the relatively high intensity of the (002) and (004) reflections also support the notion that the growth of the elongated plate-like nanocrystals occurs along the c-axis direction of HAp. In addition, prominent diffraction rings corresponding to (002) and (004) planes of HAp were also observed in all SAED patterns of the nanocomposites, which might also indicate a c-axis growth direction of HAp. This kind of orientation is very similar to that in vertebrate bone [49]. Moreover, the atomic calcium to phosphorus ratio of HAp in nanocomposites was determined by STEM-EDS measurements to be around 1.73 ± 0.09, which is close to the stoichiometric value of pure HAp [$Ca_{10}(PO_4)_6(OH)_2$]. The slightly higher Ca/P ratio of HAp in our samples could be due to the carbonate substitution of the phosphate, which is in agreement with the FTIR results.

7.5 Conclusions

The results of our present biomimetic study (Table 7.2) showed that the morphology and the size of apatite crystals in HAp nanocomposites were quite similar to the apatite present in the bone. Nanosized carbonated HAp with broad diffraction peaks is the main component of bone mineral [31, 48] and was detected in our synthetic nanocomposites. In electron micrographs, the apatite in bone and in the synthetic nanocomposites appears as plate-like crystals with average dimensions of ~50 nm in length, ~25 nm in width, and 2-5 nm in thickness, and with strong preferred orientation in their c-crystallographic (002) axis. SAXS confirmed the formation of thin, elongated crystallites, whereas solid-state NMR proved the formation of nanocomposites. The inorganic content in the nanocomposites was much higher than in those synthesized without the hydroxyapatite-nucleating peptides [19] but it is still lower than that found in natural bone.

In summary, we have successfully developed biomimetic polymer-hydroxyapatite nanocomposites using hydroxyapatite-nucleating peptides conjugated to self-assembling block copolymers. The thermoreversible gelation properties of these nanocomposites could potentially enable them to serve as injectable biomaterials for bone/cartilage tissue repair.

7.6 Acknowledgments

This work was supported by the United States Department of Energy (DOE) Office of Basic Energy Services under Contract No. DE-AC02-07CH11358. This work benefited from the use of APS and the IPNS, funded by the United States DOE, Office of Science, Office of Basic Energy Science under Contract No. DE-AC02-06CH11357.

Pluronic F127

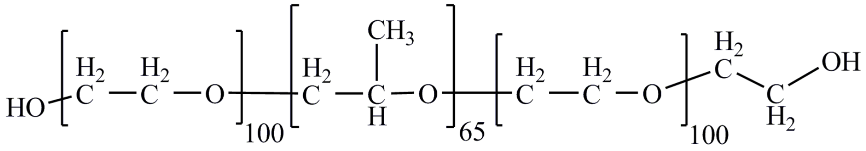

PentaPZ

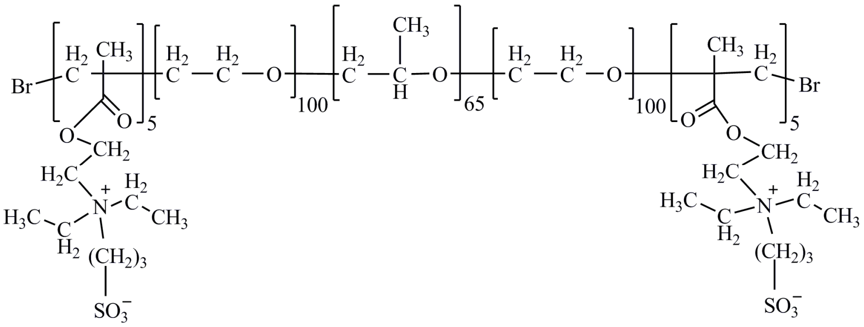

PentaPAA

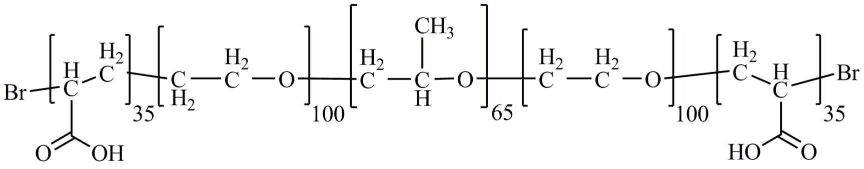

Scheme 7.1. Block copolymer structures.

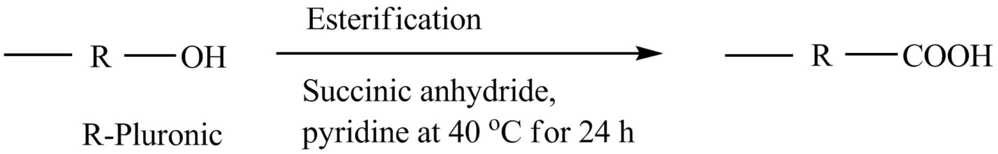

Scheme 7.2. Pluronic end group modification.

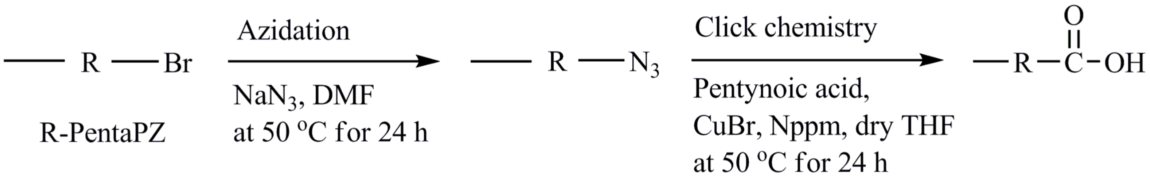

Scheme 7.3. PentaPZ end group modification.

a. NHS chemistry on carboxyl endgroups of Pluronic and PentaPZ

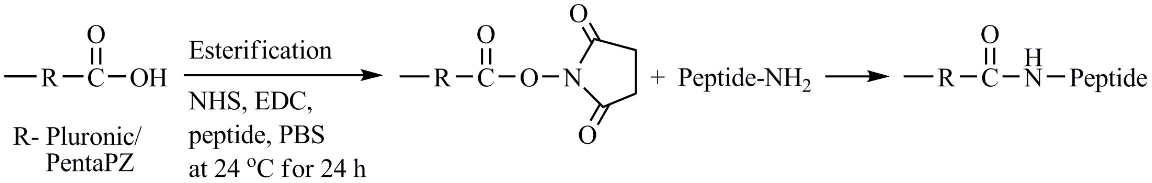

b. NHS chemistry on acrylic acid groups of PentaPAA

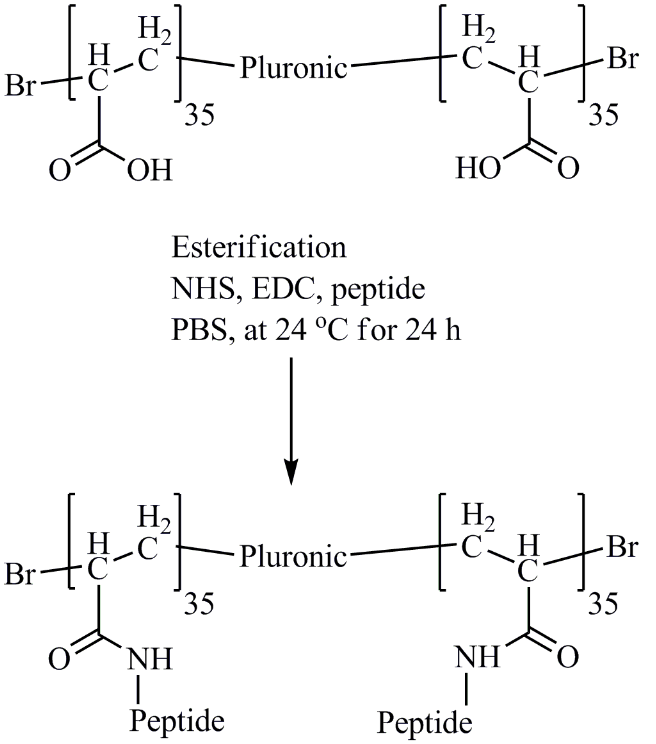

Note: Here peptides were attached randomly to acrylic acid groups.
Only few acrylic acids blocks were conjugated with peptides.

Scheme 7.4. Pluronic and pentablock copolymers peptide conjugation.

Table 7.1. The Possible assignments of FTIR peaks in Figures 7.4 and 7.5 [25, 43, 50, 51].

Group Frequency (cm^{-1})	Assignment
3570-3200 (broad)	Hydroxy group, H-bonded OH stretch
3430 (broad) / 1620	Water absorption bands
2970 / 2885	Methyl C-H asym./sym. stretch
1650-1550	N-H bend
1610-1550 / 1420-1430 and 960-850	Carboxylate (Carboxylic acid salt) and H bonded O-H out-of-plane bending
1465-1430 / 1380-1330	Methyl C-H asym./sym. bend
1300 -700	Methyne C-H vibrations
1250 + 890-800	Epoxy (C-O-)
1210-1150	C-N stretch
1150-1050	Alkyl-substituted ether, C-O stretch (C-O-C)
1050	C-O Primary alcohol, C-O stretch
871 / 1420 / 1475	Carbonate ν_2 / ν_{3a} / ν_{3b} (for B-CO_3HAp)
710-685	Thiol or thioether, CH_2-S- (C-S stretch)
470 / 565-602-635 / 965 / 1050-1095	Phosphate bands of HAp ν_2 / ν_4 / ν_1 / ν_3

Table 7.2. Summary of characterization studies of the biomimetic hydrogel/CaP nanocomposites

Samples	XRD	XRD, FTIR	NMR	STEM, HRTEM, SAED	SAXS, SANS	TGA
	Gel	Vacuum dried	Vacuum dried	Gel diluted to 5 wt% Polymer	Gel morphology	Dried
Pluronic30-8	HAp	HAp	HAp	Elongated plate-like HAp	FCC	35 wt% CaP
Pluronic-Pep22-8	HAp	HAp	HAp	Elongated plate-like HAp	FCC	45 wt% CaP
PentaPAA-Pep30-8	HAp	HAp	HAp	Elongated plate-like HAp	BCC	40 wt% CaP
PentaPZ-Pep45-8	HAp/ Brushite	HAp	HAp/ Brushite	Elongated plate-like HAp	HCPC	30 wt% CaP

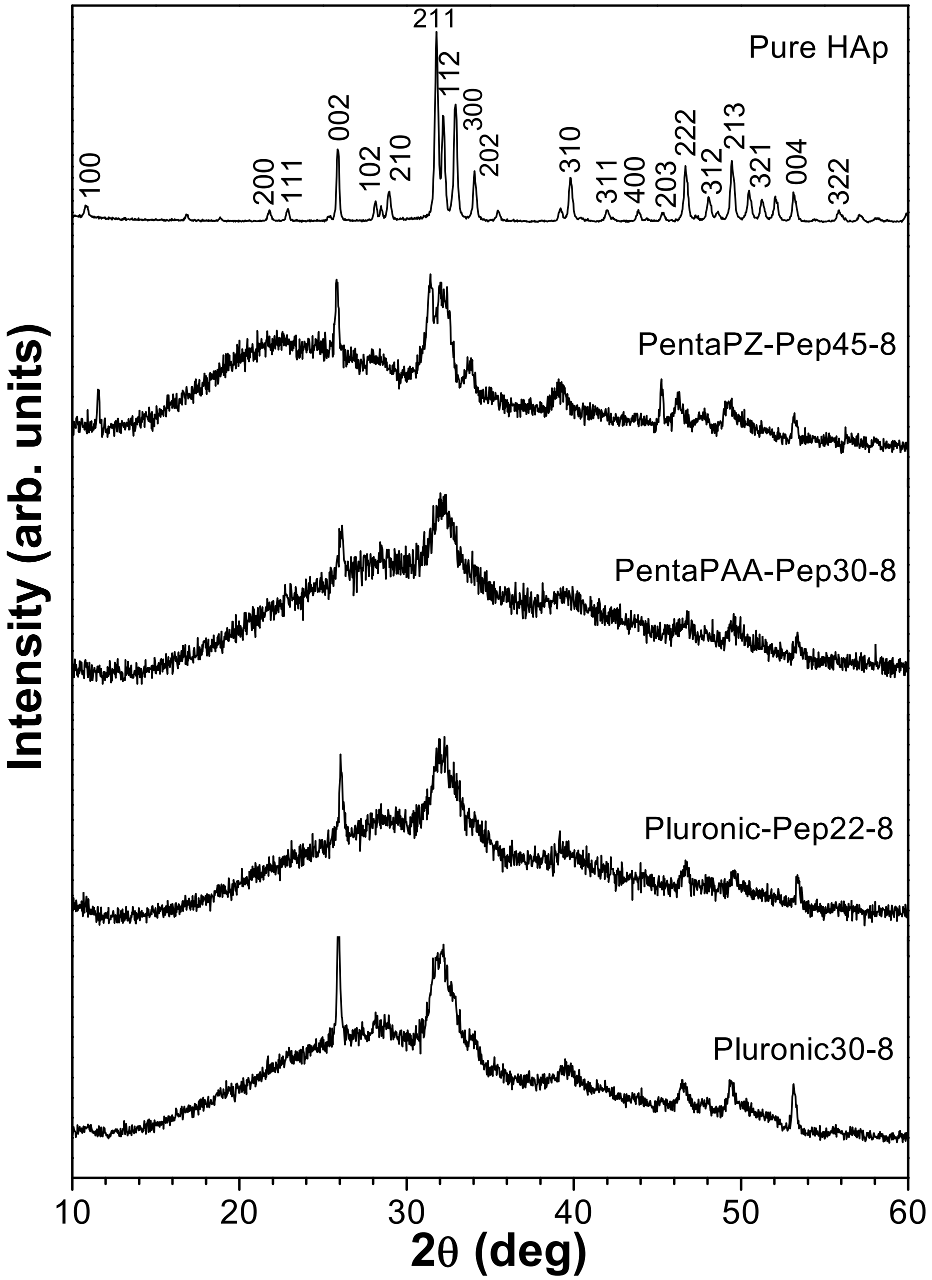

Figure 7.1. XRD patterns of as-prepared calcium phosphate/hydrogel nanocomposites PentaPZ-Pep45-8, PentaPAA-Pep30-8, Pluronic-Pep22-8, Pluronic30-8, and pure HAp (Standard Reference Material® 2910).

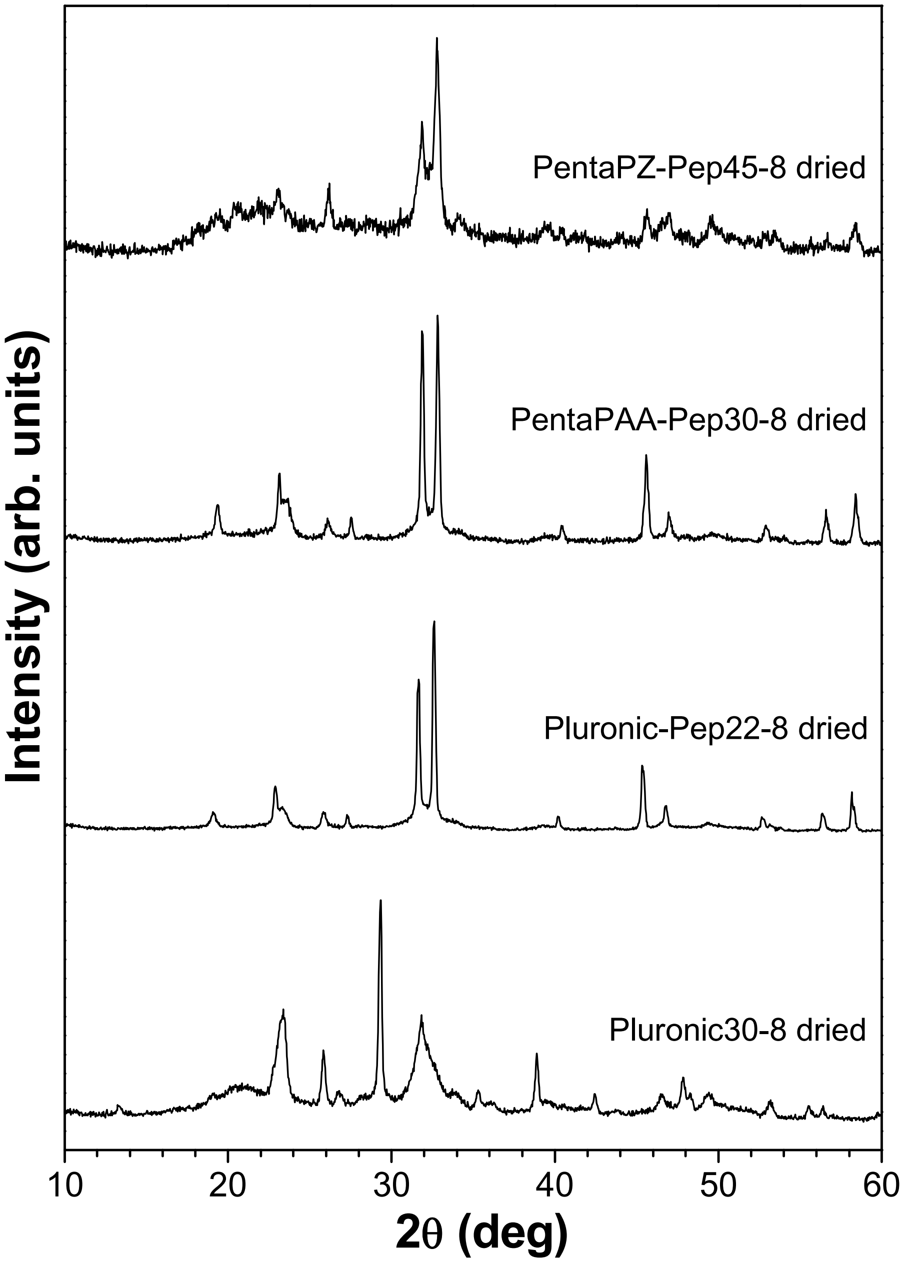

Figure 7.2. XRD patterns of vacuum-dried PentaPZ-Pep45-8, PentaPAA-Pep30-8, Pluronic-Pep22-8, and Pluronic30-8.

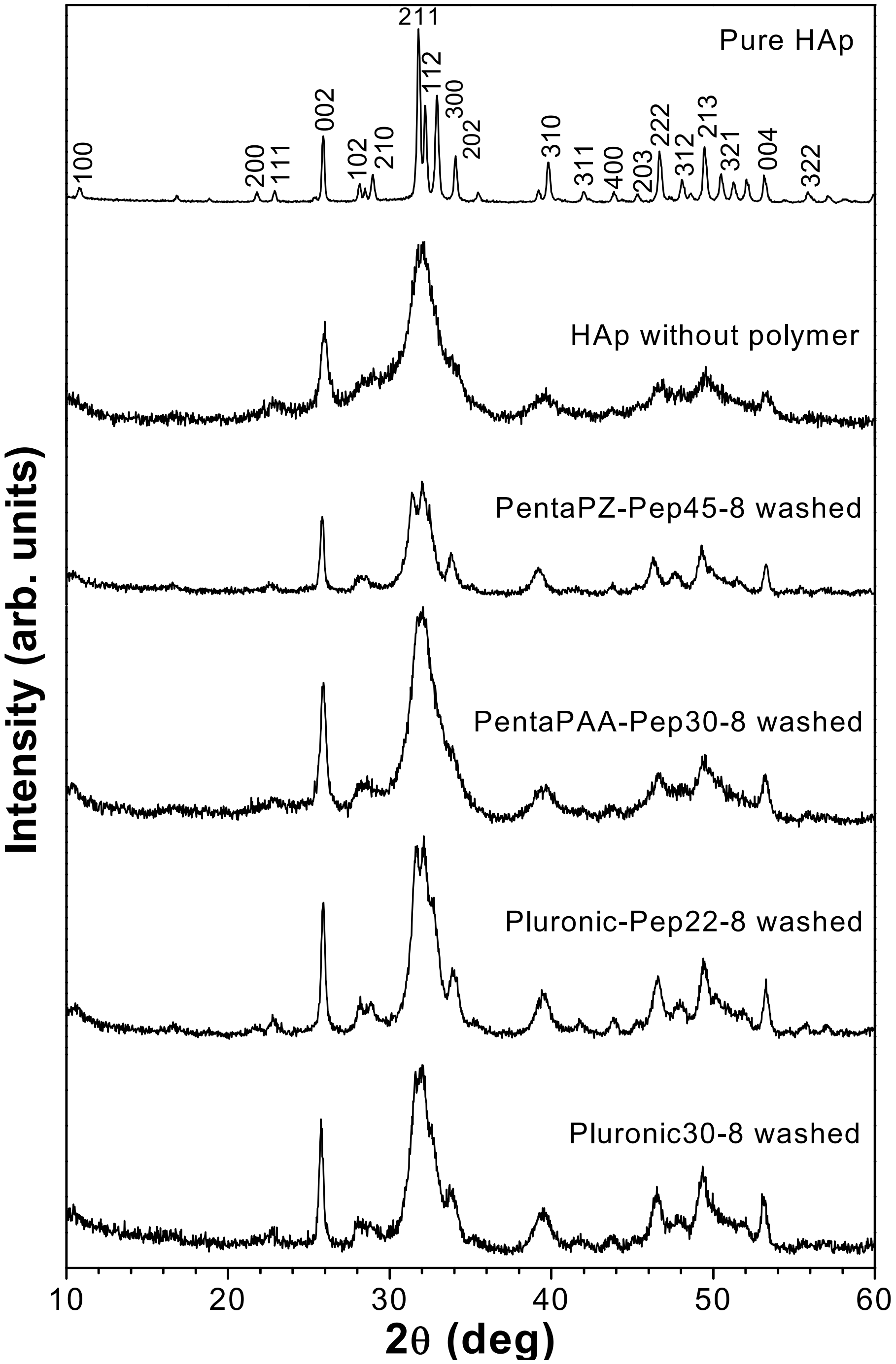

Figure 7.3. XRD patterns of washed PentaPZ-Pep45-8, PentaPAA-Pep30-8, Pluronic-Pep22-8, Pluronic30-8, HAp precipitated from an aqueous solution at pH~8 without any polymer and Pure HAp (Standard Reference Material® 2910).

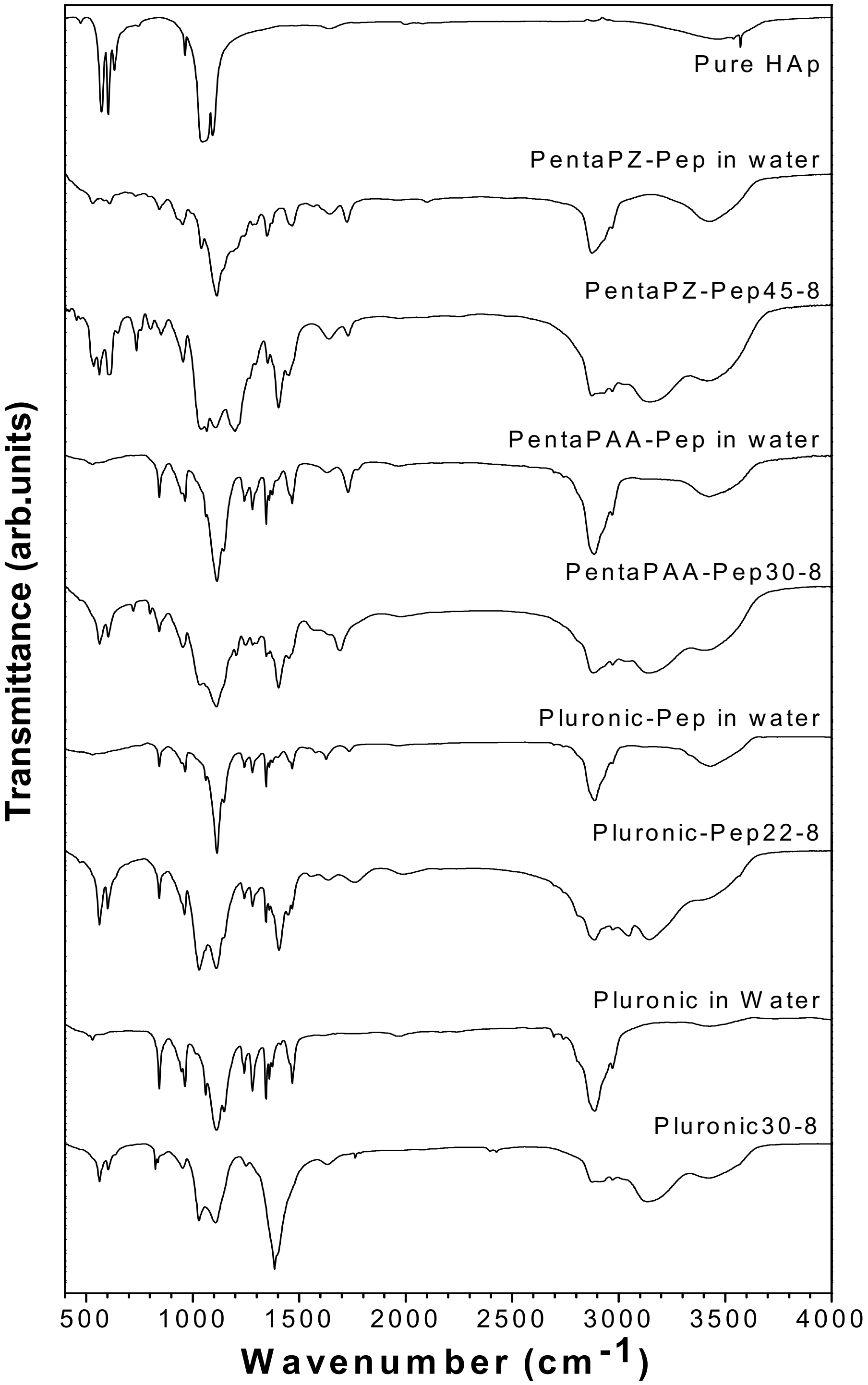

Figure 7.4. The FTIR spectra of the vacuum-dried HAp/nanocomposite samples, corresponding vacuum-dried polymer/water samples (control solutions), and pure HAp (Standard Reference Material® 2910).

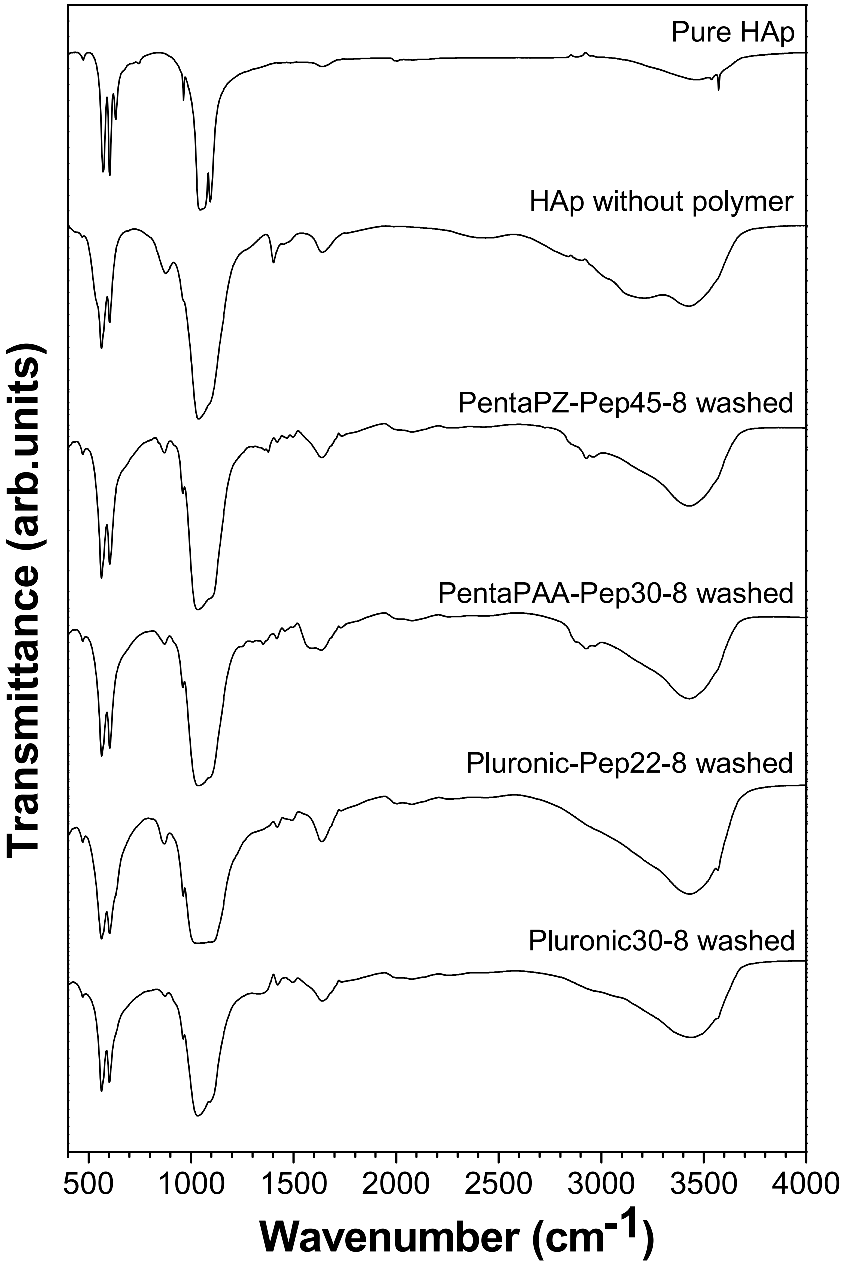

Figure 7.5. FTIR spectra of the polymer-removed HAp/nanocomposite samples, HAp precipitated without any polymer, and Pure HAp (Standard Reference Material® 2910).

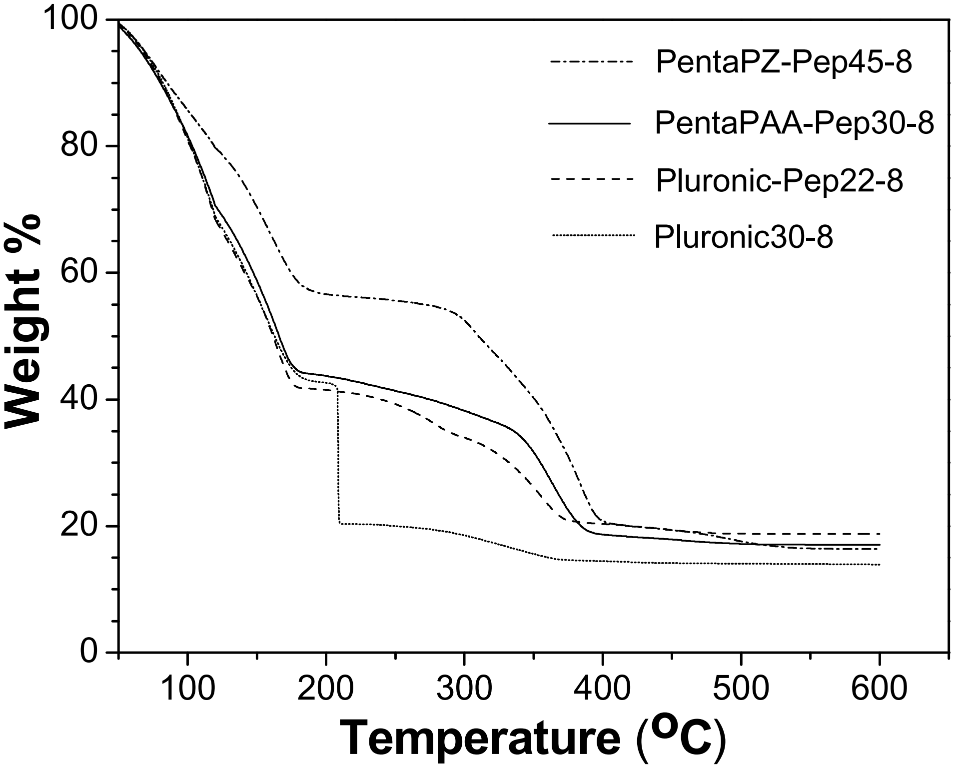

Figure 7.6. TGA traces of PentaPZ-Pep45-8, PentaPAA-Pep30-8, Pluronic-Pep22-8, Pluronic30-8 hydrogel samples.

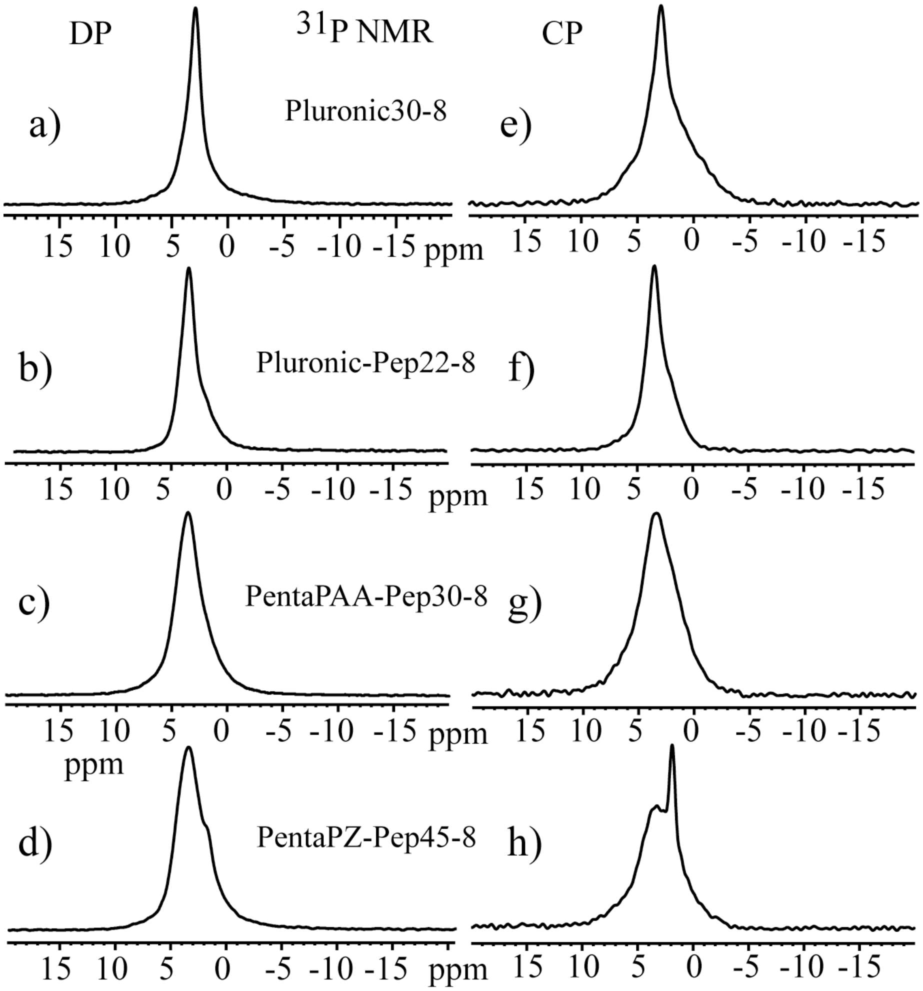

Figure 7.7. (left column) DP/MAS and (right column) CP/MAS ^{31}P NMR spectra of synthesized nanocomposites. (a) and (e) Pluronic30-8. (b) and (f) Pluronic-Pep22-8. (c) and (g) PentaPAA-Pep30-8. (d) and (h) PentaPZ-Pep45-8.

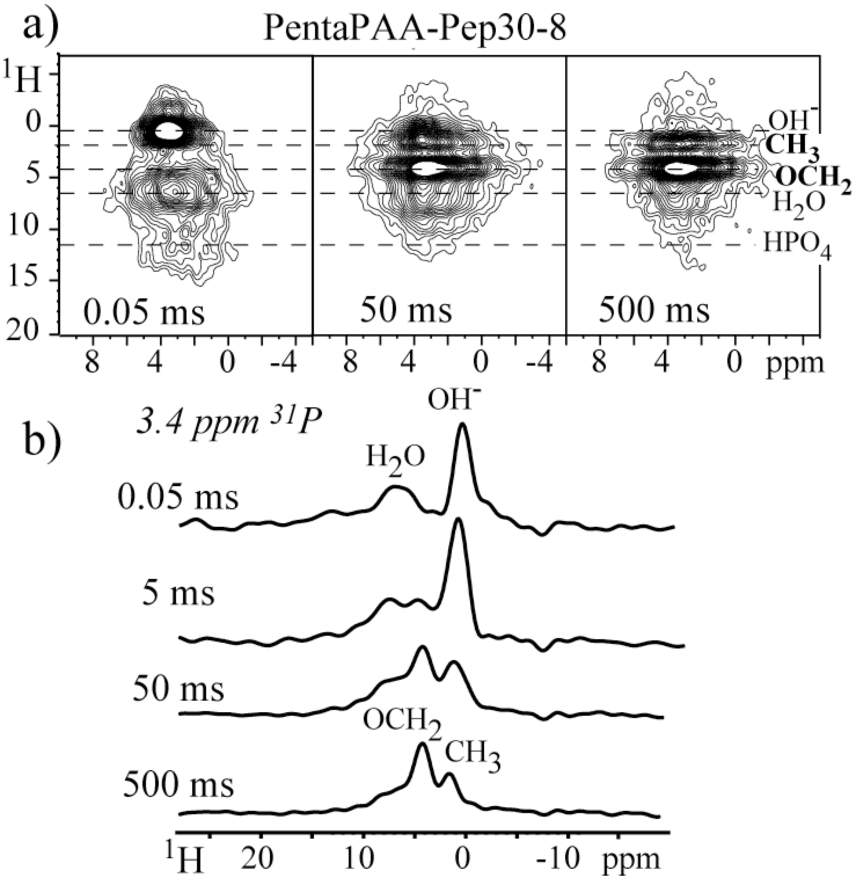

Figure 7.8. (a) 2D ^{1}H-^{31}P HETCOR NMR spectra of PentaPAA-Pep30-8 with spin diffusion mixing times of 0.05, 50, and 500 ms. (b) Cross-sections of the 2D spectra at 3.4 ppm (^{31}P).

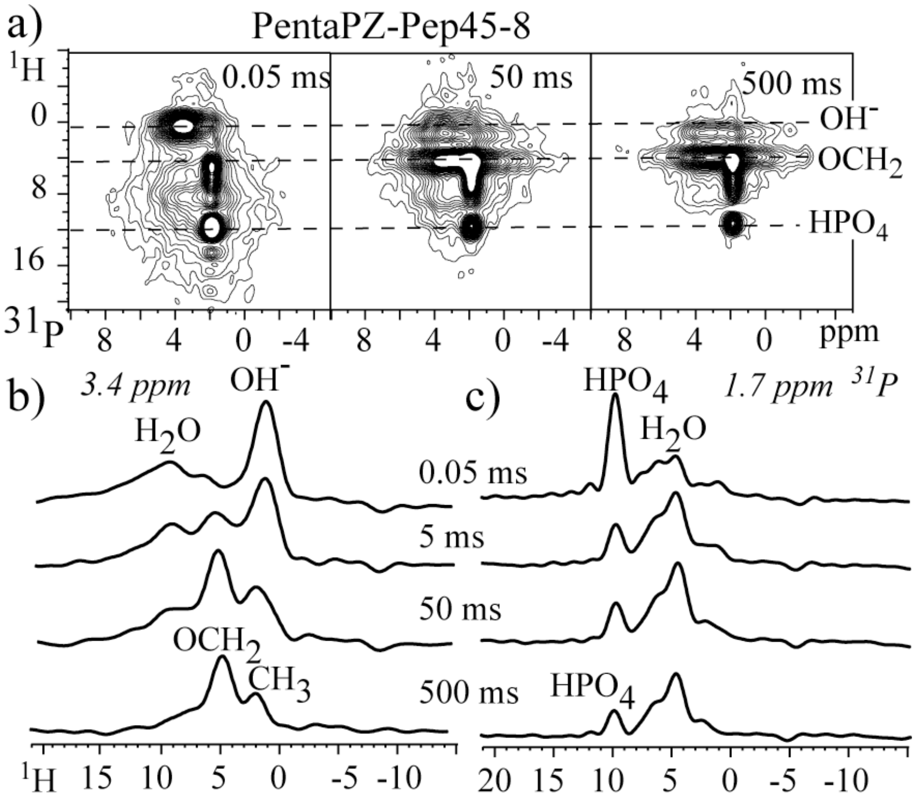

Figure 7.9. (a) 2D ^{1}H-^{31}P HETCOR NMR spectra of PentaPZ-Pep45-8 with spin diffusion mixing times of 0.05, 5, 50, and 500 ms. (b) and (c) Cross-section of the 2D spectra at 3.4 ppm and 1.7 ppm (^{31}P).

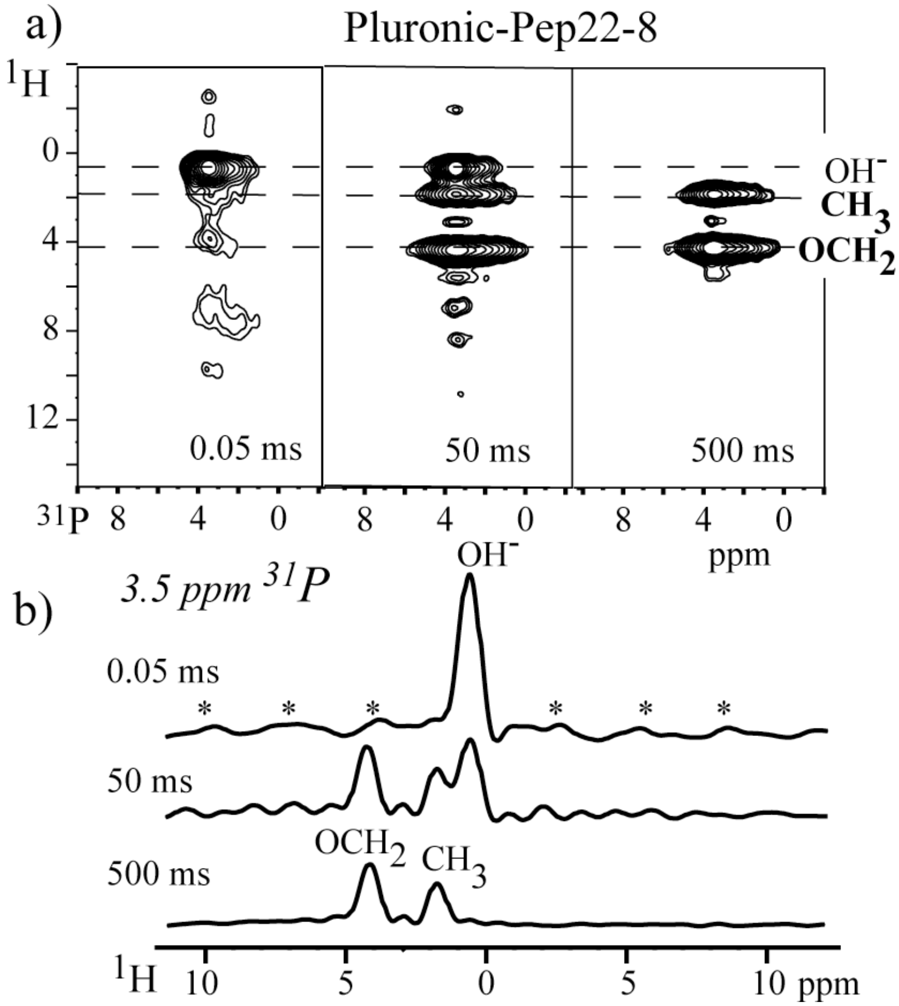

Figure 7.10. (a) 2D ^{1}H-^{31}P "WISE" NMR spectra of Pluronic-Pep22-8 with spin diffusion mixing times of 0.05, 50, and 500 ms. (b) Cross-section from the 2D at 3.5 ppm (^{31}P). The H_2O signal shows spinning sidebands, marked by asterisks.

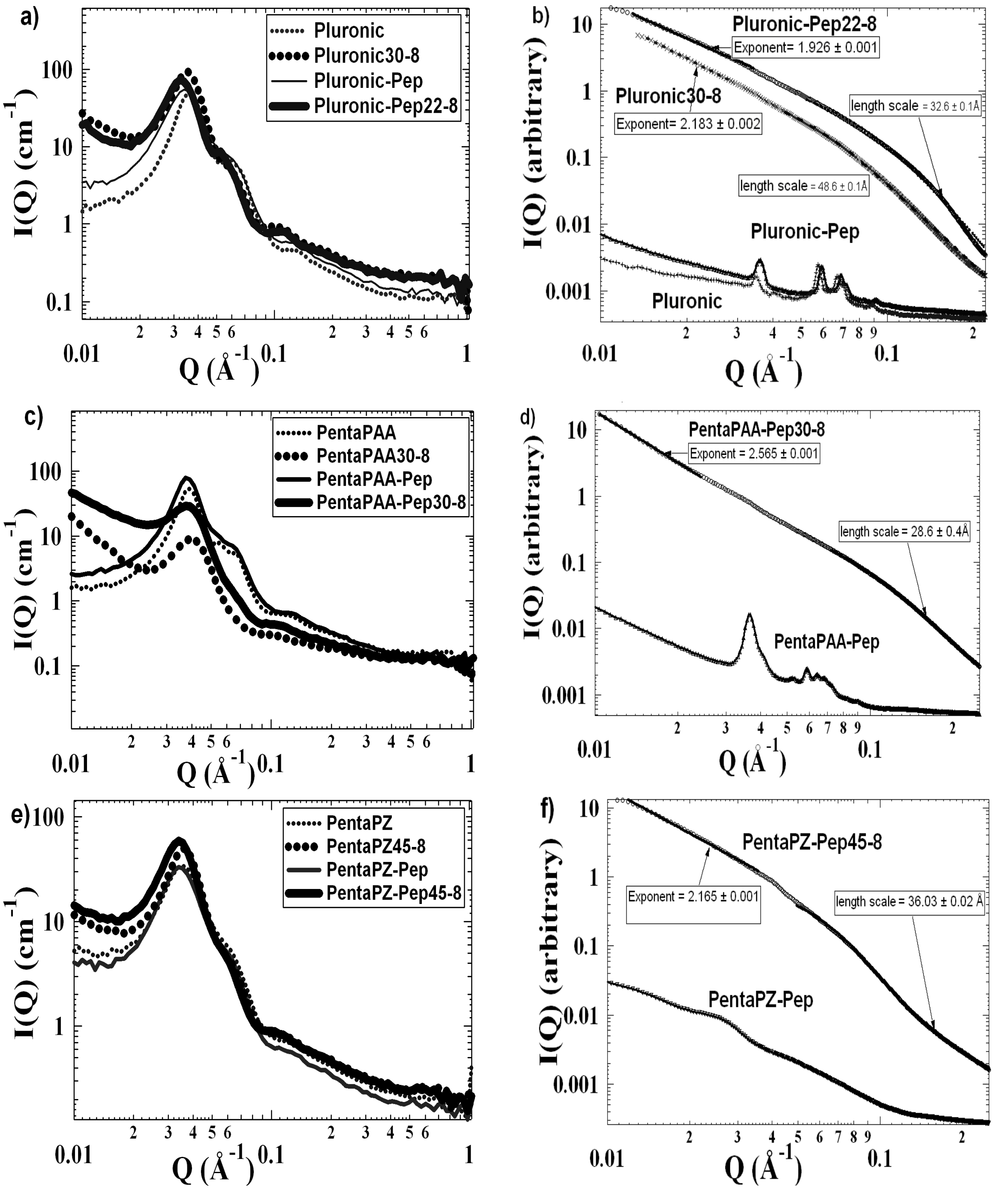

Figure 7.11. (a) SANS and (b) SAXS of gels of neat Pluronic, Pluronic-Pep, and corresponding nanocomposites at pH 8.0; (c) SANS and (d) SAXS of gels of neat PentaPAA-Pep and corresponding nanocomposite; (e) SANS and (f) SAXS of the gels of PentaPZ-Pep and corresponding inorganic nanocomposite. The high Q regions of the SAXS data were fitted using a combined equation consisting of an exponential and a power law, and the low Q data were fitted using a power law.

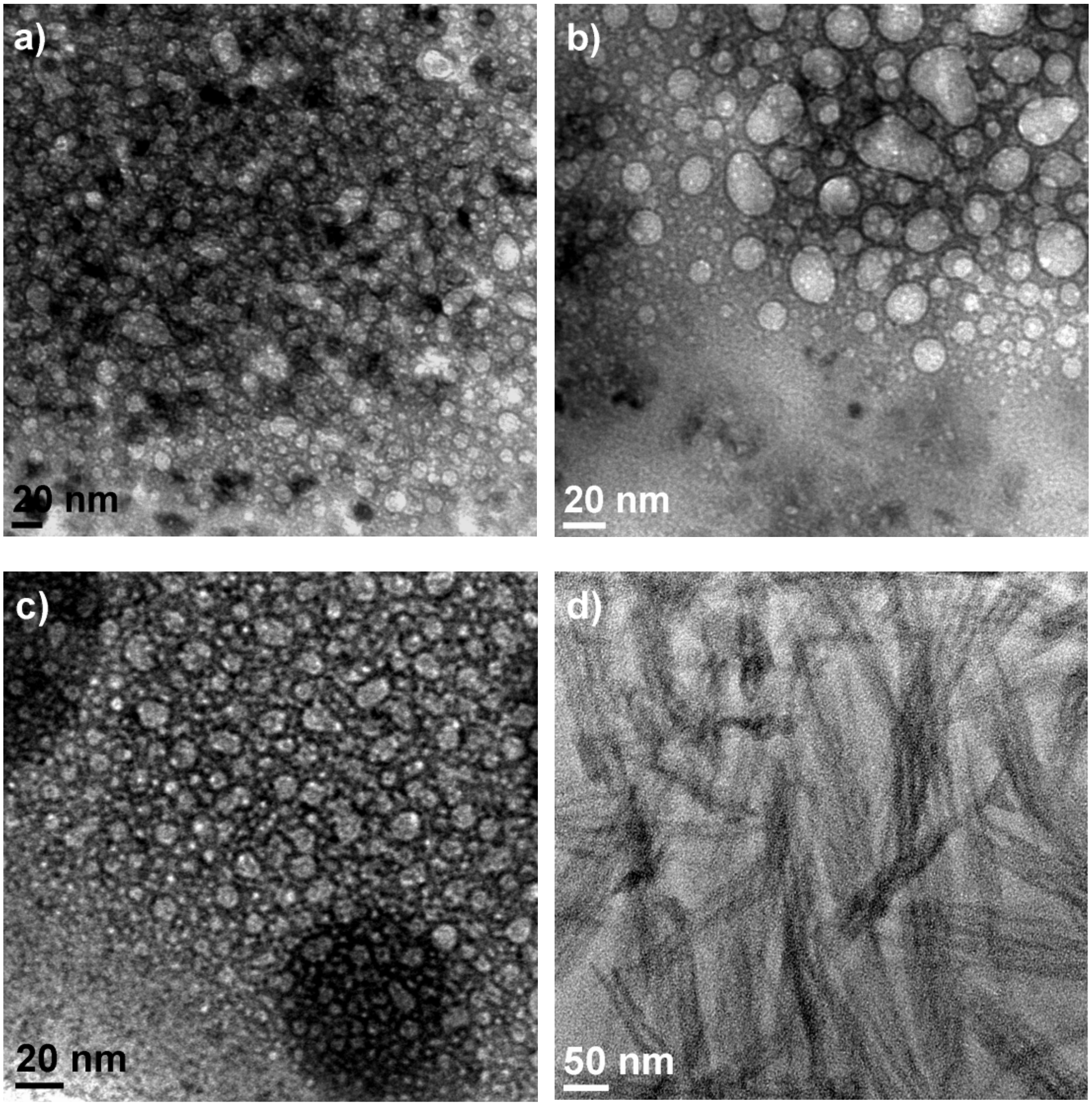

Figure 7.12. STEM/HAADF micrographs of 5 wt% of polymer solutions prepared in deionized water and stained; (a) Pluronic, (b) Pluronic-Pep, (c) PentaPAA-Pep, and d) PentaPZ-Pep. Light regions: Polymer.

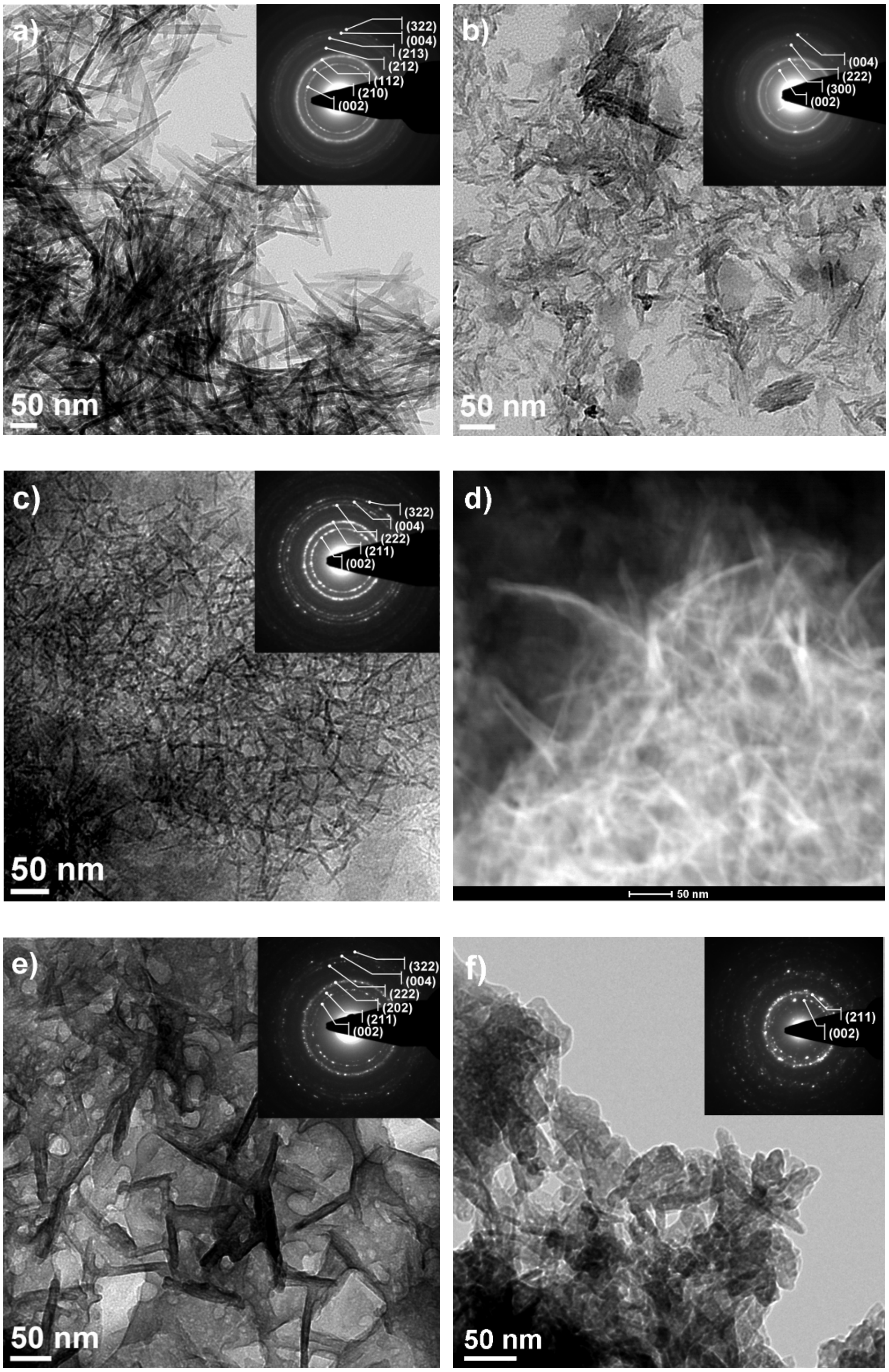

Figure 7.13. BF-TEM images and corresponding SAED patterns of 5 wt% (a) Pluronic30-8, (b) PentaPAA-Pep30-8, (c) Pluronic-Pep22-8, (e) PentaPZ-Pep45-8, and (f) HAp nanocrystals obtained by direct synthesis from an aqueous solution at pH ~ 8 without any polymer. d) STEM image of Pluronic-Pep22-8.

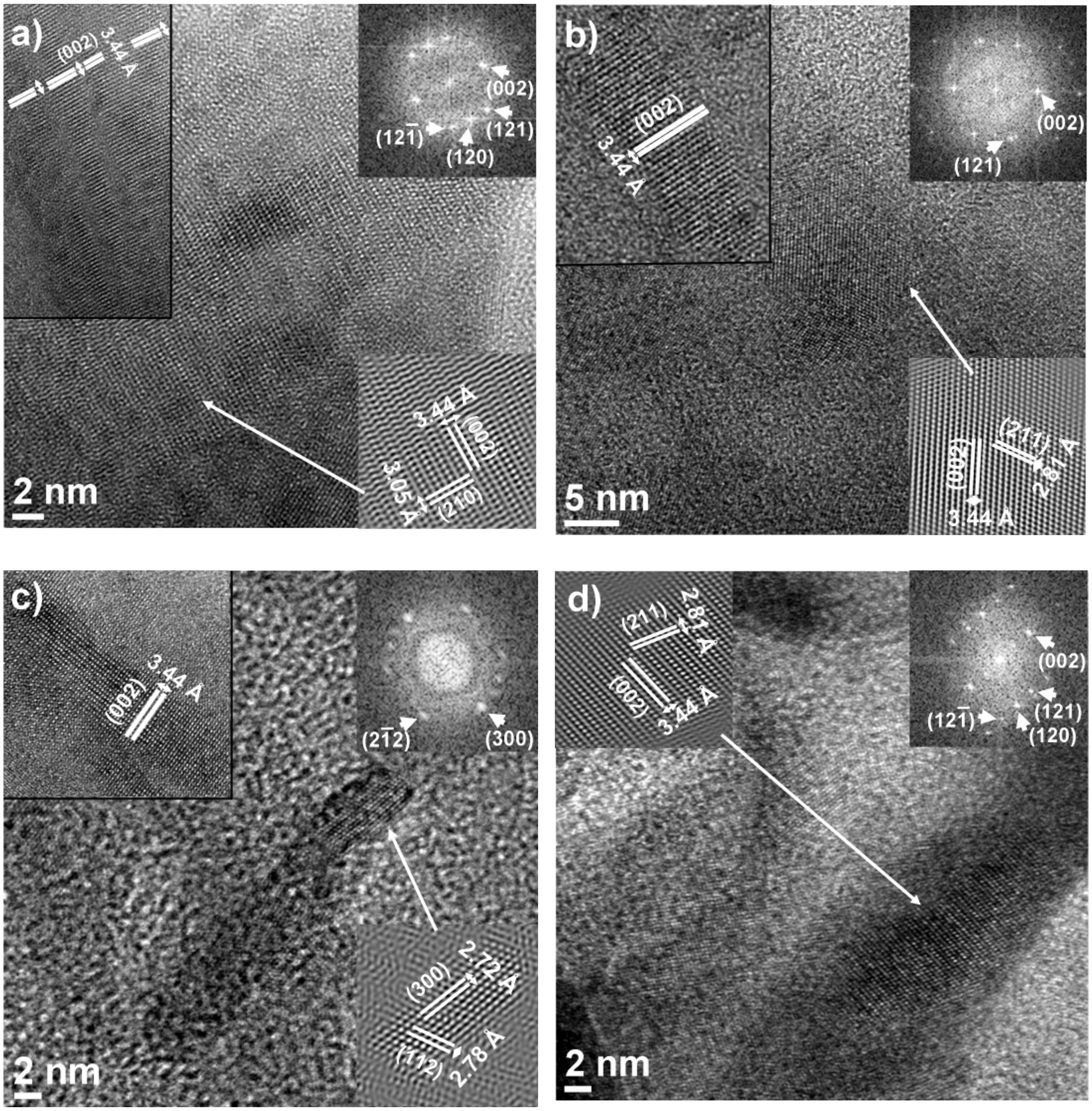

Figure 7.14. HRTEM images of (a) Pluronic30-8, (b) PentaPAA-Pep30-8, c) Pluronic-Pep22-8, (d) PentaPZ-Pep45-8. The upper right and lower insets show the FFT patterns and filtered inverse-FFT images, respectively, while the upper left insets show HRTEM images taken from plate-like crystals in longitudinal sections.

7.7 References

1. J. Aizenberg. *Advanced Materials*, (2004); 16, p: 1295-1302.
2. J.L. Arias, A. Neira-Carrillo, J.I. Arias, C. Escobar, M. Bodero, M. David, and M.S. Fernandez. *Journal of Materials Chemistry*, (2004); 14, p: 2154-2160.
3. B.L. Smith, G.T. Paloczi, P.K. Hansma, and R.P. Levine. *Journal of Crystal Growth*, (2000); 211, p: 116-121.
4. Z.Y. Tang, N.A. Kotov, S. Magonov, and B. Ozturk. *Nature Materials*, (2003); 2, p: 413-U418.
5. M. Aizawa, H. Ueno, K. Itatani, and I. Okada. *J. European Cer. Soc.*, (2006); 26, p: 501-507.
6. E.G. Bellomo and T. Deming. *JACS*, (2006); 128, p: 2276-2279.
7. J.N. Cha, G.D. Stucky, D.E. Morse, and T.J. Deming. *Nature*, (2000); 403, p: 289-292.
8. G. Falini, M. Gazzano, and A. Ripamonti. *J. Mater. Chem.*, (2000); 10, p: 535-538.
9. J.L. Sumerel, W. Yang, D. Kisailus, J.C. Weaver, J.H. Choi, and D.E. Morse. *Chem. Mater.*, (2003); 15, p: 4804-4809.
10. V. Bansal, D. Rautaray, A. Bharde, K. Ahire, A. Sanyal, A. Ahmad, and M. Sastry. *J. Mater. Chem.*, (2005); 15, p: 2583-2589.
11. V.M. Rusu, N. C.H., M. Wilke, B. Tiersch, P. Fratzl, and M.G. Peter. *Biomaterials*, (2005); 26, p: 5414-5426.
12. J. Song, V. Malathong, and C.R. Bertozzi. *JACS*, (2005); 127, p: 3366-3372.
13. J. Song, E. Saiz, and C.R. Bertozzi. *JACS*, (2003); 125, p: 1236-1243.
14. G. Xu, I. Aksay, and J.T. Groves. *JACS*, (2001); 123, p: 2196-2203.
15. J. Song, E. Saiz, and C.R. Bertozzi. *J. European Cer. Soc.*, (2003); 23, p: 2905-2919.
16. D. Enlow, A. Rawal, M. Kanapathipillai, K. Schmidt-Rohr, S. Mallapragada, C.T. Lo, P. Thiyagarajan, and M. Akinc. *J Mater. Chem.*, (2007); 17, p: 1570-1578.
17. S. Chang, H. Chen, J. Liu, D. Wood, P. Bentley, and B. Clarkson. *Calc. Tiss. Int.*, (2006); 78, p.
18. M. Determan, S. Seifert, P. Thiyagarajan, and S.K. Mallapragada. *Polymer*, (2005); 46, p: 6933-6946.
19. M. Kanapathipillai, Y. Yusufoglu, A. Rawal, Y. Hu, C.T. Lo, P. Thiyagarajan, Y. Kalay, M.A. Akinc, S.K. Mallapragada, and K. Schmidt-Rohr. *Chem. Mater.*, (2008); In press, p.
20. J.-F. Lutz, H.G. Boerner, and K. Weichenhan. *Macromolecular Rapid Communications*, (2005); 26, p: 514-518.
21. F. Zeng, H. Lee, and C. Allen. *Bioconjugate Chemistry*, (2006); 17, p: 399-409.
22. D. Bali, L. King, and S. Kim. *Australian Journal of Chemistry*, (2003); 56, p: 293-300.
23. V. Coessens, Y. Nakagawa, and K. Matyjaszewski. *Polymer Bulletin (Berlin)*, (1998); 40, p: 135-142.
24. K. Schmidt-Rohr. *Macromolecules*, (1992); 25, p: 3273-3277.
25. J.C. Elliott. *Studies in Inorganic Chemistry Volume 18: Structure and Chemistry of the Apatites and Other Calcium Orthophosphates,* (1994)*;* p: 404 pp.
26. S.V. Dorozhkin. *J. Mater. Sci.*, (2007); 42, p: 1061-1095.

27. Y. Yusufoglu and M. Akinc. *J. Am. Cer. Soc.*, (2008); 91, p: 77-82.
28. M. Kumar, H. Dasarathy, and C. Riley. *J. Biomed. Mater. Res.*, (1999); 45, p: 302-310.
29. R. Stulajterova and L. Medvecky. *Colloids and Surfaces, A: Physicochem. Eng. Aspects*, (2008); 316, p: 104-109.
30. S. Liao, F. Watari, M. Uo, S. Ohkawa, K. Tamura, W. Wang, and F. Cui. *J. Biomed. Mater. Res. Part B: Appl. Biomaterials*, (2005); 74B, p: 817-821.
31. M. Vallet-Regi and J.M. Gonzalez-Calbet. *Prog. in Solid State Chem.*, (2004); 32, p: 1-31.
32. S.A. Hutchens, R.S. Benson, B.R. Evans, H.M. O'Neill, and C.J. Rawn. *Biomaterials*, (2006); 27, p: 4661-4670.
33. Z. Li, Y. Li, A. Yang, X. Peng, X. Wang, and Z. Xiang. *J. Mater. Sci.: Materials in Medicine*, (2005); 16, p: 213-219.
34. C. Lai, S. Tang, Y. Wang, and K. Wei. *Materials Letters*, (2004); 59, p: 210-214.
35. E. Landi, G. Celotti, G. Logroscino, and A. Tampieri. *J. Eur. Cer. Soc.*, (2003); 23, p: 2931-2937.
36. J. Barralet, J.C. Knowles, S. Best, and W. Bonfield. *J. Mater. Sci.: Materials in Medicine*, (2002); 13, p: 529-533.
37. B. Feng, J.Y. Chen, S.K. Qi, L. He, J.Z. Zhao, and X.D. Zhang. *Biomaterials*, (2001); 23, p: 173-179.
38. W.L. Murphy and D.J. Mooney. *JACS*, (2002); 124, p: 1910-1917.
39. K. Sato. *Topics in Current Chemistry*, (2007); 270, p: 127-153.
40. S.V. Dorozhkin. *JACS*, (2007); 90, p: 244-249.
41. W.L. Suchanek, P. Shuk, K. Byrappa, R.E. Riman, K.S. TenHuisen, and V.F. Janas. *Biomaterials*, (2001); 23, p: 699-710.
42. D. Tadic and M. Epple. *Biomaterials*, (2004); 25, p: 987-994.
43. I. Manjubala, S. Scheler, J. Bossert, and D. Jandt Klaus. *Acta biomaterialia*, (2006); 2, p: 75-84.
44. W.P. Rothwell, J.S. Waugh, and J.P. Yesinowski. *J. Am. Chem. Soc.*, (1980); 102, p: 2637-2643.
45. J.P. Yesinowski and H. Eckert. *Journal of the American Chemical Society*, (1987); 109, p: 6274-6282.
46. S.S. Hou, F.L. Beyer, and K. Schmidt-Rohr. *Solid State Nucl. Magn. Reson.*, (2002); 22, p: 110-127.
47. P. Fratzl, N. Fratzl-Zelman, K. Klaushofer, G. Vogl, and K. Koller. *Calcif. Tissue Int.*, (1991); 48, p: 407-413.
48. X. Su, K. Sun, F.Z. Cui, and W.J. Landis. *Bone* (2003); 32, p: 150-162.
49. M. Kikuchi, T. Ikoma, S. Itoh, H.N. Matsumoto, Y. Koyama, K. Takakuda, K. Shinomiya, and J. Tanaka. *Comp. Sci. Technol.*, (2004); 64, p: 819-825.
50. J.P. Coates. *Appl. Spectr. Rev.*, (1996); 31, p: 179-192.
51. D.S.R. Krishna, A. Siddharthan, S.K. Seshadri, and T.S.S. Kumar. *J. Mater. Sci.: Materials in Medicine*, (2007); 18, p: 1735-1743.

CHAPTER 8. SELF-ASSEMBLED CALCIUM PHOSPHATE NANOCOMPOSITES USING BLOCK COPOLYPEPTIDE TEMPLATES

A paper accepted by *Soft Matter*

Yanyan Hu[a+], Yusuf Yusufoglu[a+], Mathumai Kanapathipillai[a], Chu-Ya Yang[b], YaQiao Wu[a], Papannan Thiyagarajan[c], Timothy Deming[b], Mufit Akinc[a], Klaus Schmidt-Rohr[a], and Surya Mallapragada[a-]

8.1 Abstract

Polylysine and polyleucine based block copolypeptides ($K_{170}L_{30}$) that form gels at very low concentrations in aqueous media are used as templates for forming self-assembled calcium phosphate nanocomposites. The synthesis method allows for simultaneous formation of the self-assembled block copolypeptide gel and of the inorganic phase, providing inorganic contents of over 50 wt% in the nanocomposite, approaching the inorganic content in bone. The self-assembled nanocomposites are characterized by thermogravimetric analysis, X-ray diffraction (XRD), Fourier transform infrared (FTIR) spectroscopy, solid state nuclear magnetic resonance (NMR), transmission electron microscopy (TEM) and small angle X-ray scattering (SAXS). The nanocomposites formed in the presence of the block copolypeptide templates exhibit very different nanoparticle morphologies than those formed in the absence of the organic phase. Multinuclear solid state NMR methods are used to prove nanocomposite formation and characterize the secondary structure and mobility of the block copolypeptide template. The data from XRD, FTIR, and ^{31}P NMR consistently show that the

inorganic phase present in the nanocomposite is carbonated hydroxyapatite of nano-scale dimensions, with an elongated plate-like morphology, observed by TEM and SAXS, very similar to the mineral phase of natural bone. Overall, this approach allows a bioinspired bottom-up approach to self-assembled hydroxyapatite nanocomposites using block copolypeptide templates, which could have applications in tissue repair.

[+] Primary researchers and both authors contributed equally to the work
[a] Ames Laboratory, Iowa State University, Ames, IA 50011
[b] Department of Bioengineering, University of California, Los Angeles, CA 90095
[c] Argonne National Laboratory, 9700 S. Cass Ave, Argonne, IL 60439
[-] Author for correspondence

8.2 Introduction

In biological systems, calcium phosphate ceramics are the most important inorganic components of hard tissues, and synthetic substitutes have been used in medicine and dentistry for more than 20 years [1]. Among the six principal calcium salts of orthophosphoric acid, hydroxyapatite (HAp: $Ca_{10}(PO_4)_6(OH)_2$) is the best known because of its compositional and biological similarities to the mineral phase of the human bone. For instance, apatite in the form of carbonated hydroxide-deficient hydroxyapatite (CO_3HAp) including a variety of other minor dopants is present in natural bone to impart stiffness and hardness [1, 2]. It accounts for approximately 65 wt% of total bone mass with the remaining being mainly collagen and water [3, 4]. In bone formation, biomineralization produces a nanocomposite with layers of collagen molecules alternating with thin and elongated nanocrystals of carbonated apatite [5], in a process involving more than 200 different proteins [6]. These proteins act as inhibitors and nucleators for the growth of apatite nanocrystals, anchored to the collagen [5, 7]. The combination of inorganic and organic components provides increased toughness compared to HAp alone [8, 9]. As a result, biomaterials such as bone as well as dentine in teeth, in which the organic matrix acts as a guide and imparts toughness to the otherwise brittle inorganic phase, have attracted the interest of researchers into the investigation and development of novel organic-inorganic biocomposite materials suitable for prosthetic medical applications [8, 10].

Biocomposites of HAp in conjunction with various synthetic polymers [11-16] and natural polymers such as collagen [17-20], chitosan [8, 21-23], cellulose [24-26] and gelatin [4, 27, 28] have been investigated extensively. We have shown successful templating of calcium phosphates by self-assembling thermo-reversible cationic and Pluronic block-copolymer gels with 15 wt % inorganic content [29]. This method enabled the formation of self-assembled nanocomposites from solution by changing temperature. Subsequently, self-assembling thermo-reversibly gelling anionic and zwitterionic pentablock copolymers conjugated to hydroxyapatite nucleating peptides were used as templates for precipitation of calcium phosphate nanostructures [30]. The inorganic fraction of the nanocomposites was increased to about 30 - 40 wt% [31]. The inorganic content in these nanocomposites was still significantly lower than that seen in nature (65 wt %). The high polymer concentrations (~25wt %) needed for gel formation in these block copolymer systems is one limitation to increasing the weight fraction of the inorganic phase using these synthetic block copolymer templates.

In contrast, the Deming group has synthesized a family of novel block copolypeptides that form gels at very low concentrations (~0.5 wt %) and can serve as templates for biomineralization [32-35]. This paper investigates the use of these block copolypeptides as templates for forming self-assembled calcium phosphate nanocomposites. We demonstrate the formation of HAp/block copolypeptide ($K_{170}L_{30}$) polymer nanocomposites with a maximum inorganic content of approximately 53 wt %. This approach is similar to nature where protein templates commonly control the nucleation and growth of the inorganic nanocrystalline phase in biomaterials such as bone.

Wet-chemical methods lend themselves to the formation of calcium phosphate ceramics with good crystallinity, physiological stability, and morphological characteristics resembling those of hard tissues [36]. A number of papers have described different wet-chemical methods including chelate [37-39] or urea decomposition [40-42], precipitation [36, 43-46], and hydrolysis of calcium phosphate precursors [47-50]. In the present study, we used a precipitation method on the self-assembling block copolypeptide templates to obtain polymer-inorganic hydrogel composites. Compared to other methods, this is a relatively simple technique utilizing mild experimental conditions that preclude polymer degradation. The resulting nanocomposites have been characterized by X-ray diffraction, ^{31}P NMR, Fourier-transform infrared spectroscopy, and high-resolution transmission electron microscopy (HRTEM) to identify the phosphate phase(s) formed; by ^{1}H and ^{31}P spin-diffusion NMR to prove nanocomposite formation; by TEM and small-angle X-ray scattering to determine the shape of the crystallites; and by ^{13}C NMR to determine the secondary structure and mobility of the polypeptide matrix. We believe that this work may contribute towards understanding the fundamental mechanism of biomineralization that is essential for the development of novel bioinspired materials for hard tissue repair and regeneration.

8.3 Materials and Methods

All materials used were obtained from either Sigma Aldrich or Fisher Scientific and were of laboratory grade and purity.

Polypeptide synthesis

The polypeptide $K_{170}L_{30}$ was synthesized by the previously developed procedures [51]. Briefly, first, N_ε-CBZ-L-lysine and L-leucine monomers were converted to α-aminoacid-N-carboxyanhydrides (NCAs) to facilitate ring-opening polymerization. The NCA preparation was carried out with phosgene at 40°C in dry tetrahydrofuran. The monomers were then reacted with $(PMe_3)_4Co$ initiator in THF and the polypeptide copolymerization was carried out under inert conditions at room temperature for 1 hour with sequential addition of the NCA monomers. The polymers were then dissolved in trifluoroacetic acid and deprotected by adding 33% HBr in acetic acid to solutions of copolypeptide in trifluoroacetic acid at 0° C for 1 hour. The deprotected polymers were then dissolved in deionized water, dialyzed, and freeze dried. Polymer molecular weight and other chemical characteristics were determined by nuclear magnetic resonance (NMR), Fourier transform infrared (FTIR) spectroscopy and gel permeation chromatography (GPC). FTIR was used to verify the consumption of the monomer and the formation of amide bonds in the polypeptide backbones. Tandem gel permeation chromatography/light scattering (GPC/LS) was performed at 60 °C using an SSI Accuflow Series III pump equipped with Wyatt DAWN EOS light scattering and Optilab rEX refractive index detectors. Separations were achieved using 10^5, 10^4, and 10^3 Å Phenomenex Phenogel 5 μm columns with 0.1 M LiBr in DMF as eluent and sample concentrations of 5 mg/mL. The deprotection of the polymers was then verified using ^{1}H NMR.

Block copolypeptide – hydroxyapatite nanocomposite synthesis

To prepare calcium phosphate (CaP)-polypeptide nanocomposite hydrogel samples, the following procedure was used: 0.11 g $K_{170}L_{30}$ was mixed with 1.5 mL 4.0 M $Ca(NO_3)_2 \cdot 4H_2O$ solution. To dissolve the polypeptide and form the hydrogel, the calcium containing polymer solution was kept at room temperature for two days. Then, 0.9 mL 4.0 *M* $(NH_4)_2HPO_4$ solution was added and aged at room temperature for an additional four days to form a CaP-hydrogel nanocomposite containing approximately 4.0 wt% polymer. In addition to the polypeptide and the inorganic phase, the gel contains mainly water along with some ammonium nitrate. The pH of the hydrogel sample was adjusted to ~ 8 from an initial pH of around 3 by adding NaOH solution. The formation of HAp in CaP/polymer hydrogel is believed to take place through the following simplified chemical reaction:

$$10Ca(NO_3)_2 + 6(NH_4)_2HPO_4 + 2H_2O \rightarrow Ca_{10}(PO_4)_6(OH)_2 + 12NH_4NO_3 + 8HNO_3 \qquad (1)$$

Characterization

Calcium phosphate nanocomposite samples were analyzed by using techniques of X-ray diffraction (XRD), FTIR spectroscopy, thermogravimetric analysis (TGA), NMR, small angle X-ray scattering (SAXS), transmission electron microscopy (TEM), high resolution transmission electron microscopy (HRTEM), scanning transmission electron microscopy (STEM). Moreover, the atomic Ca/P ratio was also monitored by energy dispersive X-ray spectroscopy (EDS).

The structure and crystallinity of the as-prepared nanocomposite samples were investigated by a powder X-ray diffractometer (X'Pert PRO, PANalytical Inc., Westborough, MA) using a monochromatic CuKα radiation (λ=0.15418 nm) and operating at 45 kV and 40 mA. The scanning rate was 0.008^{o}/s with a step size of 0.017^{o} over a range of $10^{o} \leq 2\theta \leq 60^{o}$. Scintag DMSNT search/match software and the ICDD 2007 database were used for the phase analysis.

Chemical analysis of the samples was carried out by a Bruker FTIR spectrometer (Bruker IFS-66v, Bruker Optics Inc., Billerica, MA) over the range between 400-4000 cm^{-1} with a resolution of 4 cm^{-1} and averaging 32 scans. NMR studies (see below) require vaccum dried samples; therefore the XRD patterns of vaccum dried samples both before and after washing were obtained, to confirm the removal of ammonium nitrate during washing.

For the FTIR analysis of all the different samples mentioned above, the samples were pressed into KBr pellets containing approximately 1 wt% sample. The inorganic phase (HAp) content of the nanocomposites was estimated with a Perkin Elmer thermo gravimetric analyzer (Perkin Elmer, TGA 7, Downers Grove IL). Approximately 50 mg of the gel sample, the vaccum dried nanocomposite and the washed sample after vaccum drying, were heated to 50^{o}C under air flow conditions, held at this temperature for 1 min, then ramped to 120^{o}C at a rate of 5.0^{o}C/min, and at a rate of 10.0^{o}C/min to 550^{o}C. XRD patterns and FTIR spectra of the calcined samples, after being subject to thermogravimetric analysis, were also obtained.

Solid State NMR. Solid state NMR experiments were performed using a Bruker DSX400 spectrometer (Bruker-Biospin, Rheinstetten, Germany) at 400 MHz for ^{1}H, 162 MHz for ^{31}P and 100 MHz for ^{13}C with a Bruker 4-mm magic-angle spinning double resonance probehead at ambient temperature. All samples were analyzed without washing, but were vacuum dried before NMR experiments because solid state NMR requires relatively dry samples to avoid power absorption by ionic conduction. The 90^{o} pulse lengths were 4 μs for ^{1}H, 4.7 μs for ^{31}P and 4 μs for ^{13}C. All the ^{31}P and ^{1}H NMR experiments were carried out at spinning speed of 6.5 kHz, while ^{13}C NMR experiments were at 4 kHz. ^{31}P direct polarization experiments, including those with gated recoupling, were performed with recycle delays of 100 s. ^{1}H-^{31}P correlation experiments without ^{1}H homonuclear decoupling, using the wideline separation (WISE) NMR pulse sequence with hypercomplex data acquisition, were carried out with 256 20-μs t_1 increments and 2-s recycle delays. 2D ^{1}H-^{31}P heteronuclear correlation (HetCor) NMR experiments were carried out with 100 44-μs t_1 increments of FSLG homonuclear decoupling and 2-s recycle delays. Lee-Goldburg cross polarization (LGCP) was used for polarization transfer from ^{1}H to ^{31}P in both "WISE" [52] and HetCor experiments with contact times of 0.7 ms and 0.5 ms, respectively. 1D ^{31}P spin diffusion experiments after 0.1 ms of cross polarization were accomplished with spin diffusion times of 0.1, 0.5, 1, 5, 10, 50, 100, 500 ms, and 1 s. ^{13}C cross polarization and cross polarization with gated decoupling of 40 μs were used to detect the mobile components in the polypeptide phase. These ^{13}C related experiments were carried out with recycle delays of 2 s and 45,056 scans. ^{1}H one-pulse NMR spectrum was obtained with 3.8 μs ^{1}H 90^0 pulse and background suppression. Two-pulse phase-modulation (TPPM) was used for heteronuclear dipolar decoupling in all these experiments. The proton peak at 0.18 ppm and ^{31}P peak at 2.8 ppm of NIST hydroxyapatite were used as secondary references to calibrate the ^{1}H and ^{31}P chemical shifts, respectively. The C=O carbon peak at 176.49 ppm of 25% ^{13}C labeled α-glycine was used for ^{13}C chemical shift calibration.

Electron Microscopy. STEM, HRTEM, Selected-Area Electron Diffraction (SAED), and EDS studies were performed with a FEI-Tecnai G^2 F20 (FEI Inc., Hillsboro, Oregon) scanning transmission electron microscope equipped with EDS (EDAX Inc., Mahwah, NJ) using a CCD camera and Digital Micrograph Software (Gatan, Pleasanton, CA). For the TEM analysis, small amount of HAp/copolypetide hydrogel sample was placed onto a Formvar-coated copper grid and a negative contrast stain consists of 1.0% ammonium molybdate at pH ~ 8 was applied. After applying the stain, the excess solution was wicked and sample was allowed to dry.

Small angle X-ray scattering (SAXS). The structural order and length scale of polymer gel structure were estimated by SAXS. Scattering measurements were performed at the 12-ID beam line at the Advanced Photon Source at Argonne National Laboratory. Gel nanocomposite samples were sandwiched between kapton tapes, and placed 2 m from the detector to investigate the nanocomposite structure and templating properties of the polypeptide. A 15 x 15 cm detector was used to measure the scattered intensity and the transmitted intensity was measured using a photodiode. The beam energy used for the analysis is 12 keV (λ = 1.035 Å) and the data were collected at 1 s exposure, and the collected 2D data were corrected, azimuthally averaged.

8.4 Results and Discussion

The polylysine segment length was determined using GPC/LS, and ^{1}H NMR was used to determine the copolymer composition. Combined, these data showed that a block copolypeptide of $K_{170}L_{30}$ with low polydispersity was obtained. The consumption of the monomer and the formation of amide bonds from the polypeptide backbones (1650 cm^{-1}, 1540 cm^{-1}) were confirmed using FTIR measurements. ^{1}H NMR in deuterated TFA (d-TFA) indicated a 97%–98% removal of benzyloxycarbonyl groups from lysine residues.

The XRD patterns of the pure polymer (a), as-prepared HAp-polymer hydrogel (b), vacuum dried HAp/polymer composite (c), washed sample (after vacuum drying) (d), calcined sample (after TGA) (e), and pure HAp (Standard Reference Material® 2910) (f) are shown in Figure 8.1. XRD patterns of pure polymer and pure HAp (Standard Reference Material® 2910) are included in the XRD Figure 8.1 to compare with that of the nanocomposite sample. For pure polymer (see Figure 8.1a), two broad humps were observed at about $2\Theta=12^{o}$ and 22^{o} indicative of the amorphous nature of polymer. The 12^{o} peak might be attributed to rod-rod packing of helical poly-leucine chains. All diffraction peaks of as-prepared composite hydrogel (Figure 8.1b) were matched to those of pure HAp (Figure 8.1e) and the ICDD standard card (JCPDS 9-432). The results are also in accordance with the calcium phosphate pH–concentration diagram [53] and experimentally shown by Yusufoglu and Akinc [39] that the most stable calcium phosphate phase is HAp at pH >6. Furthermore, the broadening and overlap of the peaks (broad peak at $2\Theta \approx 31^{o}$ is a summed contributions of the (211), (112) and (300) planes of HAp) is a sign of small size or/and poor crystallinity of HAp crystals in the hydrogel sample. However, the crystallographic structure of HAp observed in the as-prepared HAp-polymer hydrogel is very similar to natural bone mineral and human dentine [6, 54, 55]. It is also worth noting that the as-prepared nanocomposite hydrogel shows a higher $I_{(002)}/I_{(211)}$ than that of pure HAp, indicating the preferential elongation of the crystals with the *c*-axis. Moreover, in addition to the characteristic HAp peaks, the XRD pattern of vacuum dried sample displayed some additional diffraction peaks belonging to ammonium nitrate (JCPDS 1-0809 and 76-2276) as indicated with solid circles in Figure 8.1c. Further, the sharp peak at $2\Theta=29.45^{o}$ matches well with the most intense peak of ammonium sodium nitrate (JCPDS 28-0490). After washing the vacuum dried sample with deionized water, all diffraction peaks belonging to ammonium (sodium) nitrate disappeared (Figure 8.1d) and leaving only HAp peaks. In addition, it is also worth noting that HAp is the only phase present after TGA experiments as shown in Figure 8.1e.

FTIR spectroscopic characterization of the nanocomposites

The FTIR spectra of the pure polymer (a), vacuum dried nanocomposite (b), washed sample (after vacuum drying) (c) and pure HAp (Standard Reference Material® 2910) (d) are shown in Figure 8.2. The FTIR spectrum of pure HAp (see Figure 8.2d) illustrates all the characteristic bands of stoichiometric HAp [36, 40]. As expected, the spectrum of pure HAp exhibits phosphate peaks at 965 cm^{-1} (a single intense band), 470 cm^{-1}, between 1050-1095 cm^{-1} and 565,602,635 cm^{-1} (three sites) for ν_1, ν_2, ν_3 and ν_4 respectively. The band at 3570 cm^{-1} is assigned to hydroxyl stretching [56].

The FTIR spectrum of pure polymer is shown in Figure 8.2a. The absorption band around 1630 cm^{-1} relates to amide I (mainly CO group stretching mode) [57] along with a N-H stretching peak at 3280 cm^{-1} [58]. The observed 1537 cm^{-1} peak is assigned to the amide II band arising mainly from the N-H bend and the C-N stretch [59]. Furthermore, the band at 1250 cm^{-1} is associated with amide III group (C-N stretch plus N-H in-plane deformation) [23, 60]. The absorption band at 1160 cm^{-1} is believed to be due to C-N stretch of amine groups. Moreover, N-H stretching of amine groups around 3350 cm^{-1} [61] contributes along with stretching of O-H and other groups to the broad peak observed between 2500 - 3500 cm^{-1} in Figure 8.2a. The broad peak at 2050 cm^{-1} is attributed to the $-NH_3^+$ bending mode [62], which is also observable in the spectrum of vacuum dried HAp/polymer composite. As can be seen from Figure 8.2a, the methylene rocking and C-H bending also appear at around 730 cm^{-1} and 1470 cm^{-1}, respectively. The small bands in the 1300 cm^{-1} region probably arise from -CH_2- deformation and wagging modes [60]. In addition, C-H bending of methyl and methyne groups are also observable at 1390 cm^{-1} and 1350 cm^{-1}, respectively [61]. In addition, C-H stretching peaks are also expected at 2850 - 2970 cm^{-1}, which probably contribute to the very broad peak in Figure 8.2a (between 2500-3500 cm^{-1}). The C-C vibrations can also be seen between 700–1080 cm^{-1} [61].

The FTIR spectrum of vacuum dried HAp/polypeptide nanocomposite can be seen in Figure 8.2b. The absorption bands at 566-601 cm^{-1}, 962 cm^{-1} and 1040-1100 cm^{-1} are associated with the phosphate groups of HAp. Moreover, the peaks at 1380 cm^{-1} and 832 cm^{-1} are assigned for nitrate groups, which is consistent with the results obtained from XRD study. It is well established that for nitrate groups, the first absorption (at 1380 cm^{-1}) is intense and broad, and the second (at 840 cm^{-1}) has medium intensity and is narrow [61]. Furthermore, the peaks associated with nitrate groups disappeared in the FTIR spectrum of the washed sample (Figure 8.2c). This implies that washing of the vacuum dried HAp/polymer composite removed nitrate species, consistent with the XRD results. As seen in the FTIR spectrum of the washed sample, in addition to the characteristic HAp absorption bands, the weak features arising from the vibrational modes of the carbonate were also observed at 873, 1415 cm^{-1} and 1462 cm^{-1} [48, 63], suggesting that the HAp contains carbonate ions. Even though CO_3^{2-} ions can replace both the OH site (A-type substitution) and the PO_4 site (B-type substitution) in HAp structure, the CO_3 peaks shown in Figure 8.2c are assigned only to the B-type substitution (CO_3 ions replaces PO_4 site) [48]. It is found that the CO_3 substitution at the PO_4 site in HAp crystals is commonly observed for preparation in aqueous systems [64], as has been also observed in the present work. As the apatite in human bone also contains CO_3 ions at about 4–8 wt% depending upon age, its presence in the HAp structure is beneficial [6, 65]. It is reported that at low concentration, CO_3 ions substantially improve the mechanical strength of apatite [65] and the presence of CO_3 ions in HAp structure also influences the decomposition, sinterability, solubility and biological reactivity of the apatite [45]. Since no carbonate source was present in the starting materials, carbonate incorporation into the HAp might be due to the atmospheric carbon dioxide as has been observed during mineral precipitation in carbonate-free solutions [25, 59]. Further, broad absorption bands centered around 3450 and 1640 cm^{-1} are due to incorporated water molecules [53, 56], which might also be present in Figures 8.2a and 8.2b along with the polymer related peaks in the same spectral region.

The TGA results of as-prepared HAp/polypeptide hydrogel, vacuum dried HAp/polypeptide nanocomposite, washed sample and pure HAp (Standard Reference Material® 2910) are illustrated in Figure 8.3. As can be seen from the trace of as-prepared HAp/polypeptide hydrogel, there is a sharp weight decrease between 70 and 175 ^{o}C, which is assigned to the loss of free and bound water. After vacuum drying, most of the water is removed (Figure 8.3b). The weight loss in the 200 – 450 ^{o}C range is due to thermal decomposition of polymer and perhaps ammonium nitrate (as shown in Figure 8.3c, weight loss between 200 and 450 ^{o}C is decreased for washed sample after removing ammonium nitrate). There is no change in sample weight above 500 ^{o}C, indicating that the polymer and nitrate species have decomposed completely by 500^{o}C. It is well established that HAp is thermally stable below 1000^{o}C [23] and there is almost no weight change for pure HAp between 50 – 570^{o}C, as shown in Figure 8.3a. As a result, the HAp content for the CaP/polymer nanocomposite is determined to be approximately 53 wt% based on the dried sample at 175 ^{o}C. This is consistent with the theoretical yield weight ratio of HAp/block copolypeptide composite, which is calculated from the amount of hydroxyapatite formed based on Eq.1.

NMR identification and quantification of phosphates

Figure 8.4 shows direct-polarization (DP) and cross-polarization (CP) ^{31}P NMR spectra of the synthesized composite. The DP spectrum shows one dominant band, whose chemical shift (2.8 ppm) agrees with that of hydroxyapaptite [66], though the linewidth is larger than for ideal HAp. The CP spectrum, which gives higher intensity to the phosphates close to protons, presents a different lineshape from DP, indicating the existence of more than one phosphate species. The broader base and significant intensity increase of the right shoulder of the CP spectrum suggests the presence of HPO_4^{2-} or of PO_4^{3-} hydrogen bonded to H_2O, in addition to apatitic PO_4^{3-}.

These assignments can be confirmed by recording ^{31}P DP spectra with 0 ms and 0.28 ms of recoupled ^{1}H-^{31}P dipolar dephasing, see Figure S1a (in the supplementary information in Apepndix B), where a more distinct lineshape results from the different dephasing behavior of PO_4^{3-} and HPO_4^{2-}. Provided similar mobility, the signal of phosphates that are protonated or hydrogen bonded will dephase faster than that of nonprotonated ones. The dephasing curves obtained from the gated decoupling experiments are shown in Figure S1b (see supplementary information in Apepndix B). The difference in dephasing rate shows that there are two different phosphate components. One is not protonated, with very slow dephasing, and the other is monoprotonated or hydrogen-bonded to a proton.

Based on the differential dephasing of the phosphate signals, the DP/MAS spectrum can be deconvoluted into two different components as shown in Figure 8.4a (dashed lines).

The sharp component is PO_4^{3-} of hydroxyapatite, accounting for 68% of all phosphates, the broad one is HPO_4^{2-} or hydrogen-bonded PO_4^{3-}, accounting for 32%.

NMR validation of nanocomposite formation

The one-dimensional spectra show that there are two types of phosphates present in the sample, but do not reveal whether they are part of nanocomposites. This information can be obtained by two-dimensional ^1H-^{31}P heteronuclear correlation NMR experiments with ^1H spin diffusion. Cross peaks between ^1H from the organic phase and ^{31}P from the inorganic phase are characteristic of nanocomposites [29, 67]. For nanocomposites, the polymer proton peaks will show up within tens to hundreds of milliseconds. In Figure 8.5, the spin diffusion from polymer protons to protons in the inorganic phase is indeed observed within 50 ms and equilibrium is reached within 500 ms. In samples with larger domains or for short spin diffusion times, the phosphates only “see” the protons close by, i.e. in the inorganic phase.

The series of ^1H-^{31}P correlation spectra in Figure 8.5a were acquired with homonuclear decoupling in the ^1H dimension. Figure 8.5b displays ^1H cross sections from the 2D spectra at 2.8 ppm ^{31}P, which demonstrate the spin diffusion process. On the time scale of 0.05 ms, phosphates only “see” OH^-, HPO_4^{2-} and H_2O protons. After 50 ms, the peak of a different H_2O species shows up, and within 500 ms, the CH and CH_2 proton signals come up along with a significant H_2O peak. The NH_4^+ peak of the polymer should also appear, but is overlapped by the dominant H_2O peak [68]. The completion of ^1H spin diffusion within 500ms is signified by the disappearance of OH^- and HPO_4 proton peaks. This proves the formation of a nanocomposite. Figure 8.5c reveals another ^1H environment associated with HPO_4^{2-} or $PO_4{\bullet}H_2O$. The appearance of the polymer proton peaks within 50 ms indicates fast spin diffusion, which is the evidence of nanocomposite formation.

Therefore, both types of phosphates, hydroxyapatite PO_4^{3-} and HPO_4^{2-}, are part of a nanocomposite.

Figure 8.6a shows a one-pulse ^1H spectrum with background suppression [69]. Several resolved peaks can be assigned according to their chemical shifts. H_2O and NH_3^+ peaks centered are at 7 ppm with a broad envelope; 7 ppm is the typical chemical shift of bound H_2O, while bulk water resonates at 5 ppm. After 18 hours of intensive vacuum drying of the samples at 105 ^oC in order to remove the mobile H_2O component, the 7 ppm peak shifted by 0.2 ppm and lost about 1/3 of its intensity, which means that the majority of H_2O in this composite is bound water. The broad peak of strongly bound water was observed at 0.05 ms in Figure 8.6b, indicating that the strongly bound water has intimate contact with the inorganic phase. The sharp peak of the weakly bound H_2O became dominant after 50 ms spin diffusion, which means that the weakly bound water is also close to the inorganic phase. After extensive drying, the previously resolved CH and CH_2 polypeptide peaks became invisible in the one-pulse ^1H spectrum, see Figure 8.6a (dashed line), which suggests that the removal of mobile H_2O reduces the mobility of the peptide. A band of NH_4^+, which happens to also resonate around 7 ppm, is present in the ^1H spectrum as a shoulder to the right of the intense water peak. ^1H T_1 measurements have shown that NH_4^+ has a longer T_1 than the components of the nanocomposite, proving that it forms a separate phase (NH_4NO_3).

The ^1H-^{31}P heteronuclear correlation experiments were also performed without ^1H homonuclear decoupling. Figure 8.6b and 8.6c displays cross sections from the 2D spectra (not shown) taken at 2.5 ppm and 0.5 ppm in the ^{31}P dimension. Without spin diffusion, the OH^- proton peak at 0.2 ppm in Figure 8.6b confirms the peak assignment of hydroxyapatite in the ^{31}P spectra of Figure 8.4. The strongly bound H_2O peak is not well resolved due to ^1H-

^{1}H homonuclear coupling, while the weakly bound H_2O presents a sharp peak on the broad base of the strongly bound H_2O. The HPO_4 peak seen in Figure 8.6c is not visible, likely also due to strong ^{1}H-^{1}H homonuclear coupling, which is common for interfacial HPO_4 species.

The 2D heteronuclear correlation experiments prove that both HPO_4 and hydroxyapatite are part of the nanocomposites, but do not establish whether they are in the same phase. This can be achieved instead by a one-dimensional ^{31}P spin diffusion experiment. If these two kinds of phosphates are in different phases, no ^{31}P spin diffusion between them will occur on the 10-s time scale. Conversely, fast spin diffusion from HPO_4 to hydroxyapatite proves that they are part of the same particle. After selection of HPO_4 ^{31}P magnetization by short cross polarization, narrowing of the line due to ^{31}P spin diffusion to PO_4^{3-} is actually observed within 1s (see Figure 8.7), confirming that HPO_4 and hydroxyapatite are in the same phase and separated by less than 10 nm. Most likely, HPO_4 is at the interface of the inorganic phase with the polymer.

NMR characterization of the polypeptide phase in the nanocomposite

^{13}C NMR experiments have been carried out to study the conformation and mobility of polypeptide in the synthesized nanocomposite. The ^{13}C spectrum is shown in Figure 8.8a (thin line). Peak assignments and literature values of solid-state ^{13}C NMR chemical shifts for α-helix and β-sheet conformations are marked above the spectra for reference [70, 71]. The chemical shifts indicate that hydrophobic leucine domain is α-helical and that most lysine segments adopt a β-sheet conformation, while the rest is in a random coil. This is consistent with the results of Deming and co-workers who have demonstrated that in hydrogels, 90% of the leucine domains of polypeptide $K_{160}L_{40}$ and $K_{180}L_{20}$ formed α-helices [51]. This shows that the α-helical structure of the poly-leucine domain [51] is retained even after the synthesis of the nanocomposite and vacuum drying. The peak intensities and the positions of the C_α and C_β signals are not consistent with the alternative assumption that the lysine segments are α-helical.

A corresponding CP ^{13}C NMR spectrum after 40 μs of gated decoupling was recorded in order to selectively detect mobile components of the polypeptide. High mobility will significantly reduce the C-H dipolar coupling, resulting in residual ^{13}C signals after gated decoupling. The resulting spectrum (thick line) in Figure 8.8a indicates that the backbone of the polypeptide is rigid, since all the C_α signals for both leucine and lysine are completely dephased. The side-chain carbons C_γ, C_δ and C_ε show significant residual intensity, which means that the side chains of the polypeptide are quite mobile.

Motions on the MHz scale generally induce fast T_1 relaxation, which enables another method to detect the mobile components. After direct polarization (DP) with a short recycle delay of 1 s, only signals of carbons with short T_1s are detected, see Figure 8.8b. Signals of all mobile carbons that are seen after gated decoupling (Figure 8.8a, thick line) are also present in Figure 8.8b, confirming the conclusions about mobility. Besides, the absence of the carbonyl (C=O) and $C\alpha$ signals in Figure 8.8b confirms the rigidity of the polypeptide backbone.

However, the 70:30 signal intensity ratio of the rigid backbone carbons of lysine components to those of leucine in the CP spectrum of Figure 8.9a does not match with the 85:15 stoichiometry of $K_{170}L_{30}$, which suggests some mobile lysine residues in the regularly vacuum dried sample are not detected in out CP spectra. In order to make these "invisible" components detectable, the intensively dried sample was studied. The ^{13}C spectra after CP and CP with gated decoupling are shown in Figure 8.9. Changes in the CP spectrum upon intensive drying are indeed observed. First, C=O signals of random-coil lysine that do not show up in Figure 8.8a, due to high mobility and resulting low CP efficiency, appear at 176 ppm after drying in Figure 8.9. Second, the C_α peak of random-coil lysine that appears as a shoulder next to the C_α signal of α-helix leucine in Figure 8.8a now shows up intensely in Figure 8.9 (thin line) and overlaps with the C_α peak from leucine. Above all, the ratio of lysine to leucine backbone carbons obtained from the CP spectrum is approaching the theoretical ratio due to the contribution of the previously “invisible” random-coil lysine. Moreover, the CP spectrum (thin line) in Figure 8.9 is less resolved than in Figure 8.8a because of more peaks showing up and less dynamic conformational averaging. Furthermore, the reduced mobility is confirmed by the gated decoupling spectrum shown in Figure 8.9 (thick line). The C_α peak of random-coil lysine vanishes, indicating that the backbone of random-coil lysine has become rigid after intensive drying. The decreased intensity of the residual signals in CP with gated decoupling in Figure 8.8 compared to Figure 8.9 confirms that the side chains are less mobile as well.

TEM of the nanocomposites

The TEM micrographs of the HAp crystals formed in the block copolypeptide gel and those obtained by direct synthesis from an aqueous solution are shown in Figure 8.10. The HAp particles in the nanocomposite exhibit thin elongated plate-like morphology with a mean length of about 50-110 nm, width of 10-20 nm, and are about 3 nm thick (Figure 8.10a). The elongated plate-like morphology of the HAp nanocrystals can also be seen from the STEM high ange annular dark field (HAADF) image in Figure 8.10b. Appearance of needle-like morphology (see Figures 8.10a and 8.10b) is due to curled on-edge viewing angle of plate-like crystallites. Further, the morphology of HAp observed in the present study is quite similar to the apatite crystals found in human woven bone and mineralized dentin [72, 73]. In general, bone mineral consists of plate-like crystals with average dimensions ~50-100 nm or more in length, ~25-50 nm in width, ~2-6 nm in thickness [59, 72, 74] and their small size is a crucial factor related to the solubility [6]. The SAED pattern of the as-prepared hydrogel sample given as an inset in Figure 8.10a demonstrates well-defined broad ring patterns proving polycrystalline and nano-size nature of HAp phase. The observed diffraction rings can be indexed to HAp and these observations are in good agreement with the XRD and FTIR results. Moreover, Figure 8.10c shows the bright-field TEM image of the washed sample (after vacuum drying) with the corresponding SAED pattern and it can be seen from the micrograph that the morphology of the HAp nanoparticles is very similar to that observed in the as-prepared hydrogel nanocomposite. In addition, it is also worth noting that the apatite crystals in the nanocomposites appear elongated plate-like, while the material prepared in the absence of polymer exhibit crystals with irregular shapes (see Figure 8.10d). Furthermore, the SAED pattern of HAp particles prepared in the absence of polymer shows many spots that do not form well defined rings (except (112) plane), indicating larger HAp crystals compared to the as-prepared nanocomposite sample.

Bright-field (BF) and dark-field (DF) transmission electron micrographs of the HAp/polypeptide nanocomposite taken from same area are displayed in Figures 8.11a and 8.11b, respectively. The lower inset in Figure 8.11a shows the corresponding SAED pattern with (300) and (002) diffraction rings of HAp. The DF-TEM image in Figure 8.11b was obtained by isolating the HAp (002) diffraction in the nanocomposite. The mineral phase (HAp) appears as highlights in Figure 8.11b, showing the HAp nanocrystals distribution in the amorphous polymer matrix. Moreover, the atomic calcium to phosphorus ratio of inorganic phase was found to be 1.71 ± 0.07 by STEM-EDS measurements, which is in accordance with the stoichiometric value of pure HAp ($Ca_{10}(PO_4)_6(OH)_2$). The slight increase in Ca/P ratio of HAp over 1.67, the stoichiometric ratio, could be due to the carbonate substitution of the phosphate, consistent with FTIR results.

High-resolution TEM (HRTEM) analysis of the nanocomposites also confirmed the existence of HAp in the nanocomposite. The lattice fringe measurements from the HRTEM micrographs in Figures 8.11c and 8.11d revealed d spacings of 3.44, 2.81, and 2.72 Å, corresponding to the (002), (211) and (300) HAp reflections, respectively. The upper inset in Figure 8.11c demonstrates the filtered inverse-FFT image with (002) HAp planes from the indicated area of the HRTEM image. In addition, Figure 8.11d shows the (002) and (211) HAp planes with an interplanar angle of ~66^{o}, and the (002) and (300) HAp planes with an interplanar angle of 90^{o}, which are consistent with the calculated values of HAp (JCPDS 9-432, a hexagonal unit cell (space group $P6_3/m$) with unit cell dimensions $a = b = 9.418$ Å and $c = 6.884$ Å). The HRTEM image of elongated plate-like nanocrystals in longitudinal sections (Figure 8.11c) revealed a lattice spacing of 3.44 Å (corresponding to the interplanar spacing of (002) planes for hexagonal HAp), indicating that the growth of the plate-like nanocrystals occurs in the (001) direction. The intense (002) reflection in XRD (Figure 8.1) also indicates that the *c*-axis is the preferred growth direction, which is similar to bone where nano-size apatite plate-like crystals associated with the collagen fibrils show strong preferred orientation in their *c*-axis [1, 54, 72].

SAXS characterization

The nanocomposites were characterized with small angle X-ray scattering. The nanocomposites exhibited power law scattering (see Figure 8.12) similar to that observed in bone. The characteristic length scale of the particles was found to be around 3 nm. In the SAXS data we observe signatures for the average size of the inorganic nanocrystals in the high Q region and power law scattering in the low Q region consistent with the elongated particles observed in TEM. Further, modified Guinier analysis for the cross-sectional dimensions show the thickness of the particles to be around 3 nm, consistent with the TEM measurements.

8.5 Conclusions

HAp/copolypeptide nanocomposites were obtained via a simple co-precipitation method at room temperature with the block co-polypeptides serving as the organic template, similar to natural bone that is a complex inorganic (HAp)–organic (collagen) nanocomposite material. This method allows for simultaneous formation of the self-assembled block copolypeptide gel and of the inorganic phase, thereby enabling formation of a self-assembled nanocomposite. Block copolypeptide templates that form gels at very low weight fractions (0.5-4 wt%) compared to previously investigated synthetic block copolymers, allow for inorganic content in the nanocomposites of over 50wt%, more closely approaching the inorganic content seen in natural bone. Solid state NMR studies proved the existence of a nanocomposite, with the inorganic phase comprising mainly of hydroxyapatite but also HPO_4. The morphology of the inorganic nanoparticles is very different from that obtained by precipitation in the absence of the block copolypeptides. The data obtained from XRD, FTIR, S/TEM, SAED, HRTEM, EDS, solid state NMR and small angle scattering studies are consistent and lead us to the premise that the inorganic phase present in the nanocomposite is carbonated HAp of nano-scale dimensions, with elongated plate-like morphology very similar to the mineral phase of the bone. Overall, this approach allows us to synthesize self-assembled calcium phosphate nanocomposites using organic templates, which could have a potential impact in soft tissue repair.

8.6 Acknowledgments

This work was supported by the U.S. Department of Energy under contract number DE-AC02-07CH11358. This work benefited from the use of APS and the IPNS, funded by the U.S. DOE, Office of Science, Office of Basic Energy Science under contract no DE-AC02-06CH11357. Supplementary information is given in the Appendix B.

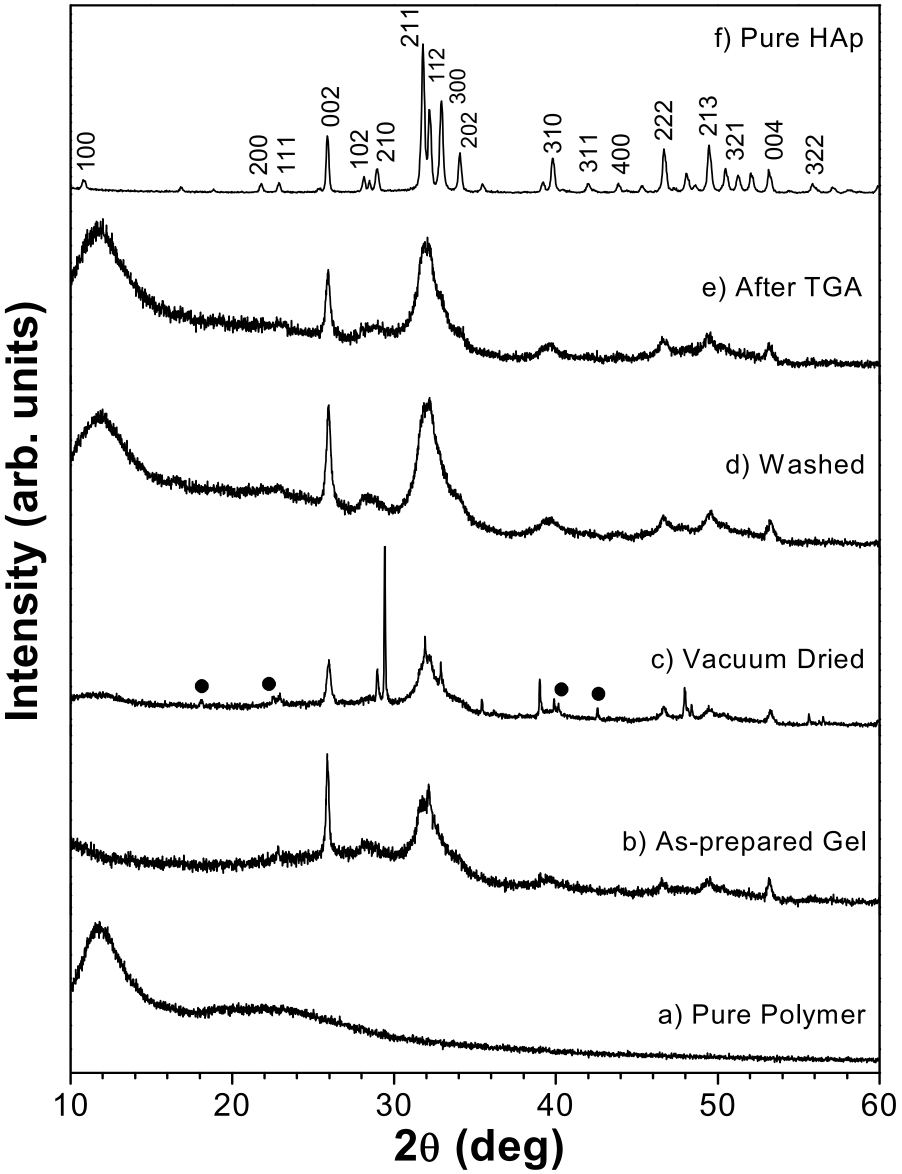

Figure 8.1. X-ray diffraction patterns of a) pure polymer, b) as-prepared calcium phosphate/hydrogel nanocomposite, c) vacuum dried nanocomposite, d) washed sample (after vacuum drying), e) calcined sample after TGA experiments and f) pure HAp (Standard Reference Material® 2910).

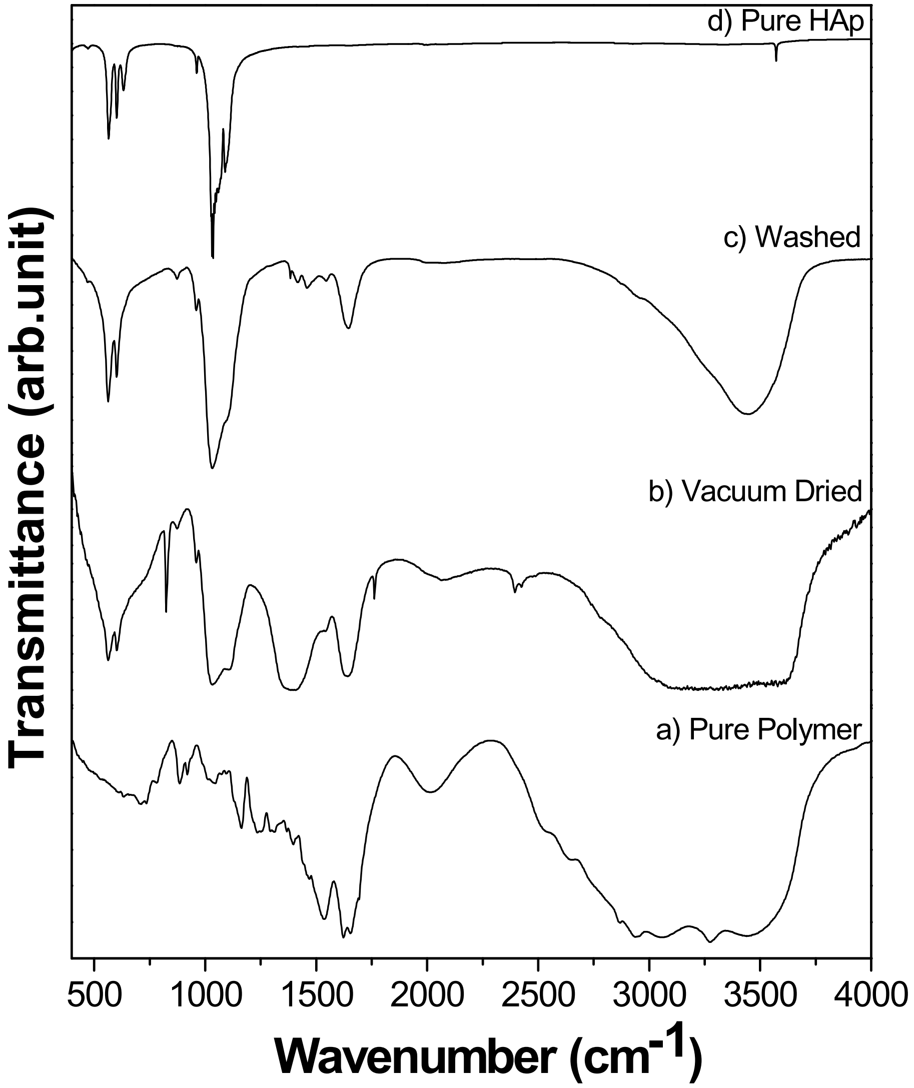

Figure 8.2. FTIR spectra of the a) pure polymer, b) vacuum dried HAp/polypeptide hydrogel nanocomposite, c) washed sample (after vacuum drying), and d) pure HAp (Standard Reference Material® 2910).

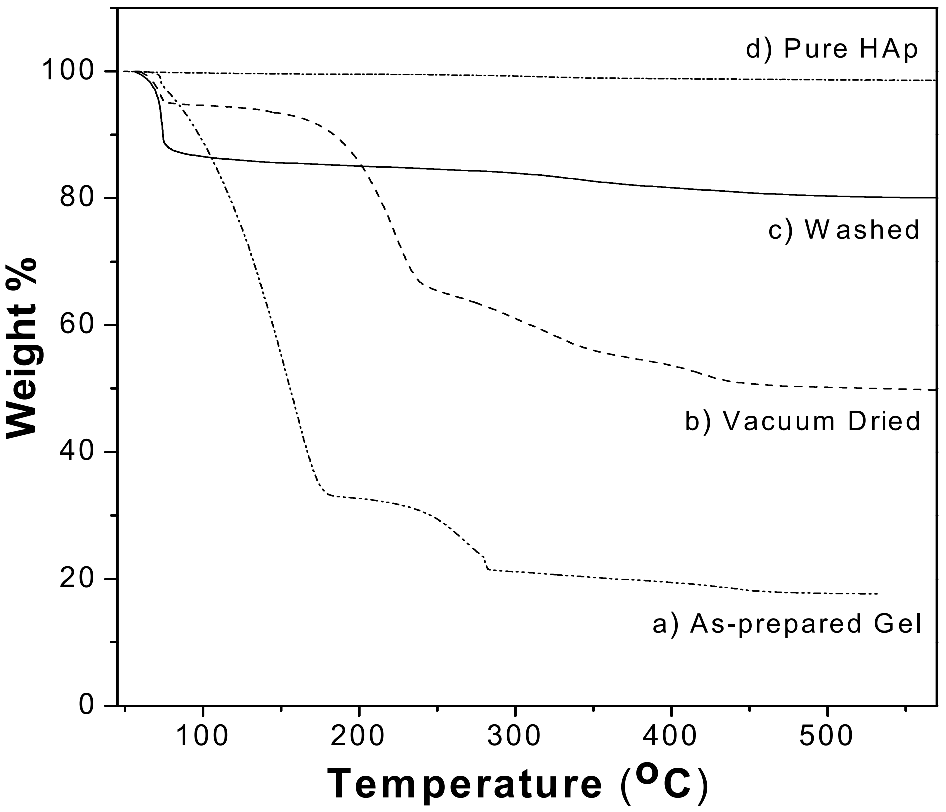

Figure 8.3. TGA thermographs of a) as-prepared HAp/polypeptide hydrogel, b) vacuum dried HAp/polypeptide nanocomposite, c) washed HAp/polypeptide nanocomposite and d) pure HAp (Standard Reference Material® 2910).

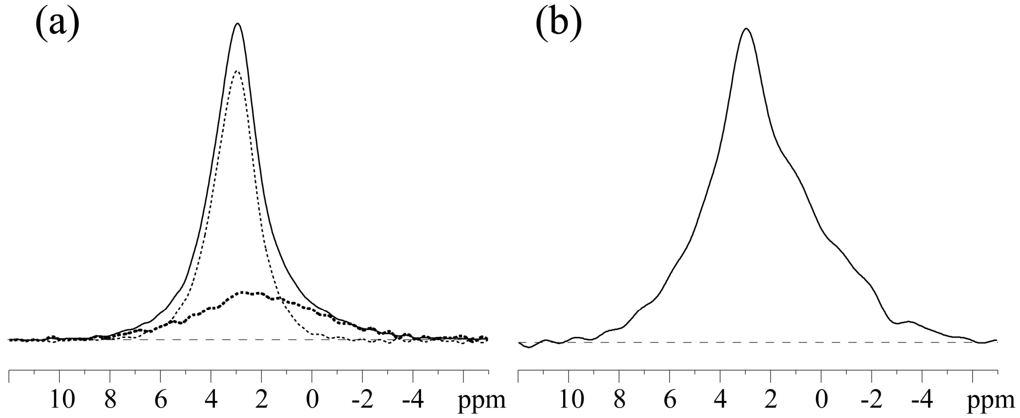

Figure 8.4. ^{31}P NMR spectra of the synthesized composite. (a) Solid line: DP/MAS spectrum of all phosphates. Deconvolution based on ^{1}H-^{31}P dipolar dephasing is also shown; thin dashed line: PO_4^{3-}, 68%; thick dashed line: protonated or H-bonded phosphate, 32%. (b) CP/MAS with 1-ms cross polarization time.

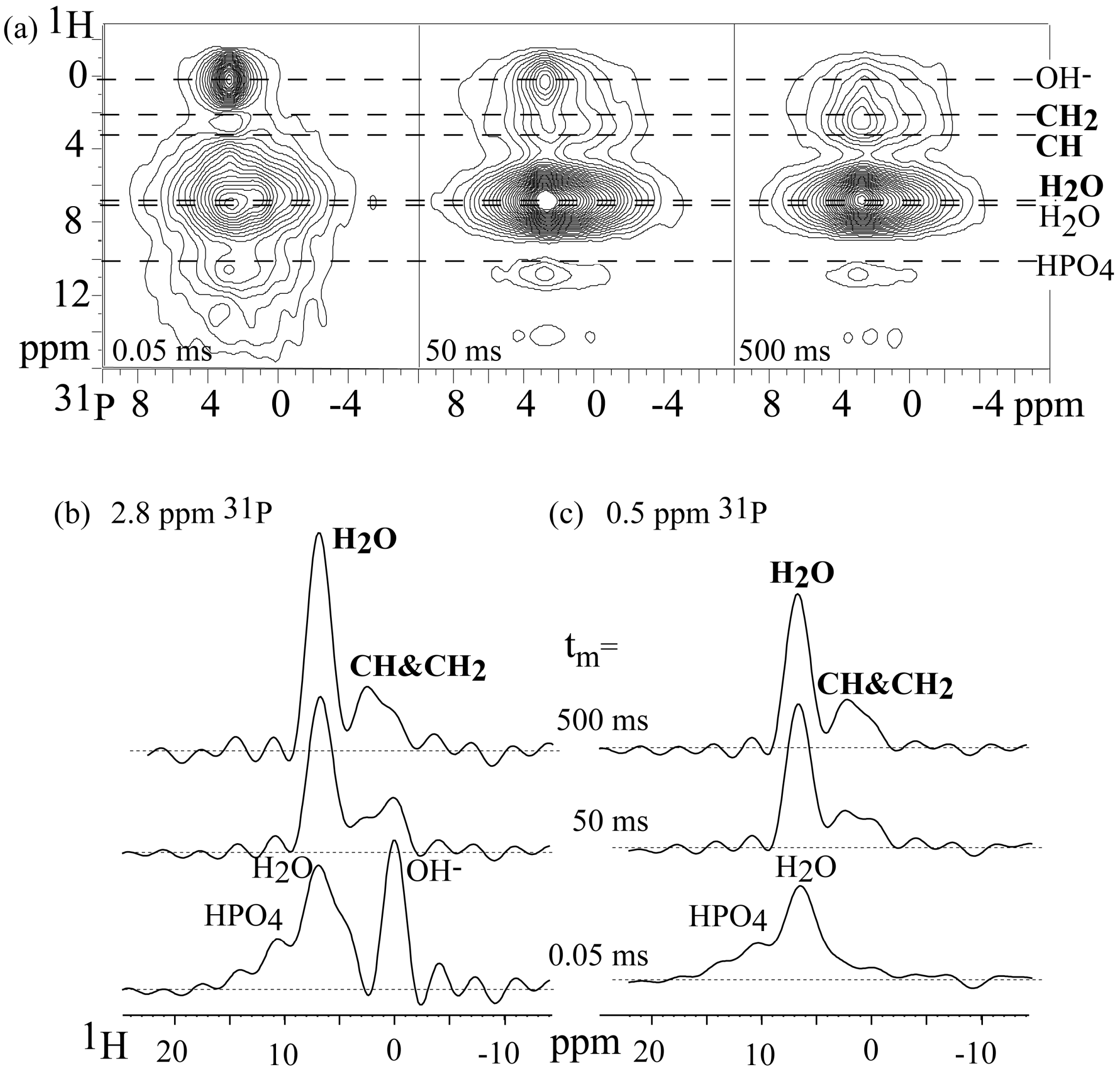

Figure 8.5. (a) 2D ^1H-^{31}P HETCOR NMR spectra of the synthesized composite, with spin diffusion mixing times of 0.05 ms, 50 ms, and 500 ms. (b) and (c): Cross sections of the 2D spectra at 2.8 ppm and 0.5 ppm ^{31}P, respectively.

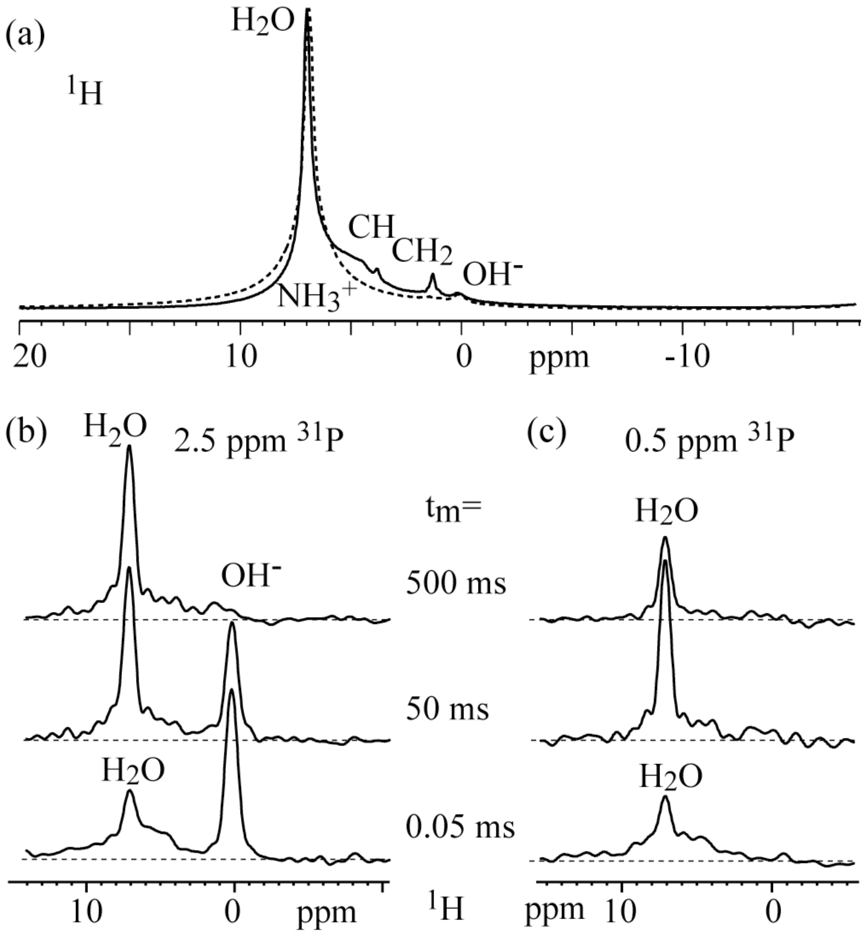

Figure 8.6. ^{1}H spectra of the synthesized composite. (a) One-pulse ^{1}H spectrum of regular vacuum dried sample (solid line) and intensively dried sample (dashed line). (b, c) Cross sections from 2D "WISE" spectra at 2.5 ppm and 0.5 ppm ^{31}P, respectively, for a series of spin-diffusion times.

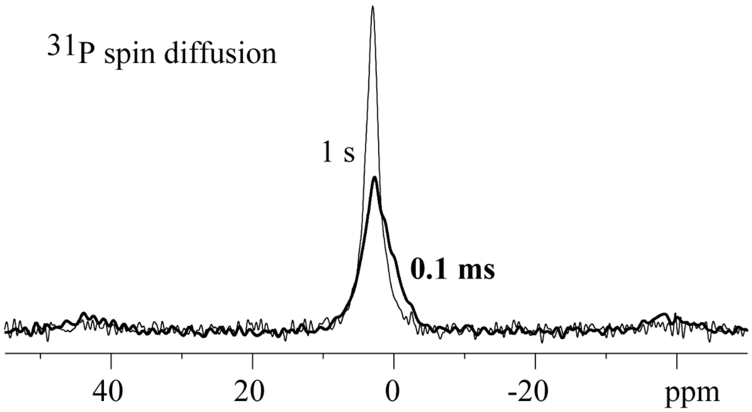

Figure 8.7. ^{31}P NMR of the nanocomposite, with ^{31}P spin diffusion for 0.1 ms (thick line) and 1 s (thin line) after short (0.1-ms) cross polarization that selectively polarizes the protonated phosphates. MAS frequency: 6.5 kHz.

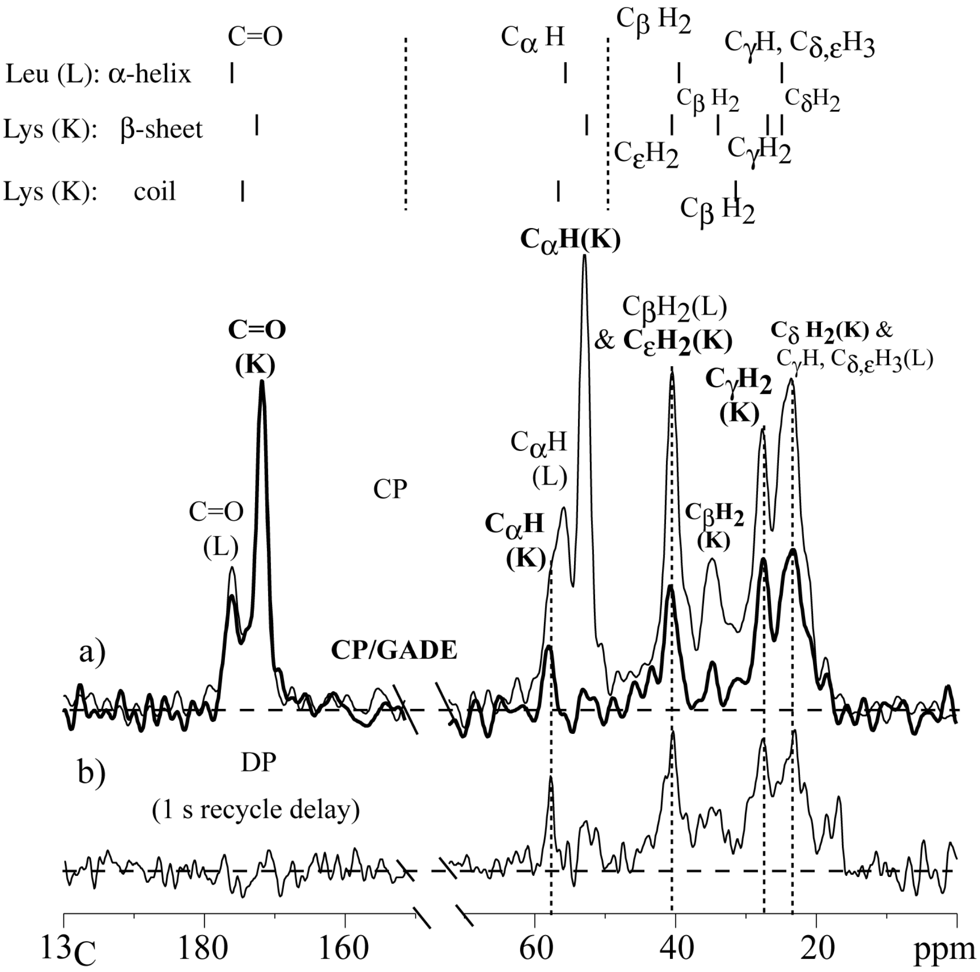

Figure 8.8. Solid-state ^{13}C NMR spectra of $K_{170}L_{30}$ in the nanocomposite. a) CP (thin line) and CP with 40 μs gated decoupling (thick line). b) direct polarization (DP) with 1 s recycle delay. Literature values of the solid-state ^{13}C chemical shifts are listed above the spectra for different peptide secondary structures.

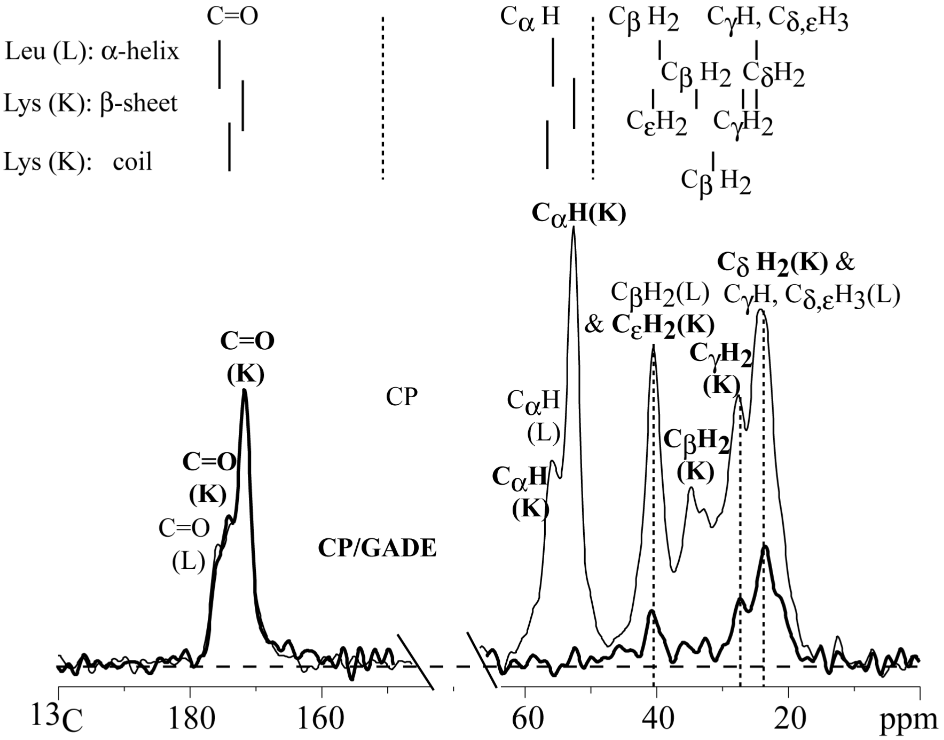

Figure 8.9. Solid-state ^{13}C NMR spectra of the nanocomposite after intensive drying. CP (thin line) and CP with 40 μs gated decoupling (thick line).

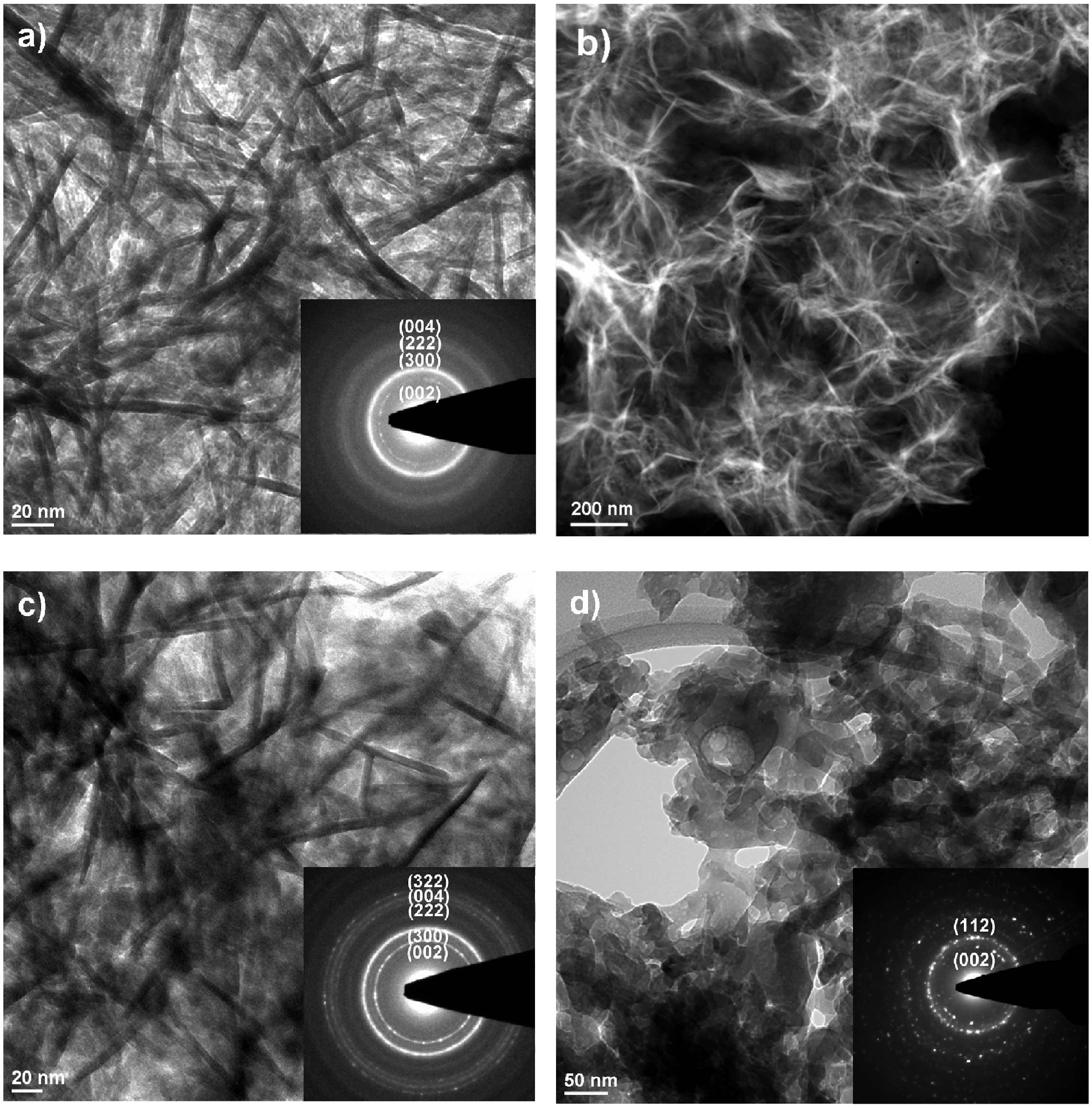

Figure 8.10. TEM images and corresponding SAED patterns of HAp/polypeptide nanocomposite: a) bright field, b) STEM/HAADF, c) washed HAp/polypeptide nanocomposite (after vacuum drying), d) HAp nanocrystals obtained by direct synthesis from an aqueous solution in the absence of polymer

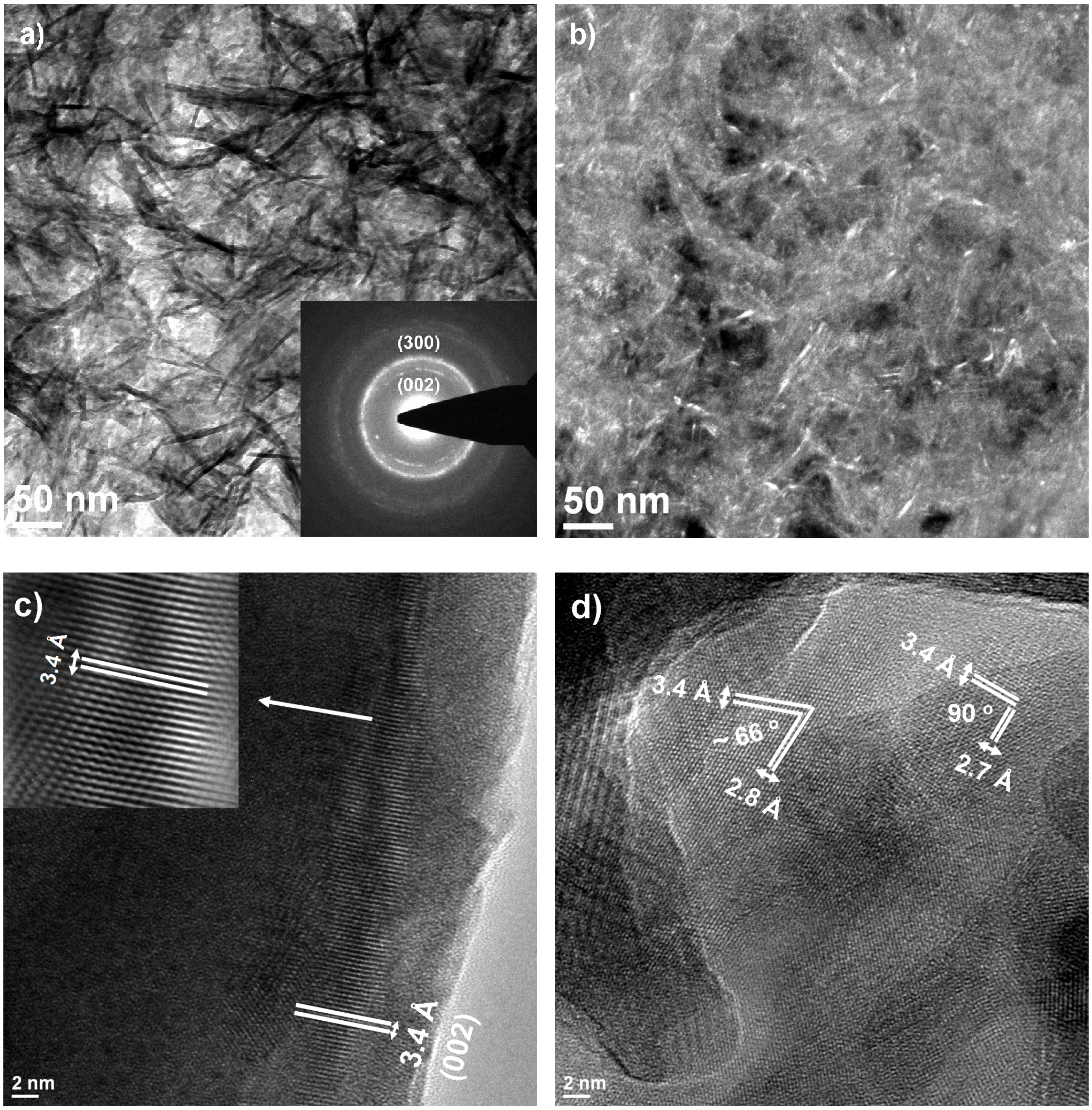

Figure 8.11. a) BF-TEM and b) corresponding DF-TEM images of HAp/polypeptide nanocomposite, c-d) HRTEM images of HAp/polypeptide nanocomposite. The lower inset in Fig.11a shows the corresponding SEAD pattern and the upper inset in Fig.11c shows the filtered inverse-FFT image of the indicated area.

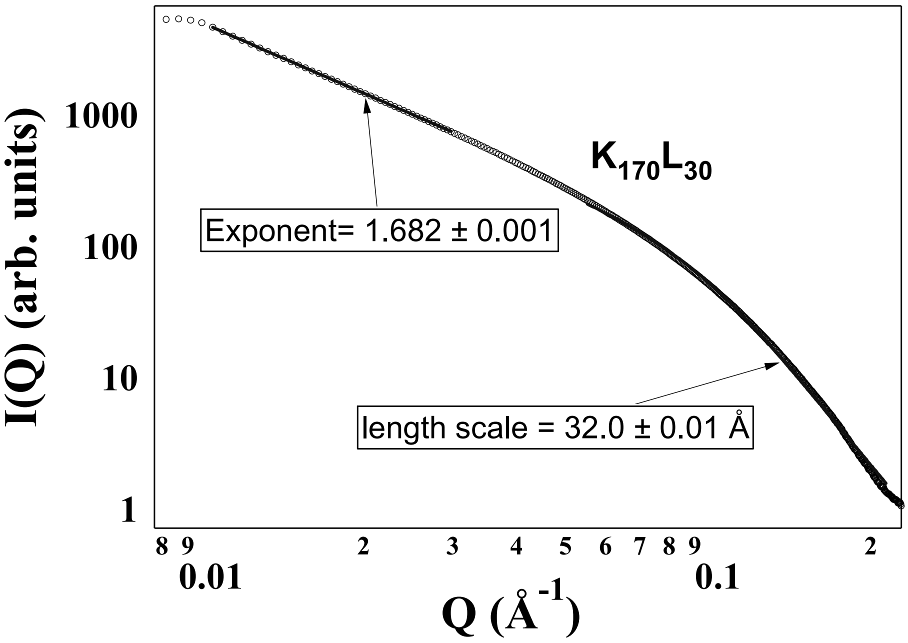

Figure 8.12. SAXS of polypeptide nanocomposite. SAXS data were fitted using a combined equation consisting of an exponential and a power-law for the high Q region and power-law fitting was used for the low Q region.

8.7 References

1. S.V. Dorozhkin and M. Epple. *Angewandte Chemie, International Edition*, (2002); 41, p: 3130-3146.
2. R.K. Roeder, G.L. Converse, R.J. Kane, and W. Yue. *Jom*, (2008); 60, p: 38-45.
3. M. Vallet-Regi. *Dalton Transactions*, (2006); p: 5211-5220.
4. A. Bigi, E. Boanini, S. Panzavolta, N. Roveri, and K. Rubini. *Journal of Biomedical Materials Research*, (2002); 59, p: 709-715.
5. J.Y. Rho, L. Kuhn-Spearing, and P. Zioupos. *Med Eng Phys FIELD Full Journal Title:Medical engineering & physics*, (1998); 20, p: 92-102.
6. M. Vallet-Regi and J.M. Gonzalez-Calbet. *Progress in Solid State Chemistry*, (2004); 32, p: 1-31.
7. S. Mann. *Biomimetic Materials Chemistry,* (1996)*;* p: 383 pp.
8. Z. Li, Y. Li, A. Yang, X. Peng, X. Wang, and Z. Xiang. *Journal of Materials Science: Materials in Medicine*, (2005); 16, p: 213-219.
9. S. Mann. *Biomineralization: Principles and Concepts in Bioinorganic Materials Chemistry,* (2001)*;* p: 240 pp.
10. Z. Amjad. *Calcium Phosphates In Biological And Industrial Systems,* (1998)*;* p: 58-59; Boston, Kluwer Academic Publishers.
11. A. Sinha, S. Nayar, A. Agrawal, D. Bhattacharyya, and P. Ramachandrarao. *Journal of the American Ceramic Society*, (2003); 86, p: 357-359.
12. J. Song, V. Malathong, and C.R. Bertozzi. *Journal of the American Chemical Society*, (2005); 127, p: 3366-3372.
13. N. Spanos, V. Deimede, and P.G. Koutsoukos. *Biomaterials*, (2001); 23, p: 947-953.
14. T. Taguchi, A. Kishida, and M. Akashi. *Journal of Biomaterials Science, Polymer Edition*, (1999); 10, p: 795-804.
15. W. Tjandra, P. Ravi, J. Yao, and K.C. Tam. *Nanotechnology*, (2006); 17, p: 5988-5994.
16. Y.F. Zhao and J. Ma. *Microporous and Mesoporous Materials*, (2005); 87, p: 110-117.
17. N. Degirmenbasi, D.M. Kalyon, and E. Birinci. *Colloids and Surfaces, B: Biointerfaces*, (2006); 48, p: 42-49.
18. L.F. Sukhodub, C. Moseke, L.B. Sukhodub, B. Sulkio-Cleff, V.Y. Maleev, M.A. Semenov, E.G. Bereznyak, and T.V. Bolbukh. *Journal of Molecular Structure*, (2004); 704, p: 53-58.
19. M. Kikuchi, S. Itoh, S. Ichinose, K. Shinomiya, and J. Tanaka. *Biomaterials*, (2001); 22, p: 1705-1711.
20. F.Z. Cui, Y. Wang, Q. Cai, and W. Zhang. *Journal of Materials Chemistry*, (2008); 18, p: 3835-3840.
21. I. Manjubala, S. Scheler, J. Bossert, and D. Jandt Klaus. *Acta biomaterialia*, (2006); 2, p: 75-84.
22. V.M. Rusu, C.-H. Ng, M. Wilke, B. Tiersch, P. Fratzl, and M.G. Peter. *Biomaterials*, (2005); 26, p: 5414-5426.
23. L. Wang and C. Li. *Carbohydrate Polymers*, (2007); 68, p: 740-745.

24. S.A. Hutchens, R.S. Benson, B.R. Evans, H.M. O'Neill, and C.J. Rawn. *Biomaterials*, (2006); 27, p: 4661-4670.
25. L. Hong, Y.L. Wang, S.R. Jia, Y. Huang, C. Gao, and Y.Z. Wan. *Materials Letters*, (2006); 60, p: 1710-1713.
26. P. Cromme, C. Zollfrank, L. Mueller, F.A. Mueller, and P. Greil. *Materials Science & Engineering, C: Biomimetic and Supramolecular Systems*, (2007); 27, p: 1-7.
27. K.R. Mohamed and A.A. Mostafa. *Materials Science & Engineering, C: Materials for Biological Applications*, (2008); 28, p: 1087-1099.
28. M.C. Chang, C.-C. Ko, and W.H. Douglas. *Biomaterials*, (2003); 24, p: 3087-3094.
29. D. Enlow, A. Rawal, M. Kanapathipillai, K. Schmidt-Rohr, S. Mallapragada, C.T. Lo, P. Thiyagarajan, and M. Akinc. *Journal of Materials Chemistry*, (2007); 17, p: 1570-1578.
30. M. Kanapathipillai, Y. Yusufoglu, A. Rawal, Y.Y. Hu, C.T. Lo, P. Thiyagarajan, Y.E. Kalay, M. Akinc, S. Mallapragada, and K. Schmidt-Rohr. *Chemistry of Materials*, (2008); p: ACS ASAP.
31. Y. Yusufoglu, Y.Y. Hu, M. Kanapathipillai, K. Matthew, Y.E. Kalay, P. Thiyagarajan, M. Akinc, K. Schmidt-Rohr, and S. Mallapragada. *J. Mater. Res*, (2008); p.
32. J.N. Cha, G.D. Stucky, D.E. Morse, and T.J. Deming. *Nature*, (2000); 403, p: 289-292.
33. L.E. Euliss, S.G. Grancharov, S. O'Brien, T.J. Deming, G.D. Stucky, C.B. Murray, and G.A. Held. *Nano Lett.*, (2003); 3, p: 1489-1493.
34. V. Krikorian, M. Kurian, M.E. Glavin, A.P. Nowak, T.J. Deming, and D.J. Pochan. *Polym. Sci. Polym. Phys.*, (2002); 40, p: 2579-2586.
35. M.M. Tomczak, D.D. Glawe, L.F. Drummy, C.G. Lawrence, M.O. Stone, C.C. Perry, D.J. Pochan, T.J. Deming, and R.R. Naik. *J. Am. Chem. Soc.*, (2005); 127, p: 12577-12582.
36. K. Donadel, M.C.M. Laranjeira, V.L. Goncalves, V.T. Favere, J.C. de Lima, and L.H.M. Prates. *J. Am. Ceram. Soc.*, (2005); 88, p: 2230-2235.
37. K. Kandori, N. Horigami, A. Yasukawa, and T. Ishikawa. *J. Am. Ceram. Soc.*, (1997); 80, p: 1157-1164.
38. A. Lopez-Macipe, J. Gomez-Morales, and R. Rodriguez-Clemente. *Adv. Mater.*, (1998); 10, p: 49-53.
39. Y. Yusufoglu and M. Akinc. *Journal of the American Ceramic Society*, (2008); 91, p: 77-82.
40. M. Aizawa, A.E. Porter, S.M. Best, and W. Bonfield. *Biomaterials*, (2005); 26, p: 3427-3433.
41. M. Aizawa, H. Ueno, K. Itatani, and I. Okada. *J. Eur. Ceram. Soc.*, (2006); 26, p: 501-507.
42. M. Kinoshita, K. Itatani, S. Nakamura, and A. Kishioka. *Gypsum Lime*, (1990); 227, p: 207-215.
43. A. Barroug, J. Lemaitre, and P.G. Rouxhet. *J. Alloys. Compd.*, (1992); 188, p: 152-156.
44. K. Ishikawa, E.D. Eanes, and M.S. Tung. *J. Dent. Res.*, (1994); 73, p: 1462-1469.
45. A. Slosarczyk, Z. Paszkiewicz, and C. Paluszkiewicz. *J. Mol. Struct.*, (2005); 744-747, p: 657-661.

46. T. Iizuka and A. Nozuma. *J. Ceram. Soc. Japan*, (1998); 106, p: 820-823.
47. R.Z. LeGeros, J.P. LeGeros, O.R. Trautz, and W.P. Shirra. *Adv. X-Ray Anal.*, (1971); 14, p: 57-66.
48. E.A.P. De Maeyer, R.M.H. Verbeeck, and D.E. Naessens. *Inorg. Chem.*, (1993); 32, p: 5709-5714.
49. J. Liu, X. Ye, H. Wang, M. Zhu, B. Wang, and H. Yan. *Ceram. Int.*, (2003); 29, p: 629-633.
50. H. Monma and T. Kamiya. *J. Mater. Sci.*, (1987); 22, p: 4247-4250.
51. A.P. Nowak, V. Breedveld, L. Pakstis, B. Ozbas, D.J. Pine, D. Pochan, and T.J. Deming. *Nature (London, United Kingdom)*, (2002); 417, p: 424-428.
52. K. Schmidt-Rohr, J. Clauss, and H.W. Spiess. *Macromolecules*, (1992); 25, p: 3273-3277.
53. J.C. Elliott. *Structure and Chemistry of the Apatites and Other Calcium Orthophosphates; Elsevier: Amsterdam*, (1994); p.
54. S.N. Danilchenko, C. Moseke, L.F. Sukhodub, and B. Sulkio-Cleff. *Crystal Research and Technology*, (2004); 39, p: 71-77.
55. S. Liao, F. Watari, M. Uo, S. Ohkawa, K. Tamura, W. Wang, and F. Cui. *Journal of Biomedical Materials Research, Part B: Applied Biomaterials*, (2005); 74B, p: 817-821.
56. N.A. Zakharov, Z.A. Ezhova, E.M. Koval, V.T. Kalinnikov, and A.E. Chalykh. *Inorganic Materials*, (2005); 41, p: 509-515.
57. M. Rozenberg and G. Shoham. *Biophysical Chemistry*, (2007); 125, p: 166-171.
58. J.D. Hartgerink, E. Beniash, and S.I. Stupp. *Science (Washington, DC, United States)*, (2001); 294, p: 1684-1688.
59. E. Sachlos, D. Gotora, and J.T. Czernuszka. *Tissue Engineering*, (2006); 12, p: 2479-2487.
60. A.D. Roddick-Lanzilotta and A.J. McQuillan. *Journal of Colloid and Interface Science*, (1999); 217, p: 194-202.
61. J.P. Coates. *Applied Spectroscopy Reviews*, (1996); 31, p: 179-192.
62. R. Gonzalez-McQuire, J.-Y. Chane-Ching, E. Vignaud, A. Lebugle, and S. Mann. *Journal of Materials Chemistry*, (2004); 14, p: 2277-2281.
63. G. Xu, I.A. Aksay, and J.T. Groves. *Journal of the American Chemical Society*, (2001); 123, p: 2196-2203.
64. K. Sato. *Topics in Current Chemistry*, (2007); 270, p: 127-153.
65. R. Murugan, S. Ramakrishna, and K.P. Rao. *Materials Letters*, (2006); 60, p: 2844-2847.
66. W.P. Rothwell, J.S. Waugh, and J.P. Yesinowski. *Journal of the American Chemical Society*, (1980); 102, p: 2637-2643.
67. S.S. Hou, F.L. Beyer, and K. Schmidt-Rohr. *Solid State Nuclear Magnetic Resonance*, (2002); 22, p: 110-127.
68. K. Wuthrich. *NMR of Proteins and Nucleic Acids,* (1986)*;* p: 304 pp.
69. Q. Chen, S.S. Hou, and K. Schmidt-Rohr. *Solid State Nuclear Magnetic Resonance*, (2004); 26, p: 11-15.
70. Y. Wang. *Journal of Biomolecular NMR*, (2004); 30, p: 233-244.

71. C. Ye, R. Fu, J. Hu, L. Hou, and S. Ding. *Magnetic Resonance in Chemistry*, (1993); 31, p: 699-704.
72. X. Su, K. Sun, F.Z. Cui, and W.J. Landis. *Bone (New York, NY, United States)*, (2003); 32, p: 150-162.
73. P. Houlle, J.C. Voegel, P. Schultz, P. Steuer, and F.J.G. Cuisinier. *Journal of Dental Research*, (1997); 76, p: 895-904.
74. W.J. Landis, M.J. Song, A. Leith, L. McEwen, and B.F. McEwen. *Journal of structural biology*, (1993); 110, p: 39-54.

CHAPTER 9. GENERAL CONCLUSIONS

9.1 Conclusions

Hydroxyapatite (HAp) with carbonate incorporation in its structure is the main inorganic content of bone and many other hard tissues of human body. It is well established that carbonate substitution in HAp structure influences stability, solubility, biological reactivity, and mechanical properties of the apatite. In this regard, synthesizing HAp with carbonate content has gained considerable attention in recent years. In chapter 4, we synthesized carbonated hydroxyapatite (CO_3HAp) by using a chelate decomposition method. In this study, we have investigated the effect of pH on the carbonate incorporation into the HAp structure. We found that carbonate content in the apatite increased up to approximately 8 wt% at pH of 10. We also reported that with carbonate incorporation, the lattice parameters showed systematic changes with pH. Following this study and using the same chelate decomposition method, CO_3HAp was precipitated on a polymeric substrate, corona treated poly-methylmethacrylate (PMMA) films; this study was presented in chapter 5. An approximately 15-µm-thick continuous layer of CO_3HAp was obtained on PMMA films with adhesive strength of ~1.7 MPa between apatite/PMMA interfaces. The apatite deposited in the PMMA films was B-type CO_3HAp, in which carbonate ions occupy the phosphate sites, similar to the biological apatites. We believe this work can contribute to gaining insight into how hydroxyapatite forms on polymeric substrates when implanted at defect bone sites.

Inspired by nature, we have developed self-assembling calcium phosphate-block copolymer nanocomposites by using a bottom-up approach. In chapter 6, we demonstrated an experimental bottom-up approach to nanocomposite design based on templating of brushite and hydroxyapatite by polymer micelles. The self-assembling thermo-reversibly gelling anionic and zwitterionic pentablock copolymers having hierarchical structural ordering with micelle particles on the nanometer scale were used as templates for the calcium phosphate precipitation. These pentablock copolymers exhibit thermo-reversibility due to the poly(propylene oxide) blocks and pH-sensitive behavior due to the anionic (acrylic acid) and zwitterionic (sulfobetaine) blocks. Although the TEM characterization of polymer-inorganic gel composites was extremely difficult, we successfully showed the polymer micelles surrounded with the calcium phosphate in the polymer gels. ^{1}H-^{31}P NMR with ^{1}H spin diffusion and scattering measurements of polymer-inorganic gel composites proved nanocomposite formation and templating of the phosphate by the polymer micelles. The inorganic fraction of the nanocomposites was found to be around 30%. This is a significant increase compared to our earlier polymer cationic and polar templates, suggesting that ionic interactions with carboxylic or zwitterionic groups are favorable for inorganic precipitation. Subsequently, in addition to the electrostatic interactions that cause the precipitation of the inorganic phase on the polymer micelles, block copolymers conjugated to hydroxyapatite-nucleating peptides were used to better control the calcium phosphate precipitation process as presented in chapter 7. In this study, three different polymer templates were employed with varying charges on the polymer chains to investigate the role of charge on mineralization. The morphology and the size of the apatite crystals in the nanocomposites were similar to the apatite in the bone. Even though the inorganic content was increased to approximately 40 wt% in these nanocomposite systems, it was still lower than that seen in bone and other biological sytems. In chapter 8, we presented the synthesis of a novel diblock copolypeptide-hydroxyapatite nanocomposite with inorganic content around 55 wt%. The high polymer concentrations (~30 wt%) needed for gel formation in the previous block copolymer systems was one of the limitation to increasing the weight fraction of the inorganic phase in the nanocomposites. To overcome this limitation we used diblock copolypeptides that form gels at very low concentrations (~4 wt%). This approach is similar to biological systems where protein templates commonly control the nucleation and growth of the inorganic nanocrystalline phase in biomaterials such as bone. Moreover, this study may offer routes for bioinspired bottom-up approaches for the development of self-assembling injectable nanocomposite biomaterials for potential orthopedic applications.

In summary, the findings in our studies provide information for developing guidelines for design of novel HAp-polymer nanocomposites and for the understanding of the mechanism of biomineralization. Understanding the mechanism involved in the biomineralization process could provide the basic principles that scientist need to facilitate fabrication of bone-like materials for tissue regeneration. In addition, the results of our studies indicate that the block copolymers could be used as ideal templates to prepare other polymer-inorganic nanocomposites that find different applications. The bottom-up approach to polymer-inorganic nanocomposites design reported in our study might be extended to other inorganic syntheses where the ionic solutions could be mixed with concentrated polymer solutions followed by induction of nucleation and growth of the inorganic phase.

9.2 Future Directions

Even though calcium phosphates were a good example for bioinspired model experiments, for energy related applications other oxides and semiconductors might be also relevant and interesting.

Zirconia is an important structural and functional material and has excellent physical and functional properties [1]. This multifunctional ceramic material finds many applications in different fields such as ceramic engines, solid electrolytes, biosensors, ceramics colors, gemstones, piezoelectrics, etc. [2-4]. It is widely used as a solid oxygen conductor in oxygen sensors and fuel cells [5-8]. Zirconia powders are also used in making a number of tough ceramics and finds many applications as a support in catalysis [9, 10]. As a result, zirconia has been a topic of considerable interest to both basic and applied scientists [11].

Pacheco *et al.* [12] synthesized mesoporous zirconia with anionic templates. They showed that mesoporous zirconia can be prepared by hydrolyzing the zirconium propoxide in the presence of anionic surfactant (alkyl-phosphate, $C_{12}H_{25}OP(OH)_2$) and subsequent ageing.

In a recent study, Rezaei *et al.* [13] prepared nanocrystalline zirconia powders with high surface area, mesoporous structure and tetragonal phase by using of Pluronic P123 block copolymer as template. Moreover, Yang *et al.* [14] have also shown block copolymer templating synthesis of mesoporous zirconia. Deng *et al.* [4] employed collagen fiber as a template for the synthesis of hierarchical mesoporous zirconia fiber. A few other reports on polymer-zirconia composites recently appeared in the literature [15-18].

We will extend the knowledge gained from the hydroxyapatite study into other oxides in particular, zirconia (ZrO_2). The block copolymer templates used for the HAp nucleation and growth will be used to control the growth of zirconia phases as well.

In our initial experiments we have used three different polymers as template for the precipitation of ZrO_2. The polymers that we have employed were Pluronic® F127, poly(diethylaminoethylmethacrylate), and anionic pentablock copolymer. The preliminary results have indicated that the zirconia obtained in the presence of polymer templates shows some differences compared the one obtained from an aqueous solution without any polymer. In the future, we will apply different characterization methods on these nanocomposites to observe the effects of polymer templating on the zirconia phases.

9.3 References

1. R.C. Garvie, R.H. Hannink, and R.T. Pascoe. *Nature*, (1975); 258, p: 703-704.
2. C. Huang, Z. Tang, Z. Zhang, and K.J. Bowman. *J. Am. Ceram. Soc.*, (2001); 84, p: 1637-1638.
3. J. Zhao, W. Fan, D. Wu, and Y. Sun. *J. Non-Cryst. Solids*, (2000); 261, p: 15-20.
4. D. Deng, X. Liao, X. Liu, and B. Shi. *J. Mater. Res.*, (2008); 23, p: 3263-3268.
5. B.C.H. Steele and A. Heinzel. *Nature*, (2001); 414, p: 345-352.
6. B.C.H. Steele. *Mater. Sci. Eng., B*, (1992); B13, p: 79-87.
7. Y.W. Zhang, Y. Yang, S. Jin, S.J. Tian, G.B. Li, J.T. Jia, C.S. Liao, and C.H. Yan. *Chem. Mater.*, (2001); 13, p: 372-378.
8. S. Chen, Y. Yin, D. Wang, Y. Liu, and X. Wang. *J. Cryst. Growth*, (2005); 282, p: 498-505.
9. G.K. Chuah. *Catal. Today*, (1999); 49, p: 131-139.
10. R. Srinivasan, M.B. Harris, S.F. Simpson, R.J. DeAngelis, and B.H. Davis. *J. Mater. Res.*, (1988); 3, p: 787-797.
11. E. Karapetrova, R. Platzer, J.A. Gardner, E. Torne, J.A. Sommers, and W.E. Evenson. *J. Am. Ceram. Soc.*, (2001); 84, p: 65-70.
12. G. Pacheco, E. Zhao, A. Garcia, A. Sklyarov, and J.J. Fripiat. *Chem. Commun.*, (1997); p: 491-492.
13. M. Rezaei, S.M. Alavi, S. Sahebdelfar, and Z.-F. Yan. *J. Porous Mater.*, (2008); 15, p: 171-179.
14. P. Yang, D. Zhao, D.I. Margolese, B.F. Chmelka, and G.D. Stucky. *Chem. Mater.*, (1999); 11, p: 2813-2826.
15. R. Mishra and K.J. Rao. *Ceram. Int.*, (2000); 26, p: 371-378.
16. C.A. Borgo and Y. Gushikem. *J. Colloid Interface Sci.*, (2002); 246, p: 343-347.
17. T. Uma, T. Mahalingam, and U. Stimming. *J. Mater. Sci.*, (2004); 39, p: 2901-2904.
18. S. Roy. *J. Sol-Gel Sci. Technol.*, (2007); 44, p: 227-233.

APPENDIX A

Supporting information for the manuscript "Synthesis and characterization of ionic block copolymer templated calcium phosphate nanocomposites"

M. Kanapathipillai, Y.Yusufoglu, A. Rawal, Y.-Y. Hu, C.-T. Lo, P. Thiyagarajan, Y.E. Kalay, M. Akinc, S. Mallapragada, K. Schmidt-Rohr

This supporting information provides details on the experimental techniques and associated sample preparation, as well as basic materials characterization including differential scanning calorimetry and thermogravimetry. It also presents dynamic mechanical analysis of the gels. Further, it shows additional two-dimensional ^{31}P-^{1}H NMR spectra, discusses the length scale probed in ^{1}H spin diffusion NMR, and displays additional electron micrographs of the nanocomposites. References additional to those in the main text are given at the end.

Pentablock Copolymer Characterization. NMR and GPC measurements were performed to determine the composition and molecular weights of the block copolymers. All ^{1}H NMR measurements were performed using a Varian VXR400 (400 MHz) spectrometer, in D_2O and chloroform-d solvents. Molecular weight and polydispersity index (PDI) of the copolymers were estimated using four PLgel columns 100, 500, 1x10^4, 1x10^5 Å from Polymer Laboratories at 40 °C equipped with a Waters 510 pump, Waters 717 autosampler, a Wyatt Optilab DSP refractometer, and a Wyatt Dawn EOS light scattering detector. Aqueous solutions of the polymers at various concentrations were prepared in 1mM tris-HCl. Simple tube inversion was used to find the gelation temperature. Titration measurements were carried out to find the pK_a and iep values and differential scanning calorimetry (DSC) was used to find the critical micellization temperatures of the copolymer solutions. The micelle formation in water is an endothermic first-order transition due to the enthalpy of dehydration of the hydrophobic block [29]. Measurements were carried out using a Thermal Analysis DSC instrument Q 20 equipped with an auto sampler. Samples with masses ranging from 5 to 20 mg were heated from -5 to 50°C at a rate of 5°C/min. The data were corrected by sample weight normalization and subtraction of the linear baseline.

Titration measurements were carried out to obtain the degree of ionization. Potentiometric titrations were carried out using a Corning 313 pH/temperature meter at room temperature. Samples were prepared by dissolving 500 mg of polymer in 50 mL nanopure water. In the case of Penta-PZ copolymers, after the complete dissolution of the polymer in water, the solution was titrated using 1.0 M NaOH. A pH vs [OH^-] concentration plot was obtained and the iep value was obtained from the inflection point. For the anionic pentablock copolymer, the solution pH was first raised to pH 12 by adding 1.0 M NaOH and then back titrated using 1.0 M HCl. The degree of ionization, α, was calculated from the ratio of the net concentration of H^+ ions (C_H-C_{OH}) and COOH groups (C_A) in solution, $\alpha = \frac{(C_H - C_{OH})}{C_A}$ [30].

Methods for Nanocomposite Characterization. Thermogravimetric analysis (TGA) was performed with a Perkin Elmer thermogravimetric analyzer (Perkin Elmer, TGA 7, Downers Grove IL). Approximately 60 mg of the gel sample was placed in a platinum pan and the experiments were performed in a flowing air environment. The program was set to heat up to 50 °C, hold at this temperature for 1 min, then heat from 50 °C to 120 °C at a rate of 5.00 °C/min, and finally, heat from 120 °C to 600 °C at a rate of 10.00 °C/min.

Scanning transmission electron microscopy (STEM) images were captured on a JEOL 1200EX II (Japan Electron Optic Laboratories, Peabody, MA) and FEI-Tecnai G^2-F20 (FEI

Inc., Hillsboro, Oregon) scanning transmission electron microscope equipped with EDX (EDX Inc., Mahwah, NJ). The former uses a Megaview III digital camera and SIS Pro. Software (Soft Imaging Systems Inc., LLC, Lakewood, CO), the latter a CCD camera and Digital Micrograph Software (Gatan, Pleasanton, CA). Furthermore, high resolution TEM examination was performed using the same FEI-Tecnai G^2 F20 scanning/transmission electron microscope. For the TEM study, the hydrogel samples were diluted to obtain 5.0 weight % polymer solutions. Approximately 50 μL of the aqueous sample was placed onto a Formvar coated copper grid and the contents allowed to settle for 1 min. Most of the supernatant was wicked away and 1% phosphotungstic acid (pH ~ 5) was applied for 30 seconds as a negative contrast stain. The grid was wicked and allowed to dry.

Wide-angle X-ray diffraction patterns were obtained using a theta-theta x-ray diffractometer (Scintag, XDS-2000, Cupertino, CA) operating at 45 kV and 40 mA, and the scanning rate was 0.60^o/min with a sampling interval of 0.02^o over a range of $10 \leq 2\theta \leq 60^o$. To minimize drying, hydrogel XRD samples were prepared and analyzed immediately. Scintag DMSNT search/match software and the ICDD database were used for the phase analysis.

SAXS measurements were performed at the 12-ID beam line at the Advanced Photon Source in Argonne National Laboratory. We used 1 mm thick samples of the gels sandwiched between 25 micron thick Kapton tapes. X-rays with an energy of 12 keV (λ = 1.035 Å) and a 15x15 cm^2 mosaic Mar CCD at a sample to detector distance of 2 m were used to measure the scattered intensity and a pin diode on the beam stop to measure the transmitted beam intensity. For each sample we collected five 1 s exposures and the collected 2D data were corrected and azimuthally averaged to obtain I(Q) data, where $Q = 4\pi \sin \theta/\lambda$

with the scattering angle 2θ and the wavelength λ of the X-rays.

SANS measurements were carried out using the time-of-flight small-angle neutron diffractometer (SAND) at IPNS at Argonne National Laboratory. The SAND instrument provides data in the *Q* range of 0.004-0.5 $Å^{-1}$ in a single measurement by using a 40x40 cm^2 position-sensitive ^{3}He detector and neutrons with wavelengths in the range of 1.5-14 Å. The neat polymer gel samples of PentaPZ46-5, PentaPAA27-5, PentaPAA36-5 and the corresponding nanocomposite gel samples were prepared in 1m M Tris-HCl at pH 5.5, in D_2O solution. The gel samples were sealed in Suprasil cylindrical cells with 1 mm path length for the SANS measurements. The scattering data were corrected for empty cell scattering, detector sensitivity, and sample transmission. The differential scattering cross section *I*(*Q*) was placed on an absolute scale in the units of cm^{-1}.

Solid-state NMR experiments were performed using a Bruker DSX400 spectrometer (Bruker-Biospin, Rheinstetten, Germany) at 400 MHz for ^{1}H and 162 MHz for ^{31}P. A Bruker 4-mm double-resonance magic-angle spinning (MAS) probehead was used for 6.5-kHz and 7-kHz MAS ^{1}H-^{31}P NMR experiments. ^{31}P{^{1}H} HARDSHIP NMR experiments were performed at 13-kHz MAS with 2.5-mm rotors in a Bruker double-resonance probehead. The 90° pulse lengths were 5 μs for ^{1}H and 4 μs for ^{31}P in the 4-mm probe, and 2.5-μs in the 2.5-mm probe for both ^{1}H and ^{31}P. The direct-polarization experiments, including those with gated recoupling, were carried out with recycle delays of 100 s at 7 kHz MAS. 2D ^{1}H-^{31}P correlation experiments without homonuclear decoupling, using the wideline separation (WISE) NMR pulse sequence with hypercomplex data acquisition, were carried out with 256 20-μs t_1 increments and 5-s recycle delays. 2D ^{1}H-^{31}P heteronuclear correlation (HetCor) NMR experiments were carried out with 100 44-μs t_1 increments and 15-s recycle delays.

Lee-Goldburg cross polarization (LGCP) was used for polarization transfer from ^{1}H to ^{31}P in both "WISE" and HetCor experiments with contact times of 0.7 ms and 0.5 ms, respectively. Two-pulse phase-modulation (TPPM) was used for ^{1}H-^{31}P dipolar decoupling. The hydroxide proton peak at 0.18 ppm and ^{31}P peak at 2.8 ppm in NIST hydroxyapatite were used as secondary chemical shift references to calibrate the ^{1}H and ^{31}P chemical shifts, respectively. All NMR experiments were carried out at ambient temperature.

Rheological experiments were carried out using an ARES rheometer (TA Instruments, New Castle, Delaware). Polymer gels samples of 46 wt% PentaPZ (Mw 15,000) and 27 wt% Penta-PAA (Mn 17,538) were used for the study. Parallel plates with diameters of 50 mm and gap of 1.0 mm were used for all samples. All the measurements were performed in dynamic strain controlled (50%) mode at room temperature. Frequency sweeps were carried out with angular frequency varied from 1 rad/s to 0.001 rad/s, and the modulus measurements were recorded.

Basic Materials Characterization. Figure S1 shows DSC thermographs of PentaPZ polymers. As can be seen from the thermograph, critical micellization temperature decreases with increase in concentration. Compared to the zwitteronic pentablock copolymer, the anionic polymer is less ionic. This also can be seen from the DSC thermograph, where the critical micellization temperature is lower for the anionic polymer at similar concentrations.

The TGA curves are shown in Figure S2. The significant weight loss up to 200 ^{o}C is due to the elimination of adsorbed and lattice water. Weight loss observed between 200-400 ^{o}C is due to the pyrolysis of the polymer. The origin of the sharp drop in mass at 200-225 ^{o}C is not clear; it has been observed reproducibly in similar samples. The remaining solid after the polymer burn-out is the inorganic phase.

Dynamic-Mechanical Measurements. Dynamic strain controlled rheological measurements were performed on polymer nanocomposite gels to test the stiffness of the formed materials (Figure S3). Measurements indicated an increase in modulus with the inorganic nanocrystals compared to polymer gels alone. The polymer gels alone were not stiff enough due to charge repulsions by the ionic side chains, where the moduli ranged from 0.01-10 Pa. With the formation of the inorganic nanocrystals, the nanocomposites show an increase of modulus by several orders of magnitude depending on the shear rate. Such a large increase may be attributed to neutralization of surface charges on the micelle surface by calcium phosphate phase leading to aggregation of the nanoparticles, or coating of soft polymeric micelles by rigid inorganic particles, or both.

Additional 2D NMR spectra. Figure S4 displays a series of ^{1}H-^{31}P HETCOR spectra of PentaPZ46-5, for spin diffusion times of 0.05, 50, and 500 ms. It shows slow spin diffusion from the polymer to the ^{31}P sites with sharp peaks (Figure S4b, d), but the low broad component centered at –1.8 ppm, which in spite of its low peak height accounts for 66% of the phosphate, exhibits close contact with the polymer (Figure S4c).

^{1}H-^{31}P dephasing curves. Figure S5 shows dephasing of the ^{31}P NMR signal of the polymer-calcium phosphate composites and model compounds under ^{31}P{^{1}H} dipolar recoupling for up to two rotation periods, applying a 180^{o} pulse every half rotation period. The faster dephasing of protonated phosphates (HPO_4^{2-}) compared to the unprotonated phosphates (PO_4^{3-}) is clearly seen.

Length Scale of ^{1}H Spin-Diffusion NMR Experiments. It is clear that the spin diffusion between different phases occurs the faster the smaller the domains. Thus, it should be possible to convert the time constant of spin diffusion into an estimate of the domain size.

The transformation from time constant to length scale is enabled by the spin diffusion coefficient D, which has units of length^2/time. Simple geometric analysis of the initial regime of spin diffusion between two components of equal proton density [32] gives the following relation between the domain size of the dispersed component A and the equilibration time t_{sd}*:

$$d_A = \varepsilon/f_B\ (4/\pi\ D\ t_{sd}{*})^{1/2} \qquad (1)$$

where $f_B = 1 - f_A$ is the proton/volume fraction of component B, and ε is the "dimensionality" of the morphology (ε =1 for lamellar structures, ε =2 for cylinders, and ε = 3 for spheres or other discrete particles). The proton densities and spin diffusion coefficients of the organic and inorganic phases in our samples are not equal, but equation (1) nevertheless provides a basis for domain-size estimates. Reduced ^{1}H linewidths in both organic and inorganic components compared to those of glassy polymers [31, 32] allow us to conclude that the effective spin diffusion coefficient will be smaller than 0.4 nm^2/ms. Given that the SAXS experiments discussed below demonstrate that the inorganic phase fills the spaces between the polymer micelles, we should take component A to be the polymer micelles, with ε ~ 3 and a volume/proton fraction of $f_A \sim 0.85$. For t_{sd}* = 50 ms, this gives

$$d_{micelle} < 20\ (25)^{1/2}\ \text{nm} = 100\ \text{nm} \qquad (2)$$

Note that the thickness of the interstitial phosphate layers in this system would be only between 10 and 20 nm. The SAXS and the HARDSHIP NMR data shown below indicate that the RHS of inequality (2) overestimates the true size of the micelles by a factor of six, at least in part due to a significant overestimate of the spin diffusion coefficient and likely also of the equilibration time, which should be obtained by extrapolation of the initial-rate regime of spin diffusion [32].

Additional Electron Micrographs. Figure S6 illustrates the micelles in PentaPAA27-5 and PentaPAA36-5. Some of them are surrounded by a calcium phosphate phase, as observed for PentaPAA36-5 in Figure S6c. Spherical black spots in the HAADF image of an unstained sample, Figure S6d, are assigned to the calcium phosphate phase in the polymer. Since the TEM image in Figure S6d was taken without any stain decoration, the polymer micelles are invisible.

Figure S7 show HRTEM images of PentaPAA27-5 and PentaPAA36-5. Calcium phosphate nanoparticles of 5-10 nm size can be clearly seen. The upper and lower insets in Figure S7c show the FFT pattern and filtered inverse-FFT image, respectively. The XRD and NMR analysis have shown the presence of brushite and hydroxyapatite for PentaPAA27-5. Measurements from several HRTEM images indicated lattice spacings of less than 3.1 Å. An example for this is illustrated in Figure S7c. It shows a lattice spacing of 3.1 Å, which is close to the interplanar spacing of {210} planes for hydroxyapatite and {041} planes for brushite. This makes it difficult to distinguish between brushite and hydroxyapatite phases in PentaPAA27-5.

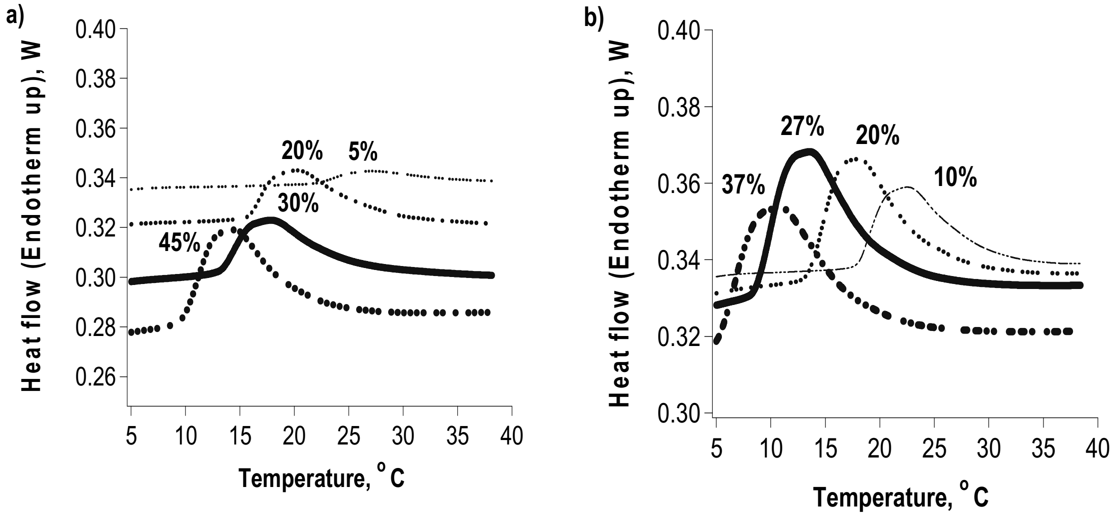

Figure S1. Endothermic micellization peaks of (a) PentaPZ (Mn, 15000) (b) PentaPAA (Mn 17538, PDI- 1.196) pentablock copolymers obtained from DSC thermographs.

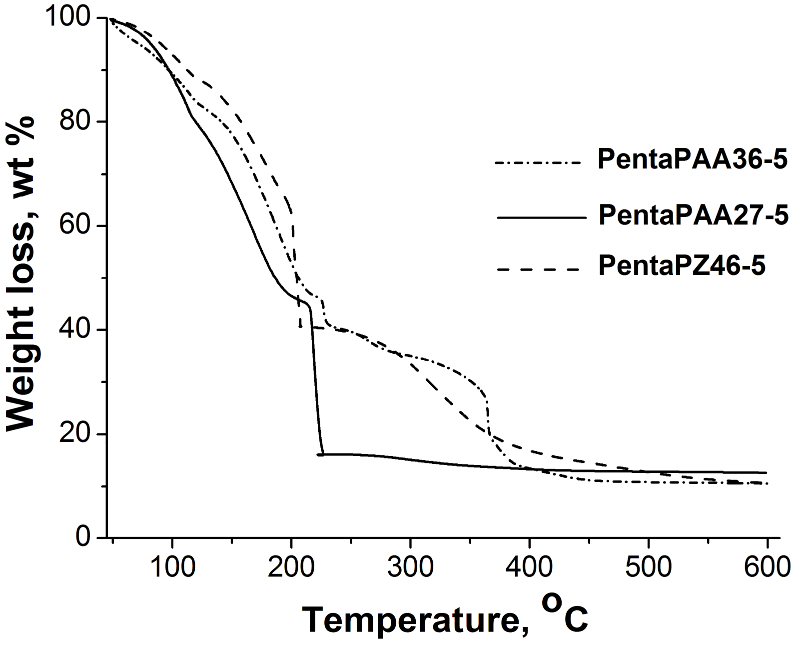

Figure S2. TGA traces of PentaPZ46-5, PentaPAA27-5 and PentaPAA36-5 hydrogels.

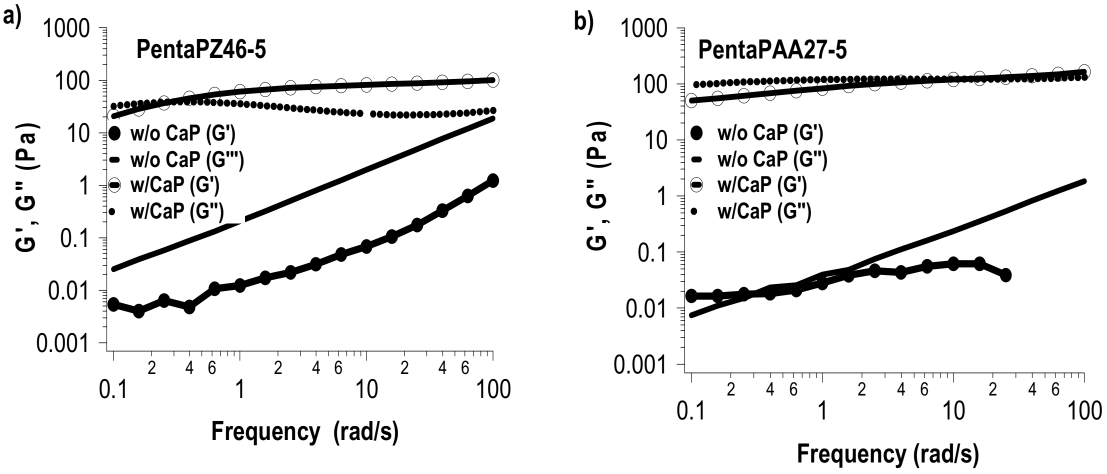

Figure S3. a) Dynamic strain controlled frequency sweep of PentaPZ46-5 and b) PentaPAA27-5 pentablock copolymers with and without calcium phosphate nanocrystals.

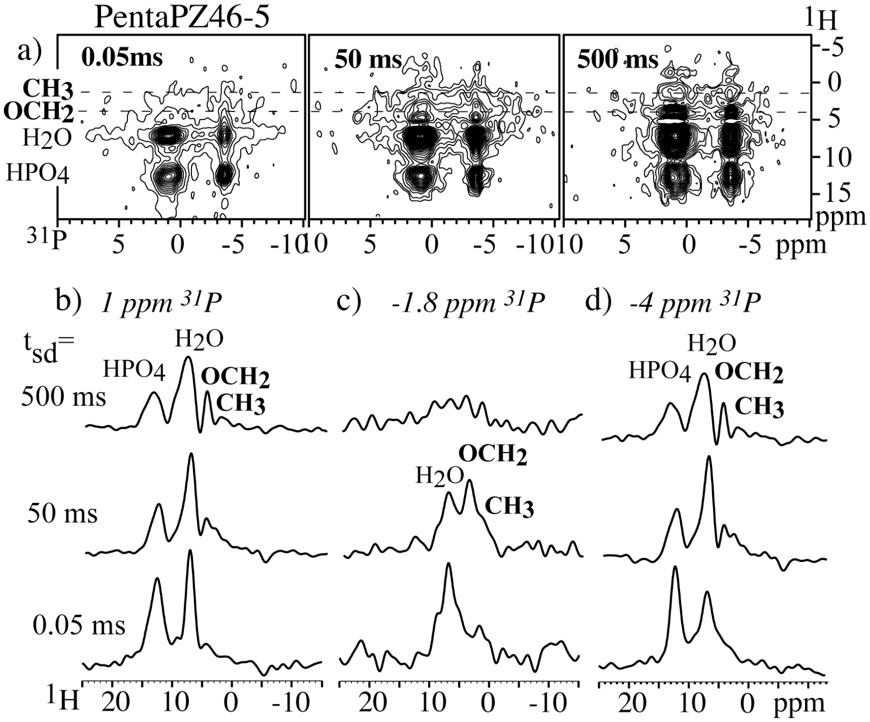

Figure S4. a) 2D ^{1}H-^{31}P HETCOR NMR spectra of PentaPZ46-5 with spin diffusion mixing times of 0.05 ms, 50 ms, and 500 ms. b), c) and d) are cross sections of the 2D spectra at 1.0, -1.8 and -4.0 ppm ^{31}P.

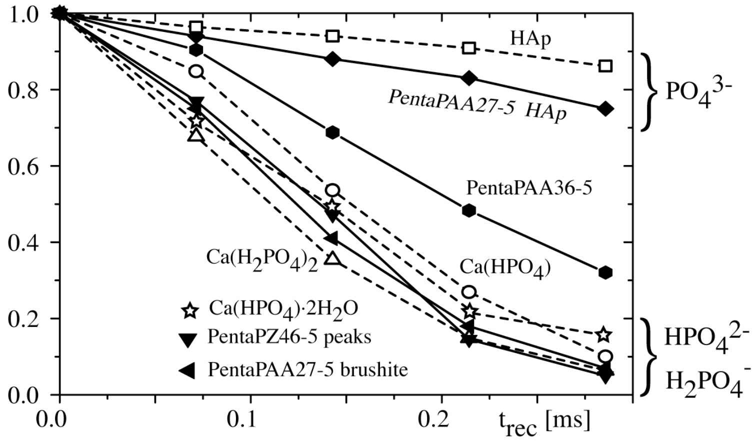

Figure S5. Dephasing of ^{31}P NMR signal under ^{31}P{^{1}H} dipolar recoupling for the polymer—calcium phosphate composites and model compounds. Corresponding spectra for recoupling times of 0 and 2 t_r are shown in Figure 2 of the main text. Spinning frequency: 7 kHz.

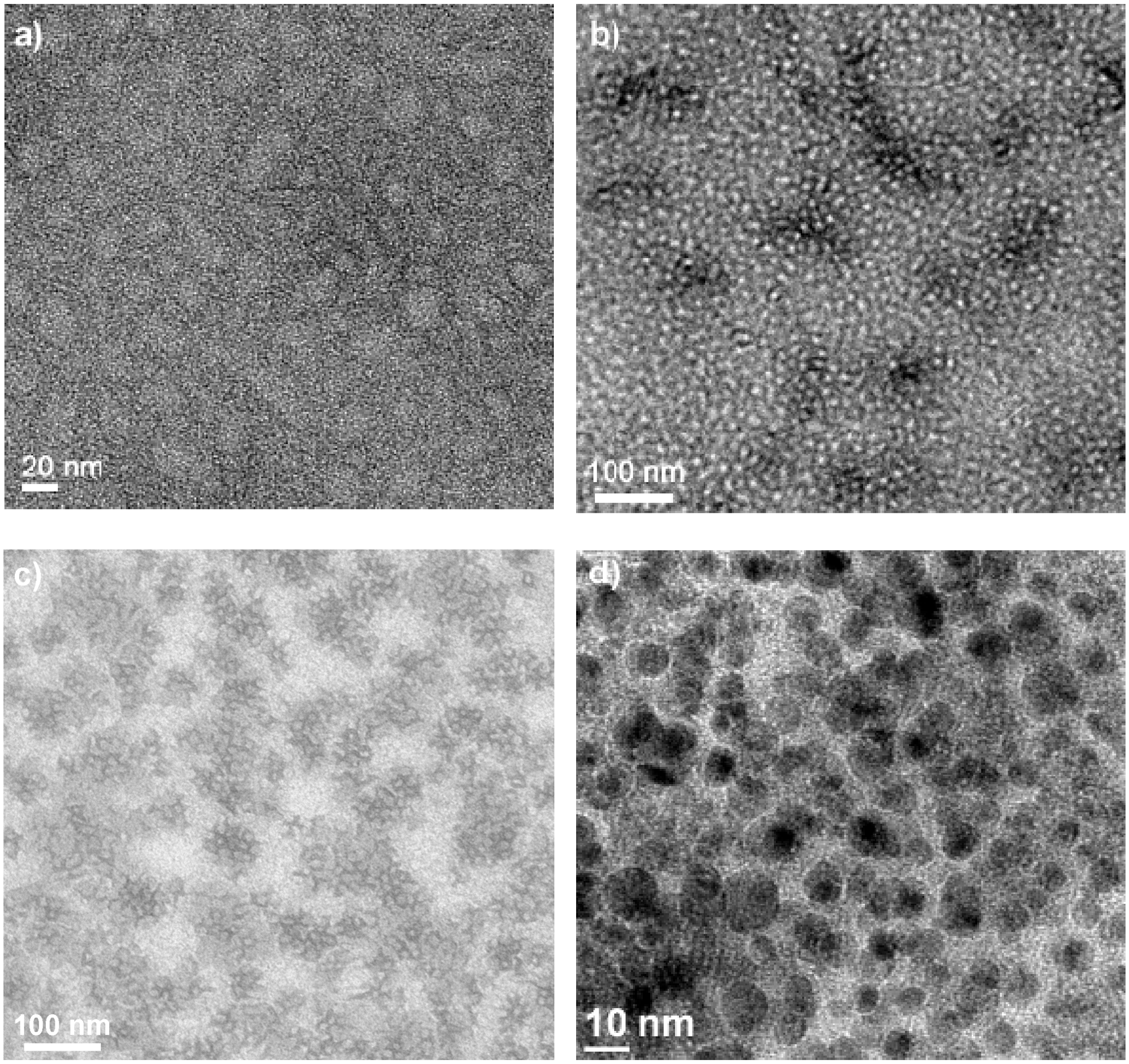

Figure S6. Transmission electron micrographs of stained a) 5 wt% PentaPAA polymer prepared in deionized water, and b) PentaPAA27-5 nanocomposite deposited from a suspension diluted to 5 wt% polymer. Bright spots: unstained polymer. c) PentaPAA36-5 nanocomposite deposited from a suspension diluted to 5 wt% polymer. d) High-angle annular dark field (HAADF) image of diluted PentaPAA27-5 without stain decoration.

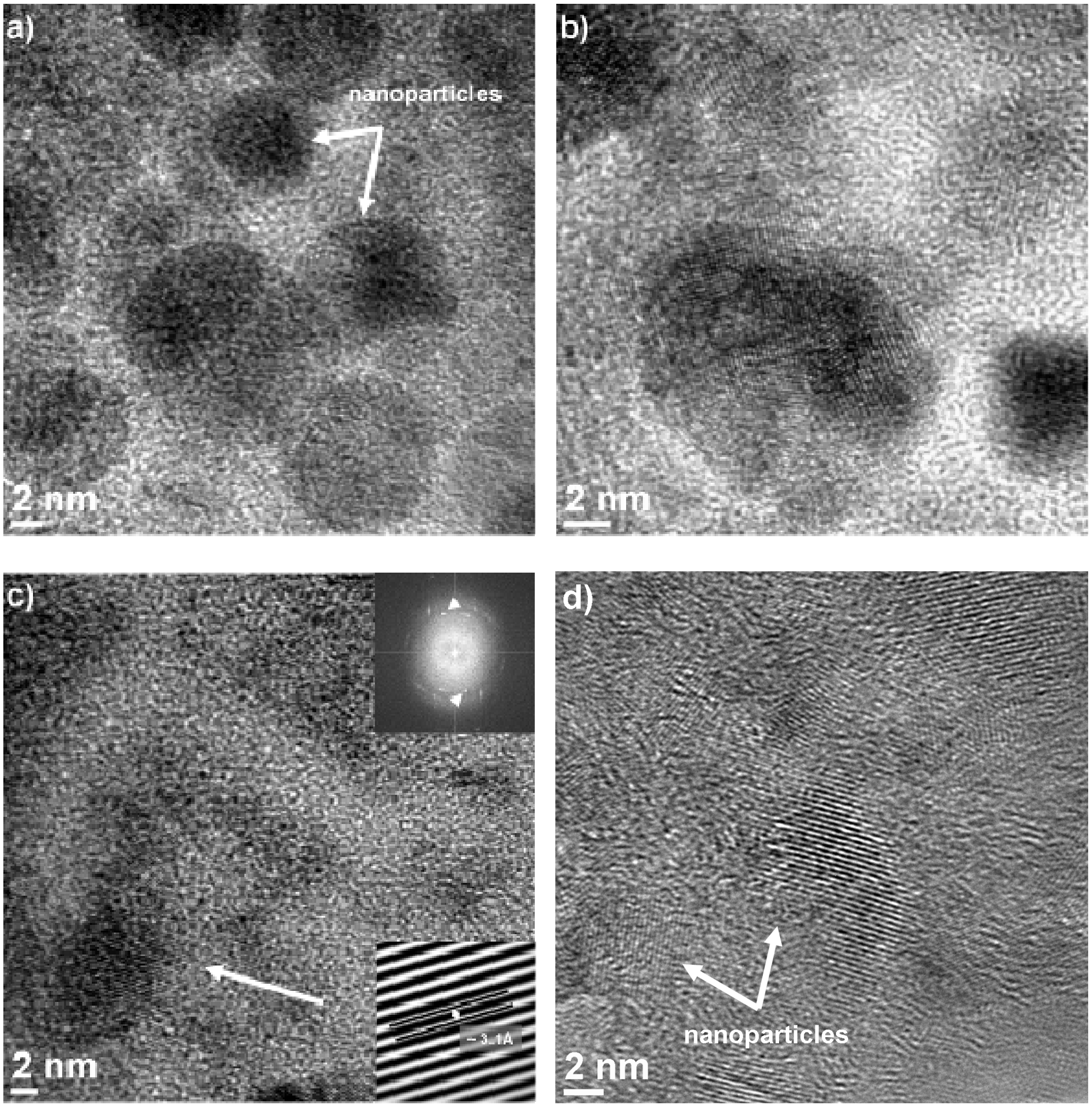

Figure S7. HRTEM images of a-c) PentaPAA27-5, and d) PentaPAA36-5. The upper and lower insets show the FFT patterns and filtered inverse-FFT images, respectively. Calcium phosphate nanocrystals with sizes on the order of 5-10 nm were observed in PentaPAA27-5 sample. The existence of brushite was confirmed in PentaPAA27-5. Moreover, the analysis of c) showed that hydroxyapatite might also be present in PentaPAA27-5, consistent with NMR.

Additional References

29. Wanka, G.; Hoffmann, H.; Ulbricht, W. Macromolecules 1994, 27, 4145-4149.
30. Petrov, A. I.; Antipov, A. A.; Sukhorukov, G. B. Macromolecules 2003, 36, 10079-10086.
31. Chen, Q.; Schmidt-Rohr, K. Solid State NMR 2006, 29, 142-152.
32. Clauss, J.; Schmidt-Rohr, K.; Spiess, H. W. Acta Polymer. 1993, 44, 1-17.

APPENDIX B

Supplementary information for the manuscript "Self-assembled calcium phosphate nanocomposites using block copolypeptide templates"

Yanyan Hu, Yusuf Yusufoglu, Mathumai Kanapathipillai, Chu-Ya Yang, YaQiao Wu,
Papannan Thiyagarajan, Timothy Deming, Mufit Akinc, Klaus Schmidt-Rohr, and
Surya Mallapragada

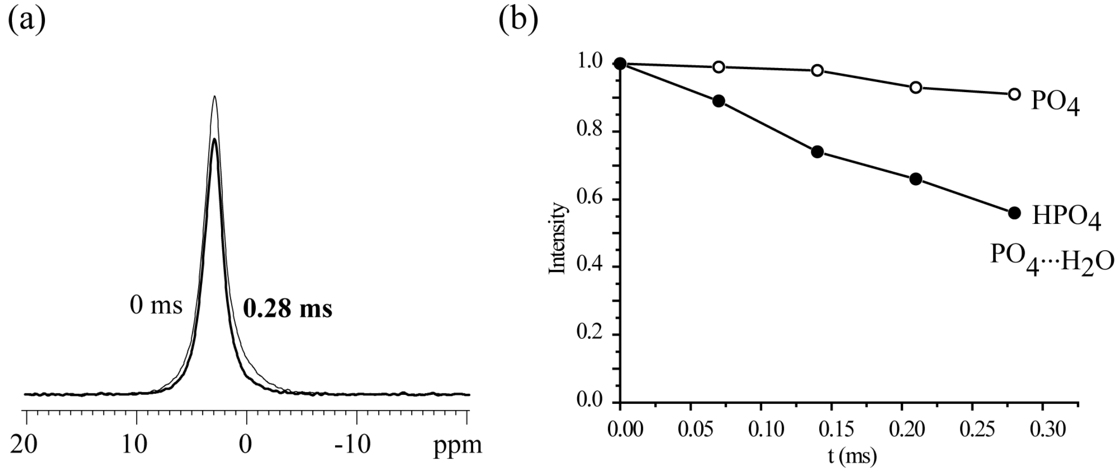

Figure S1. Determination of phosphate protonation state by ^{31}P NMR. (a) DP/MAS with recoupled ^{1}H-^{31}P dipolar dephasing for zero (thin line) and two rotation periods (thick line). (b) Plot of normalized ^{31}P NMR intensity as a function of dipolar dephasing time.

ACKNOWLEDGMENTS

I would like to give my special thanks to my advisor Dr. Mufit Akinc for his guidance and constant support throughout my PhD study. I have learned a great deal under his guidance and encouragement during my research work. His contribution to this work is greatly appreciated.

I would like to give a big thanks to my committee members, Dr. Surya Mallapragada, Dr. Klaus Schmidt-Rohr, Dr. Matthew J. Kramer, and Dr. Zhiqun Lin for their efforts, suggestions and fruitful discussions on the bioinspired materials project.

I would also like to thank the bioinspired materials collaborative project group members Mathumai Kanapathipillai, Yanyan Hu, Mowen Li, Drew Enlow for their help and support. Thanks to Yunus E.Kalay, Yaqiao Wu, Pratik K. Ray, Zhihong Tang, and In-Seok Seo for their assistance throughout this work.

It is my pleasure to thank my parents and my sister for their love, support and encouragement throughout my career.

This document has been authorized by the Iowa State University of Science and Technology under Contract No. DE-AC02-07CH11358 with the U.S. Department of Energy. The U.S. Government retains a non-exclusive, paid-up, irrevocable, world-wide license to publish or reproduce the published form of this document, or allow others to do so, for U.S. Government purposes.